Vanadium And Niobium Additions In Pressure Vessel Steels.

INFORMATION TO USERS

This manuscript has been reproduced from the microfilm master. UMI films the text directly from the original or copy submitted. Thus, some thesis and dissertation copies are in typewriter face, while others may be from any type of computer printer.

The quality of this reproduction is dependent upon the quality of the copy submitted. Broken or indistinct print, colored or poor quality illustrations and photographs, print bleedthrough, substandard margins, and improper alignment can adversely affect reproduction.

In the unlikely event that the author did not send UMI a complete manuscript and there are missing pages, these will be noted. Also, if unauthorized copyright material had to be removed, a note will indicate the deletion.

Oversize materials (e.g., maps, drawings, charts) are reproduced by sectioning the original, beginning at the upper left-hand corner and continuing from left to right in equal sections with small overlaps. Each original is also photographed in one exposure and is included in reduced form at the back of the book.

Photographs included in the original manuscript have been reproduced xerographically in this copy. Higher quality 6" x 9" black and white photographic prints are available for any photographs or illustrations appearing in this copy for an additional charge. Contact UMI directly to order.

U·M·I

University Microfilms International
A Bell & Howell Information Company
300 North Zeeb Road, Ann Arbor, MI 48106-1346 USA
313/761-4700 800/521-0600

Order Number 9226089

Vanadium and niobium additions in pressure vessel steels

Xu, Peiyuan, Ph.D.

Lehigh University, 1992

U·M·I
300 N. Zeeb Rd.
Ann Arbor, MI 48106

Alan W. Pense

VANADIUM AND NIOBIUM ADDITIONS IN PRESSURE VESSEL STEELS

By
Peiyuan Xu

A Dissertation
Presented to the Graduate Committee of
Lehigh University
in Candidacy for the Degree of
Doctor of Philosophy
in
The Department of Materials Science and Engineering

Lehigh University
April 1992

Certificate of Approval

Approved and recommended for acceptance as a dissertation in partial fulfillment of the requirement for the degree of Doctor of Philosophy.

15 May 1992
(Date)

Alan W. Pense
Dr. Alan W. Pense
Professor in Charge

Accepted 15 May 1992
(Date)

Special Committee directing
the doctoral work of Peiyuan Xu

Alan W. Pense
Dr. Alan W. Pense
Chairman

Bruce R. Somers
Dr. Bruce R. Somers

John W. Fisher
Dr. John W. Fisher

David B. Williams
Dr. David B. Williams

ACKNOWLEDGEMENT

The author wishes to express his sincere gratitude to Dr. Alan W. Pense, his dissertation advisor, for giving the timely and valuable encouragement, support and guidance that enabled him to pursue his Ph.D. program. The constant advice of Dr. Bruce R. Somers throughout the course of this dissertation research is also gratefully acknowledged. Appreciation is also expressed to the other members of the author's Special Committee: Dr. John W. Fisher and Dr. David B. Williams, for their suggestions and assistance.

The author also wishes to express his gratitude to Dr. Robert P. Wei for encouragement and support in the early stages of the Ph.D. study.

The helpful discussions and technical assistance of Dr. Eric Kaufmann, Dr. Ming Gao, Dr. Weifang Qin and Mr. Dezhou Chen are greatly appreciated.

Appreciation is extended to Mr. Arlan Benscoter, Mr. Dave Ackland, Ms. Andrea Pressler and Ms. Kathy Repa for lab assistance.

The financial support of this project by the Pressure Vessel Research Committee and the ATLSS Center is gratefully acknowledged.

The author deeply appreciates the understanding, patience and sacrifices of his wife Mrs. Fengmei Xu and his son Mr. Dingying Xu, particularly his son's suffering from three and half years separation from his parents. Thanks are finally extended to author's brothers, Mr. John Z. Xu and Mr. James Q. Xu for their constant encouragement throughout the Ph.D. study.

TABLE OF CONTENTS

LIST OF FIGURES

LIST OF TABLES

ABSTRACT

A statistically designed series of vanadium and niobium microalloyed C-Mn HSLA steels was used for an investigation of heat-affected zone (HAZ) toughness in multipass welds. The vanadium additions were in the range 0.005 to 0.097 Wt.% and the niobium additions were in the range 0.004 to 0.06 Wt.%. GMAW processes with welding heat inputs of 3kJ/mm and 5kJ/mm and post-weld heat treatments (PWHT) at 620°C for 2 and 10 hours were employed. The detrimental effect of the additions of microalloy elements V and Nb on multipass HAZ toughness in the as-welded and PWHT conditions was confirmed. The 50 Joule transition temperature (TT50J) for HAZs in all weld conditions correlated with maximum HAZ hardness. Increases in HAZ hardness and TT50J caused by PWHT were observed. Hence PWHT is not recommended for V/Nb microalloyed HLSA steels.

The randomly distributed precipitation of V and Nb carbides (V,Nb)C, including dislocation precipitation and matrix precipitation with particle sizes of 5-15nm, is the predominant alloy carbide precipitate morphology in these steels. Banded morphology of (V,Nb)C precipitation is rarely observed in the HAZ. The volume fraction of (V,Nb)C precipitates increases as increasing V and/or Nb contents in the experimental heats. The volume fraction of precipitates also increases with increasing the PWHT time.

The crack initiation sites in Charpy specimens of HAZs tested at the approximate transition temperature are shifted from the highest stress triaxiality location to a higher hardness location. This is found to be characteristic of fracture in the multipass HAZ of the microalloyed steel. An analytical study shows that the influences of additions of microalloy elements V and Nb on yield stress, σ_{ys}, and fracture stress, σ_f, eventuate in the increase of transition temperature in these materials.

1. INTRODUCTION

Microalloyed high-strength low alloy (HSLA) steels have been in existence for approximately three decades and have permeated many sections of modern industry. They are more and more widely used in different welded structures such as pressure vessels, natural gas and petroleum pipelines, off-shore platforms, ships, bridges, industrial and commercial vehicles because they provide desired mechanical properties, and satisfactory weldability, formability and product cost. The additions of precipitation-hardening alloy elements Nb, V and Ti allow higher yield strength while maintaining the ductility and toughness and keeping the welding crack susceptibility very low. Compared with the conventional high strength quenched-and-tempered steels, microalloyed steels have the potential for being welded with little or no preheat, and with less stringent process control.

Vanadium and niobium were added as microalloying elements in HSLA steels in later 1950s and earlier 1960s, respectively. The increasing importance of microalloy in HSLA steels can be illustrated by following: while world steel production increased by no more than 5% from 1970 to 1982, the consumption of niobium as a microalloying element doubled during the same period [1].

The carbide-forming elements vanadium and niobium are used separately or jointly in C-Mn HSLA steels in small amounts to

achieve small grain sizes by inhibiting the grain growth of recrystallized austenite by carbide/nitride particles. The fine-grained microstructure is beneficial as it contributes to the optimum combination of higher strength and ductility. Moreover, vanadium and/or niobium carbides/nitrides precipitate during or after the austenite-ferrite phase transformation to further enhance strength, albeit with the sacrifice of some toughness.

Although HSLA steels with excellent combinations of strength and ductility were developed by adding the micro-alloying elements V and/or Nb, detrimental effects on impact toughness and fracture toughness have been observed, particularly on the toughness of the heat-affected zone (HAZ), which is critical in welded structures. This has been shown by comparisons of weldments made of plates containing V and/or Nb to those made of plates with the same nominal compositions but without V and/or Nb additions [2][3][4][5].

In this respect, however, there are contradictory views. Most investigators have concluded that V and/or Nb additions are detrimental to the HAZ toughness, whilst other authors reported that HAZ toughness increased with the addition of Nb at low carbon (0.08%) content or with the addition of V at higher C levels (0.18%) in C-Mn HSLA steels [6]. Japanese sources also indicated that V could exhibit a beneficial influence on the HAZ impact toughness [7]. Kozasu summarized that in the C-Mn system, even a small addition of 0.01%Nb is

effective in increasing strength or improving the Fracture Appearance Transition Temperature (FATT) in 400-500MPa tensile grades and vanadium acts primarily as precipitation hardening element with little influence on FATT [8]. The issue whether or not, and under which circumstances vanadium and/or niobium additions are detrimental to the HAZ toughness needs to be addressed.

Actually, the HAZ toughness in microalloyed HSLA steels depends on the complex interplay of microstructural constituents, grain size, carbide/nitride dissolution and reprecipitation, base plate chemistry and HAZ cooling rate. Vanadium and/or niobium carbides/nitrides dissolve during the heating cycle of fusion welding and reprecipitate if cooling is slow enough. It follows that the effect of the addition of vanadium and/or niobium on HAZ toughness depends on cooling rate from welding, i.e., on the welding heat input, the plate thickness and the effect of soluble V and/or Nb and on the phase transformation occurring during cooling. The situation will be more complicated when two or more microalloying elements are presented in the steel.

For the use of microalloyed HSLA steels in pressure vessel applications, a lower hardness HAZ is generally required to prevent hydrogen-assisted cold delayed cracking during manufacture or stress-corrosion cracking during service. An HAZ hardness of HV350 is considered as the level inducing cracking and an HAZ hardness of HV300 is normally desired. In

as-welded HSLA steels the requirements of low HAZ hardness may not always be met and therefore post-weld heat treatment (PWHT) is usually employed to reduce HAZ hardness as well as relieve residual stresses. The HAZ hardness, however, in V/Nb bearing HSLA steels sometimes unexpectedly increases after PWHT due to V/Nb carbide/nitride precipitation [9]. The dissolved V and/or Nb carbides/nitrides in the HAZ may not fully precipitate during fast cooling. The ferrite remains supersaturated to room temperature. The subsequent PWHT will promote further precipitation hardening in the HAZ. The authors at Lehigh also pointed out that PWHT does not consistently improve HAZ toughness over the as-welded condition and thus PWHT was suggested not to be used in ASTM A710 steel [10].

Multipass welding, which is a routine procedure in constructional welding practice, complicates the effect of V/Nb additions on HSLA steel HAZ toughness. In a multipass welding, a range of cycles of progressively lower peak temperature will be superimposed at a single HAZ location. The HAZ microstructure of each bead will be altered by the subsequent weld thermal cycle. The multiple thermal cycles which create the HAZ are responsible for various precipitate reactions and phase changes. As a result, the metallurgical heterogeneity existing in the HAZ of these welds is extremely large. Certain physical properties, such as fracture resistance, are sensitive to the heterogeneity of the HAZ, and

this sensitivity may manifest itself as data scatter.

A number of studies dealing with vanadium and/or niobium additions in HSLA steels have been published, but much of this work has failed to completely clarify the role vanadium and/or niobium additions play in determination of mechanical properties of the multipass HAZ in HSLA welds, as well as provide microstructural interpretation of the effects of these heat treatments.

Therefore, the objectives of this research work have been as following: (1) To develop data on HAZ impact toughness and hardness under various metallurgical conditions, including various vanadium and niobium contents, low and high welding heat inputs and various PWHT conditions. (2) To identify the specific microstruc-tural details that can lead to significant changes in the HAZ toughness and hardness, especially the functions of vanadium and niobium additions, welding heat inputs and post-weld heat treatment. (3) To investigate the fracture mechanism in a multipass HAZ, including crack initiation and crack propagation, and the mechanical and microstructural aspects that are in control of fracture process.

2. BACKGROUND

2.1. FUNDAMENTAL ASPECTS OF MICROALLOYED HSLA STEELS

2.1.1. BASIC DESCRIPTION

The development of microalloyed HSLA steels was a successful metallurgical innovation in which alloying additions and thermomechanical processing have been brought together effectively to obtain improved strength-toughness-formability-weldability combinations through microstructural control. All microalloyed HSLA steels contain small concentrations of one or more strong carbide and nitride forming elements, notably vanadium, niobium and titanium. These carbide-forming elements under most circumstances combine preferentially with carbon to form very fine dispersive carbides. Cementite or alloyed cementite can form only if carbon is present in excess of the stoichiometric limit required to satisfy the stronger carbide formers V, Nb and Ti.

Generally speaking, the carbide-forming elements V and Nb have several roles in HSLA steels. Firstly, the dissolved V and/or Nb give solid solution strengthening. In ferrite, solid solution formation gives rise to a lattice distortion and an increase in ferrite hardness. In austenite, the effect is to hinder diffusion and hence to delay transformation. Secondly, V and/or Nb refine grain size during controlled rolling, with a subsequent substantial influence on ferrite

grain size resulting from austenite-ferrite transformation. Thirdly, the main role of V and/or Nb additions is precipitation hardening. A fine carbide/nitride dispersion forms during and after phase transformation. The particles of vanadium and/or niobium carbides/nitrides have sizes of approximately 10 nm and hardness HV2094 for VC, HV1520 for VN, HV2400 for NbC and HV1396 for NbN [11]. The fine, hard and dispersed particles strengthen the metal effectively. In a welding process in microalloyed steels, precipitation in the HAZ may not be fully complete due to fast cooling rates. The extent of supersaturation of V and Nb in ferrite depends on the original concentration of V and/or Nb in the steel, the welding heat input and plate thickness. Age hardening takes place during PWHT. It then counteracts the softening by stress relief and the decomposition of lower temperature transformation products such as martensite and bainite. The reduction in HAZ hardness by PWHT may be considerably suppressed under these circumstances.

2.1.2. BASIC INFORMATION OF VANADIUM AND NIOBIUM CARBIDES IN STEELS

The ratio r_c/r_m of the atomic radius of carbon r_c to the atomic radius of the transition metal r_m determines the carbide crystalline structure. For the carbides with $r_c/r_m<0.59$, a simple lattice will exist with carbon atoms in the interstitial positions of the lattice such as VC, NbC, TiC

and ZrC. The r_c/r_m values for V, Nb, Ti, Zr are 0.57, 0.53, 0.53, 0.48, respectively [11], and thus they meet this condition. The V-C phase diagram and Nb-C phase diagram are shown as Figure 2.1 and Figure 2.2, respectively [12]. The V-C phase diagram shows that at elevated temperature only two intermediate phases exist, V_2C and VC, both exhibiting wide ranges of homogeneity. In the carbon-rich side, below the eutectic equilibrium temperature (2670°C) the boundary of the VC phase is almost vertical. VC has a NaCl structure with a lattice parameter from 0.4126nm to 0.4175nm, depending on the carbon content, as illustrated in Figure 2.3 [13]. The fact that the lattice parameter increases with increasing carbon content implies that vacancies exist in the crystal and the VC phase could be hypostoichiometric. The ratio of carbon atoms in VC may vary in the range of 43-50 at%.

The Nb-C phase diagram shown in Figure 2.2 indicates the wide and homogeneous NbC field on the C-rich side. NbC has the NaCl crystalline structure with a lattice parameter 0.4460nm [14]. The propotion of carbon atoms in NbC may vary in the range of 36-50 at.% with a corresponding variation in lattice parameter. The hardness of both VC and NbC will decrease with decreasing the carbon atomic concentration in carbides.

A V-Nb binary diagram shown in Figure 2.4 indicates that V and Nb form a continuous solid solution over the full concentration range [12]. Also, the carbides and nitrides of

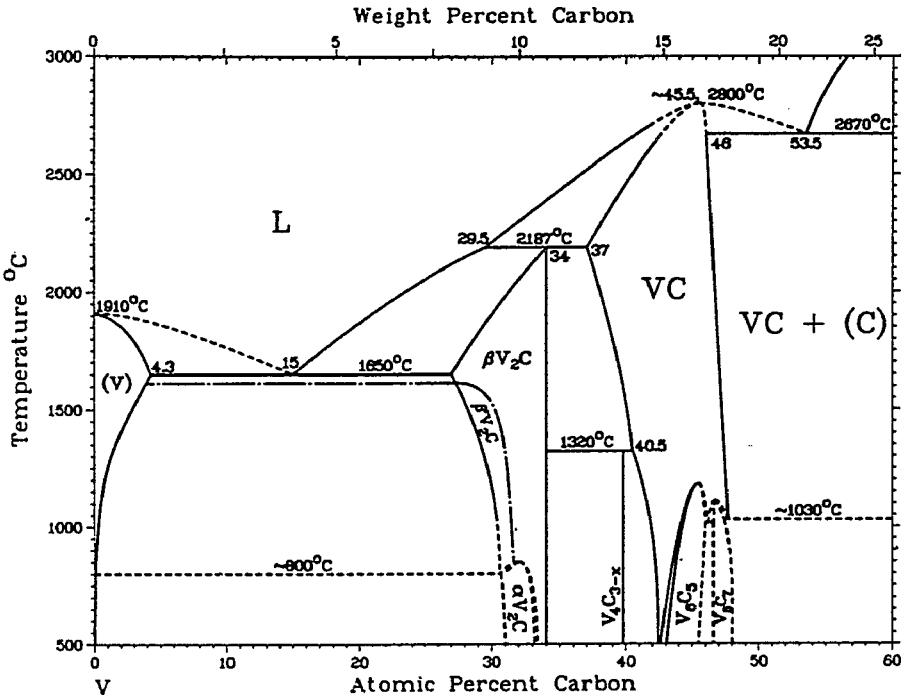

Figure 2.1 Assessed V-C phase diagram [12]

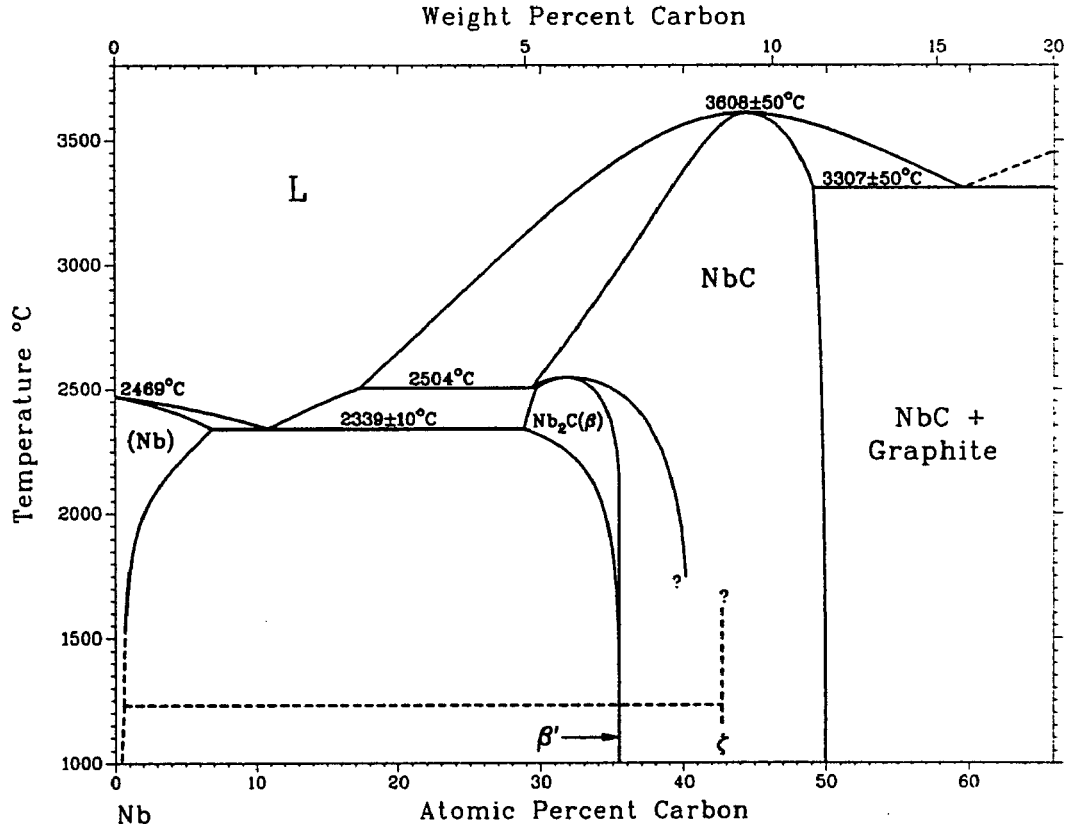

Figure 2.2 Nb-C phase diagram [12]

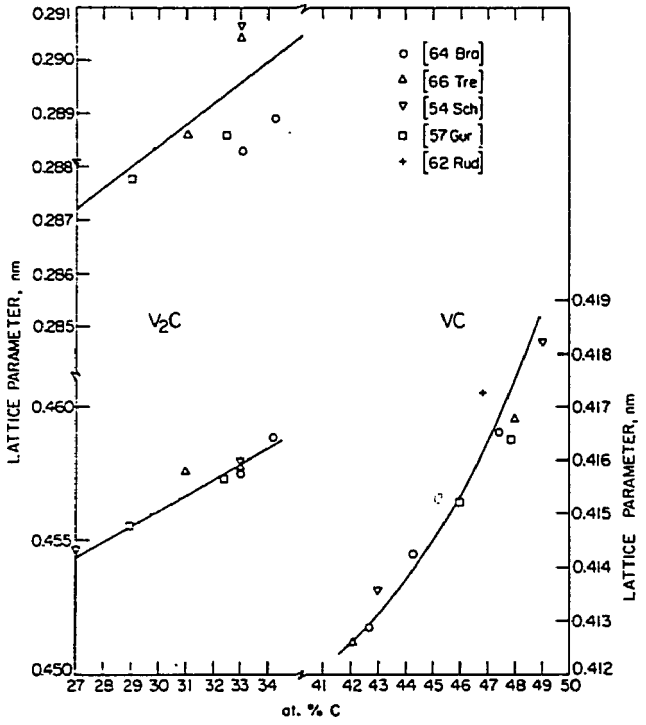

Figure 2.3 Lattice parameters for V_2C and VC phase fields [13]

V and Nb are isomorphous. They are expected to form a wide range of compositions in which both the metallic (V and Nb) and non-metallic (C and N) atoms can be substituted [15]. The above information will assist the electron microscopic analysis in this research work.

Figure 2.5 illustrates the precipitation and dissolution characteristics of vanadium and niobium carbides in austenite [16]. It is well established that VC is much more soluble in austenite than NbC. A steel microalloyed with Nb will exhibit NbC precipitation at much higher temperature than a V-containing steel will precipitate VC. These differences in

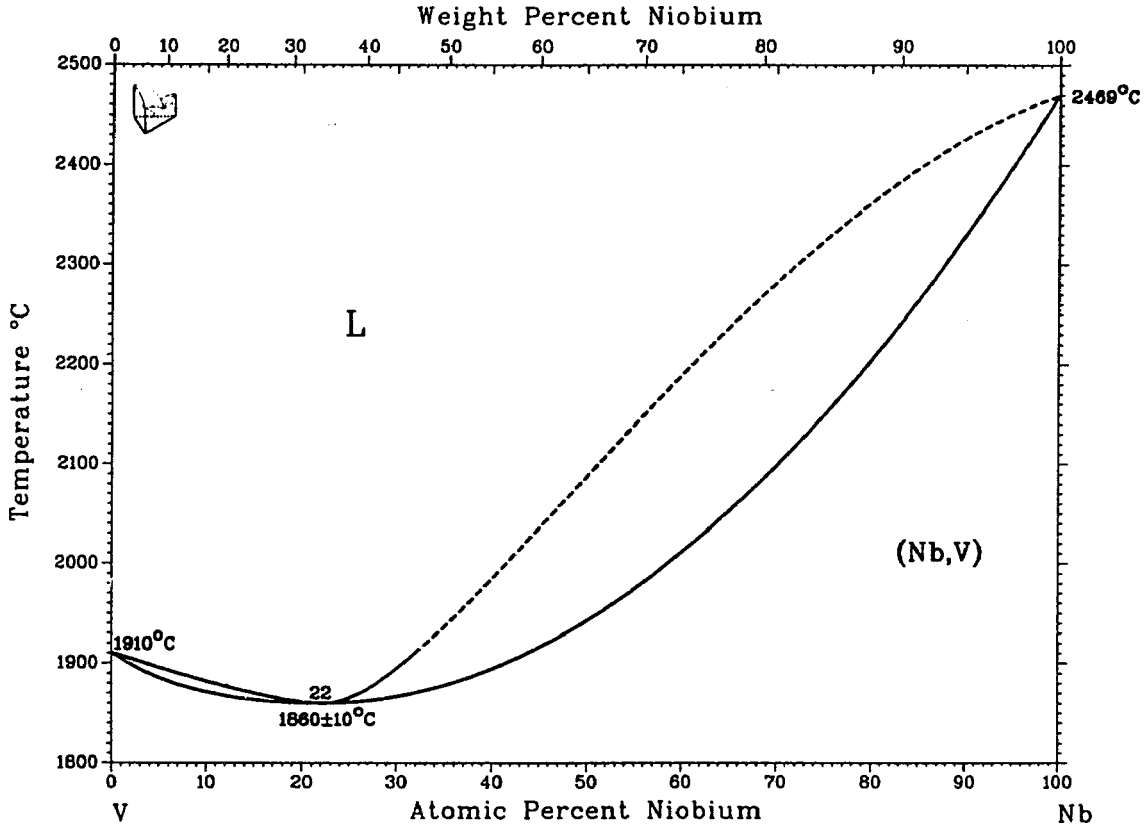

Figure 2.4 V-Nb phase diagram [12]

precipitation and dissolution between VC and NbC may result in differences in microstructure and mechanical properties in V-bearing steel and Nb-bearing steel.

Irvine reported that [17] at the normalizing temperature of 950°C, the C-Mn steel containing 0.02% Nb has a refined grain size, but there is no precipitation strengthening because of the insolubility of niobium carbide at this temperature. Reheating at 1100°C and 1250°C produces grain coarsening and significant precipitation strengthening which increases as the reheating temperature increases. Figure 2.6

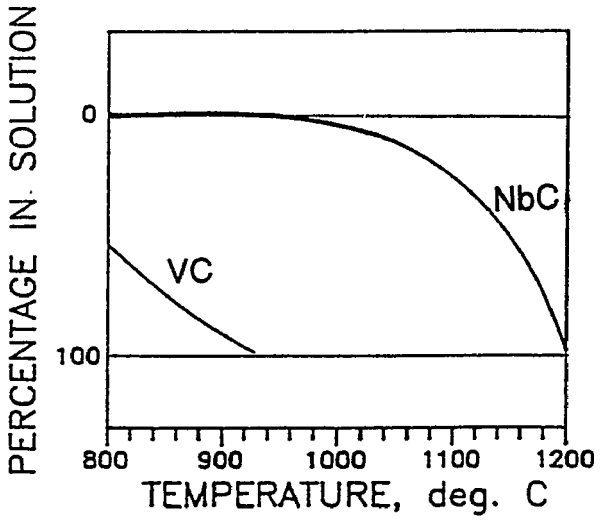

Figure 2.5 The solubility of VC and NbC in austenite [16]

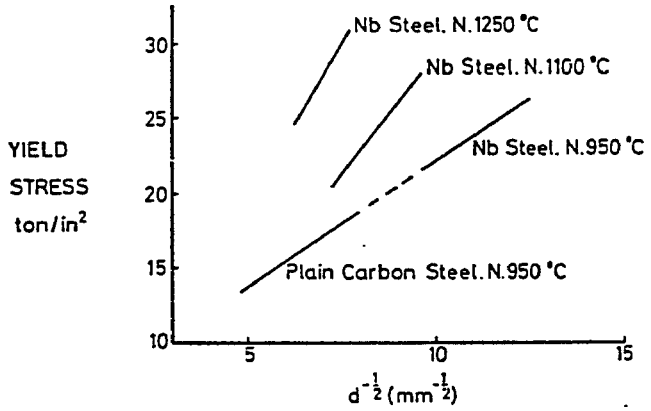

Figure 2.6 Effect of austenitizing temperature on niobium strengthening [17]

shows the effect of reheating temperature on yield stress of C-Mn steel containing 0.02%Nb. A different effect is obtained when a C-Mn steel containing 0.05% V is reheated. At the normalizing temperature (950°C) the V-containing steel has a refined grain size compared with the V-free steel and there is substantial precipitation strengthening due to the readily soluble vanadium carbide. Reheating at 1100°C and 1250°C

produces grain coarsening but little increase in precipitation strengthening.

In the as-rolled condition, however, the final microstructure and mechanical properties depend not only on Nb and V additions but also on the rolling schedule. The degree of grain refinement is controlled by the roll finishing temperature. Most of the niobium carbide taken into solution during reheating remains in solution during the rolling operation with precipitation occurring during subsequent cooling. The final properties for Nb-steel will depend on the reheating temperature prior to rolling. The V-steel has the same response to rolling, except that the properties are not sensitive to the reheating temperature prior to rolling. This is because full solution of vanadium carbides is obtained at all reheating temperatures.

The effect of V and/or Nb additions on the microstructure and mechanical behavior of weld heat-affected zone (HAZ) in HSLA steel will be discussed later on.

2.1.3. PRECIPITATION PROCESSES OF V AND Nb CARBIDES/NITRIDES

2.1.3.1. PRECIPITATION IN AUSTENITE

Precipitation is sluggish in undeformed austenite, but much more rapid in deformed and unrecrystallized austenite. The intensity of such precipitation is controlled by the amount of strain and the degree of supersaturation [18]. V and Nb retard the rate of recovery, which in turn delays the onset

of recrystallization. The precipitates formed at lattice imperfections and at grain boundaries, inhibit the growth of recrystallized austenite via the pinning of grain boundaries, sub-boundaries and dislocation arrays. Gladman has shown [15] that the grain growth is inhibited providing the particle size is below a critical radius r_c

$$r_c = \frac{6R_o f}{\pi} \left(\frac{3}{2} - \frac{2}{Z} \right)^{-1} \qquad (2.1)$$

where f=volume fraction of precipitates, R_o=original grain size, Z=ratio of radii of growing grains to original grains (R/R_o) which is described as a grain size heterogeneity. The critical particle size increases as f or R_o is increased. The stability of grain boundaries at high temperature is ensured if precipitation occurs at as high a temperature as possible, and if the precipitates are sufficiently fine to pin the boundaries. Three criteria must be satisfied by the dispersion:

1. Particle size and spacing must be below critical values.

2. Sufficient volume fraction of precipitates must be present to maintain spacing below critical values.

3. Low rate of coarsening of precipitation must occur to maintain dispersion below critical parameters.

To meet the above requirements, niobium in the form of Nb(CN) is one of the best grain pinning precipitates. Vanadium is not as efficient a grain refiner, although it has the

advantage of forming denser dispersions in ferrite for strengthening.

2.1.3.2. PRECIPITATION DURING THE AUSTENITE/FERRITE TRANSFORMATION

The kinetics of the ferrite→austenite transformation would be influenced by the precipitation prior to transformation, and the morphology of the ferrite/austenite interface would be modified. There is some evidence to suggest that the ferrite/austenite interface can be pinned by precipitates formed in the austenite [19].

It is important that the solid solubilities of carbides of V and Nb are approximately an order of magnitude less in ferrite than in austenite. It follows that substantial precipitation of V and/or Nb carbides should take place when austenite is replaced by ferrite. In a plain carbon steel, the precipitation of Fe_3C is mainly in the form of pearlite if the cooling rate is slow enough. In V and/or Nb microalloyed steels, provided the carbon content is above that needed to combine V and/or Nb, the V and/or Nb are not usually precipitated in direct association with pearlite. Precipitation of V and/or Nb carbides takes place during γ/α transformation on a much finer scale compared with Fe_3C because the nucleation and growth depends on the diffusivity of V and/or Nb. The precipitates exhibit four morphologies, as shown in Figure 2.7 [15].

1, Planar interface precipitation - parallel bands of discrete (Figure 2.7a).

2, Non-planar interface precipitation - apparently random precipitation arrays (Figure 2.7b).

3, Non-planar interface precipitation - curved and irregular band of particles (Figure 2.7c).

4, Growth of fine carbide fibers (Figure 2.7d).

Several morphologies of VC and NbC were observed in this research work and the relevant mechanisms will be discussed later.

2.1.3.3. PRECIPITATION AFTER THE AUSTENITE/FERRITE TRANSFORMATION

The studies on precipitation during continuous cooling subsequent to the $\gamma \rightarrow \alpha$ transformation reveal that not all precipita-tion occurs in association with γ/α interface. Smith and Honeycombe indicated that the dislocation densities in the ferrite of a microalloyed steel Fe-0.2Ti-0.08C were much higher than in the plain carbon steels. Fine TiC particles were found on the disloca-tions which would markedly reduce movement by climb and would partly account for the high densities observed [20]. Research work on simple niobium steel by Sakuma and Honeycombe has shown at an isothermal transformation temperature as low as 750°C the very finely dispersed matrix precipitation of NbC formed extensively from supersaturated ferrite [21][22]. At even lower temperature

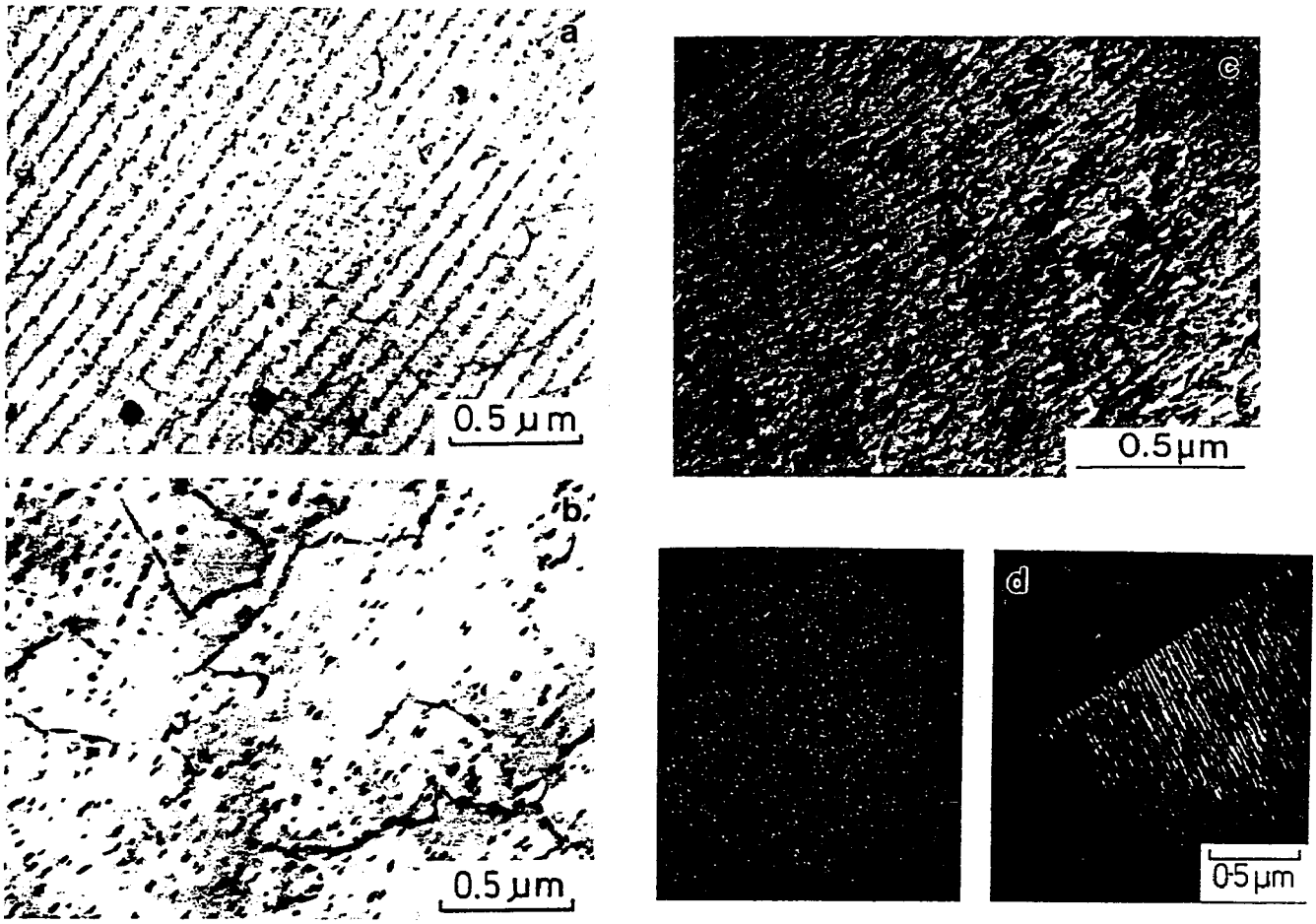

Figure 2.7 Various morphologies of NbC precipitation [15]

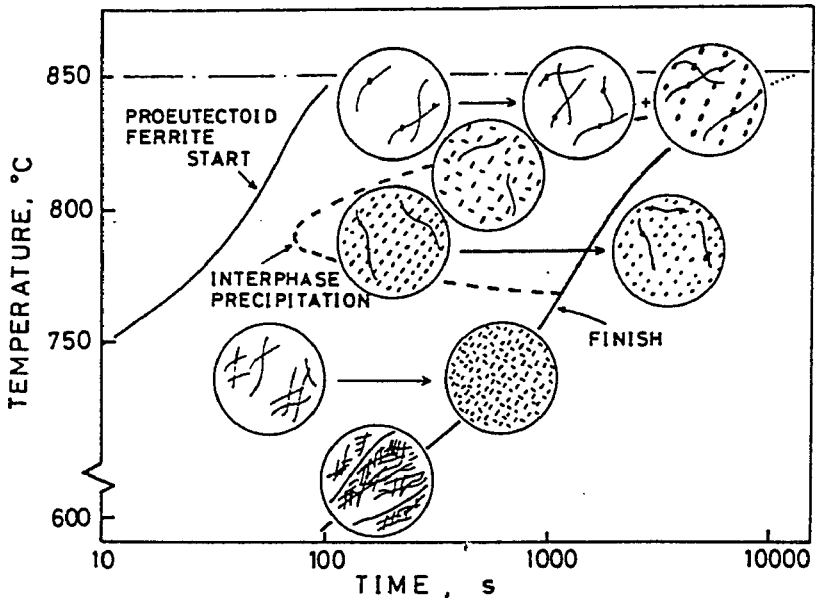

Figure 2.8 Microstructures formed by isothermal transformation [21]

(about 700°C), uniform precipitation of NbC is suppressed probably as a result of the low diffusivity of niobium. The microstructures (dislocations and precipitates) formed by isothermal transformations in Nb-bearing steel are summarized in Figure 2.8 [21].

If the cooling rate from austenization is so fast that the precipitation of alloy carbides prior to, during and subsequent to the $\gamma \rightarrow \alpha$ transformation is not completed, such as in the case of the thermal cycle of welding, the precipitation will take place during the subsequent tempering or annealing, e.g., the post-weld heat treatment for weld stress relief, resulting in secondary hardening of microalloyed steels.

2.2. THE HEAT-AFFECTED ZONE (HAZ) IN THE WELD

2.2.1. GENERAL DESCRIPTION OF THE HEAT-AFFECTED ZONE

In a fusion welded joint of structural steel, the heat-affected zone is usually a "weak link" in the weldment due to its higher hardness and lower toughness. Considering the additional unfavorable welding residual stress distribution, the HAZ is thus the most critical portion of a welded construction.

The true HAZ is the portion of the welded joint that has experienced peak temperature high enough to produce solid-state microstructural changes but too low to cause any melting. The HAZ for a transformable steel can be divided into a number of sub-zones and this is typically illustrated in

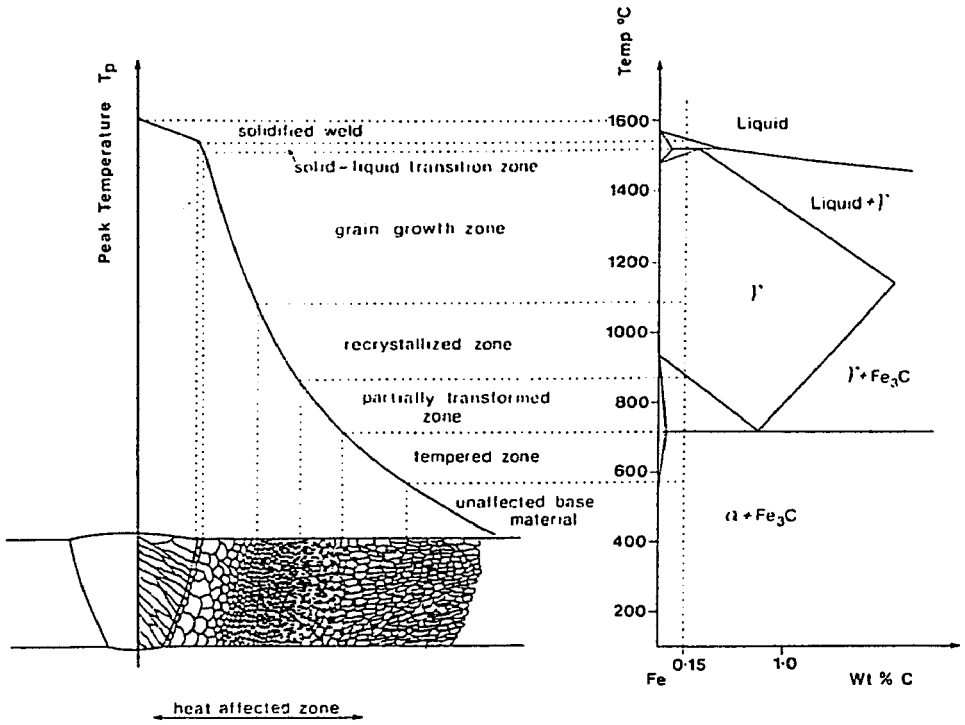

Figure 2.9 A schematic diagram of the various sub-zones of HAZ in 0.15 Wt.%C steel [23]

Figure 2.9 [23].

Two main regions can be conveniently observed in the HAZ in transformable steels: the grain-growth region (or called coarse-grained region) which lies adjacent to the weld interface, and the grain-refined region which is farther away from the weld interface.

The development of the grain-growth region which has experienced peak temperature approaching the solidus of the base metal depends on the peak temperature, the holding time at the temperature, the activation energy of grain growth of the steel, the prior thermal and mechanical history of the steel and, as described above, the effect of microalloyed

elements V and Nb. The grain-refined region has been thermally cycled only briefly into the low-temperature portion of the austenite region, resulting in significant grain refinement. This grain-refining reaction occurs by the nucleation of new grains each time the A_1 and A_3 lines are crossed, either upon heating or cooling in welding.

Each HAZ sub-zone refers to a different type of microstructure which is governed by the steel chemistry and the thermal cycle experienced. The mechanical properties vary across the different sub-zones. Among the HAZ sub-zones the grain-growth region which experienced the most severe thermal cycle usually possesses the worst mechanical properties and the most attention is usually given to this portion in alloy design and welding procedure. Increase in the peak temperature, the time at peak temperature and the cooling rate through the transformation range will promote the formation of higher hardness constituents in the microstructure of the grain-growth region. All these variables are related to the weld heat input, weld geometry and material hardenablity. The cooling time Δt_{8-5} through the range 800°C - 500°C as descriptive of a given weld has been widely adopted in welding circles as an important index. The temperature of 800°C in most HSLA steels approximately represents the A_3 transformation temperature and the γ/α transformation takes place through 800°C - 500°C. The parameter Δt_{8-5} can be either measured experimentally or calculated with the equation [23]:

$$\Delta t_{8-5} = \frac{q/v}{2\pi\lambda\Theta_1} \qquad (2.2)$$

where q is the heat input, in terms of welding current and voltage and the efficiency of the arc; v is the arc speed and q/v represents the heat input per unit length; λ is the thermal conductivity; Θ is defined as:

$$\frac{1}{\Theta} = \left(\frac{1}{773-T_o} - \frac{1}{1073-T_o} \right) \qquad (2.3)$$

where T_o is the initial temperature prior to welding (or pre-heat temperature).

2.2.2. THE GRAIN GROWTH REGION

Two cycles, the heating cycle and the cooling cycle are involved in a fusion welding process. The rate of heating to the peak temperature determines the temperature of recrystallization, the degree of superheating in the $\alpha \rightarrow \gamma$ transformation and the rate of coarsening of carbides and nitrides in microalloyed HSLA steels. These factors affect the degree of grain growth in the HAZ. The cooling cycle, on the other hand, affects the final microstructure. Both heating and cooling cycles determine the final properties of the HAZ.

As described in Section 2.1.3, the pinning of particles of carbide and nitride inhibits the grain growth. Several cases in microalloyed steel can be observed. In most steels, experimental observations have indicated that grain growth in many steels occurs predominantly at temperature above the

equilibrium solubility limits of carbides and nitrides. This is the case, for example, in a C-Mn-Mo pressure vessel steel where the most stable Mo carbide dissolves at a relatively low temperature. In V and/or Nb microalloyed steels the V and/or Nb carbides may also be expected to dissolve during the heating cycle if the peak temperature is high enough. In the case of carbide dissolution, the grain growth may be estimated by the part of the weld thermal cycle which exceeds the solubility temperature of carbides and nitrides, during which time unrestricted grain growth can occur. In other cases, for example, in Ti-microalloyed steels, the TiN particles remain stable during the weld thermal cycle. To estimate the grain growth extent in this case, even though the TiN does not dissolve, the fact that mean particle size increases while the particle spacing increases has to be taken into account.

It is noted that, in real welds, the geometry of the weld may not always give a uniform HAZ width. As observed in some bead-on-plate welds in this research work, the coarse-grained HAZ width is not uniform along the fusion line due to differences in local thermal environment.

2.2.3. THE HAZ IN MULTIPASS WELD

In steel-structure fabrication, the multipass welding process is commonly employed. The HAZ microstructure of each bead in a multipass process will be altered by subsequent weld thermal cycle. An effective grain refinement or "normalizing"

in the previously deposited weld metal and HAZ will always occur. Figure 2.10 is a schematic comparison of the microstructures of single pass and multipass welds [23]. Figure 2.11 [24] and Figure 2.12 [25] show the details or how a portion of each weld pass becomes the HAZ of the subsequent pass, and each interpass HAZ recrystallizes into a fine-grained structure.

In multipass welding, grain refinement is achieved by metal transforming to austenite upon heating and transforming to lower temperature transformation products upon cooling. The

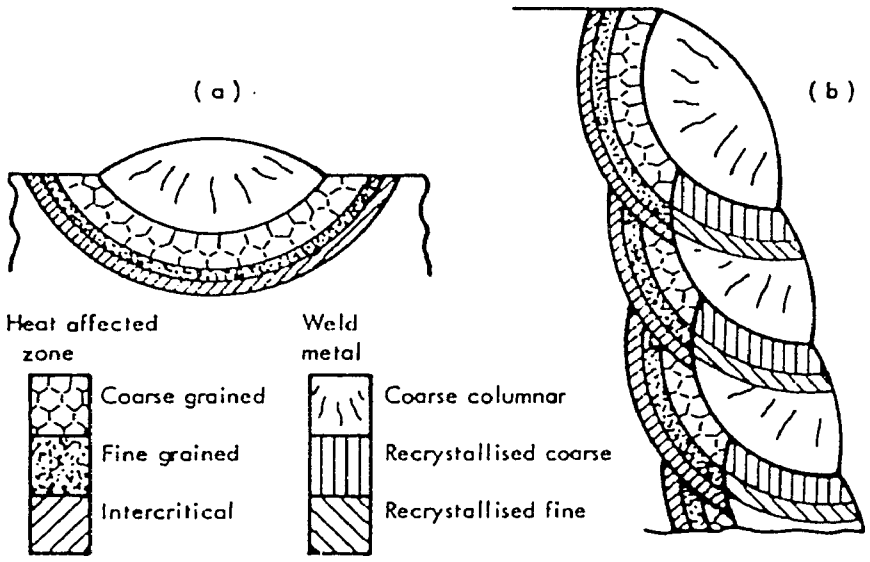

Figure 2.10 A schematic comparison of the microstructures of single pass and multipass welds [23]

larger the number of beads the greater the volume of reheated metal. Changes in toughness and reduction in residual stress may result from grain refinement in multipass welding. A weld deposited on 2-inch-thick steel plate in 50 passes with the

SMAW process will produce a much finer grain size in both the weld and HAZ than a similar weld deposited in one pass with the extremely high heat input electro-slag welding (ESW) process and hence the multipass process seems beneficial [25]. Economical requirements, however, generally lead fabricators to increase the feasible weld deposit size by using higher heat input and larger electrodes. The optimum weld procedure must be chosen by balancing the merits of microstructure, and thus properties, and productivity.

2.3. PRECIPITATION STRENGTHENING MECHANISM

2.3.1. GENERAL DESCRIPTION

As all metallic materials, steel can be strengthened by several basic mechanisms, that is, strain (transformation or work) hardening, solid solution hardening by interstitial atoms, grain size refinement and precipitation hardening. Desired mechanical properties are usually achieved by the combined use of several strengthening mechanisms. The microalloyed HSLA steels are mainly characterized by precipitation strengthening and grain refinement strengthening. Fine precipitates formed in the matrix create a barrier to the movement of dislocations. In the deformation of metal, dislocations move along the slip plane. If the precipitate particles block the dislocations, they must either cut through the particles of precipitates or take a path around the obstacles.

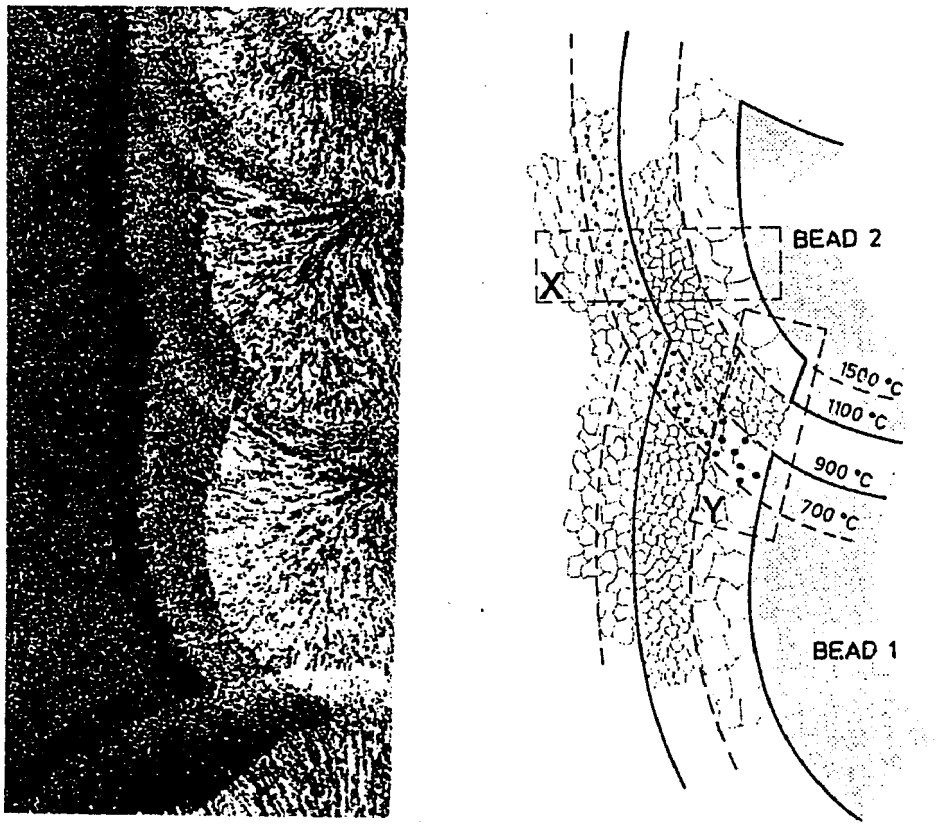

Figure 2.11 Part of the HAZ in a multipass weld with identification of the various HAZ microstructure [24]

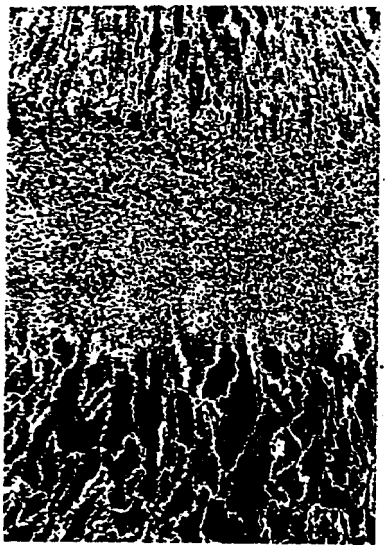

Figure 2.12 Two weld passes and grain-refined HAZ between passes [25]

2.3.2. CUTTING MECHANISM

When the interface between the precipitates and matrix is coherent, the cutting mechanism applies. Mott and Nabarro introduced the first dislocation theory of aged alloys in 1948 which described the interaction between a dislocation line and spherical solute atoms or group of solute atoms, as illustrated in Figure 2.13 [26]. The theory can also be applied to the G.P. Zone in precipitation hardened aluminum alloys. The critical shear stress in terms of cutting mechanism is:

$$\tau_o = 8G\theta r_o^3 N \qquad (2.4)$$

where G is shear modulus, r_o is particle radius, N is the number of particles per unit volume and θ is the misfit parameter.

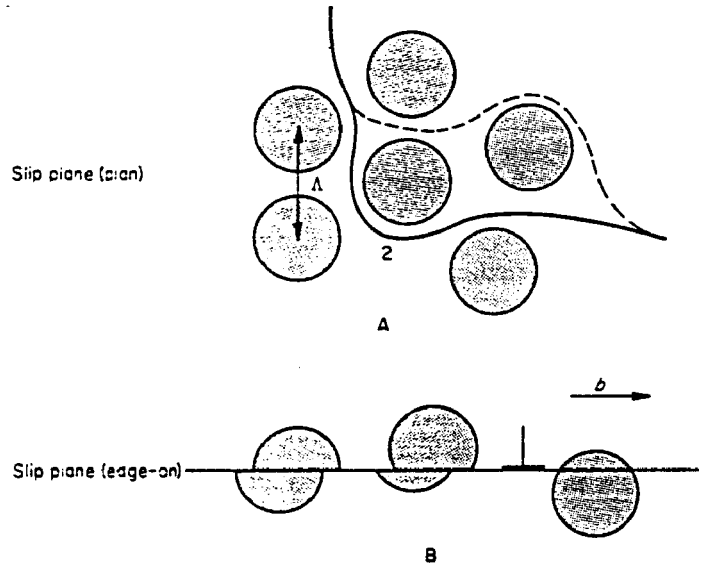

Figure 2.13 Interaction of a dislocation line with zones in an alloy - cutting mechanism, a) plan view, b) edge-on to slip plane [26]

In this early expression, G is assumed to be constant, and τ_o is independent of the particle spacing. Experimental results revealed that for incoherent particles the yield stress is related inversely to the particle spacing and the shear moduli of particle and matrix are more likely different. When particle cutting occurs, the resistance to shear is governed by several factors. As Kelly and Nicholson have pointed out, they are [27]:

1, The interaction of the dislocation with the stress field of the precipitate.

2, If the precipitate has an ordered lattice, work will be done in creating a disordered interface across the slip plane.

3, Difference in the lattice parameters of the matrix and precipitate - misfit dislocations must be created at the precipitate-matrix interface during shearing of the particles.

4, Difference in the elastic moduli of matrix and precipitate:the larger stress must be provided to force dislocations through the particles than through the matrix if the shear modules of the particles is greater.

5, Difference in atomic volumes of matrix and precipitate: a hydraulic interaction would be expected between a moving disloca-tion and a precipitate.

In the case of lattice parameter difference, the strengthening contribution of misfit hardening was found to be [28][29]:

$$\tau \propto G\epsilon^{3/2}(rf)^{1/2} \qquad (2.5)$$

where ϵ is misfit strain, r is particle radius, f is volume fraction of precipitated second phase and G is shear modulus.

In the case of ordered-lattice precipitate, the passage of a single dislocation destroys the periodicity of the superlattice and contributes markedly to strengthening. It is suggested that the streng-thening contribution is of the form [28-33]:

$$\tau \propto \gamma^{3/2}(rf/G)^{1/2} \qquad (2.6)$$

where γ is anti-phase-domain boundary energy.

2.3.3. LOOPING MECHANISM

If the cutting mechanism as described above is not operative, for example because the particles have become incoherent, the spacing is within a critical range or the particle structure is very different from that of the matrix, then dislocations may loop around the particles. This is shown in Figure 2.14 and is known as the Orowan Model, presented by Orowan in 1948 [34].

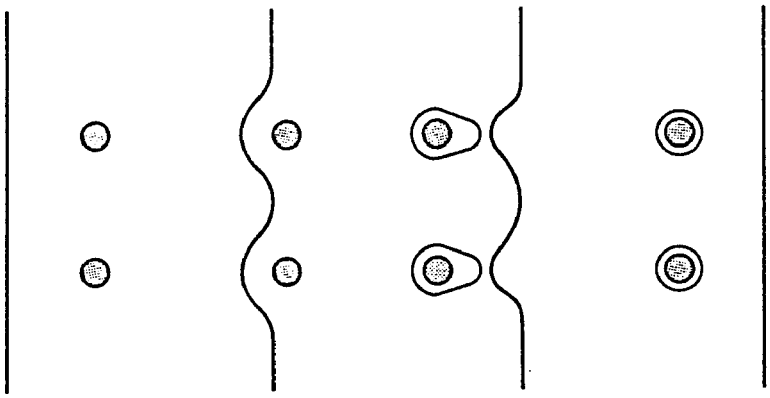

Figure 2.14 Interaction of dislocation line with particles - looping mechanism [34]

The model is similar to the dislocation looping with the Frank-Read mechanism for dislocation multiplication. The stress necessary for the dislocations to loop around the precipitate is

$$\tau = Gb/l \qquad (2.7)$$

where b is Burger vector of dislocation and l is the distance between particles. The disadvantage of overaging in precipitation strengthening can be well explained with this model. For a given volume fraction of second-phase particles, l increases as the precipitates grow larger and consequently the stress necessary for the dislocation to loop around the precipitate should decrease with increasing particle size. Moreover, in the Orowan model, when the particles are by-passed but leave residual dislocation loops around each particle, these loops exert stresses on the particles that are often small perfect crystals of high hardness, e.g. carbide/nitride in niobium, vanadium, titanium microalloyed steels. The stresses from the loops oppose further slip on the slip plane by acting on the dislocation sources. Consequently this causes rapid strain hardening of the matrix. The increment in flow stress due to the strain hardening resulting from the loops was found to be [35]

$$\tau_p = af^{3/2} \qquad (2.8)$$

where f is volume fraction of precipitates and a is a constant. Thus the strain hardening increases with either increasing fineness of precipitate or the volume fraction of

precipitate. Ansell and Lenel took the Orowan model further [36]; they concluded that appreciable plastic flow will take place when the particles are fractured as a result of the stress concentration caused by dislocations piling up against them. These pile-ups must be in the form of multiple loops or rings of dislocations around the particles. The theory gives a relationship for the flow stress τ_o in terms of the volume fraction of precipitate f

$$\tau_o = \tau_s + \frac{G'}{4a}\left(\frac{f^{1/3}}{0.82 - f^{1/3}}\right) \qquad (2.9)$$

where τ_s is the yield stress of a particle-free matrix, a is a constant and G' is the shear modulus of the particles.

In some alloy systems, both particle cutting and looping can occur simultaneously.

2.4. TRANSITION TEMPERATURE APPROACH AND CHARPY IMPACT TEST

It has been widely adopted as a typical example in the literature and text-books that the Liberty Ships' failures in the winter during the World War II were related to low service temperatures. The fatal failures in ships, bridges, railways, large containers and other steel structures in low temperature environments have also been reported. The structural materials for ships, bridges and pressure vessels are typically carbon and HSLA steels, bcc metals. The yield strength of bcc metals is very sensitive to temperature and strain rate. The nature of this sensitivity is related to the temperature-sensitive

Peierls-Nabarro stress contribution to yield strength. In bcc metals, the dislocation width is narrow, the Peierls-Nabarro stress rises rapidly with decreasing temperature and represents a large component of the yield strength in the low-temperature regime [37].

The transition temperature approach to fracture control, one of the most significant mechanical tests, was developed for application to most structural steels and welds. Three special experimental conditions are introduced into transition temperature testing to suppress the capability of plastic deformation of metals. They are

1, low test temperatures - temperature must be low enough to determine the defined transition temperature and lower shelf energy;

2, high stain rates - commonly using a pendulum or drop weight for loading;

3, multiaxial stress state - specimens notched or pre-cracked.

The Charpy V-notch (CVN) impact test, which provides these severe conditions, is the most popular procedure used in the transition temperature approach. Significant information can be obtained from CVN test, such as, impact energy data, the curve of absorbed energy versus test temperature, the defined tough-brittle transition temperature, upper shelf energy and lower shelf energy, lateral expansion ductility and fracture surface morphology.

Although the Charpy impact toughness has limited prediction capacity in fracture-safe design and service life estimation for a given component when compared with fracture toughness criteria, it is still a meritorious technique. CVN testing is simple and fast to perform, the CVN specimens are easy to prepare and, the test machinery and testing are low in cost. One may recall that as a results of study of the failures of Liberty Ships in 1940s, the 15-ft-lb transition temperature was determined at that time for ship plates and welds to be an acceptable criterion for failure control. This criterion has successfully been serving in material selection and manufacturing quality control roles ever since.

CVN data are sensitive to the metallurgical quality. The imperfections such as interior flaws, inclusions, temper embrittlement, overheat and anisotropy may be manifested in CVN results.

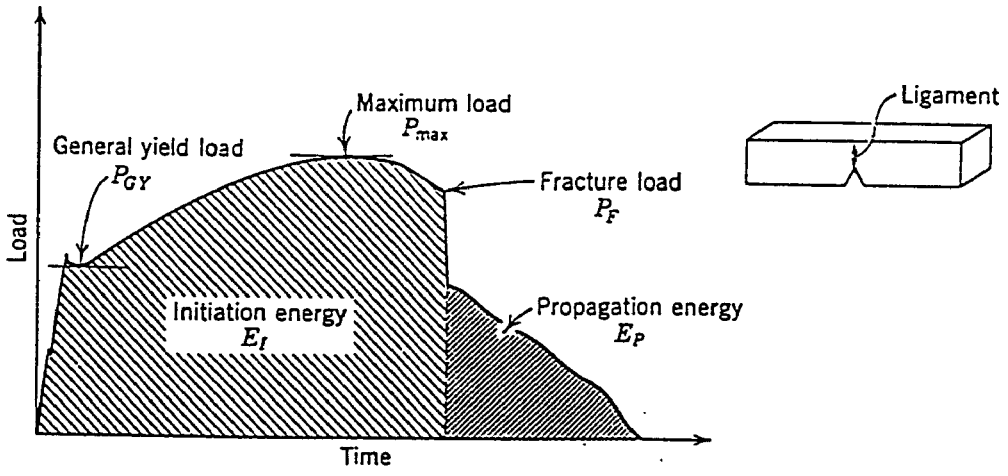

Figure 2.15 Schematic load-time curve from an instrumented Charpy test [45]

The total CVN energy E_T normally consists of two components, the crack initiation energy E_I and the crack propagation energy E_P. Different materials may show the same E_T but different fractions of E_I and E_P and hence behave quite differently in toughness/brittleness response.

The instrumented Charpy impact test has also been developed. The total fracture energy E_T and the components E_I and E_P can be calculated from the load-time curve obtained in instrumented CVN test, as shown in Figure 2.15 [45]. Taking note of the points of yield load, maximum load and fracture load in the curve, the clear images of various stages in the fracture process can be provided.

3. EXPERIMENTAL WORK

3.1. EXPERIMENTAL MATERIALS

3.1.1. BASE PLATES

To evaluate the specific contribution of the microalloy elements V and Nb, nine statistically designed experimental heats were supplied by USS Technical Center, USX Corp. The compositions of the experimental heats are listed in Table 3.1.

Table 3.1 Chemical composition of experimental heats, Wt.%

Heat code	C	Mn	P	S	Si	Al	N	V	Nb
A	0.16	1.19	0.013	0.016	0.24	0.031	0.007	0.005	0.004
B	0.16	1.19	0.014	0.016	0.23	0.032	0.007	0.050	0.005
C	0.16	1.18	0.013	0.016	0.23	0.030	0.008	0.097	0.005
D	0.16	1.20	0.014	0.016	0.24	0.030	0.007	0.005	0.030
E	0.16	1.18	0.014	0.016	0.23	0.031	0.007	0.050	0.029
F	0.16	1.19	0.014	0.016	0.23	0.030	0.007	0.098	0.031
G	0.16	1.13	0.010	0.016	0.23	0.029	0.006	0.005	0.049
H	0.16	1.16	0.012	0.016	0.23	0.030	0.006	0.049	0.053
I	0.16	1.18	0.014	0.016	0.23	0.029	0.007	0.097	0.060

Various vanadium and niobium additions in the basic composition of 0.16%C and 1.20%Mn of the experimental heats can be schematically expressed in the form of a three by three matrix, giving nine heats, coded as A, B, C, D, E, F, G, H and I, shown as below.

	0.005%V	0.05%V	0.10%V
0.005%Nb	heat A	heat B	heat C
0.03% Nb	heat D	heat E	heat F
0.06% Nb	heat G	heat H	heat I

Each heat was cast into a 3-inch-thick slab ingot. Each ingot was heated to 1230°C (2250°F) for two hours and was direct rolled to 12mm-thick (1/2-inch) plate. The plates were then normalized at 900°C (1650°F) for 1 hour followed by air cooling.

Figure 3.1 reveals the typical microstructure of these normalized plates. The microstructure contains banded pearlite together with a relatively fine equiaxed ferrite grain structure. The formation of the banded structure is related to the Mn segregation [38]. It is known that Mn lowers the A_3 temperature and therefore reduces the ferrite grain size.

The tensile properties of the normalized plates are listed in Table 3.2. The results summarized here are the average of three tests. Specimens tested were 0.252 inch-diameter with a 1.0 inch gage length. The carbon equivalent, a parameter often used as a measure of weldability, can be given by:

$$C_E = C + Mn/6 + (Cr+Mo+V)/5 + (Ni+Cu)/15$$

The C_E for these heats ranges from 0.36 for heat A to 0.38 for heat I.

Table 3.2 Tensile properties of normalized base plates

Heat code	Y.S. MPa	Y.S. Ksi	U.T.S. MPa	U.T.S. Ksi	Elong. (%)	Area Reduc (%)
A	334	48.4	483	70.0	39.9	77.2
B	342	49.6	495	71.8	39.0	76.5
C	357	51.8	513	74.4	37.4	75.4
D	373	54.1	512	74.2	38.9	76.0
E	372	53.9	505	73.2	40.3	77.2
F	383	55.5	527	76.4	38.2	75.5
G	354	51.3	499	72.4	37.8	76.9
H	380	55.1	514	74.6	38.8	76.5
I	376	54.6	527	76.5	36.8	71.9

3.1.2. FILLER MATERIALS AND SHIELDING GAS

The LINDE HI-DEP Alloy 65 1/16-inch-diameter welding wire was employed as filler material in the gas metal arc welding (GMAW) used in this program. The nominal wire composition is (Wt.%)

C	Mn	Si	S	P	Al	Zr	Ti
.04	1.20	.50	.20	.017	.10	.07	.10

The mixture of 98% argon plus 2% oxygen was used as a shielding gas. The argon protects the weld pool from the surrounding atmosphere and the small amount of oxygen stabilizes the arc.

3.2. WELDMENT PREPARATION

3.2.1. WELD JOINT DESIGN

A single-bevel-groove weld joint and a 30°-tilt position were used in welding. This design was selected to obtain a

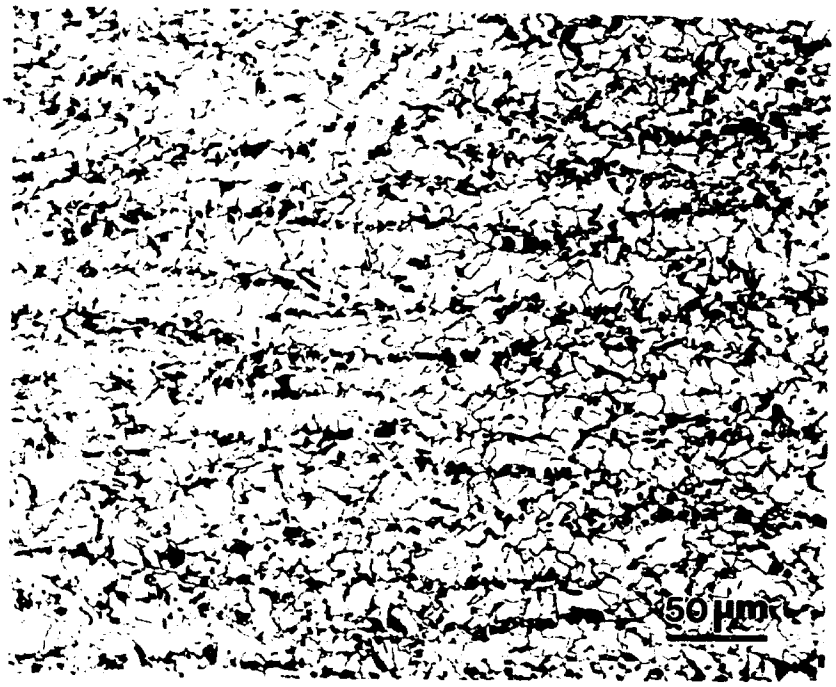

heat F

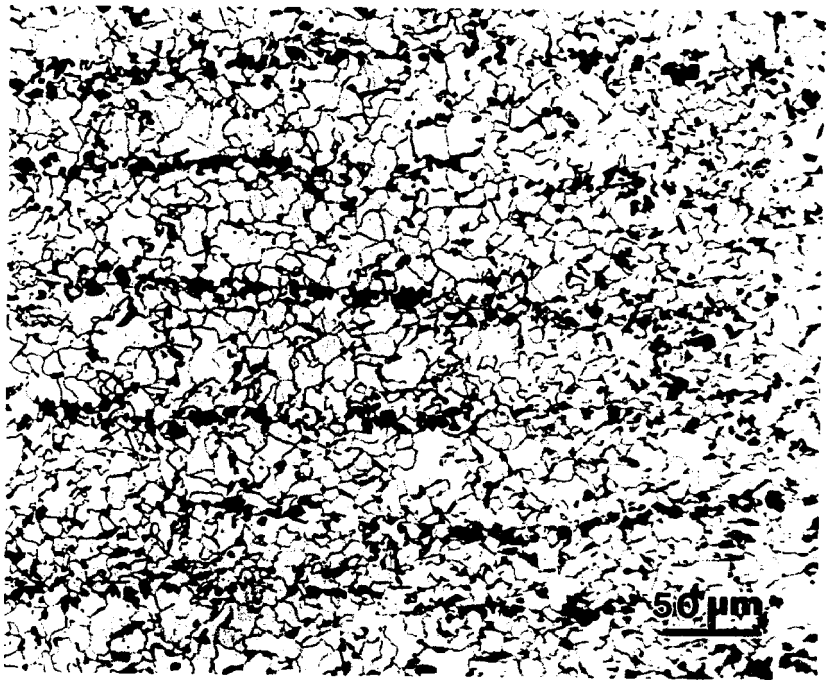

heat H

Figure 3.1 Microstructures of normalized plates, showing equiaxial ferrite grains and banded pearlite

weld geometry where the fusion line is fairly straight and the fusion plane is perpendicular to the plate surface, allowing Charpy specimens for the HAZ testing to be extracted from the weldments, as shown in Figure 3.2.

Welding heat inputs of 3kJ/mm (76kJ/in) and 5kJ/mm (127kJ/in) were selected in preparing test weldments. The welding parameters are summarized in Table 3.3.

TABLE 3.3 Welding Parameters

Heat Input	Voltage	Current	Travel Speed
5kJ/mm	30 V	400 A	145mm/min
3KJ/mm	29 V	350 A	203mm/min

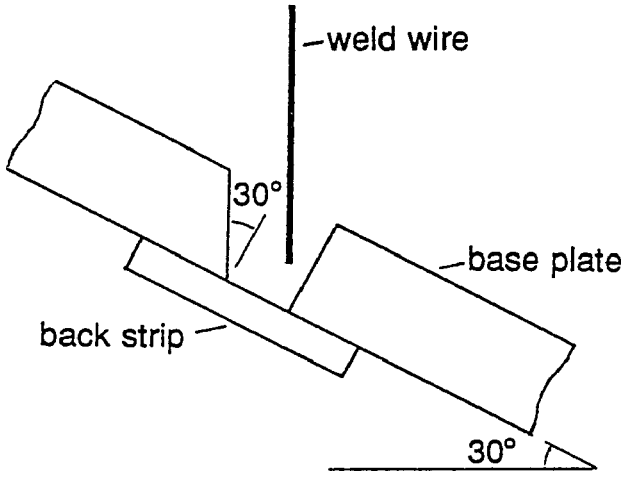

Figure 3.2 Weld geometry for preparing test weldments

A 7mm-root-opening and two passes were used for 3kJ/mm weldments and a 10mm-root-opening and three passes were used for 5kJ/mm weldments.

No preheat was used and the interpass temperature was

maintained lower than 100°C (212°F). Since a flat HAZ perpendicular to the plate surface is extremely important in investigating the coarse-grained HAZ behavior, considerable efforts were undertaken to optimize the weld joint geometry prior to experimental weldment preparation through adjusting the angle of plate, angle of torch, angle of groove and the root opening.

Figure 3.3a and Figure 3.3b are the examples of the prepared 3kJ/mm and 5kJ/mm weld joints, respectively. The welding direction was parallel to the rolling direction of the plates in order to produce transverse (TL) orientation Charpy specimens.

3.2.2. POST-WELD HEAT TREATMENT

Post-weld heat treatment (PWHT) is commonly desired because the severe heating and cooling cycle during fusion welding of thick plates can result in high stresses and strains and cause severe distortion or leave residual stresses of the order of the flow stress of the metal. PWHT will reduce these residual stresses, while at the same time it has the potential to change the microstructures in the weld metal and the HAZ, and accordingly affect mechanical properties. The PWHT was conducted in a furnace at 620°C (±10°C) for 2 and 10 hours, followed by air cooling.

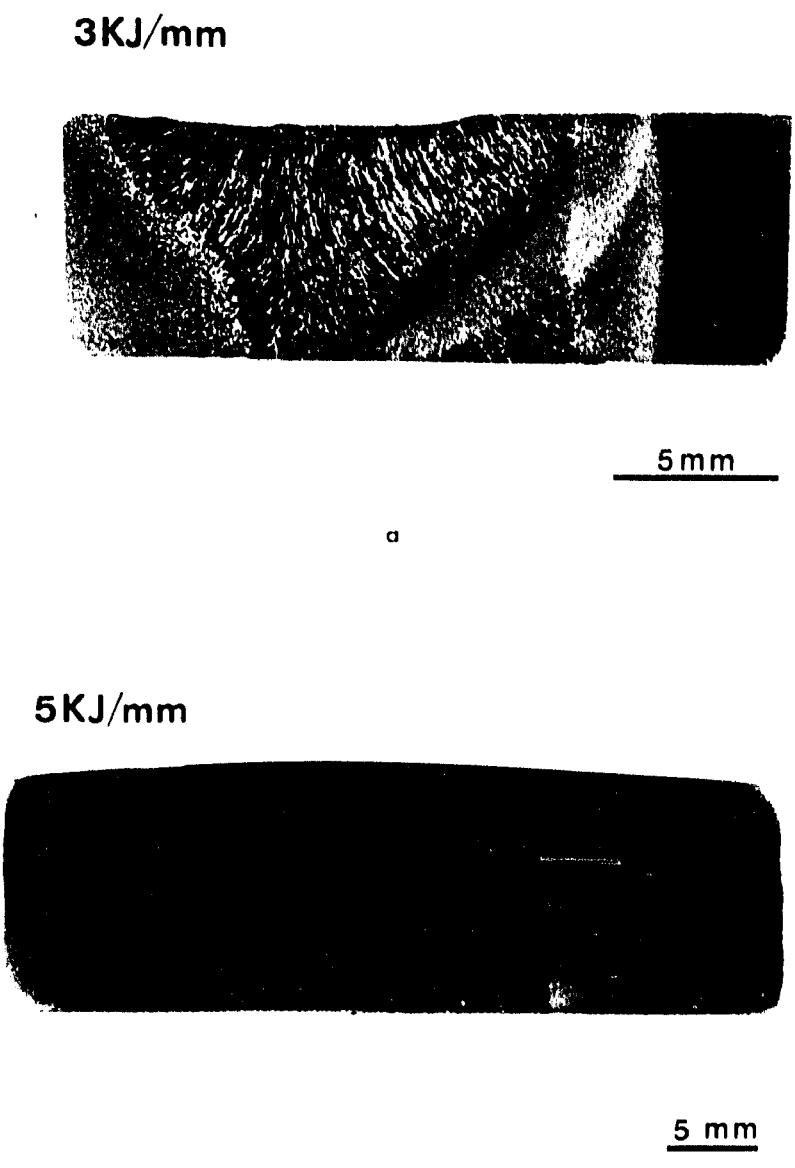

Figure 3.3 Examples of the prepared a) 3kJ/mm and 2) 5kJ/mm weld joints, showing approximately flat fusion line

3.2.3. WELDMENTS FOR AGING STUDY

The weldments of nine experimental heats for HAZ hardness examination and optical and electron microscopic observation under a series of PWHT conditions were prepared by bead-on-plate welding with a shielding gas of 98% argon and 2% oxygen. 3kJ/mm and 5kJ/mm heat inputs were employed in welding. The metallographic specimens, which also served for microhardness testing were sliced from each weldment perpendicular to the welded bead and plate surface. PWHT was conducted at 620°C (±5°C) for 1, 2, 5, 10, 20, 50, 100 hours in a tube furnace with pure dry argon protection and followed by air cooling.

3.2.4. MEASUREMENT OF Δt_{8-5}

The time from 800°C to 500°C during cooling after welding, Δt_{8-5}, was measured by embedding a thermocouple into the plate to be welded. The thermocouple tip was placed immediately adjacent to fusion boundary. A small hole was drilled for

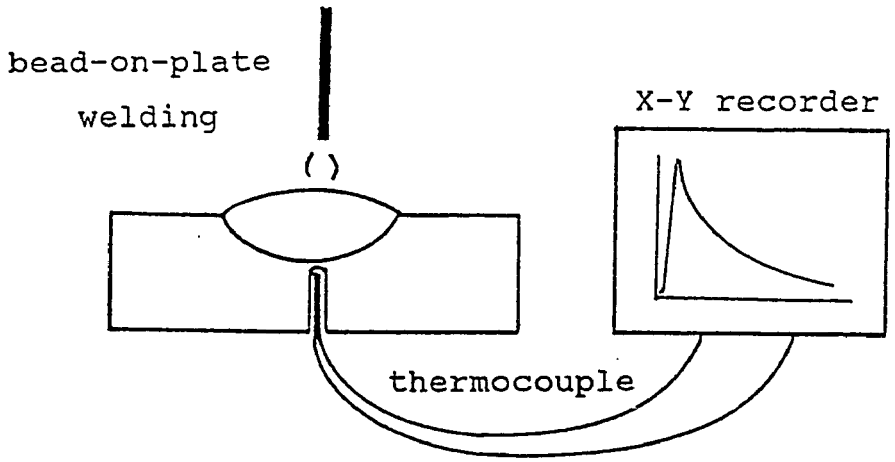

Figure 3.4 The configuration for measurement of Δt_{8-5}

embedding the thermocouple and was then sealed with Al_2O_3 powder after embedding the thermocouple. The bead-on-plate welding with 3kJ/mm and 5kJ/mm heat inputs was performed. An X-Y recorder was connected with the thermocouple to record the potential variation corresponding to the weld thermal cycle. Figure 3.4 shows the configuration for Δt_{8-5} measurement. The weldments were then dissected to determine the distance between the thermocouple tip and the fusion boundary. If this distance was less than 1mm, the results were accepted, otherwise, they were discarded.

3.3. TEST SPECIMEN PREPARATION

3.3.1. TENSILE SPECIMEN OF BASE PLATE

The 6.35mm-diameter (1/4-inch) 25.4mm-gage-length (1-inch) tensile specimens were taken from the mid-thickness of the normalized test plates in an orientation perpendicular to the rolling direction.

3.3.2. CHARPY V-NOTCH (CVN) SPECIMEN

CVN specimens were taken from normalized base plates in T-L orientation so that the "worse case" or conservative data would be produced.

CVN specimens of the HAZ were notched with the notch tip placed in 0.2-0.5mm to the fusion boundary. The prepared multipass weldments described in Section 3.2.1 were sliced perpendicular to the weld beads and machined into a 10mm-by-

10mm-section bar. All these blanks were etched with 2% Nital to reveal the HAZ detail, particularly the fusion line. The expected notch tip location was marked on each specimen for the next machining. Figure 3.5 illustrates how a Charpy specimen was taken from an etched blank where the notch position had been marked for machining.

The preparation of weldments and testing specimens are summarized in Figure 3.6.

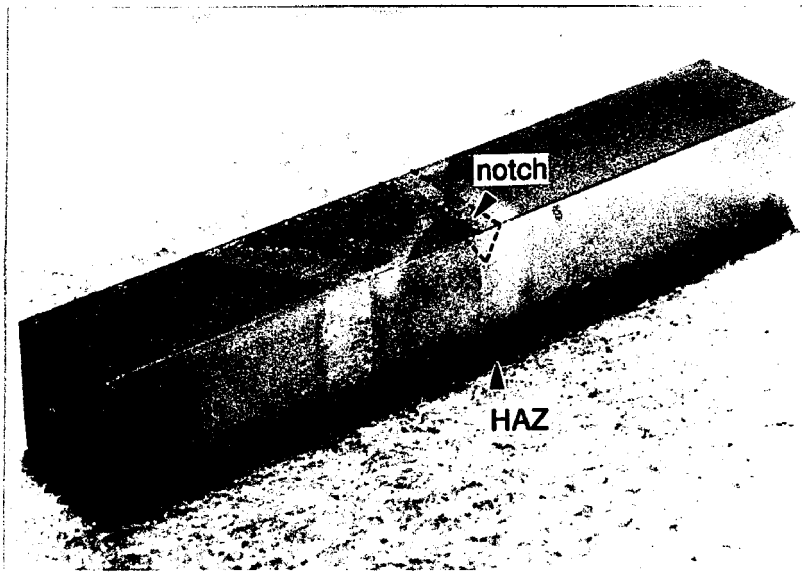

Figure 3.5 A Charpy specimen notched at multipass HAZ

3.4. MECHANICAL TESTING

3.4.1. CHARPY V-NOTCH IMPACT TESTING

CVN impact testing was performed with SATEC Systems impact Tester (Model SI 1D), in accordance with the standard test method stipulated in ASTM A370 and ASTM E23. The impact test machine was calibrated with standard CVN specimens supplied by

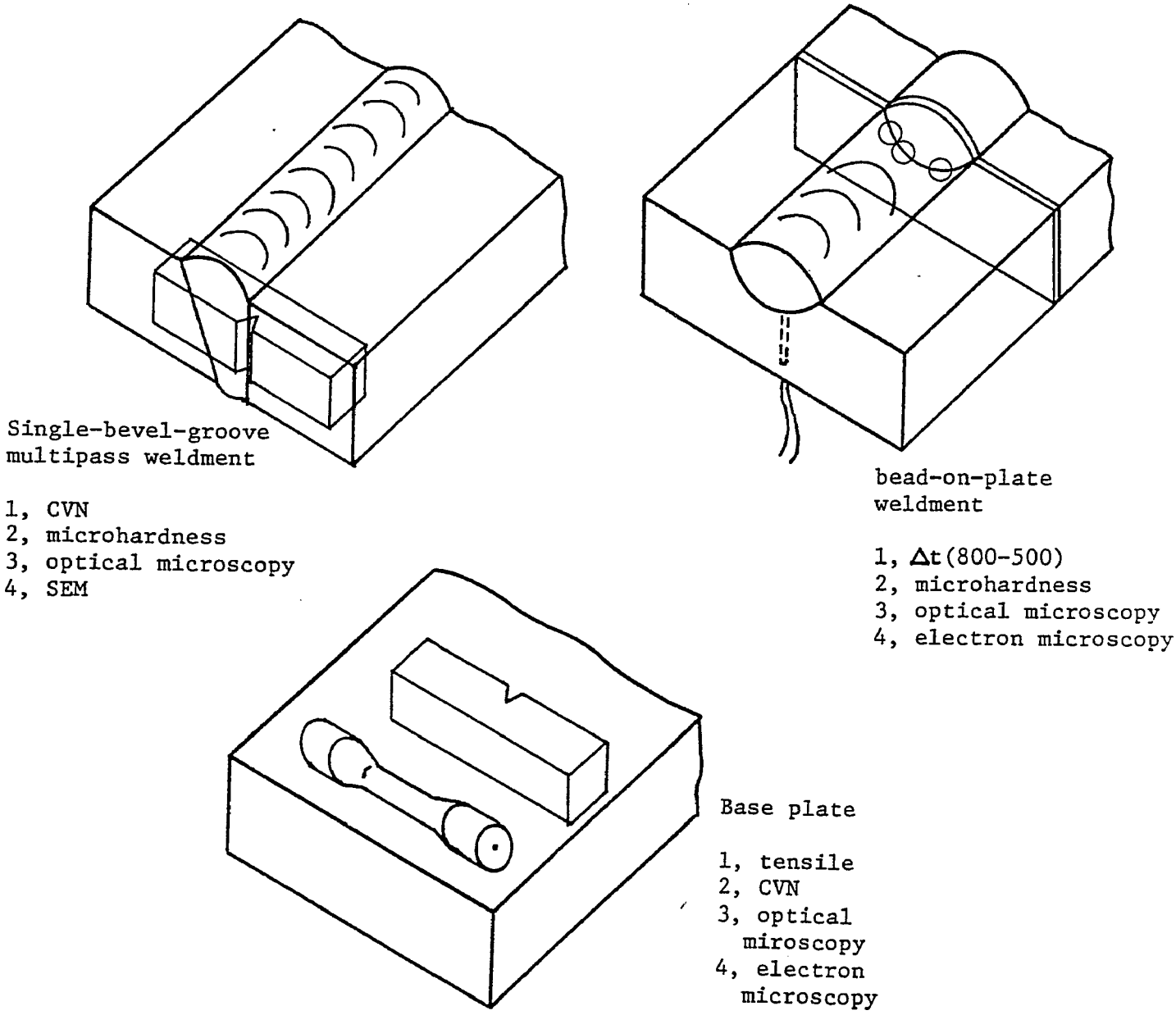

Figure 3.6 A summarization of the preparation of testing specimens

U.S. National Institute of Standards Technology at -40°F prior to the regular testing in this research work. Standard size CVN specimens were prepared from base plates and HAZs. The HAZ

specimens cover different weld heat inputs and PWHT conditions. Ethyl alcohol with liquid nitrogen added was utilized as a coolant for most sub-zero temperature testing. Some base plate specimens were broken at temperatures lower than the freezing point of ethyl alcohol; in these cases methylbutane was used as a coolant.

The amount of energy absorbed by the CVN specimen can be read directly from the dial of the impact machine. The impact energy versus test temperature for each specimen group classified by experimental heat, welding heat input and PWHT was plotted. A 50 Joule (37 ft-lbs) energy level was employed as the criterion to define the transition temperature throughout this work. The broken CVN specimens were kept in a desiccator for subsequent fracture surface study.

3.4.2. MICROHARDNESS TESTING

Microhardness testing is widely adopted for estimates of strength in weld component examination because the microhardness measurement is easy to make and of low cost. The correlation of hardness with strength has been confirmed for many steels.

Knoop microhardness testing was carried out in a LECO M-400FT microhardness tester which utilizes a pyramid-shaped diamond indentor. A 200 gram load and 20 second holding time were applied for each indentation.

Specimens for Knoop microhardness testing were sectioned

from prepared bead-on-plate weldments, polished and etched with 2% Nital. Each maximum HAZ hardness value was taken as the average of 10 readings in the coarse-grained HAZ immediately adjacent to the fusion line.

Besides maximum HAZ hardness measurements made along fusion boundaries, microhardness measurements across a fusion boundary were also made to reveal the hardness distribution in various constituents such as weld metal, HAZ and unaffected metal.

Figure 3.7 gives an example showing Knoop microhardness measurement along and across fusion boundaries.

3.5. MICROSTRUCTURAL INVESTIGATION

3.5.1. OPTICAL MICROSCOPY

Optical microscopic examination was conducted on weld metal, HAZ and parent metal under all specimen conditions (9 heats x 2 welding heat inputs x 3 PWHTs).

The general appearances across the weld joint were observed and recorded. The microstructural constituents in the HAZ were identified.

The effect of welding heat input and PWHT on the extent and grain size in HAZ was investigated.

A quantitative metallographic examination was also completed in all heats to reveal the influence of the additions of vanadium and/or niobium on the HAZ microstructural characterization.

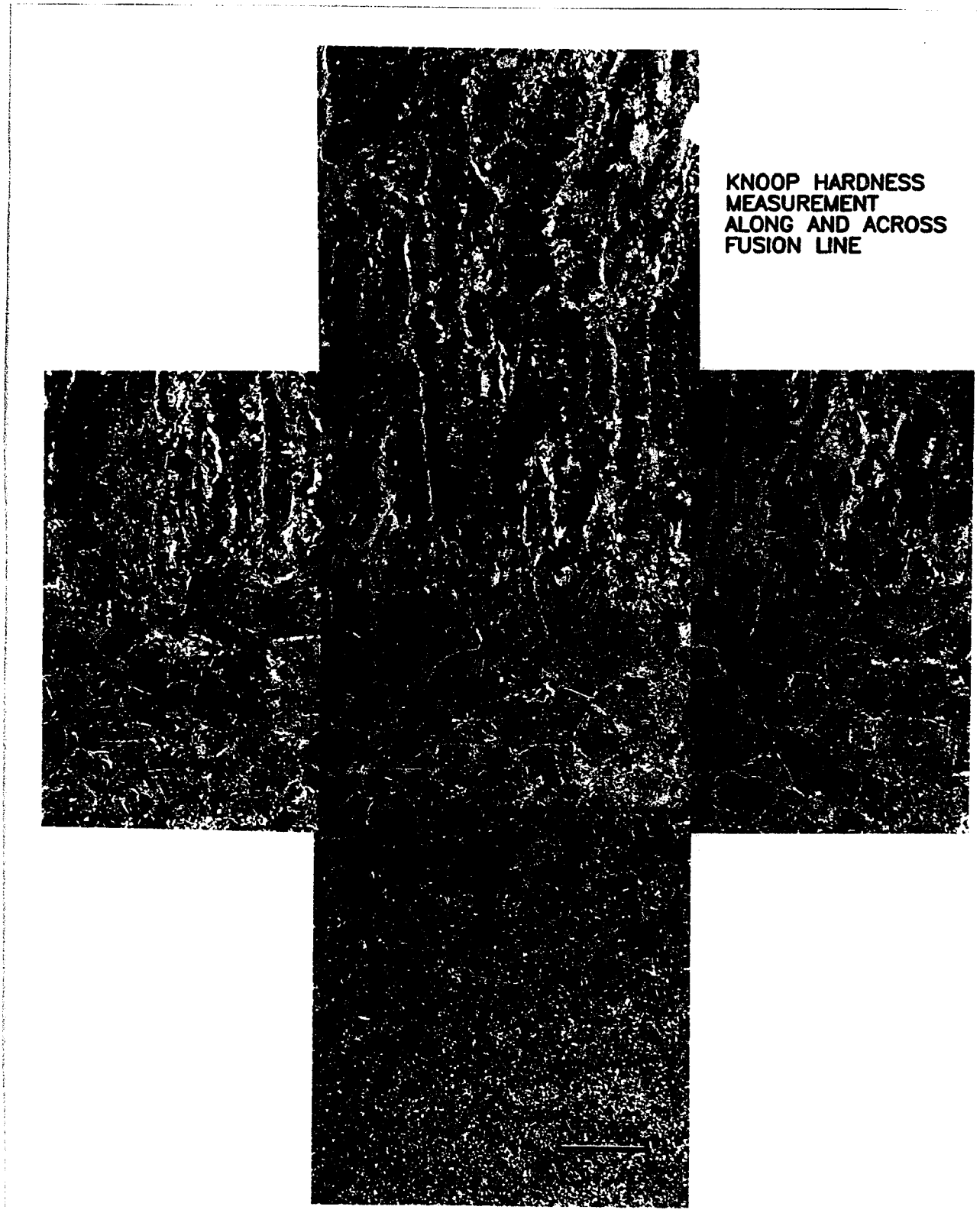

Figure 3.7 Knoop microhardness measurement along and across fusion boundary, 40x

The prior austenite grain size in the coarse grained HAZ adjacent to the fusion boundary was evaluated by measuring the diameters of 50 grains in the direction parallel to the fusion line as shown in Figure 3.8.

The amount of grain boundary (G.B.) ferrite in the coarse-

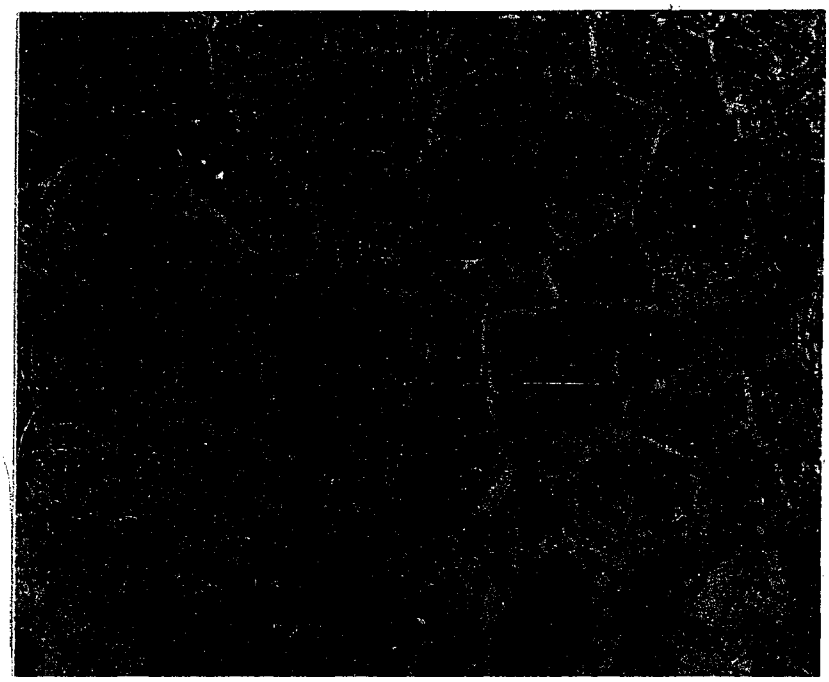

Figure 3.8 Measurements of prior austenite grain size in coarse-grained HAZ, 250x

grained HAZ was also estimated by using a point count method which determines the number of test points falling in G.B. ferrite of the microstructure on the polished plane.

3.5.2. SCANNING ELECTRON MICROSCOPIC (SEM) STUDY

The SEM technique utilized in this work was mainly for the fractographic examination of CVN specimens. In microalloyed HSLA steels, as a bcc metal, the test temperature can have a

significant effect on the fracture appearance and in many cases can result in a change in fracture mode, for example, from a microvoid coalescence fracture at high temperature to a cleavage or quasi-cleavage fracture at low temperature. Different materials may behave differently in terms of fracture surface details and in change of fracture mode. The total fracture energy of a specimen is governed by how and where the crack initiates and propagates.

Since all HAZ specimens in this study were taken from multipass weldments, the V-notch root resides in various HAZ sub-zones, e.g. the coarse-grained HAZ of the first pass, the refined coarse-grained HAZ of the first pass due to the heat of the second pass, the intercritical reheated coarse-grained HAZ and subcritical reheated coarse-grained HAZ, etc. These various microstructural constituents in the multipass HAZ CVN specimen contribute to the cracking process and may show the different fracture modes. Therefore, an overall SEM examination of the CVN specimens was conducted for better understanding of the micromechanisms of fracture under different microstructural and test conditions.

An ETEC Autoscan machine was utilized for the SEM study. The broken CVN specimens were ultrasonically cleaned in an acetone bath and then dried for SEM examination.

3.5.3. TRANSMISSION ELECTRON MICROSCOPIC (TEM) STUDY

Transmission Electron Microscopy (TEM) has become one of

the most powerful tools for fine-scale (<1μm) microstructural investigations in materials science. In this study, as described in previous sections, the mechanical behavior of the experimental heats may be significantly affected by the amount, morphology, distribution of the precipitates of vanadium and/or niobium carbides. The TEM was employed to investigate these details.

Thin foil 3mm-diameter-disc specimens were prepared for the TEM studies. The key point in disc preparation was to make a thin area (transparent to the electron beam, hopefully in the disc center) located exactly in the coarse-grained HAZ. The following procedure was employed in TEM specimen preparation.

1, Slice an approximately 0.5mm-thick section from the bead-on-plate weld with a diamond saw. The slice is taken perpendicular to the weld direction.

2, Grind and polish the section to a thin foil with a thickness approximately 50-70μm (0.002-0.003inch).

3, Etch the thin foil with 2% Nital to reveal the fusion line.

4, Mark the location where the disc to be extracted, as shown in Figure 3.9.

5, Punch out 3mm discs from the thinned foil as already marked.

For base metal, 3mm discs were punched out from ground thin foil; no etching and marking were required.

6, Electropolish the prepared discs in a twin jet electro-polisher with the following parameters:

Solution: 10% Perchloride acid

72% Ethyl Alcohol

18% Methanol

Temperature: -40°C

Voltage: 15 V

Current: 0.05 A

The result was a specimen thinned to a small hole so the edges of the hole provide the transparent area for study.

7, Inspect the electropolished specimens, those with a hole not in the center (not in the HAZ) were discarded.

8, Examine the prepared thin foil specimens as soon as possible, (refer to Section 4.5.1.4.)

A Philips EM400 was utilized to examine most of the specimens; a few specimens were examined using a Philips EM300.

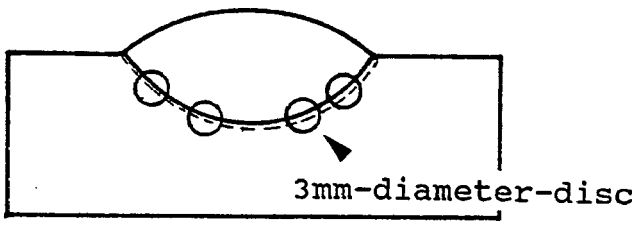

Figure 3.9 3mm-diameter-disc specimens extracted from coarse-grained HAZ

The EDAX X-ray microanalytical system attached to the EM400 was utilized for chemical analysis of precipitates.

Unfortunately no meaningful data were obtained in this part of the study because the very tiny particle size precluded the acquisition of accurate data.

4. EXPERIMENTAL RESULTS AND DISCUSSION

4.1. BASE PLATE PROPERTIES

Microstructures of base plates shown in Figure 3.1, are characterized by fine equiaxed ferrite grains and banded pearlite. The data of yield strength (Y.S.) and ultimate tensile strength (U.T.S.) of the normalized base plates listed in Table 3.2 are tabulated as following in the form of 3x3 matrix for ease of comparison.

			V% →		
			0.005	0.05	0.10
Y.S.	Nb%	0.005	(A) 334/48.4	(B) 342/49.6	(C) 357/51.8
MPa/ksi	↓	0.03	(D) 373/54.1	(E) 372/53.9	(F) 383/55.5
		0.06	(G) 354/51.5	(H) 380/55.1	(I) 376/54.6

			V% →		
			0.005	0.05	0.10
U.T.S.	Nb%	0.005	(A) 483/70.0	(B) 495/71.8	(C) 513/74.4
MPa/ksi	↓	0.03	(D) 512/74.2	(E) 505/73.2	(F) 527/76.4
		0.06	(G) 499/72.4	(H) 514/74.6	(I) 527/76.5

The strengthening by both vanadium and niobium is clearly evident in the above data. Data for heat D seem somewhat higher than expected. They are considered to be caused by experimental error.

To understand these data, recall the precipitation and

dissolution characteristics of V and Nb carbides in austenite, as illustrated in Figure 2.5. The VC has greater solubility in steel at the normalizing temperature (900°C) whilst NbC precipitates are still stable. These undissolved NbC particles restrain grain growth and retard recrystallization of austenite via pinning of grain boundaries and sub-boundaries, and hence bring about additional grain refinement both in the austenite and ferrite. Figure 4.1 shows these different effects on grain size by V, Nb and Ti. As microalloying

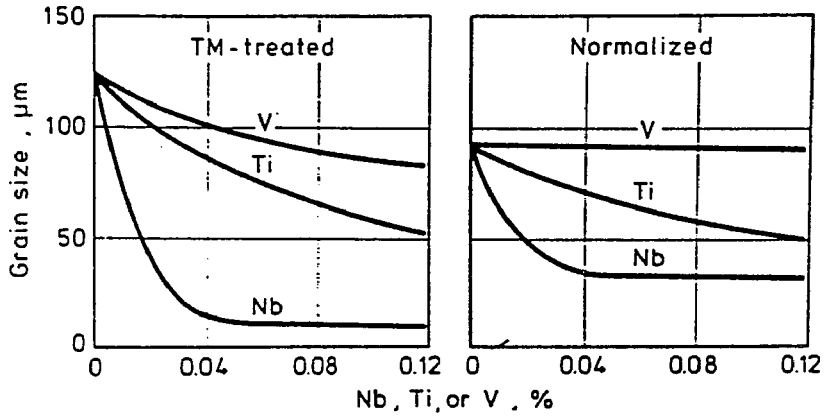

Figure 4.1 Effect of Nb, Ti and V on grain size in normalized steels [39]

content increases, the temperature range in which no more recrystallization can occur is raised substantially by Nb, less by Ti, and to no major degree by V [39]. However, metallographic examination on various normalized plate shows a very fine equiaxed ferrite grain size (approximately ASTM number 11) existing in all heats with no significant

difference in grain sizes. This result implies that the normalizing temperature of 900°C is not high enough in any of these alloys to cause extensive grain growth. The strengthening was therefore attributed to the VC and NbC precipitation.

The NbC precipitates originally formed in austenite during $\gamma \rightarrow \alpha$ transformation (to be detailed in Section 4.5.2) and/or were strain-induced during rolling. They are unlikely to be altered by the subsequent normalization. The VC precipitates are mostly dissolved at the normalizing temperature and then reprecipitated on cooling. Mayer [1] emphasized that among the microalloying elements Nb, V and Ti, niobium is characterized by particularly great strengthening effects produced at relatively low concentrations although Irvine stated that vanadium gives higher strengthening effect than niobium in a normalized C-Mn steel [17]. This latter observation is supported by these results. A firm judgement of the full effect of these two elements cannot be made at this time since both the processes of particle dissolution and reprecipitation may not be fully completed during the normalization at 900°C for 1 hour. Actually, the predominant strengthening of niobium over vanadium has been observed in the coarse-grained HAZ where a thermal cycle up to 1350°C was experienced. This will be discussed later on.

4.2. THE HAZ MICROSTRUCTURE

4.2.1. THE MEASUREMENT OF Δt_{8-5} AND THE PREDICTION OF HAZ MICROSTRUCTURAL CONSTITUENTS

The approach for measurement of Δt_{8-5} was described in Section 3.2.4. The cooling curves for 3kJ/mm welding heat input and 5kJ/mm welding heat input are shown in Figure 4.2 and Figure 4.3. The cooling times Δt_{8-5} were measured to be 54

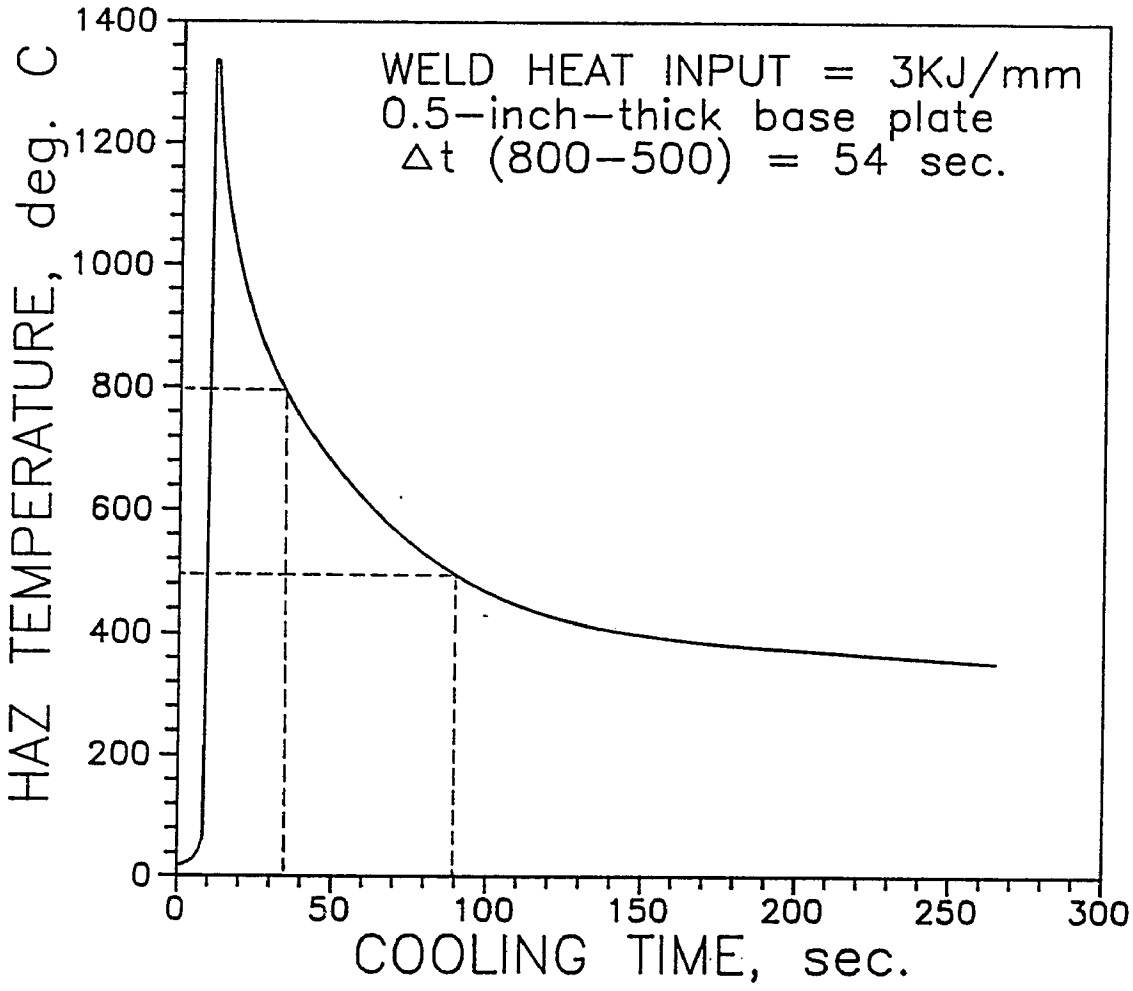

Figure 4.2 Colling time Δt_{8-5} measurement for 3KJ/mm welding heat input

seconds for 3kJ/mm and 201 seconds for 5kJ/mm. Superimposing a cooling curve on the corresponding continuous-cooling-time (CCT) diagram enables one to predict the microstructure in a HAZ at this specified cooling rate. For a given cooling time, which is normally determined by welding heat input and plate thickness, the transformation time, as well as transformation temperature, for each transformation product may be

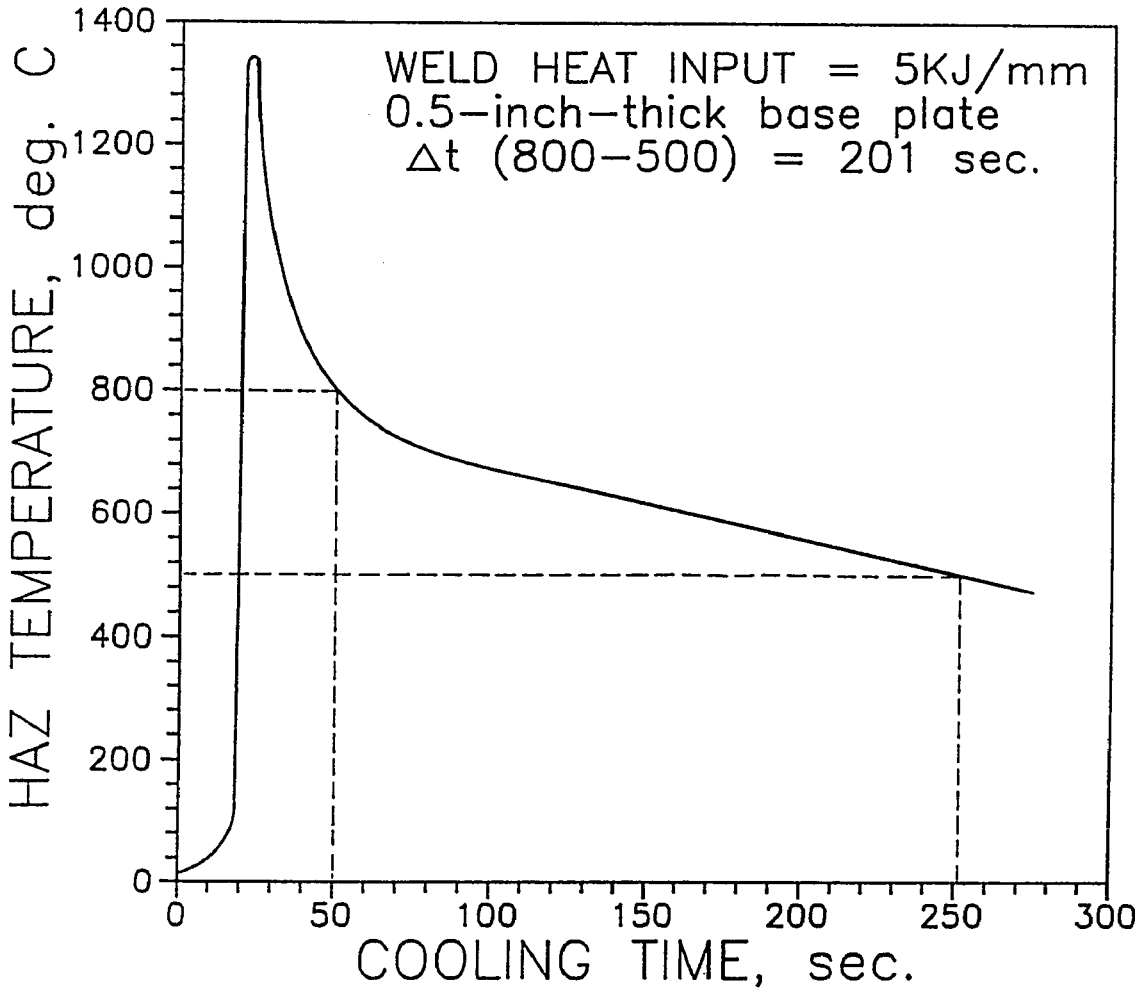

Figure 4.3 Cooling time Δt_{8-5} measurement for 5KJ/mm welding heat input

significantly affected by such factors as the types and the addition amounts of alloying and microalloying elements.

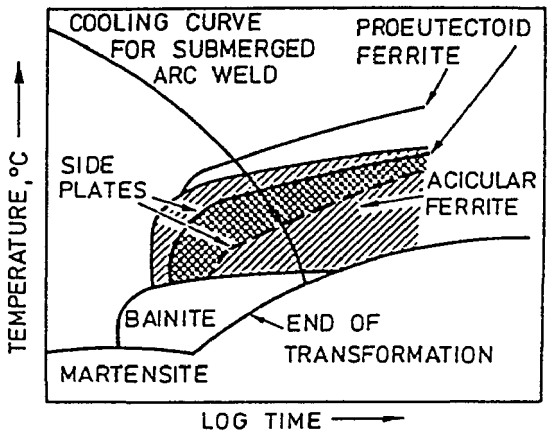

Figure 4.4 Schematic CCT diagrams showing several transformation products [40]

Figure 4.4 shows on a schematic CCT diagram [40] how the C-curves may move to longer or shorter times, and the shape or size of transformation fields may change, depending on composition. Austenite stabilizers, e.g.,C, N, Mn, Ni, Cu tend to inhibit transformation, pulling the C-curve towards longer time. Strong carbide forming elements, e.g., V, Nb and Ti, however, tend to suppress proeutectoid ferrite, but not acicular ferrite or bainite. Indeed, Nb, in particular, tends to enhance bainite formation. The additions of strong carbide forming elements may even cause the separation of ferrite and bainite curves as schematically illustrated in Figure 4.5.

The individual CCT diagram specific to each experimental heat may be required for microstructural prediction. But to develop the CCT diagrams for nine experimental heats would

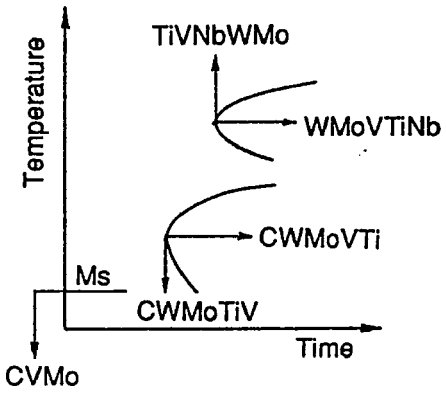

Figure 4.5 Effect of strong carbide-forming elements on the CCT curves (ferrite-upper, bainite-lower) [11]

require an extremely large amount of experimental work and is beyond the scope of this study. Thus the published CCT diagram of a low-carbon niobium-vanadium microalloyed steel shown in Figure 4.6 [41] can be utilized as a reference. The upper row of numbers in the diagram corresponds to the cooling rate in degree C per minute, the lower row of encircled numbers corresponds Vickers hardness values, and the intermediate numbers represent the percentages of microconstituents formed in each run. The measured cooling curves (dashed curves) transferred from the linear plots in Figure 4.2 and Figure 4.3 to logarithm plots were superimposed on this CCT diagram for predicting the HAZ microstructural constituents in a 0.5-inch-thick base plate under 3kJ/mm and 5kJ/mm weld heat inputs. Moreover, another diagram showing the effect of heat input on the proportion of microstructural constituents present in the grain-coarsened HAZ of a 0.17C-1.1Mn steel (Figure 4.7 [42])

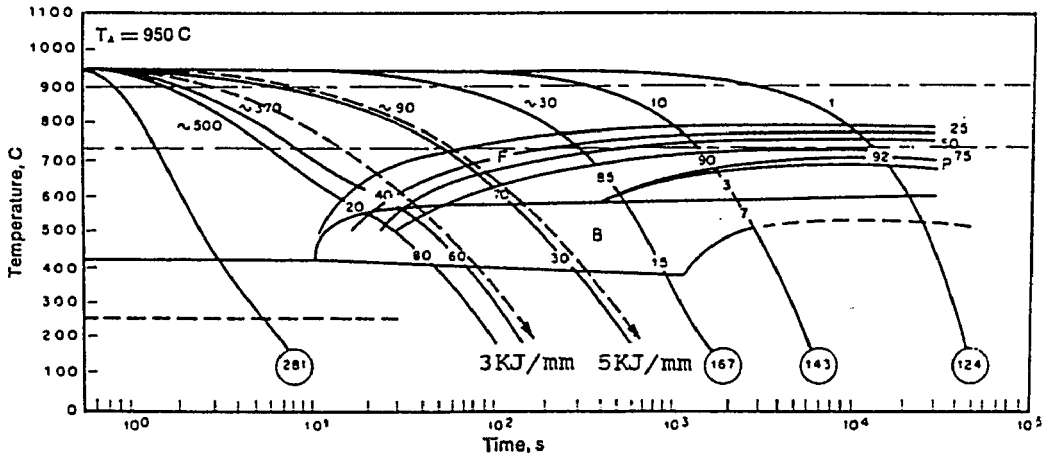

Figure 4.6 CCT diagram for a low-carbon microalloyed V-Nb steel, cooling curves for 3kJ/mm and 5kJ/mm heat inputs are superimposed in the diagram (dashed curves) [41]

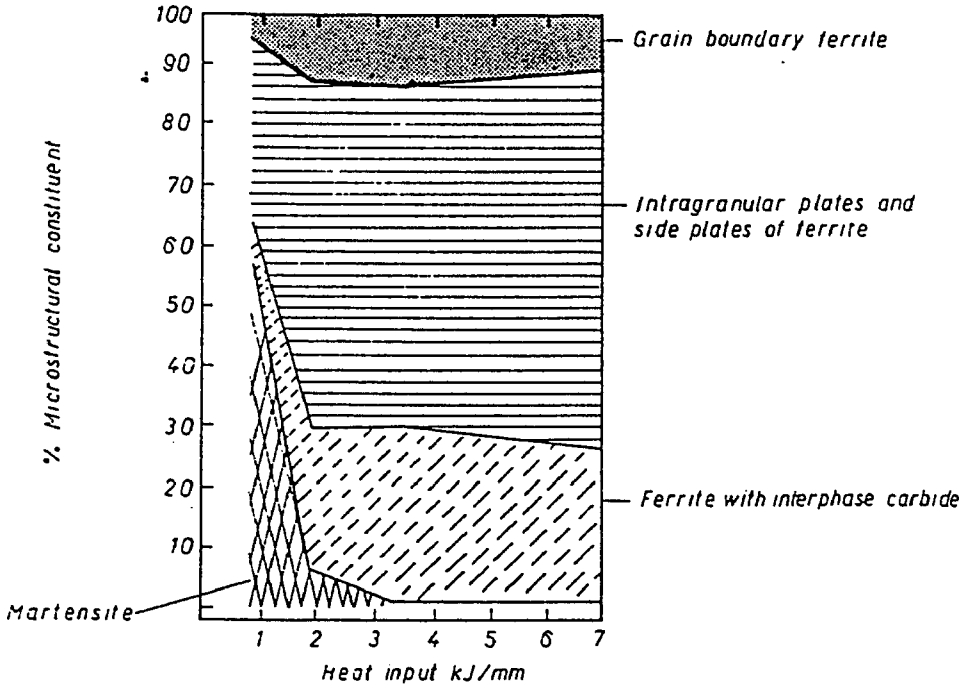

Figure 4.7 Diagram showing the effect of heat input on the proportion of microstructural constituents present in coarse-grained HAZ of a 0.17C-1.1Mn steel [42]

It is important to point out that the terminology for describing weld metal and HAZ microstructures can vary in the literature. In this text, basically, the terminology proposed by the International Institute of Welding (Commission IX-J) will be followed.

Figure 4.6 and Figure 4.7 predict the final HAZ microstructural constituents for both 3kJ/mm and 5kJ/mm heat inputs should consist of a mixture of:

1, proeutectoid ferrite (FP), often formed on prior austenite grain boundaries;

2, intragranular Widmanstatten side plates of ferrite (WF);

3, ferrite with interphase carbide (named ferrite-carbide aggregates), which is the result of the eutectoid decomposition reaction. Upper bainite in the form of ferrite laths with Fe_3C precipitating between them is one of the decomposition product;

4, ferrite with martensite/austenite and carbides (M-A-C). This is generally the predominant microstructural constituent in C-Mn steels. Ferrite with M-A-C can have an aligned (AC) or non-aligned (FN) appearance, but this variation is probably largely a sectioning effect.

These predictions will now be considered in light of the weld microstructures examined.

4.2.2. OPTICAL MICROSCOPIC EXAMINATION IN THE HAZ

4.2.2.1. BASIC MICROSTRUCTURAL CONSTITUENTS IN THE HAZ

Welding heat input has considerable effect on the grain size in coarse-grained HAZ. Figures 4.8a and 4.8b show the general view in HAZ microstructures welded with 3kJ/mm and 5kJ/mm, respectively. As expected, the grain sizes in coarse-grained region of higher heat input specimens are larger than those of lower heat input specimens . In addition, the coarse-grained HAZ is narrower at the lower heat input, resulting in higher toughness.

Both the 3kJ/mm HAZ and 5kJ/mm specimens show similar types of microstructural constituents but may differ in the relative amount of each constituent. For different heats, the amount of each constituent and grain size may also vary, depending on microalloy additions.

Figure 4.9a and Figure 4.9b show the typical features of HAZ microstructure. Arrows with letters indicate the specific constituents. Pro-eutectoid ferrite, FP, often formed at prior austenite grain boundaries and is therefore called grain boundary ferrite. Ferrite with M-A-C, having two modes, the aligned appearance, AC, and non-aligned appearance FN. This constituent may be somewhat finer in 3kJ/mm HAZ than in 5kJ/mm HAZ.

The intragranular Widmanstatten ferrite, shown as WF in Figure 4.9a is more likely visible in 5kJ/mm HAZ. It can be distinguished from ferrite laths by its characteristic basket

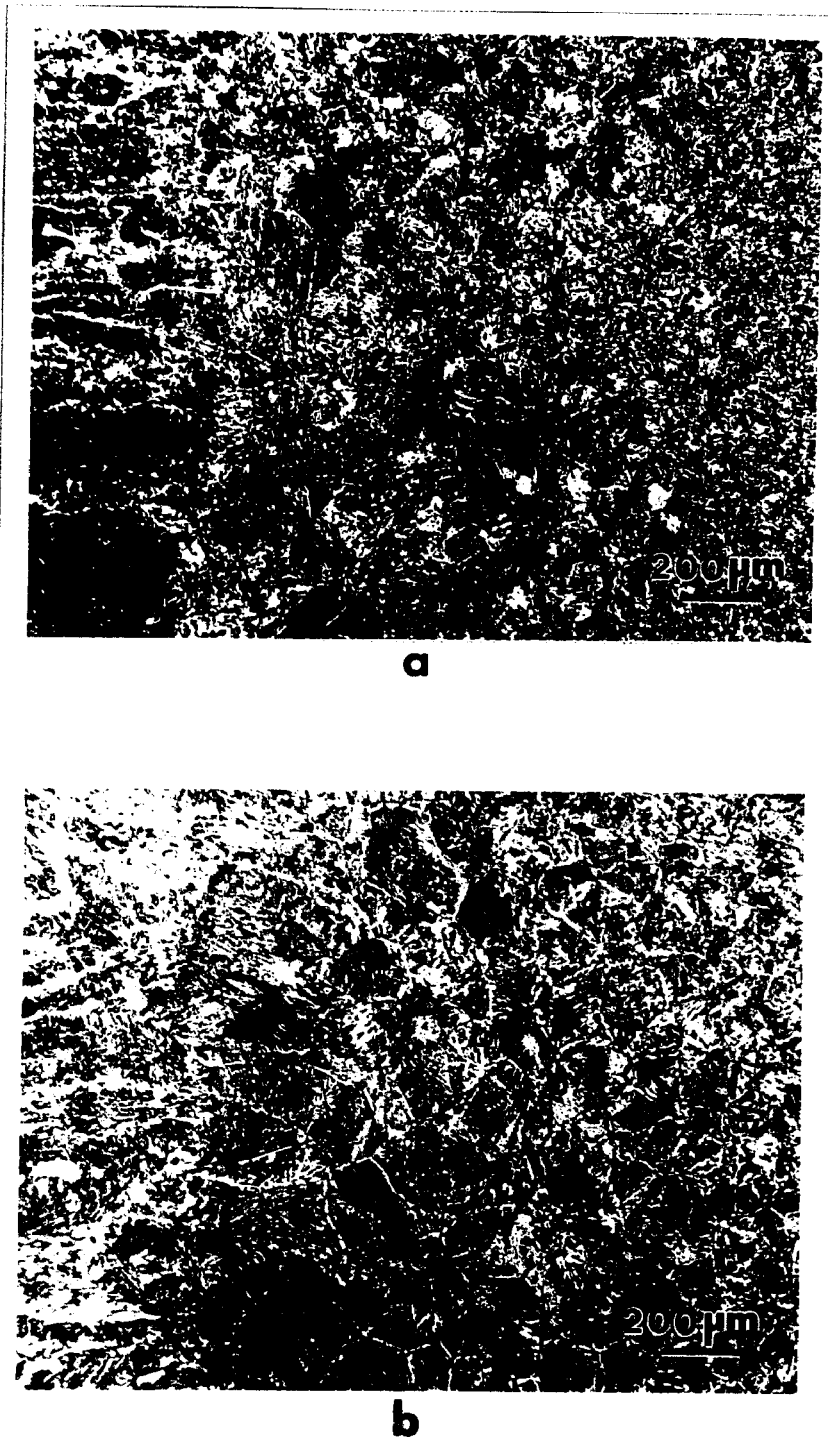

Figure 4.8 HAZ microstructure of heat D in as-welded condition, welded with (a) 3kJ/mm (b) 5kJ/mm. 50x

weave type of structure. Ferrite-carbide aggregates will be shown in Section 4.2.3.

4.2.2.2. EFFECT OF PWHT ON THE HAZ MICROSTRUCTURE

In optical microscopic observation, no significant change in microstructural characterization can be found after PWHT. Figures 4.10a,b,c,d and e give a profile of HAZ microstructure under as-welded, and PWHT at 620°C for 1, 2, 5 and 10 hours conditions.

Fine scale microstructural variations during PWHT, such as martensite decomposition and V/Nb carbides precipitation which are embodied in the variation in the HAZ hardness and toughness data, are beyond the resolution capablities of optical microscopy.

4.2.2.3. EFFECT OF V AND Nb CONTENT ON PRO-EUTECTOID FERRITE

The microstructures in Figure 4.11a and Figure 4.11b indicate how Nb additions influence the pro-eutectoid ferrite. Figure 4.11a shows the coarse-grained HAZ of heat H which contains 0.049%V and 0.053%Nb, welded with 5kJ/mm, in the as-welded condition. Figure 4.11b is the corresponding region of heat B with the same as-welded condition and same V content but the heat contains 0.005%Nb. The higher proportion of grain boundary ferrite in the low Nb content heat is clearly observed.

Quantitative metallography reveals that the amount of

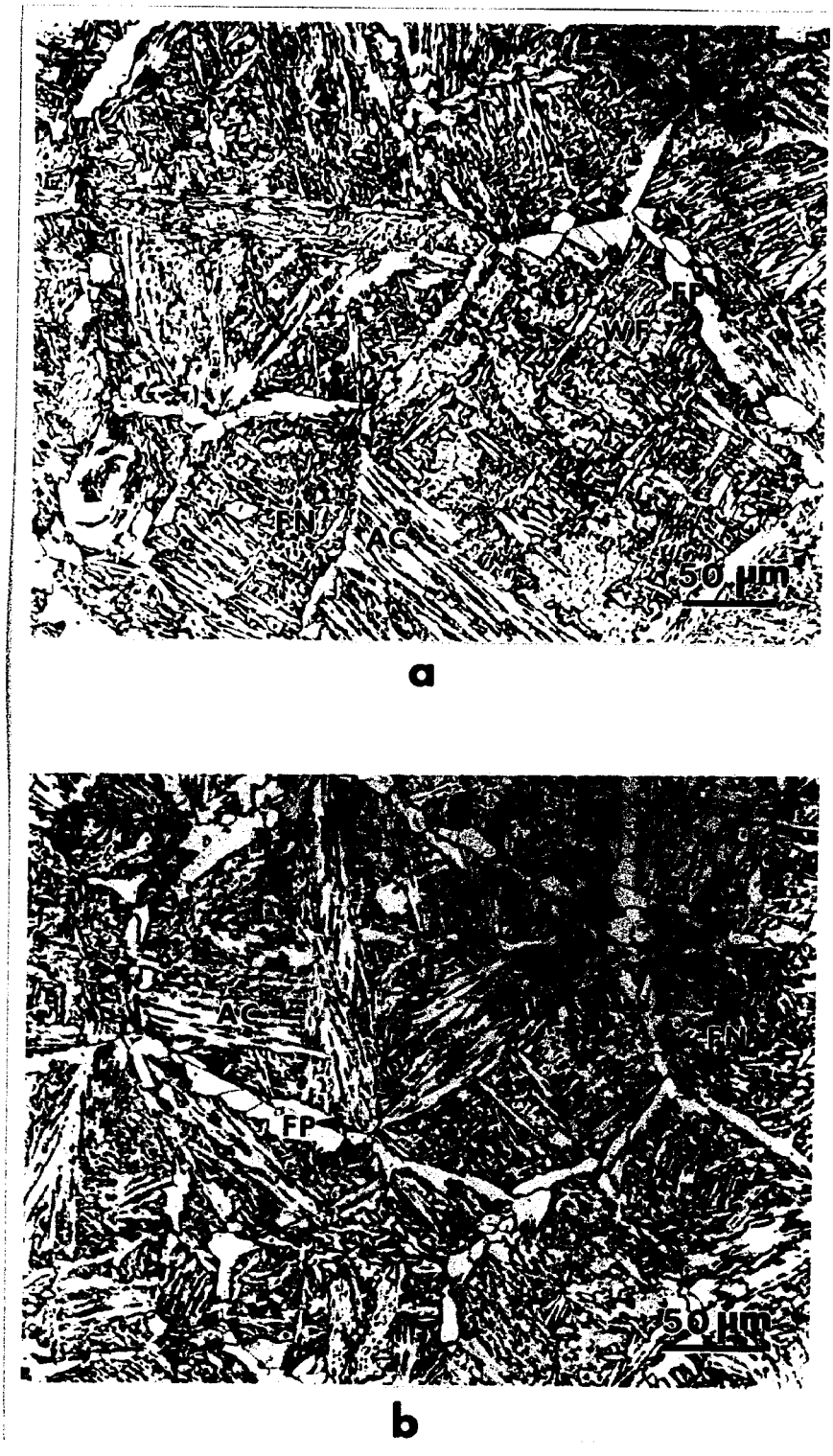

Figure 4.9 HAZ microstructure of heat I, welded with 5kJ/mm and as-welded, showing various constituents. (a) area 1 (b) area 2, 250x

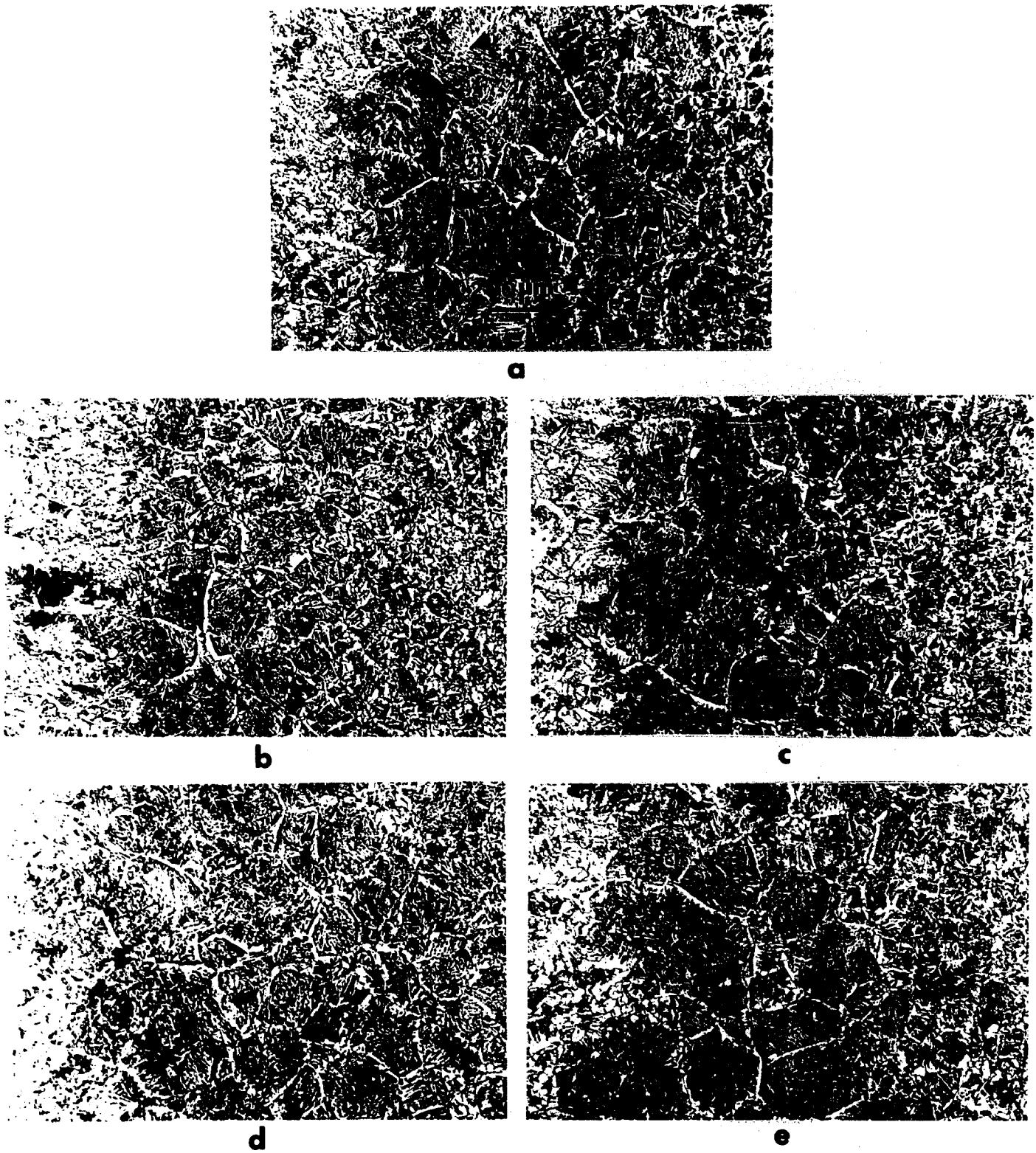

Figure 4.10 HAZ microstructure of heat B welded with 5KJ/mm, showing no significant change in optical microscopy during PWHT. (a) as-welded (b) PWHT at 620°C for 1hr. (c) PWHT at 620°C for 2hrs. (d) PWHT at 620°C for 5hrs. (e) PWHT at 620°C for 10hrs.

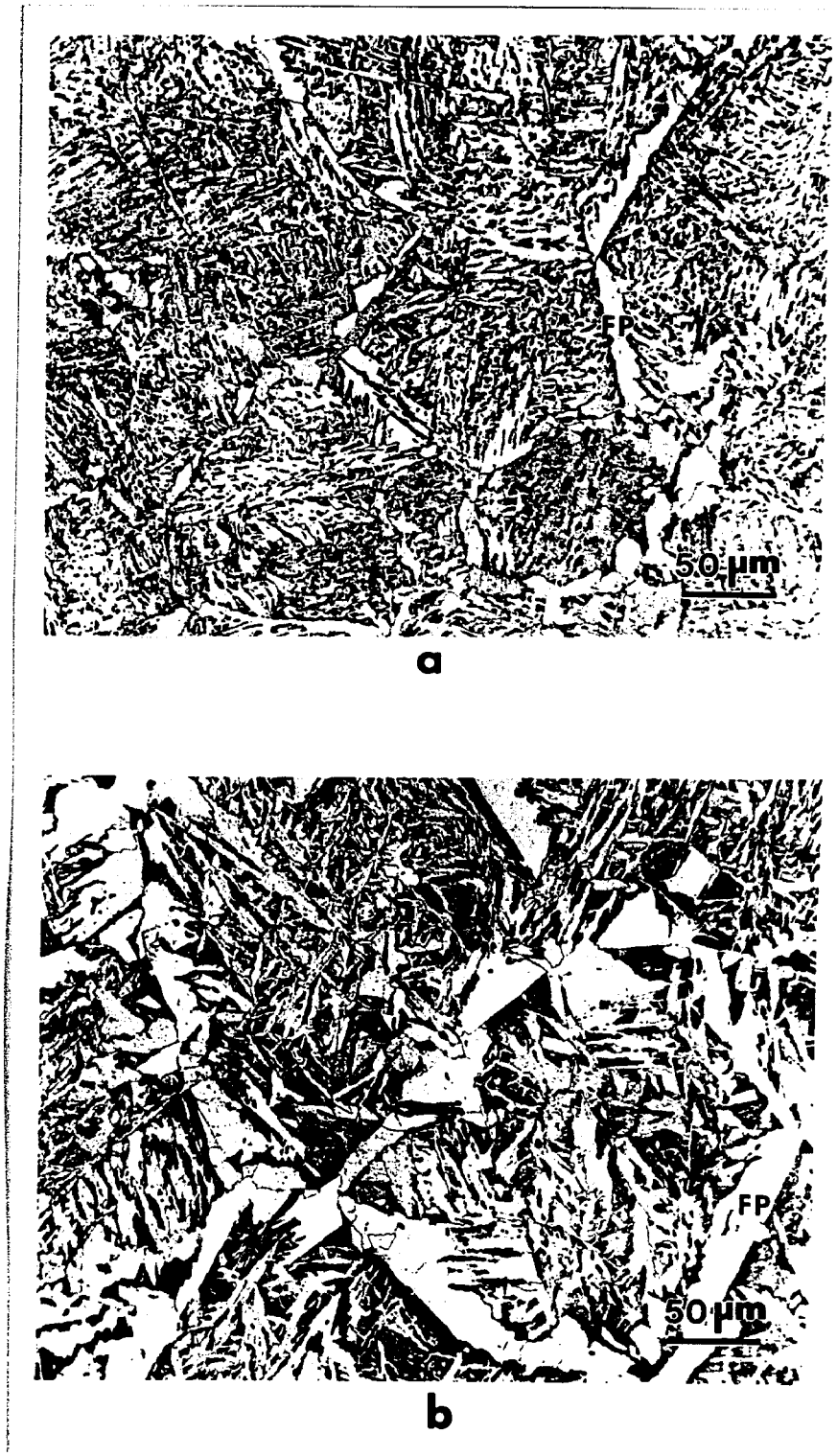

Figure 4.11 HAZ microstructure of specimens welded with 5kJ/mm and as-welded, (a) heat H (b) heat B, 250x

grain boundary ferrite is suppressed by increasing niobium and/or vanadium contents, as illustrated in Figures 4.12 and 4.13. Niobium is more effective than vanadium in suppressing grain boundary ferrite.

The separation of pro-eutectoid ferrite from austenite is controlled by the $\gamma \rightarrow \alpha$ transformation as well as the diffusion rate of carbon away from the frontier of the growing pro-eutectoid ferrite. The carbide-forming elements increase the diffusion activation energy of carbon atoms in austenite and thereby slow the diffusion of carbon atoms in austenite, resulting in inhibition of the formation and growth of pro-eutectoid ferrite. The affinity of four strong carbide-forming elements for carbon can be ranked as Ti>Zr>Nb>V [11]. The results shown in Figure 4.12 and Figure 4.13 agree with this ranking.

4.2.2.4. EFFECT OF V AND/OR Nb CONTENT ON GRAIN SIZE IN THE HAZ

As described in Section 2.1.3, a small addition of Nb or V retards the progress of static recovery and recrystallization, and the austenite grain size is reduced by means of inhibition of grain boundary migration through precipitated particles. Figure 4.14 and Figure 4.15 show the results of measurements of prior austenite grain sizes in the coarse-grained HAZ adjacent to the fusion line in the as-welded 5kJ/mm specimens. The plots indicate that at a constant

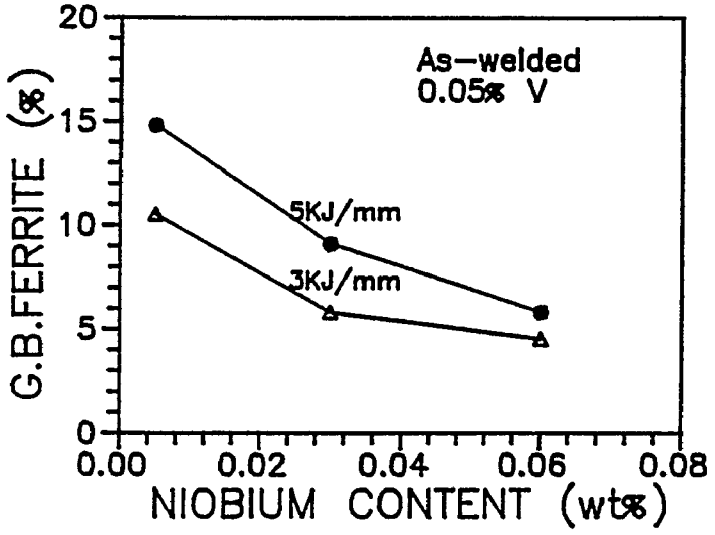

Figure 4.12 Effect of Nb addition on the proportion of pro-eutectoid ferrite

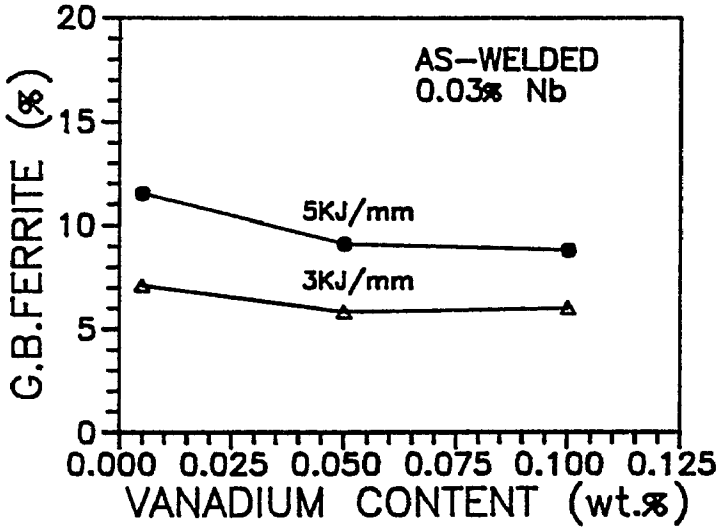

Figure 4.13 Effect of V addition on the proportion of pro-eutectoid ferrite

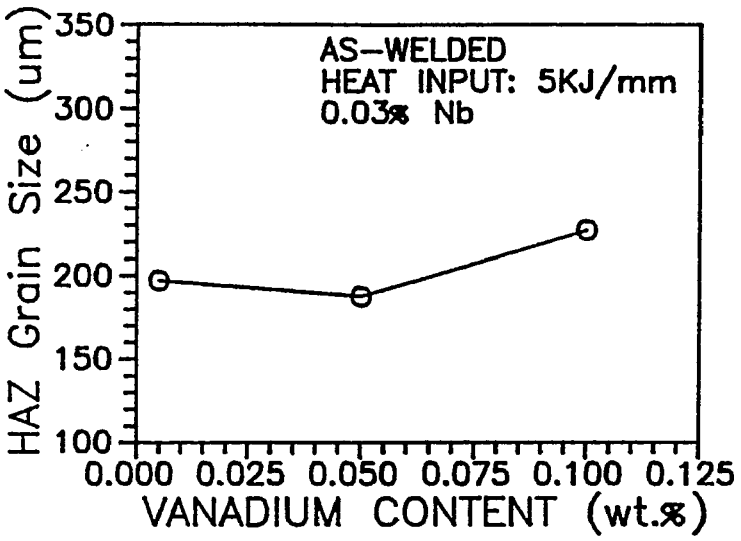

Figure 4.14 Effect of V addition on average grain size in coarse-grained HAZ

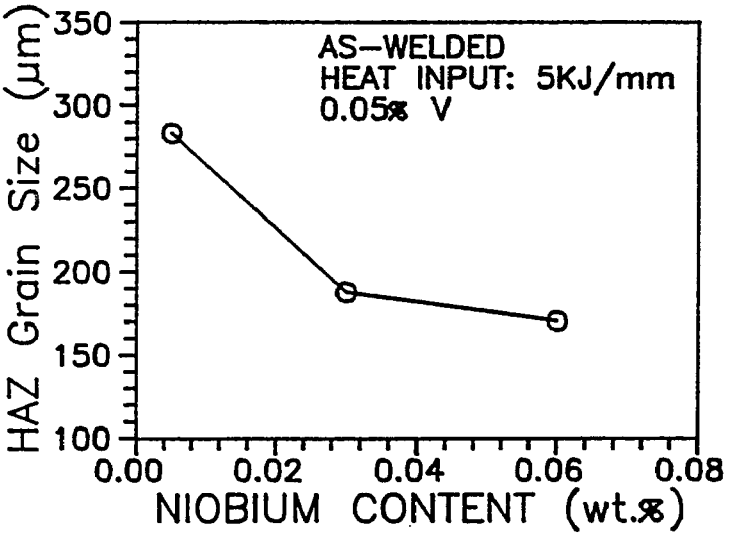

Figure 4.15 Effect of Nb addition on average grain size in coarse-grained HAZ

medium vanadium content an increase in niobium content reduces the HAZ grain size whilst at a constant medium niobium content an increase in vanadium content has little effect on the HAZ grain size. During the welding thermal cycle the peak temperature in the HAZ can be as high as 1350°C, thus vanadium and niobium behave differently in inhibiting grain growth via pinning of grain and sub-boundaries. Figure 4.16 illustrates the solubility of VC, NbC and other carbides and nitrides. The NbC is more stable than VC, especially at elevated

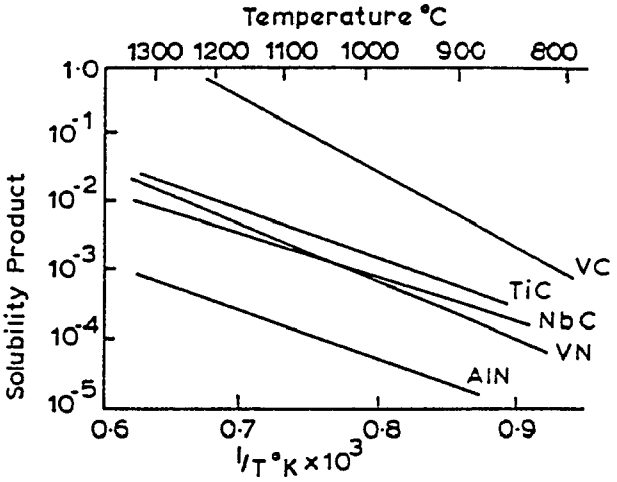

Figure 4.16 Solubility relationships for microalloy carbides and nitrides [18]

temperature. Recall Figure 2.5 which shows nearly complete solubility for VC above 950°C, implying that in V-microalloyed steel unrestricted grain growth can occur above this temperature.

For niobium, two solubility equations of NbC in steel are reported [43][44]:

$$log\ [Wt.\%\ Nb][Wt.\%\ C] = 2.96 - 7510/T \qquad (4.1)$$

$$log\ [Wt.\%\ Nb][Wt.\%\ C]^{0.87} = 3.11 - 7520/T \qquad (4.2)$$

The solubility of NbC is now calculated based on equations 4.1 and 4.2, and listed in Table 4.1. At the temperature of 1250°C the Wt.%Nb in the solution is 0.067 from equation 4.1 and 0.073 from equation 4.2. This implies that for the heats

Table 4.1 The Solubility of Niobium at Different Temperatures

Temperature °C	Wt.% Nb in Solution	
	Equation 4.1	Equation 4.2
1000	0.007	0.008
1100	0.019	0.021
1200	0.045	0.049
1250	0.067	0.073
1300	0.096	0.105

with the highest Nb content of 0.06%, the NbC precipitates will no longer inhibit grain growth at 1250°C and the grain growth in the HAZ should occur.

It would seem appropriate to calculate grain growth over the part of weld thermal cycle which exceeds the solubility temperature of carbides. For the heats with lower Nb content, the grain growth temperatures are expected to be lower, or alternatively, under the same welding thermal cycle the HAZ grain size will be bigger. By knowing some basic information such as the activation energy for self diffusion, the temperature-time profile, as well as by making appropriate

assumptions, the maximum grain size and grain size distribution in the HAZ can be estimated. It is also understandable that the width of coarse-grained HAZ in lower weld heat input specimens is narrower than that in higher weld heat input ones. Evidence for larger grains and narrower zones are always found when comparing the 3kJ/mm and 5kJ/mm HAZs in any heat.

In fact, VC and NbC can form a continuous solid solution. As described in Section 2.1.2, the carbides and nitrides of V and Nb are isomorphous. They are expected to form a wide range of compositions in which both metallic (V and Nb) and nonmetallic (C and N) atoms can be substituted, and the VC-NbC is termed (V,Nb)C, see Section 4.5.1.3. Unfortunately, the V-Nb-C and V-Nb-C-N phase diagrams are not currently available. To estimate the function of V and Nb in determining microstructure when both are present in steel, the (V,Nb)C containing less Nb is expected to behave more like VC and the (V,Nb)C containing less V is expected to behave more like NbC. These assumptions are supported by the results of this investigation.

4.2.3. ELECTRON MICROSCOPIC EXAMINATION IN THE HAZ

Characteristics of basic microstructural constituents in the HAZ were identified and recorded using TEM technique.

Figure 4.17 show the intragranular Widmanstatten ferrite which is observed in both 3kJ/mm and 5kJ/mm HAZs. Coarse

cementite $(Fe,Mn)_3C$ is present in the ferrite boundary. Figure 4.18a which shows a tempered lath martensite structure from the "ferrite with M-A-C" constituent in the HAZ of heat I, welded with 3kJ/mm and heat-treated at 620°C for 10 hours. Figure 4.19 shows a bainitic structure in the HAZ of heat A with the same heat input and PWHT. Comparison of Figure 4.18a and Figure 4.19 reveals that while the microstructures of martensite and bainite may at first seem very similar, the characteristic delineating differences in the structure are observable here.

Figure 4.17 Intragranular Widmanstätten site ferrite, heat G, 3KJ/mm, PWHT at 620°C for 10hours

As shown in Figure 4.18a, the tempered martensite is highly dislocated, with two or more variants of the laths, producing a "weave" structure with one variant dominating. This feature is schematically illustrated in Figure 4.18b where L_1 represents the dominating variant and L_2,L_3 represent the variants with different orientations. The TEM micrograph also shows the rounded, elongated, interlath and intralath tempered carbides formed during PWHT.

The upper bainite, as shown in Figure 4.19, has only a single variant of the laths with interlath carbides, and a characteristically low dislocation density when compared to the martensite in Figure 4.18a.

In a bainite transformation the lath nucleation occurs via a shear transformation, having a Kurdjumov-Sachs or Nishiyama-Wassermann orientation relationship between the austenite and bainitic lath. The lath grows rapidly, forming semicoherent interfaces. This occurs at many sites along the prior austenite grain boundaries, producing a group of similarly orientated, fine spaced ferrite laths. As the laths thicken and lengthen, the carbon content of the interlath austenite increases. The carbide particles nucleate and grow in the austenite between the laths, forming interlath carbide particles and producing what is seen here in Figure 4.19, known as upper bainite.

a

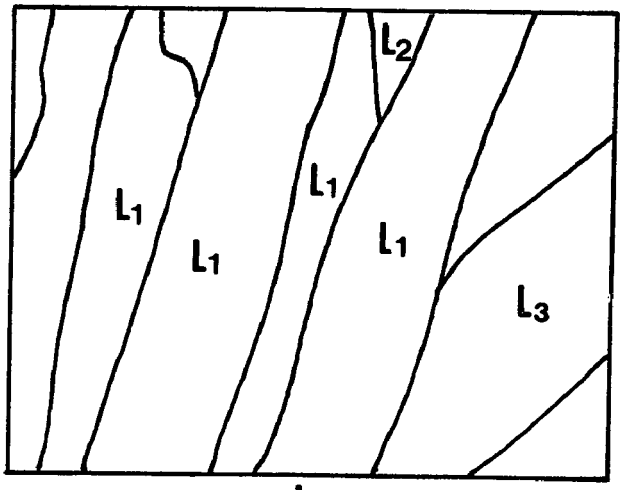

b

Figure 4.18 (a) Tempered martensite in the HAZ, showing highly dislocated laths, interlath and intralath cementites, 3kJ/mm, PWHT 620°C/10hrs.
(b) Schemetic illustration of more variants of laths

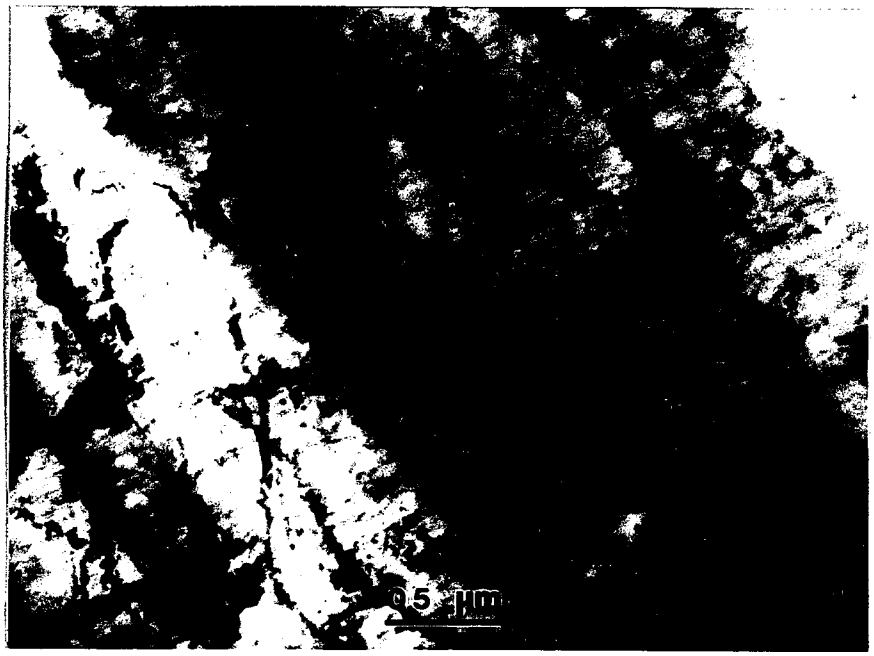

Figure 4.19 Upper bainite in the HAZ, showing single variant of lath with interlath carbides. Heat A, 3KJ/mm, PWHT 620°C/10hrs.

The TEM examination also extends to the HAZ intercritical region which corresponds to the temperature exposure range of 700-900°C. In this range, the base metal, heated between the A_1 and A_3, at first partially austenizes on heating, followed by the $\gamma \rightarrow \alpha$ transformation on cooling. The pearlite as one of the regular products of the transformation can be observed in this region, as shown in Figure 4.20. The lamellar microstructure and two pearlite colonies are visible in this micrograph.

Some spheroidized cementite particles, shown as Figure 4.21 are also observed. Spheroidization occurs even at the lower end of the intercritical temperature range. There is

relatively little $\alpha \rightarrow \gamma$ transformation during the rapid heating cycle, the lamellar pearlite changes to spheroidized particles of cementite. The agglomeration of spheroidized cementite particles at grain boundaries can be seen in Figure 4.21. This indicates that grain boundaries serve as high diffusivity channels for carbon at lower temperatures.

Sections 4.2.2 and 4.2.3 analyzed the basic microstructures in the HAZ with both optical and electron microscopy. The more important process, the precipitation, will be discussed later.

4.3. MICROHARDNESS MEASUREMENTS

4.3.1. MICROHARDNESS TRAVERSE ACROSS THE HAZ

Figure 3.7 has shown the typical appearance of a Knoop microhardness survey along and across a fusion line. The microhardness traverses across the HAZ for a 3kJ/mm weld of heat B under as-welded and different PWHT conditions are presented in Figures 4.22a through 4.22f. The results shows there is a microhardness peak adjacent to fusion line in each curve. This peak indicates the existence of high hardness constituents such as martensite and bainite in the coarse-grained HAZ. PWHTs at 620°C for 1,2,5,10,20,50 hours did not remove or reduce the hardness peak from the traverse profiles. As mentioned earlier, two parallel processes are taking place in the HAZ during PWHT: (a) the decomposition of high hardness constituents (tempering) plus stress relief, and (b) a

Figure 4.20 Pearlite in HAZ, showing lamellar microstructure and two pearlite colonies. Heat A, 5KJ/mm, PWHT 620°C/10hrs

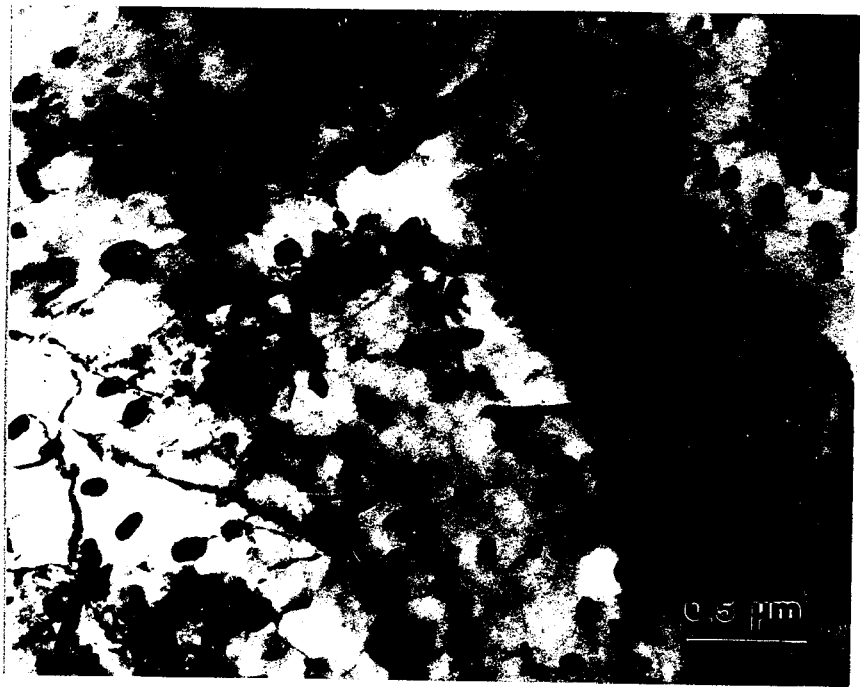

Figure 4.21 Spherodized cementite in HAZ. Heat A, 3KJ/mm, PWHT 620°C/10hrs.

hardening process, namely the precipitation of V and/or Nb carbides. The average maximum HAZ hardness which was measured immediately adjacent to the fusion line was also plotted in each corresponding curve with a square symbol and an error bar of $\pm 1.0\sigma$. This result shows the reasonable agreement between the average maximum coarse-grained HAZ data and the hardness peak in the traverse profile.

4.3.2. MAXIMUM MICROHARDNESS IN THE HAZ

The results of measurements of average maximum microhardness in the coarse-grained HAZ are summarized in Table 4.2. Each hardness value in the table was taken as the average of ten readings. Figures 4.23a,b,c and Figure 4.24a,b,c are the three-dimensional (3-d) plots that show the relationship between maximum HAZ hardness and microalloy elements V and Nb contents. Figures 4.23a,b and c represent the 3kJ/mm specimens with as-welded, PWHT 620°C/2hours and PWHT 620°C/10hours, respectively. Figure 4.24a,b and c are the plots of 5kJ/mm specimens with as-welded, PWHT 620°C/2hours and PWHT 620°C/10hours, respectively. Based on these three-dimensional plots, the following understanding can be obtained:

1, In all these six 3-d plots that represent six conditions (two heat inputs x three PWHTs) HAZ hardness notably increases as increasing V and/or Nb contents.

Table 4.2 Average maximum HAZ hardness, Knoop hardness, number in brackets represents the standard deviation

	HEAT INPUT: 3KJ/mm							HEAT INPUT: 5KJ/mm						
Heat Code	As-welded Condition	PWHT Time at 620°C, hours 1	2	5	10	20	50	As-welded Condition	PWHT Time at 620°C, hours 1	2	5	10	20	50
A	232 (3)	249 (6)	226 (4)	219 (8)	227 (3)	218 (7)	223 (6)	220 (7)	216 (7)	216 (9)	214 (9)	219 (7)	206 (9)	202 (8)
B	251 (6)	275 (8)	259 (6)	269 (5)	274 (7)	260 (7)	241 (4)	239 (8)	256 (5)	240 (4)	245 (4)	252 (5)	241 (6)	236 (2)
C	260 (5)	281 (6)	280 (5)	280 (7)	278 (9)	266 (3)	250 (7)	243 (7)	280 (3)	265 (8)	268 (7)	283 (8)	264 (6)	252 (7)
D	248 (7)	266 (5)	261 (6)	262 (5)	259 (6)	260 (5)	254 (6)	243 (8)	272 (5)	269 (8)	266 (6)	262 (10)	259 (8)	255 (8)
E	261 (6)	279 (8)	273 (5)	274 (8)	289 (5)	271 (5)	267 (6)	250 (3)	277 (8)	269 (7)	281 (7)	273 (6)	274 (7)	259 (9)
F	273 (9)	300 (4)	301 (10)	303 (10)	290 (9)	287 (7)	282 (7)	257 (6)	286 (10)	288 (9)	294 (5)	286 (9)	285 (11)	291 (10)
G	263 (7)	288 (10)	271 (8)	281 (11)	282 (8)	276 (8)	269 (7)	257 (6)	267 (7)	277 (8)	266 (9)	274 (6)	261 (7)	252 (10)
H	271 (6)	302 (9)	286 (5)	292 (5)	295 (8)	286 (9)	290 (5)	260 (8)	295 (8)	285 (6)	279 (9)	291 (6)	299 (10)	293 (9)
I	273 (7)	316 (5)	313 (8)	298 (5)	302 (7)	288 (4)	297 (8)	282 (12)	294 (3)	298 (6)	303 (8)	301 (7)	297 (10)	295 (8)

2, Among as-welded, PWHT 620°C/2hrs and PWHT 620°C/10hrs conditions, the strongest effect of V and/or Nb additions on increasing HAZ hardness is gained in PWHT 620°C/2hrs condition in both 3kJ/mm and 5kJ/mm specimens.

In 3kJ/mm specimens the HAZ hardness increases from heat A which has the least V and Nb addition to heat I which has the most V and Nb addition are 41 for as-welded, 87 for PWHT 620°C/2hrs and 75 for 620°C/10hrs. In 5kJ/mm specimens they are

62 for as-welded, 82 for 620°C/2hours and 82 for 620°C/10hrs.

In the as-welded condition, the V/Nb additions contribute to hardness through precipitation hardening, grain refinement and increasing dislocation density (due to decreasing transformation temperature). In the PWHT condition, the remarkable hardness increase with increasing V/Nb contents is attributed to the extremely fine, semi-coherent VC and NbC precipitates dispersed in the α-phase, and formed during aging.

3, In any 3-d plot whether as-welded or PWHT, Nb was found to be a stronger precipitation hardening element than V. The average increase in HAZ hardness as a function of V content at a fixed 0.005%Nb level (i.e. survey along V-axis), and the average increase in HAZ hardness as a function of Nb content at a fixed 0.005%V level (i.e. survey along Nb-axis), are presented in Table 4.3.

TABLE 4.3 HAZ Knoop hardness increment per 0.01 Wt.% of V or Nb

0.01 Wt% increasing in	3KJ/mm			5KJ/mm		
	as-welded	PWHT 620°C/2h	PWHT 620°C/10h	as-welded	PWHT 620°C/2h	PWHT 620°C/10h
V	2.9	5.7	5.4	2.4	5.2	6.7
Nb	5.6	8.2	10.0	6.7	11.0	10.0

4, In heat A which has the least V and Nb (0.005%V and 0.004%Nb), the microhardness values of 3kJ/mm specimens do

not change significantly from as-welded condition to PWHT conditions. Similarly, the data of 5kJ/mm specimens for as-welded and for PWHTs do not have significant difference. This implies that the precipitation hardening in heat A was not able to win the competition with the softening process caused by the decomposition of high hardness constituents. Only those heats with higher V and/or Nb contents than heat A will produce significant precipitation hardening during PWHT.

5, Overall, 3kJ/mm specimens show higher HAZ hardness in all three PWHT conditions than 5kJ/mm specimens do. This is because of the relatively smaller grain size in coarse grained HAZ and the relatively larger amount of high hardness microstructural constituents in the 3kJ/mm HAZ than in the 5kJ/mm HAZ. Although the decomposition of hard constituents takes place during PWHT and the precipitation hardening effect superimposes on both 3kJ/mm and 5kJ/mm HAZ hardness, the slight superiority in hardness for 3kJ/mm HAZ still remains.

6, No significant synergistic hardness effect is noted due to the combination of both microalloy elements V and Nb. This is illustrated by comparing the hardness values along a diagonal line from composition C (0.097%V and 0.005%Nb) to composition G (0.005%V and 0.049%Nb) on the surface in Figures 4.23 and 4.24. The hardness variation along this line in nearly all cases changes smoothly without maxima or minima between end points.

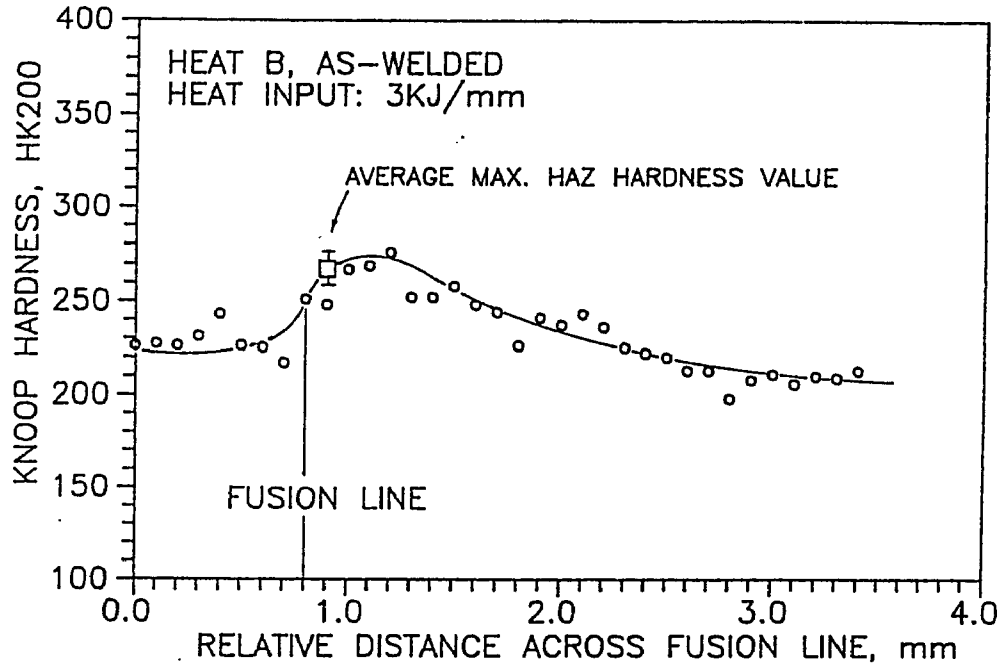

(a) as-welded

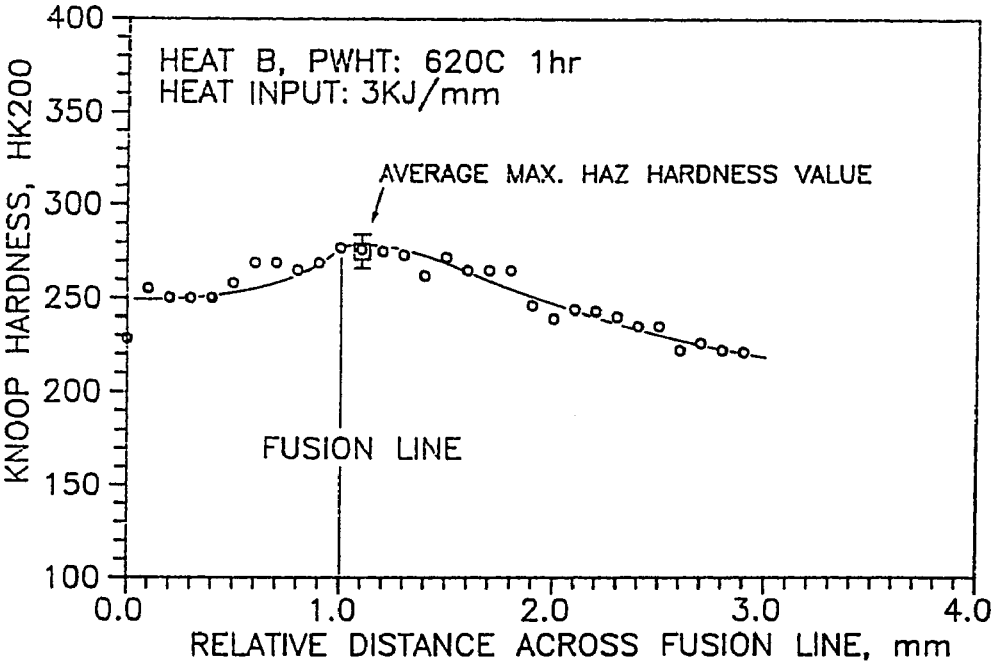

(b) PWHT 620°C/1hr.

Figure 4.22 Microhardness traverses across HAZ of heat B, welded with 3KJ/mm

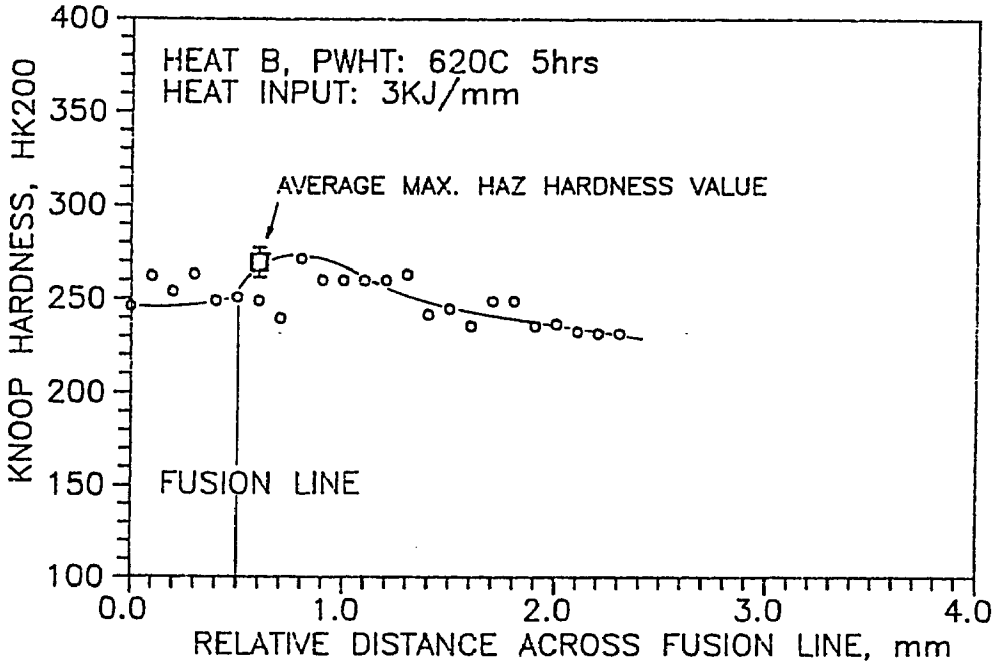

(c) PWHT 620°C/5hrs.

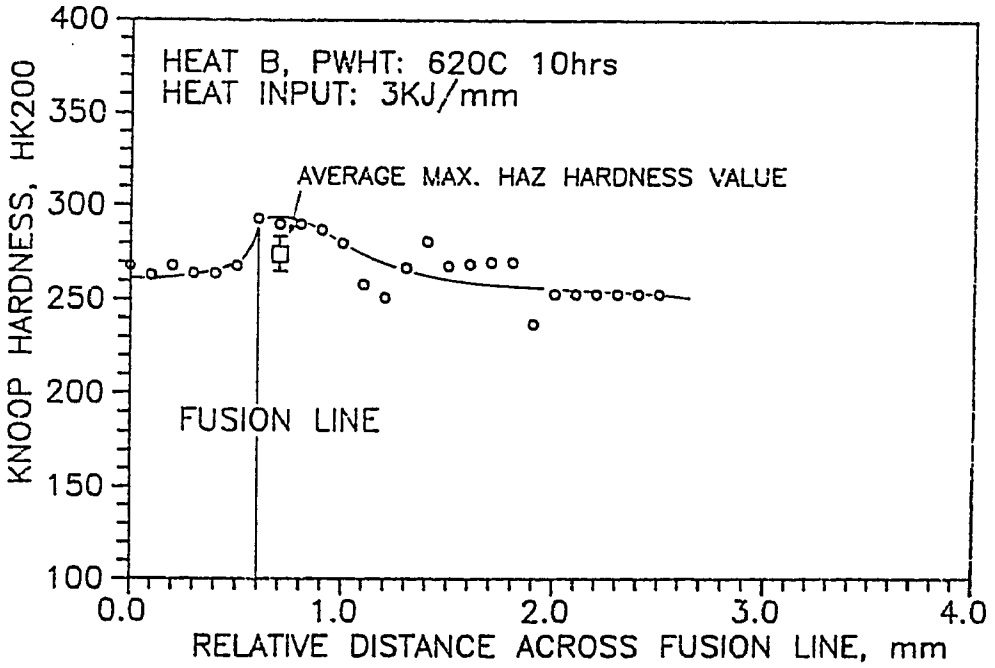

d) PWHT 620°C/10hrs.

Figure 4.22 Continued

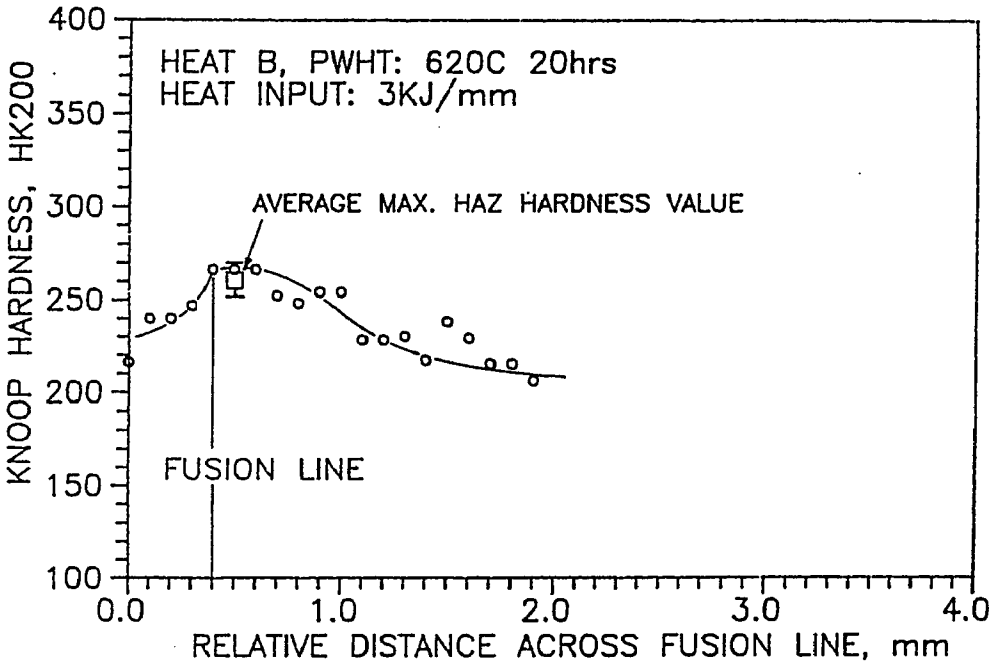

(e) PWHT 620°C/20hrs.

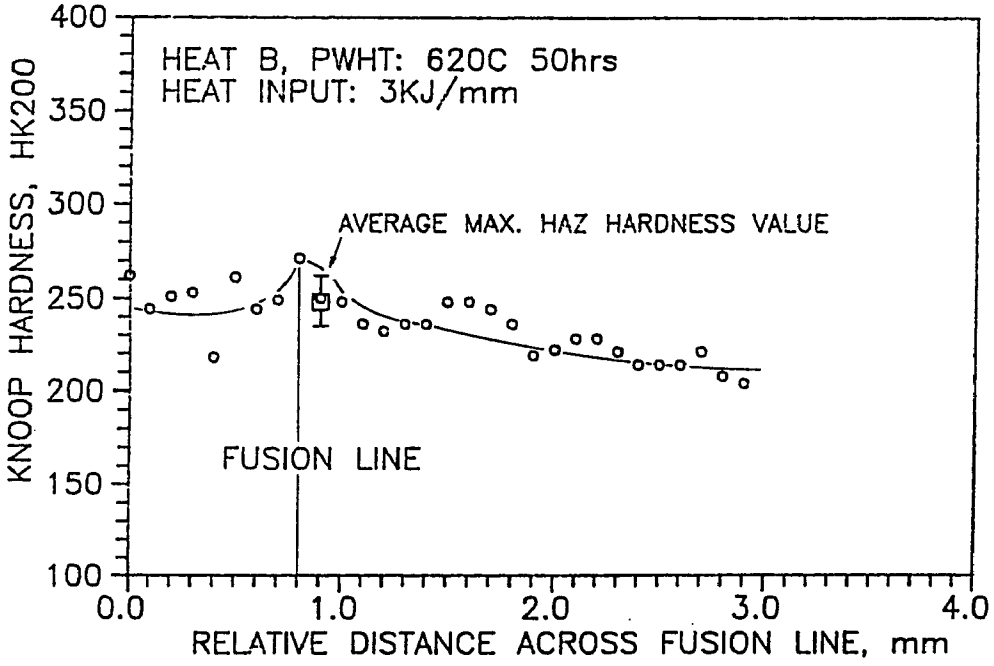

(f) PWHT 620°C/50hrs.

Figure 4.22 Continued

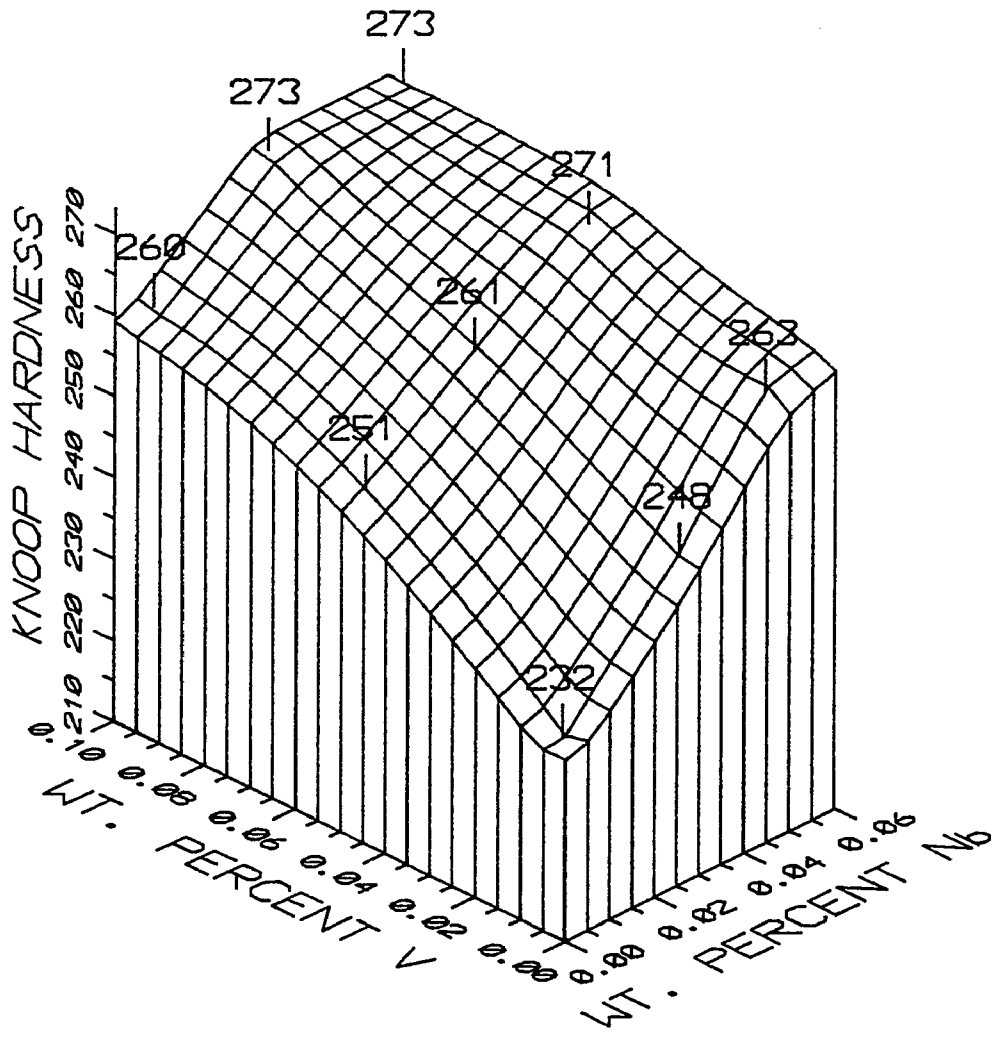

(a) as-welded

Figure 4.23 Three-dimensional representation of maximumcoarse-grained HAZ hardness of microalloyed steels, welded with 3KJ/mm, Knoop Hardness

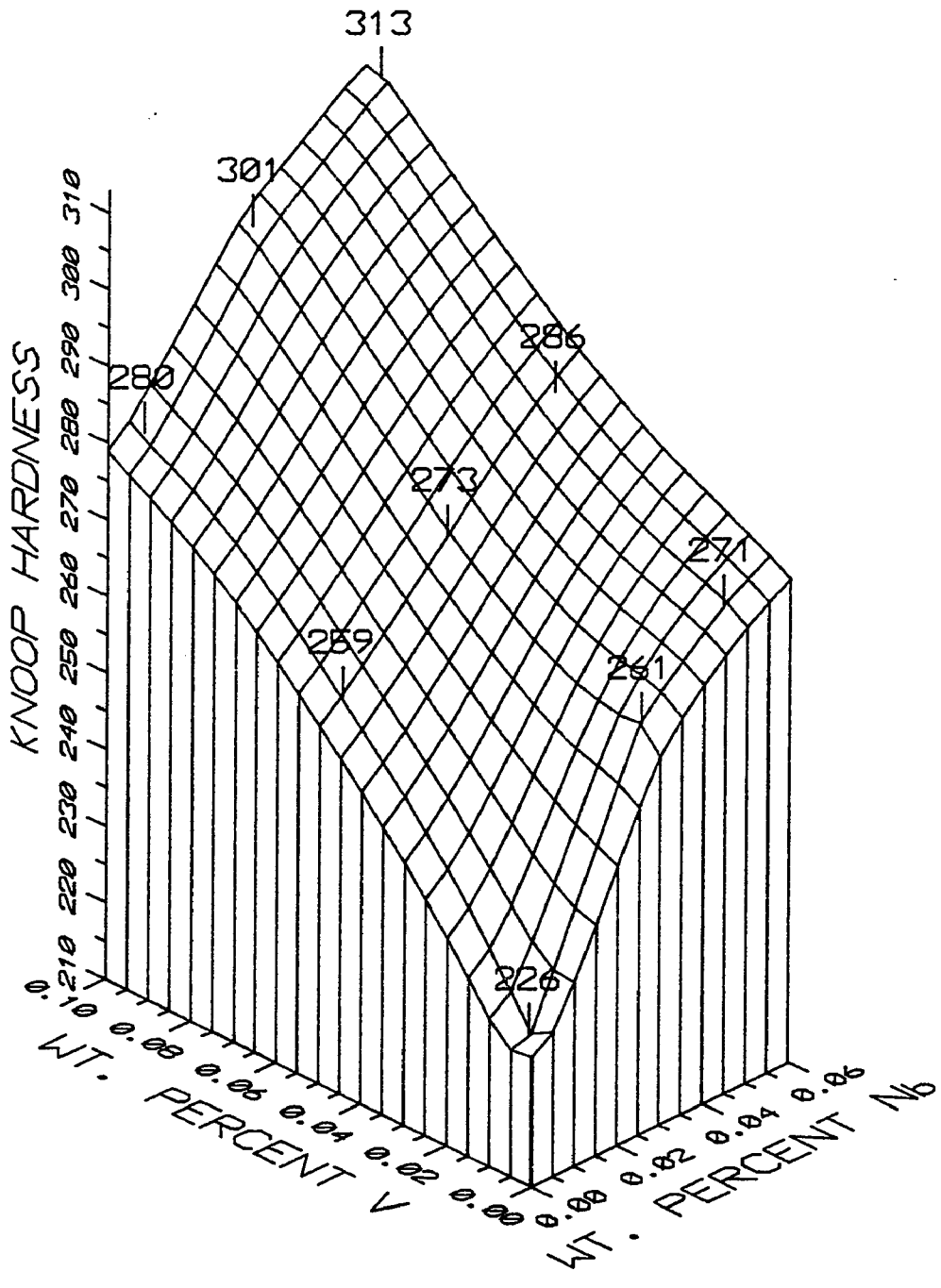

(b) PWHT at 620°C for 2 hours

Figure 4.23 Continued

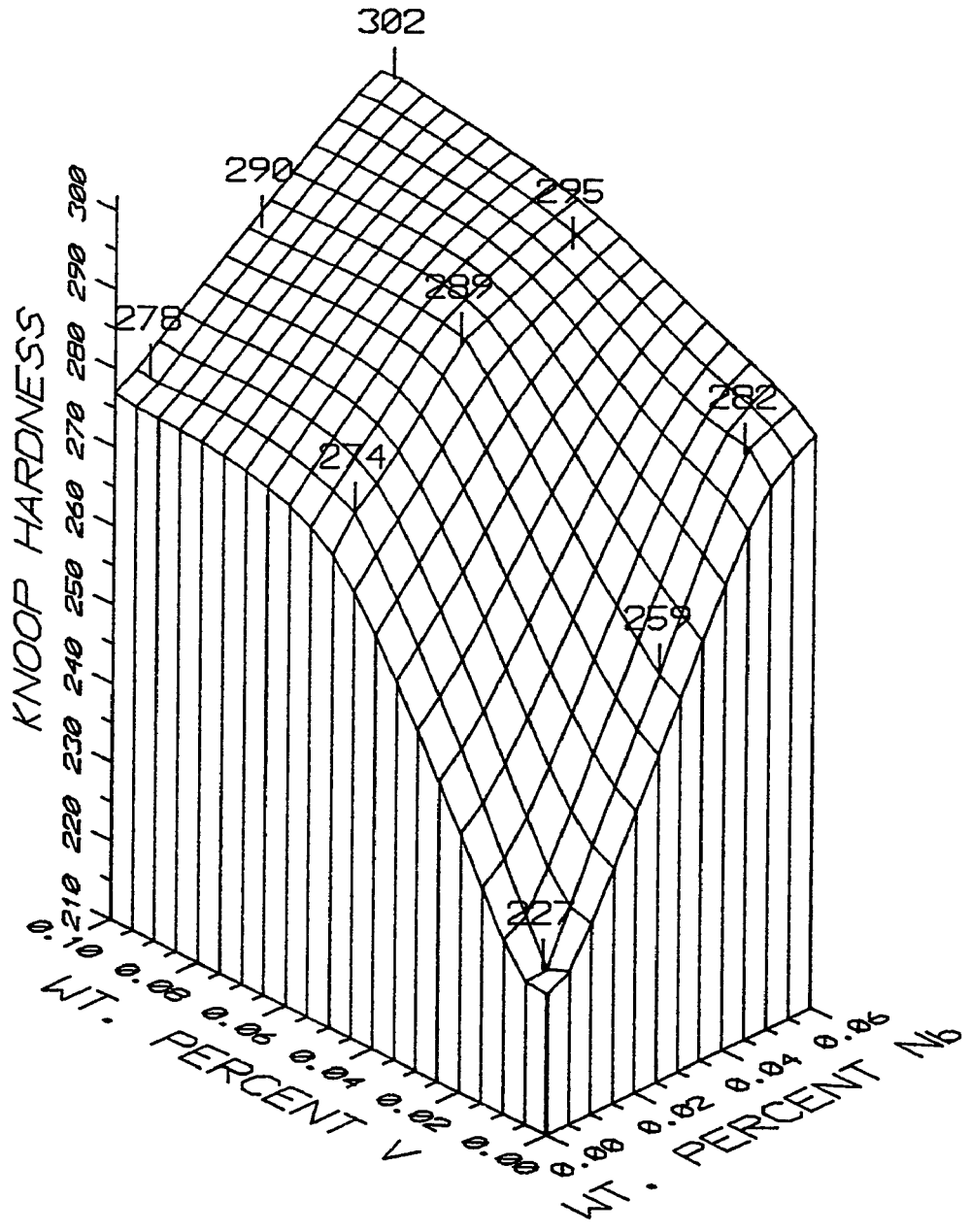

(c) PWHT at 620°C for 10 hours

Figure 4.23 Continued

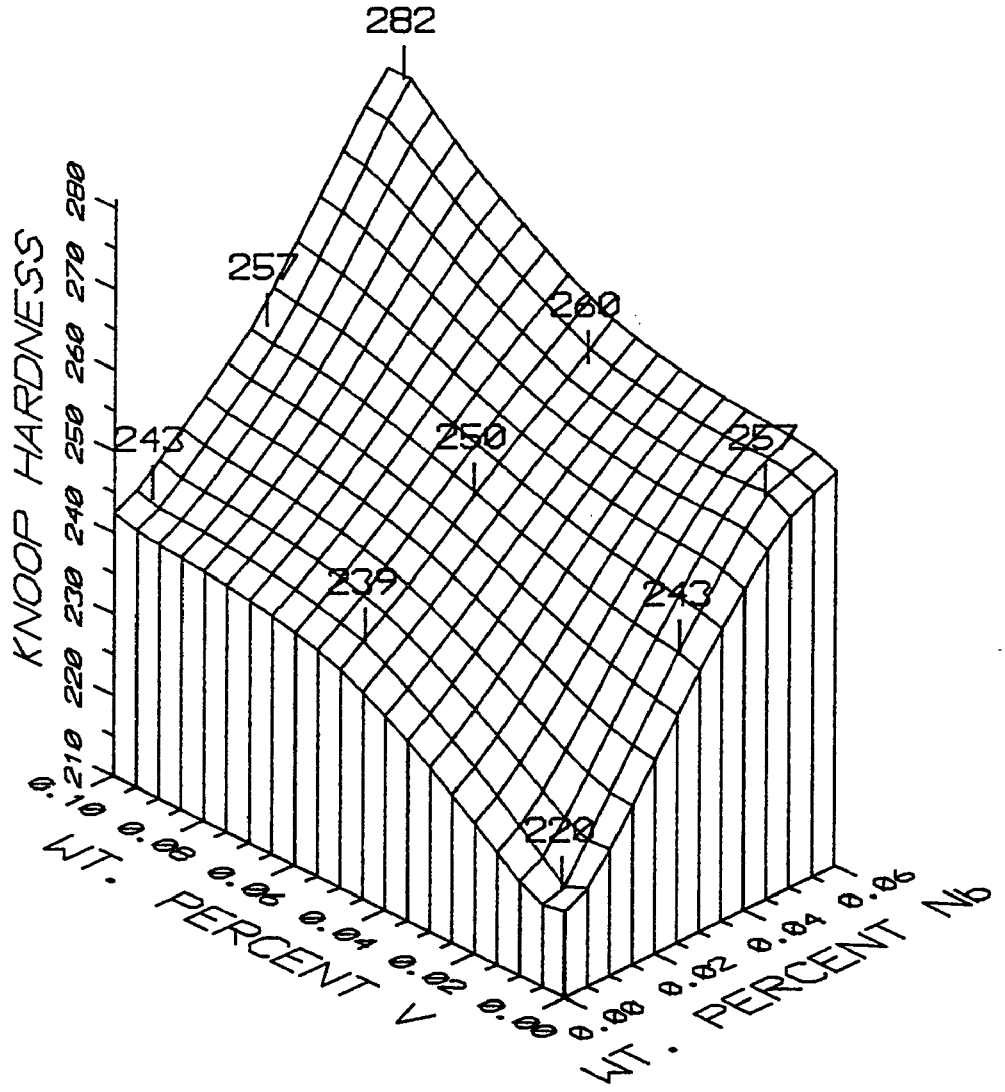

(a) as-welded

Figure 4.24 Three-dimensional representation of maximum coarse-grained HAZ hardness of microalloyed steels, welded with 5KJ/mm

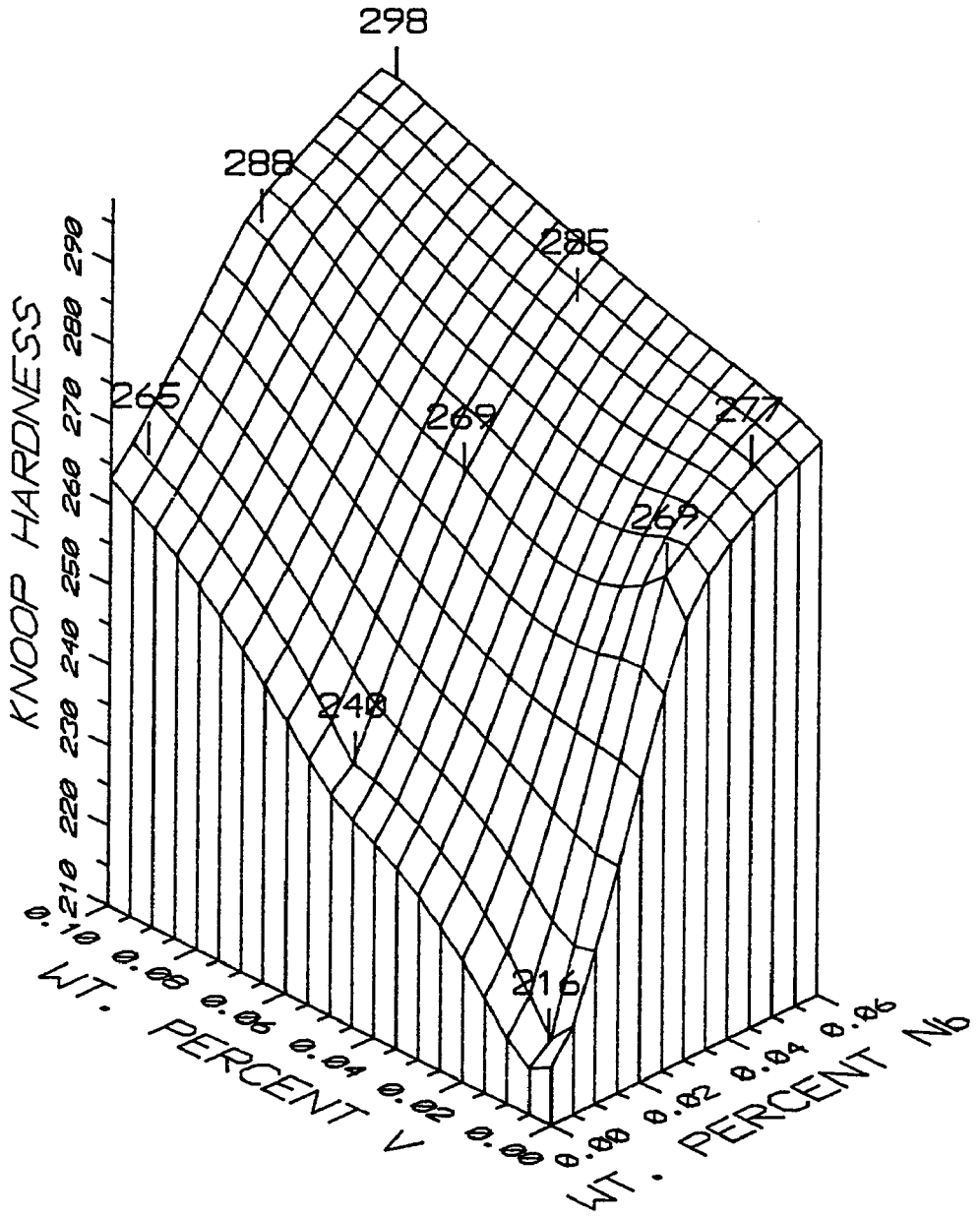

(b) PWHT at 620°C for 2 hours

Figure 4.24 Continued

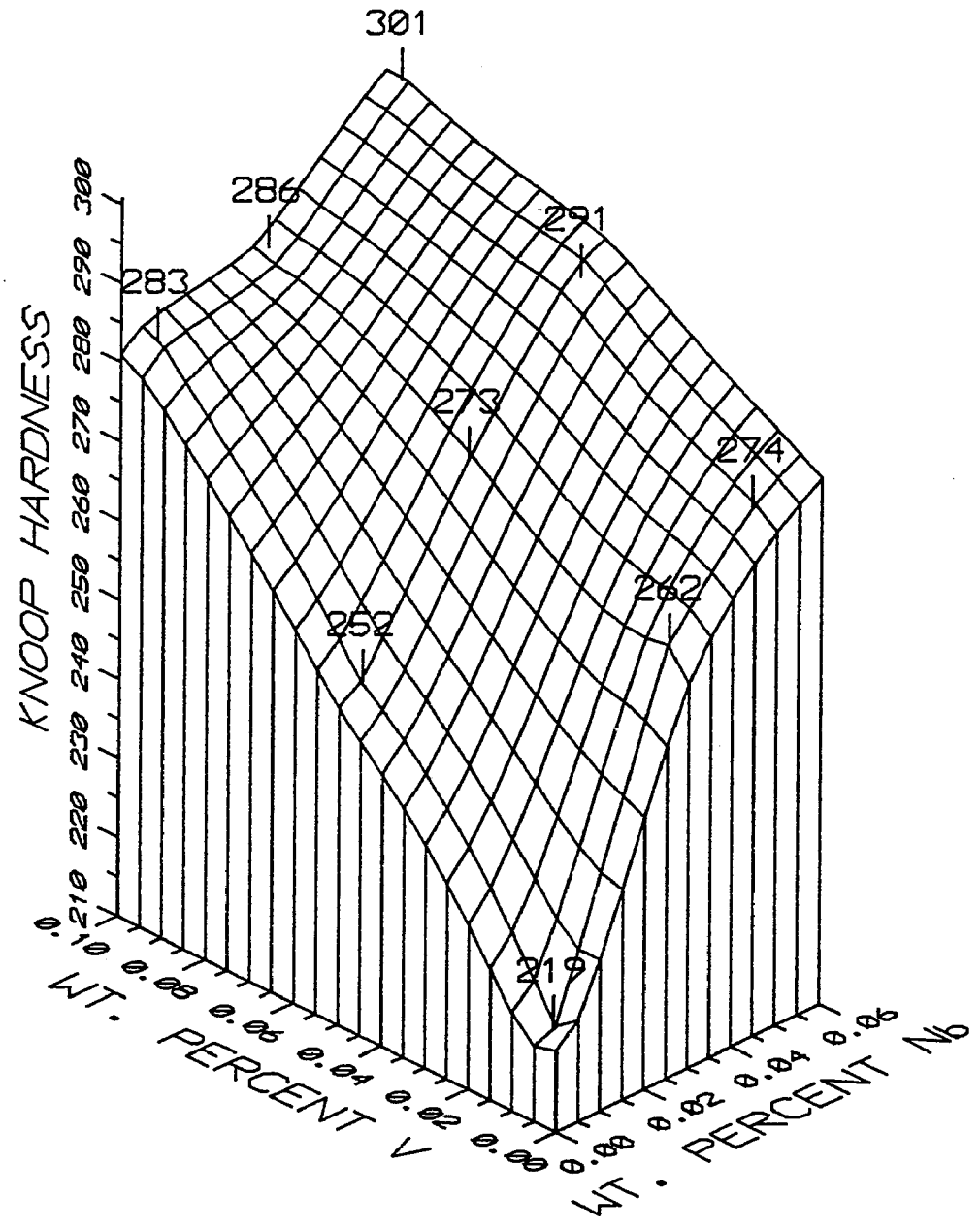

(c) PWHT at 620°C for 10 hours

Figure 4.24 Continued

4.3.3. AGING STUDY

As previously discussed, the HAZ may be supersaturated with microalloy elements V and Nb after weld cooling, and the degree of supersaturation depends on the V and/or Nb contents and cooling rate. Age hardening occurs during PWHT and the net increase in hardness will be seen if precipitation hardening is great enough to offset the microstructural softening which occurs simultaneously during aging. In this study, bead-on-plate specimens of different heats, welded with different heat inputs were heat-treated at 620°C for 1, 2, 5, 10, 20, 50 hours, protected with pure dry argon to prevent oxidation and decarburization. The maximum HAZ hardness was measured in the coarse-grained HAZ adjacent to the fusion line in each specimen.

Figure 4.25 through Figure 4.33 illustrate the results of the aging study. Although the data shows significant scatter in some plots, the aging behavior can still be confirmed and described as following:

1, The maximum hardness values showing a peak or plateau are observed in the range of 1 hour to 10 hours for most specimens. This reveals that precipitation strengthening is much greater than the loss of hardness caused by microstructural softening. For heat F, heat H and heat I that have the highest V plus Nb total microalloy contents, the precipitation hardening effect remains through until the

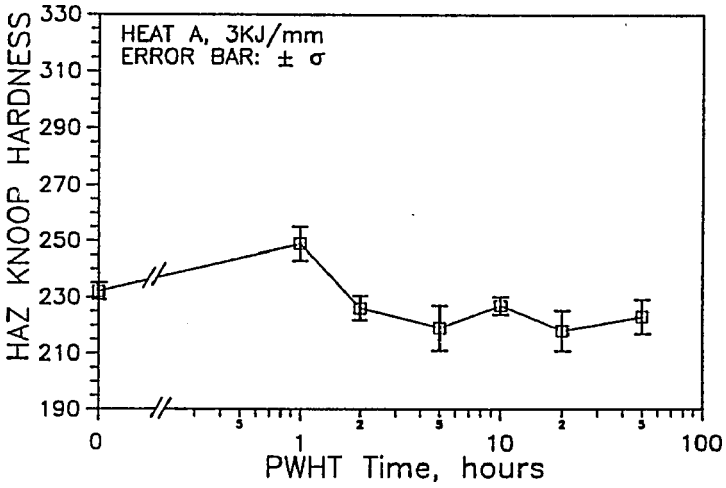

(a)

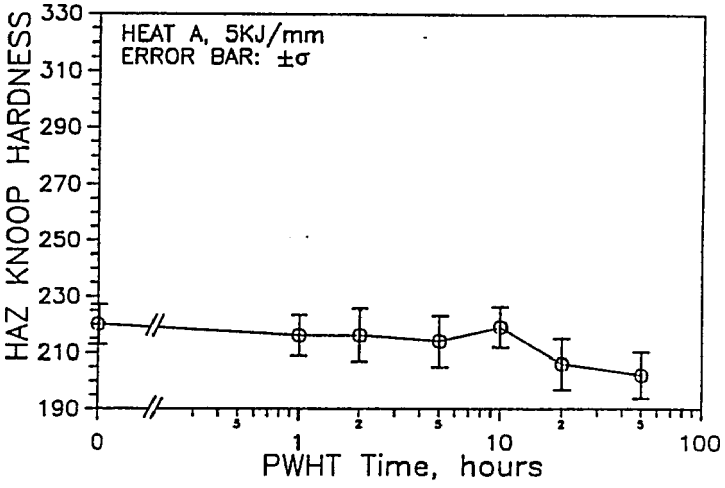

(b)

Figure 4.25 Variation of maximum coarse-grained HAZ hardness of heat A during aging (a) 3kJ/mm (b) 5kJ/mm

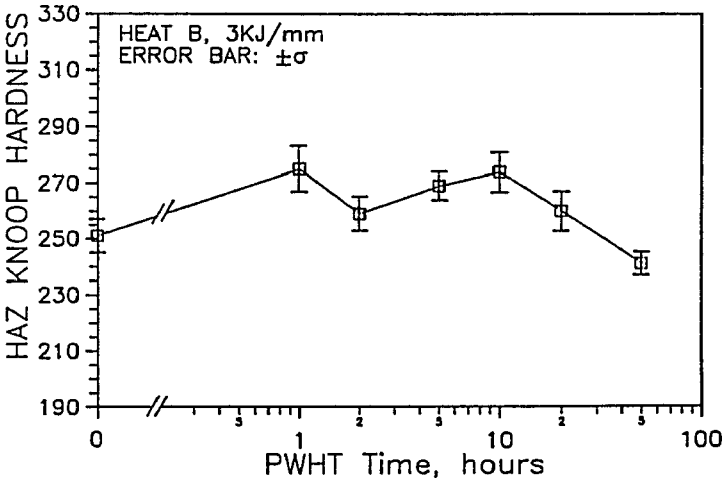

(a)

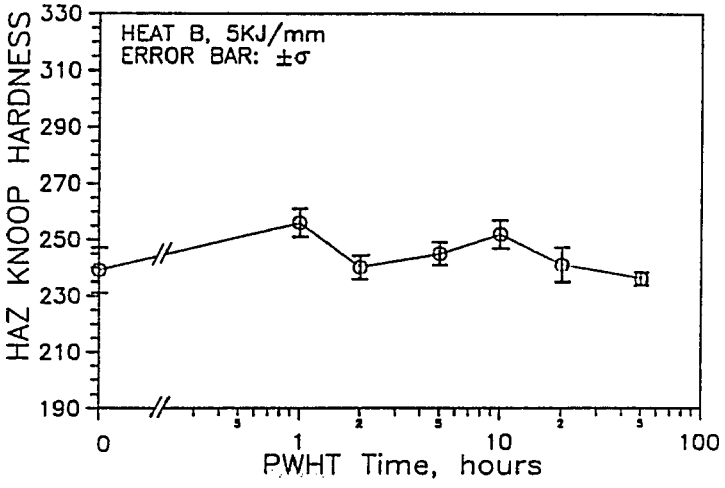

(b)

Figure 4.26 Variation of maximum coarse-grained HAZ hardness of heat B during aging. (a)3kJ/mm (b) 5kJ/mm

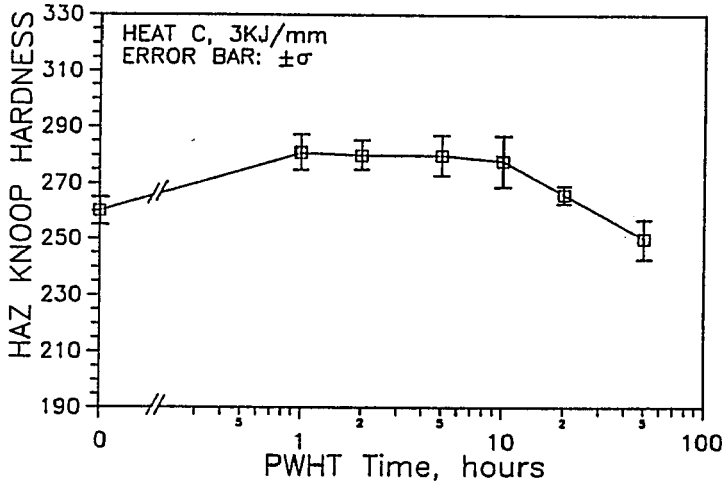

(a)

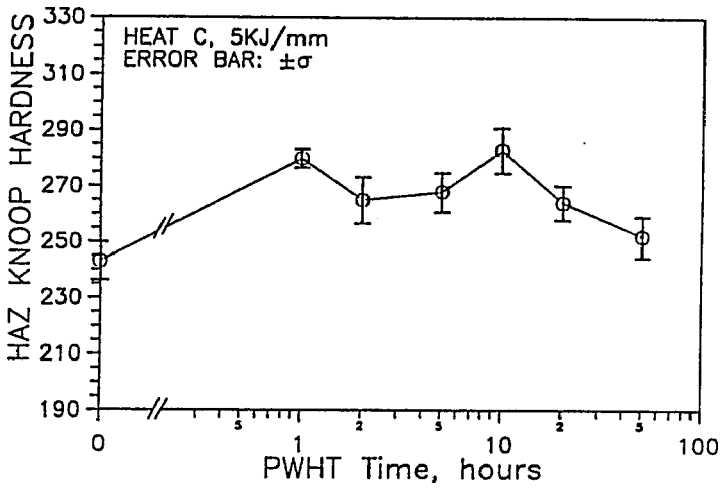

(b)

Figure 4.27 Variation of maximum coarse-grained HAZ hardness of heat C during aging. (a) 3kJ/mm (b) 5kJ/mm

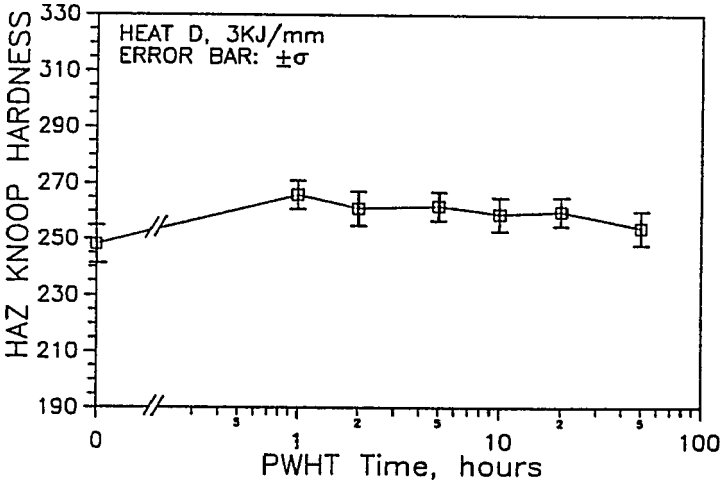

(a)

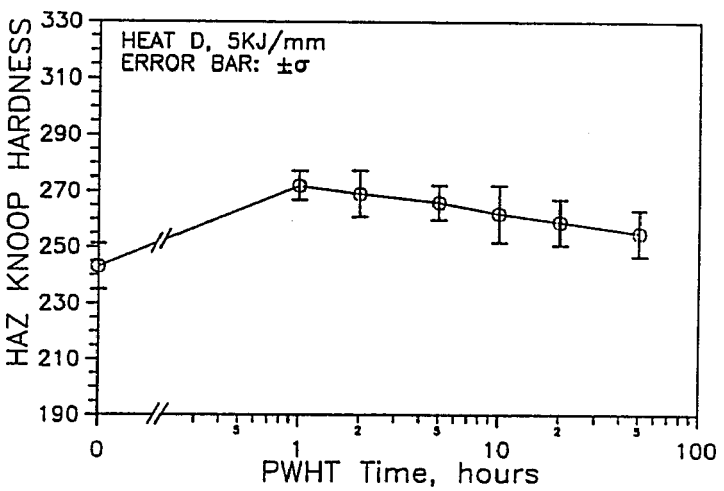

(b)

Figure 4.28 Variation of maximum coarse-grained HAZ hardness of heat D during aging. (a) 3kJ/mm (b) 5kJ/mm

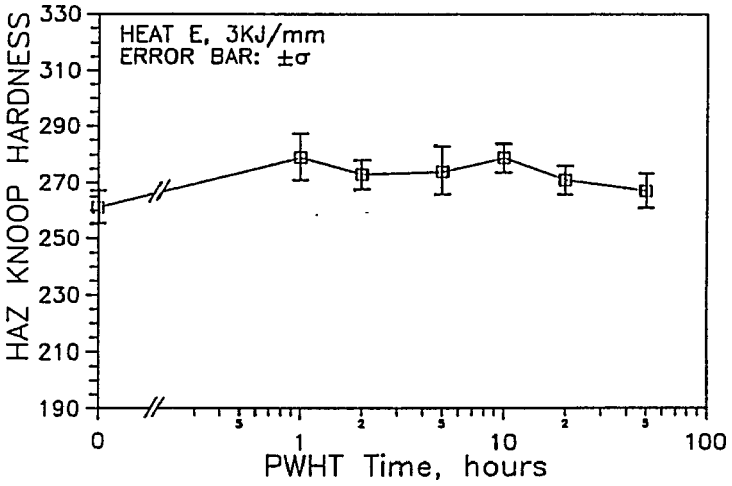

(a)

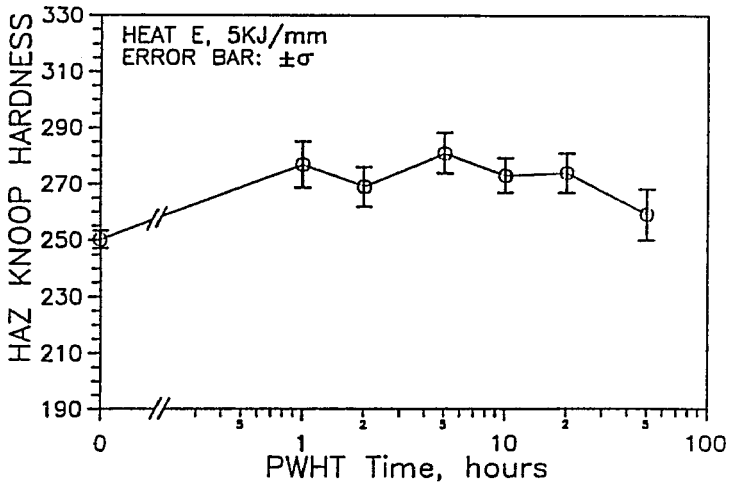

(b)

Figure 4.29 Variation of maximum coarse-grained HAZ hardness of heat E during aging. (a) 3kJ/mm (b) 5kJ/mm

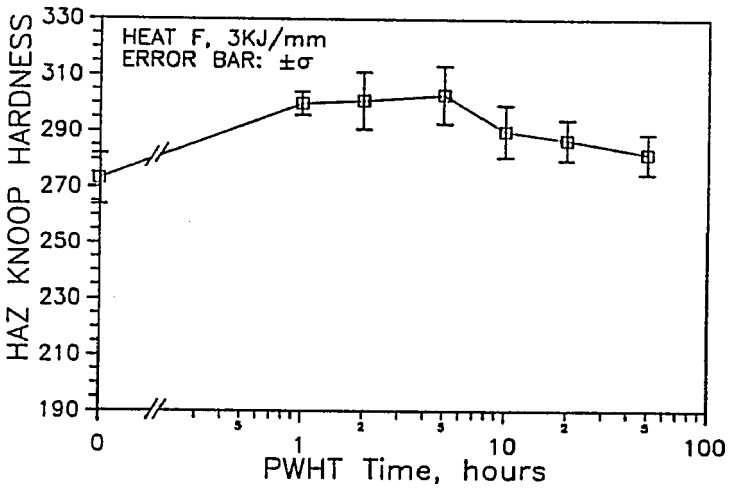

(a)

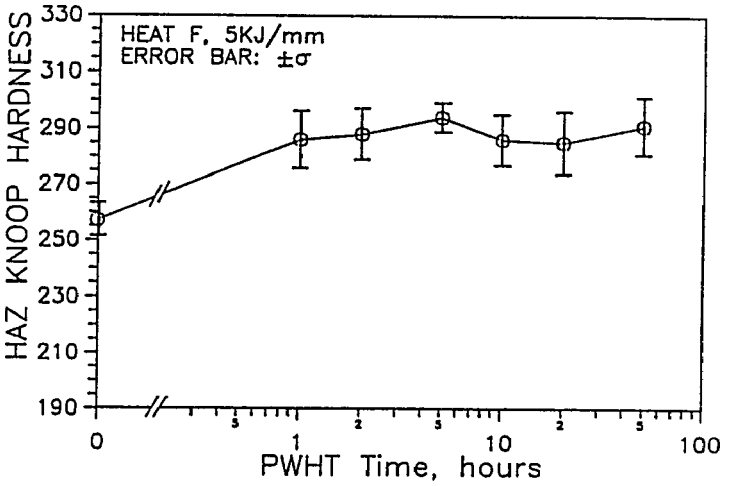

(b)

Figure 4.30 Variation of maximum coarse-grained HAZ hardness of heat F during aging. (a) 3kJ/mm (b) 5kJ/mm

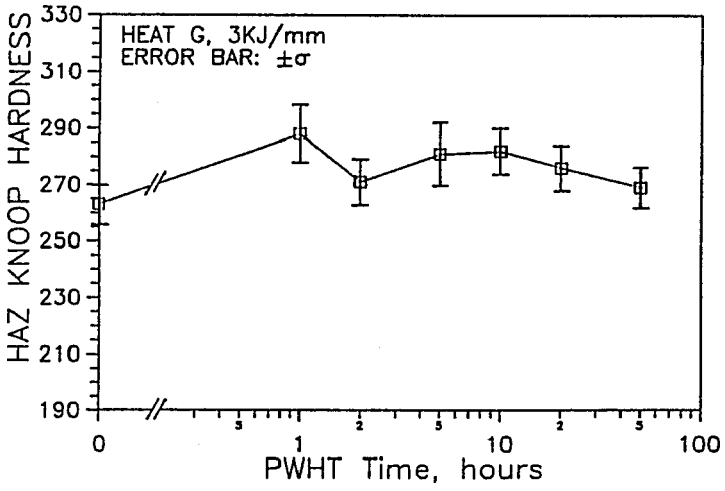

(a)

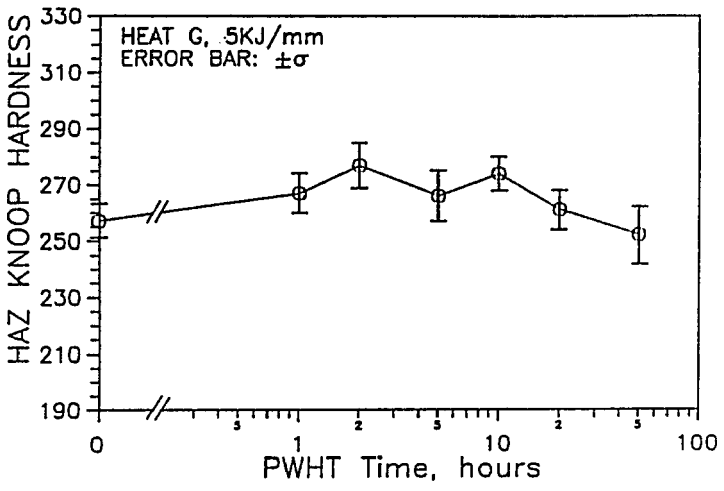

(b)

Figure 4.31 Variation of maximum coarse-grained HAZ hardness of heat G during aging. (a) 3kJ/mm (b) 5kJ/mm

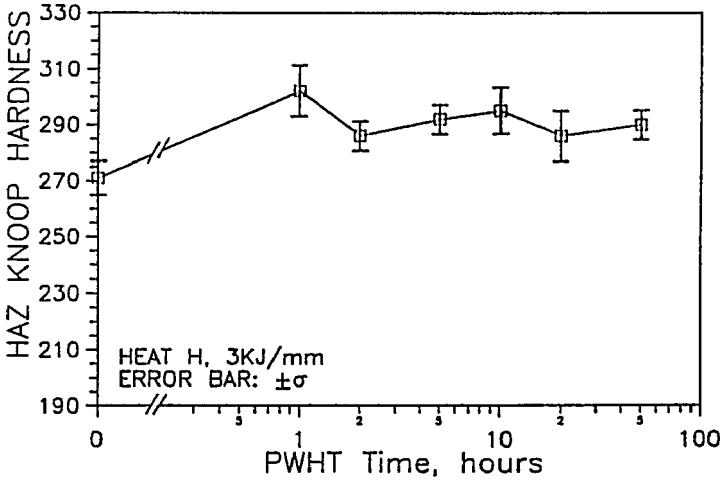

(a)

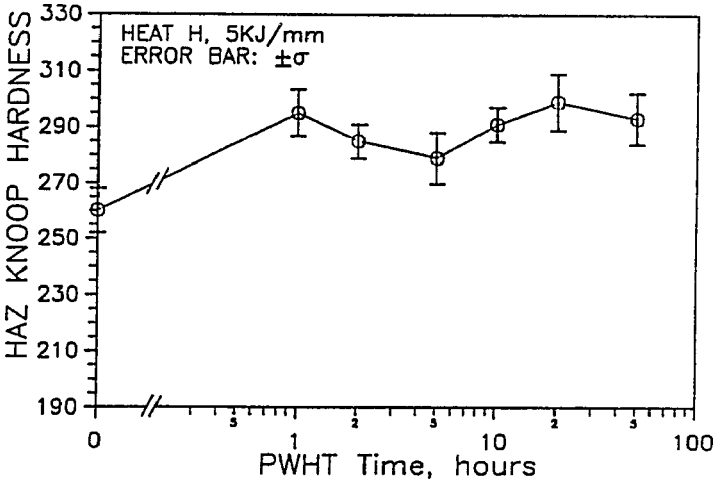

(b)

Figure 4.32 Variation of maximum coarse-grained HAZ hardness of heat H during aging. (A) 3kJ/mm (b) 5kJ/mm

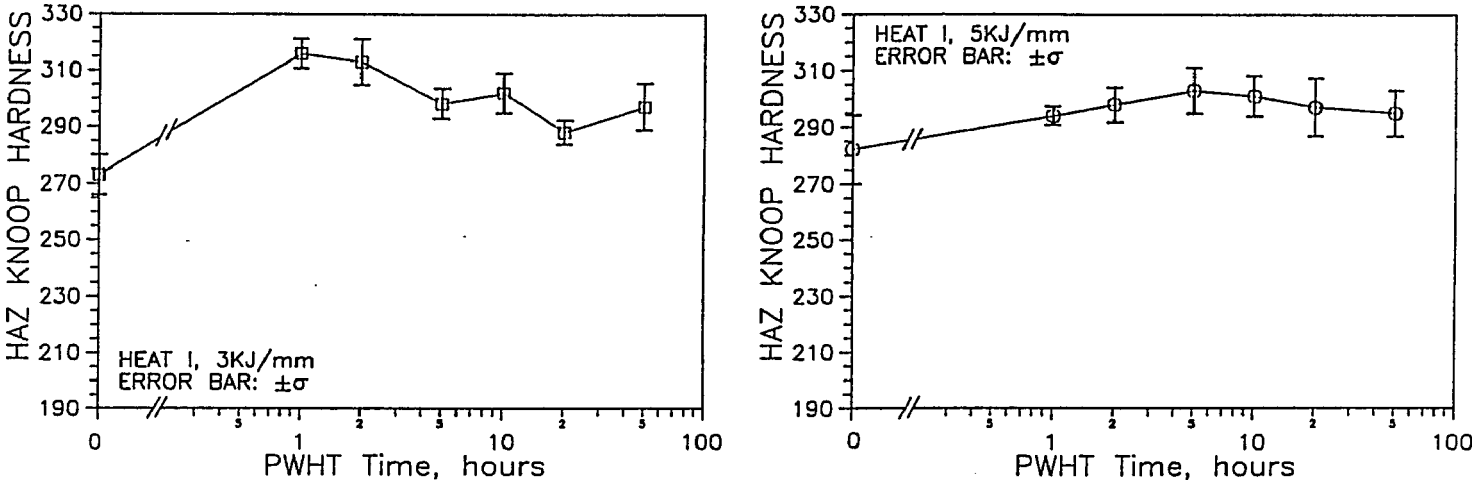

(a) *(b)*

Figure 4.33 Variation of maximum coarse-grained HAZ hardness of heat I during aging. (a) 3kJ/mm (b) 5kJ/mm

longest aging duration, 50 hours.

2, As expected, the hardness peak values for heats with higher V and/or Nb contents are higher than those for heats with lower V and/or Nb contents. This is consistent with the three-dimentional representations, shown in Figures 4.23a,b,c and 4.24a,b,c.

Having the least V and Nb contents, heat A shows no age hardening for 5kJ/mm and little aging hardening for 3kJ/mm specimen. One peak value can be seen in the one-hour position for the 3kJ/mm specimen but softening occurs between one and two hours with little additional change as aging continues.

Knowing the magnitude and variation of HAZ hardness after PWHT is desirable not only for selecting adequate PWHT

conditions but also for selecting suitable chemical compositions of steels. Okumura et al. [9] proposed an approach to predict the HAZ hardness after PWHT in Nb, V and Mo-containing steel. The basic consideration was the decomposition of martensite and the precipitation of Nb, V and Mo. As reported, good agreement between prediction and measurement has been shown for some basic oxygen converter pressure vessel steels.

This approach can briefly be evaluated with the test results in this aging study.

First, the temper parameter TP is employed to express the extent of PWHT, which is as follows

$$TP = T(20 + \log t)/10^3 \qquad (4.3)$$

where T (°K) is the PWHT temperature and t (hour) is the PWHT duration. When PWHT at 620°C, the values of TP will be 17.86 for 1 hour, 18.13 for 2 hours, 18.48 for 10 hours, 19.02 for 20 hours and 19.38 for 50 hours.

A Carbon Equivalent, CEII, as described below, is also required for this analysis:

$$CEII = C + Si/2.5 + Mn/5 + Cu/10 + Ni/18 + Cr/5 + Mo/2.5 + V/5 + Nb/2 \qquad (4.4)$$

Considering heat C as an example, we have CEII = 0.432.

The change in HAZ hardness after PWHT from that of as-welded, ΔHV, as suggested by Okumura [9], is given as:

$$\Delta HV = \{ 884C + 177 - 197CEII + 16.5(TP - 21.5)\} M + \{ 18(TP - 18)^2 - 138 \} V^{1/2} + \{ 20(TP - 18)^2 - 268 \} Nb^{1/2} + \{ 25(TP - 17.3)^2 - 55 \} Mo^{1/2} - 7CEII + 26 \qquad (4.5)$$

where C, Nb, V and Mo are the weight percent of the elements of C, Nb, V and Mo, and M is the volume fraction of martensitic structure in the HAZ; ΔHV is the change in Vickers hardness, a positive ΔHV indicates a decrease in hardness and a negative ΔHV value means an increase in HAZ hardness after PWHT.

Because the volume fraction of martensite in the HAZ is difficult to measure, literature values from a 0.17C-1.1Mn steel of 0.04 and 0.01 for M have been used as a resonable estimate for the 3kJ/mm and 5kJ/mm, respectively [43]. By substituting all the parameters and element contents into equation 4.5, the HAZ hardness under various conditions can be calculated. The results of calculation are converted from Vickers hardness ΔHV to Knoop hardness ΔHK and presented in Table 4.4. The sign of all numbers has been changed from negative to positive and should be recognized as the increase of hardness after PWHT, not reduction.

The calculated hardness increase ΔHK and measured data of HAZ hardness for 3kJ/mm specimens and 5kJ/mm specimens are plotted on the same axis for comparison, as shown in Figure 4.34 and Figure 4.35, respectively. A similar calculation and comparison has been made for heats A, C, G and I. The comparisons clearly indicate that the Okumura prediction overestimated the hardness increment. Only the decomposition of martensite was taken into account in the HAZ hardness prediction. In a PWHT process, the relief of stress, the

Table 4.4 The calculated HAZ hardness increase after PWHT, in accordance with equations 4.3, 4.4 and 4.5. Heat C. Knoop scale.

Heat input	(M)	PWHT time at 620°C					
		1hr	2hrs	5hrs	10hrs	20hrs	50hrs
3kJ/mm	0.04	34.8	34.6	32.8	30.1	26.2	19.4
5kJ/mm	0.01	40.4	40.3	38.7	36.1	32.4	25.8

recovery of ferrite, the decrease in dislocation density, the coarsening and spherodization of cementite and the microstructural changes in other constituents such as pearlite and bainite may also take place, contributing to softening the material. An accurate prediction of HAZ hardness after PWHT should be based on an appropriate evaluation of the contributions of all the softening and hardening aspects and their interplay.

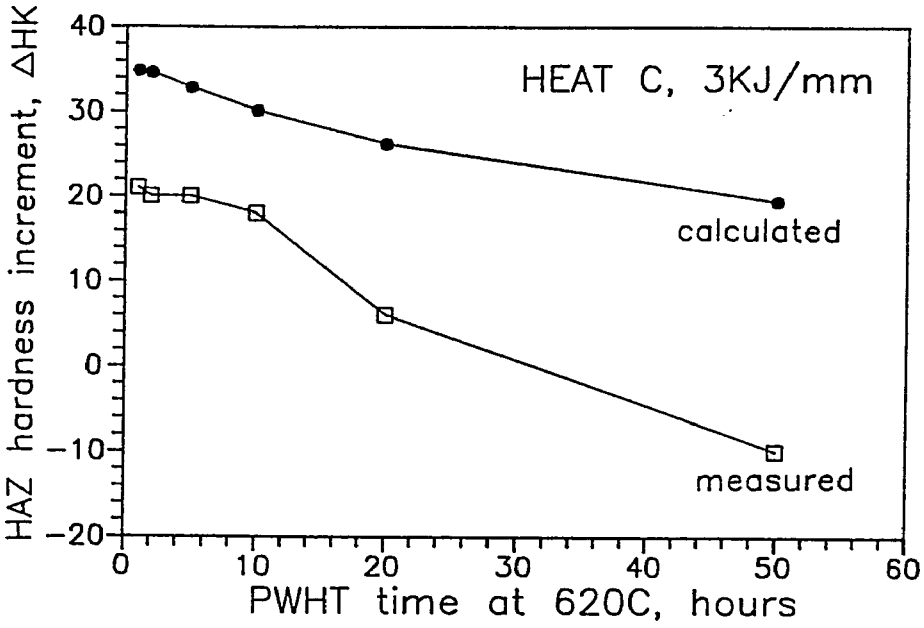

Figure 4.34 HAZ hardness increase during aging, showing measured and calculated data. Heat C, welded with 3kJ/mm

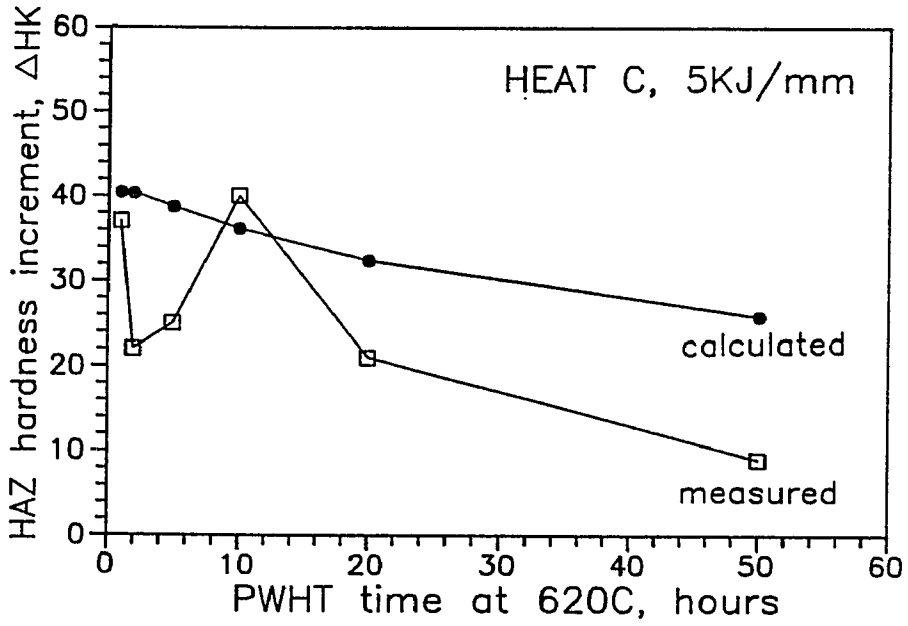

Figure 4.35 HAZ hardness increase during aging, showing measured and calculated data. Heat C, welded with 5kJ/mm

4.4. CVN IMPACT TESTING

4.4.1. CVN IMPACT ENERGY VERSUS TEST TEMPERATURE AND 50 JOULE TRANSITION TEMPERATURE

Figure 4.36a through Figure 4.36e show the plots of CVN impact energy versus test temperature in base plates . Figure 4.37 through Figure 4.46 show the plots of CVN impact energy versus test temperature in HAZs, including 3kJ/mm and 5kJ/mm welding heat inputs, as-welded and PWHT at 620°C for 2 hours and 10 hours. 50 Joule (37 ft-lbs) impact energy was employed as the criterion to determine the ductile-brittle transition temperature (TT50J). Table 4.5 summarizes the transition temperatures obtained from CVN testing of HAZs*. As with the HAZ microhardness of various heats, three-dimensional representation was utilized for TT50J. These 3-d plots effectively show the functional relationship between CVN toughness and microalloy content. Figures 4.47a, 4.47b and 4.47c represent the results of 3kJ/mm specimens with as-welded, PWHT at 620°C for 2 hours and PWHT at 620°C for 10 hours. Figures 4.48a, 4.48b and 4.48c are the corresponding plots for 5kJ/mm specimens.

By taking a general view of all these 3-d plots of TT50J vs V and Nb contents, the following understanding can be given:

---

* Data of heats A,C,G,I were taken from the results of previous research conducted by H.Smith, G.Ginsburg from Lafayette College, under the supervision of Drs. B.Somers, M.Uz and A.Pense.

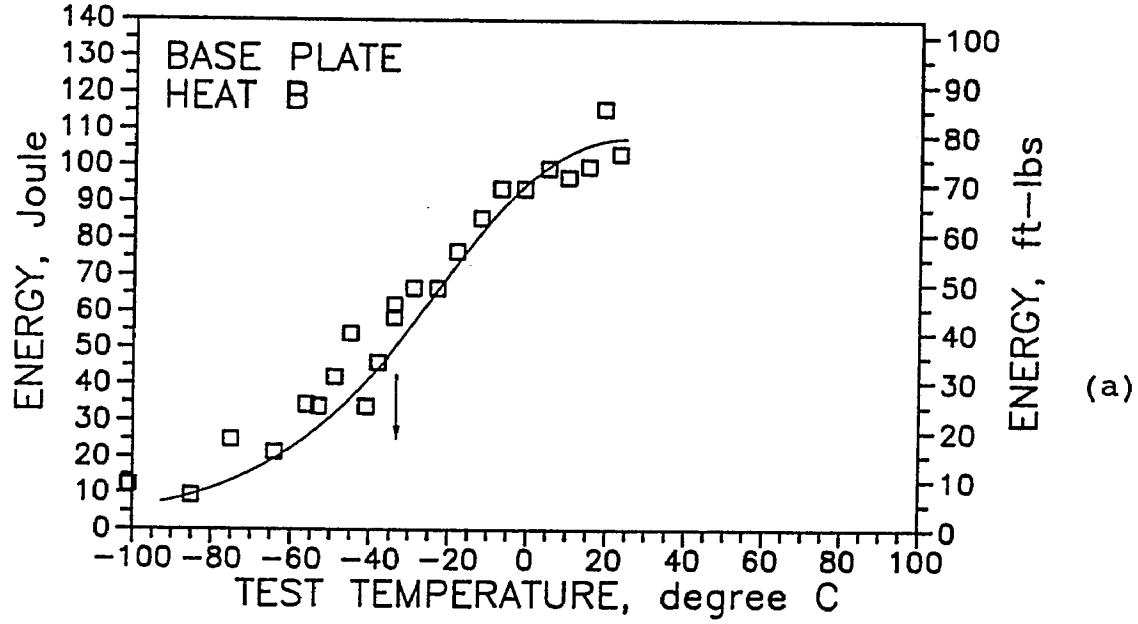

(a)

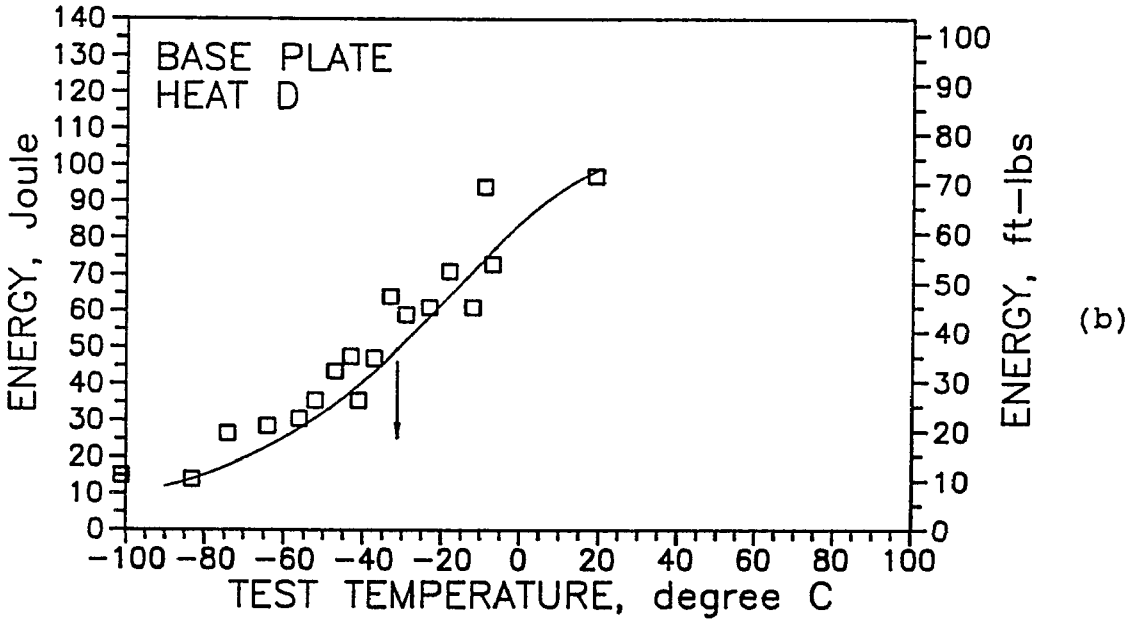

(b)

Figure 4.36 Charpy transition curves of normalized base plates.
(a) heat B (b) heat D (c) heat E (d) heat F (e) heat H

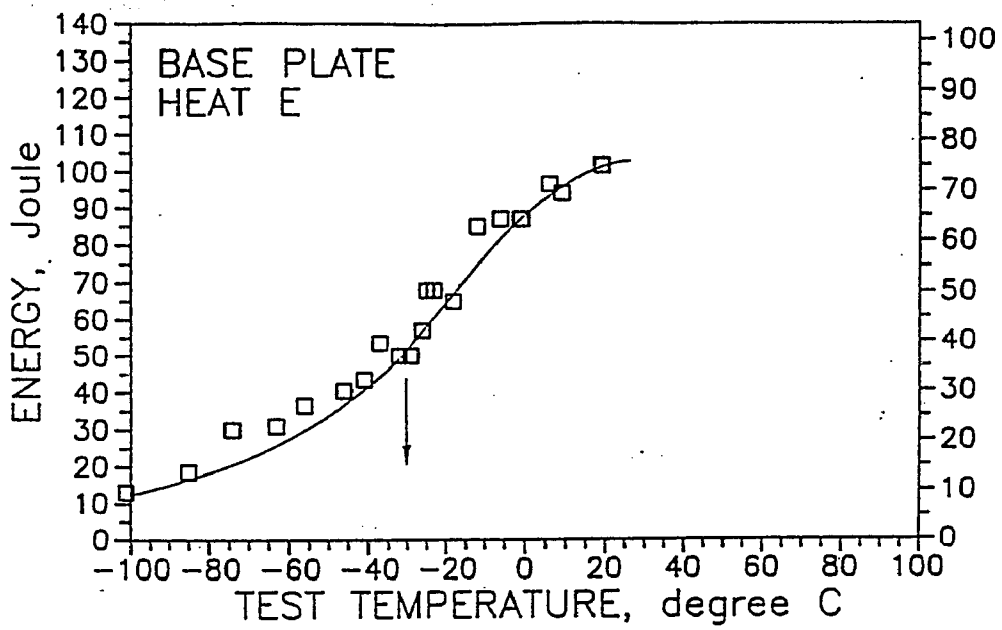

(c)

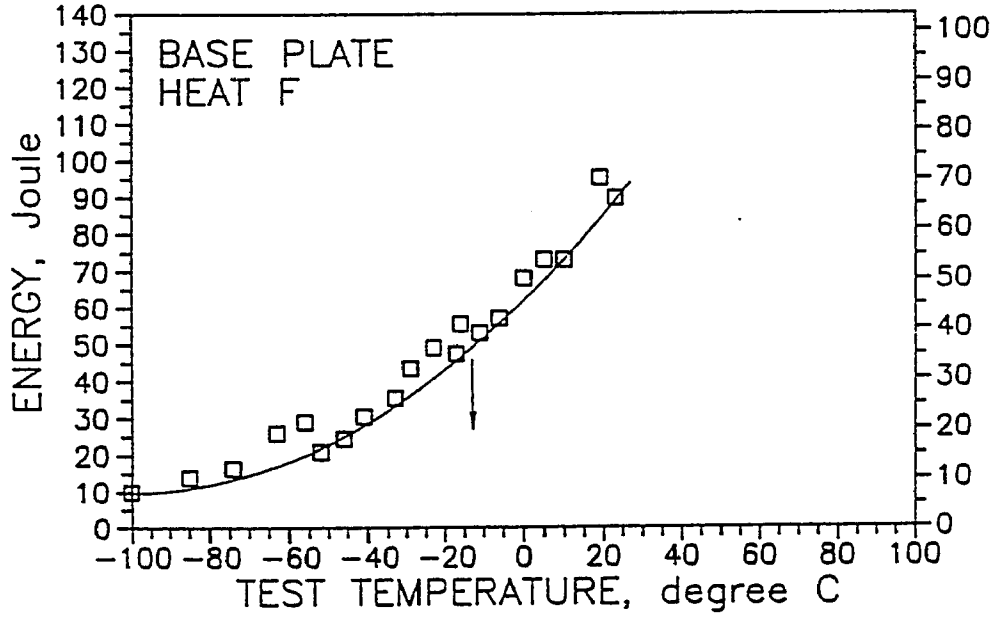

(d)

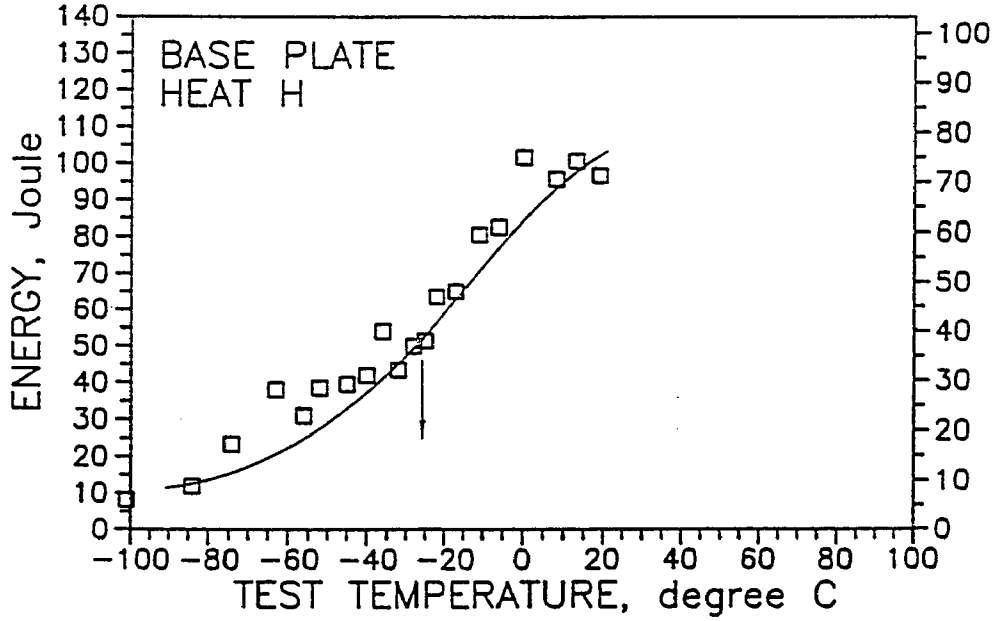

(e)

Figure 4.36 Continued

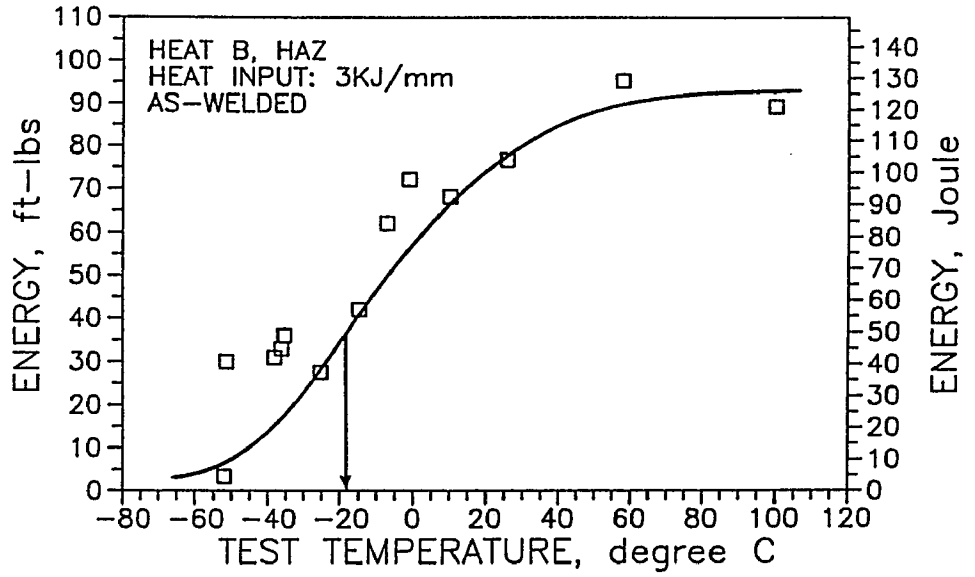

(a)

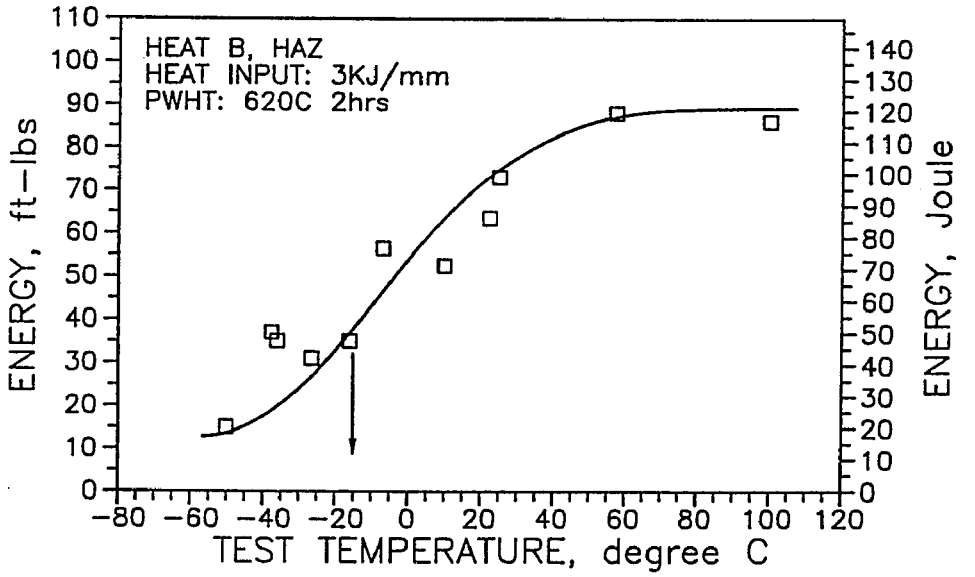

(b)

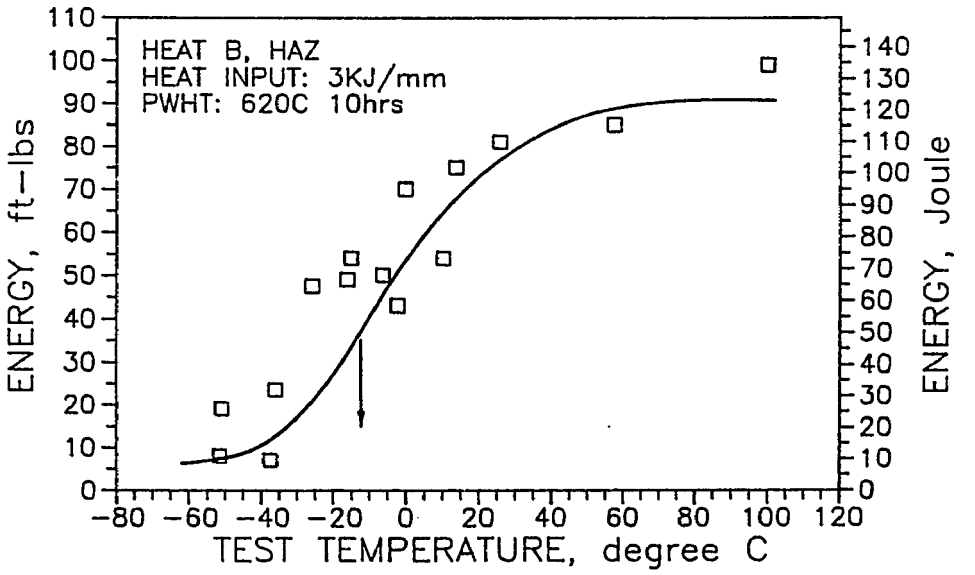

(c)

Figure 4.37 Charpy transition curves of HAZs of heat B, 3KJ/mm. (a) as-welded (b) PWHT 620°C/2hrs. (c) PWHT 620°C/10hrs.

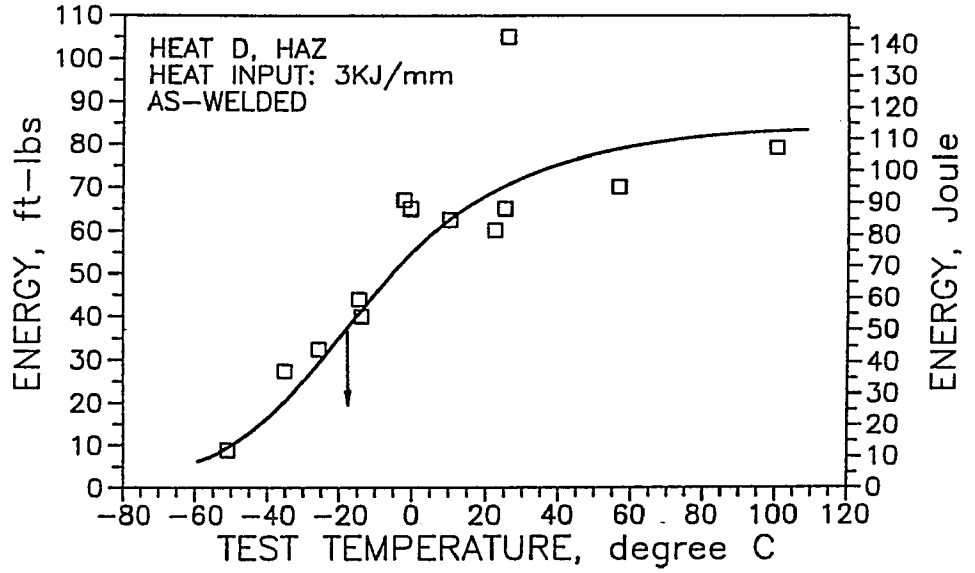

(a)

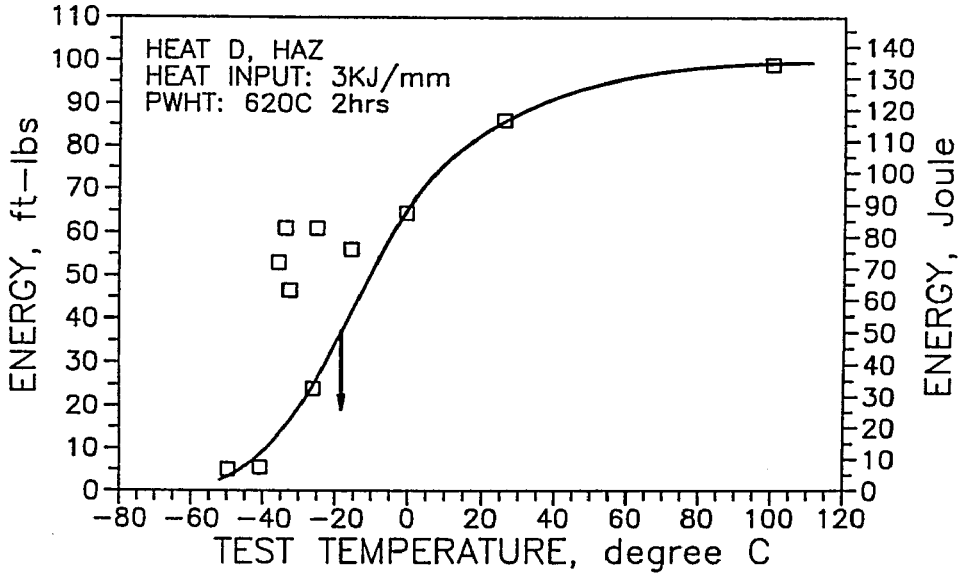

(b)

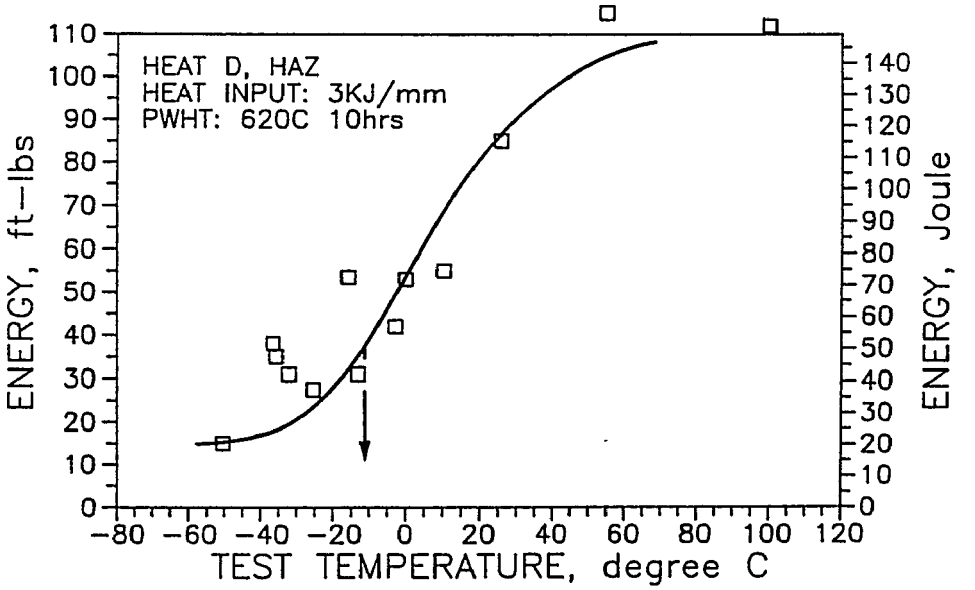

(c)

Figure 4.38 Charpy transition curves of HAZs of heat D, 3KJ/mm. (a) as-welded (b) PWHT 620°C/2hrs. (c) PWHT 620°C/10hrs.

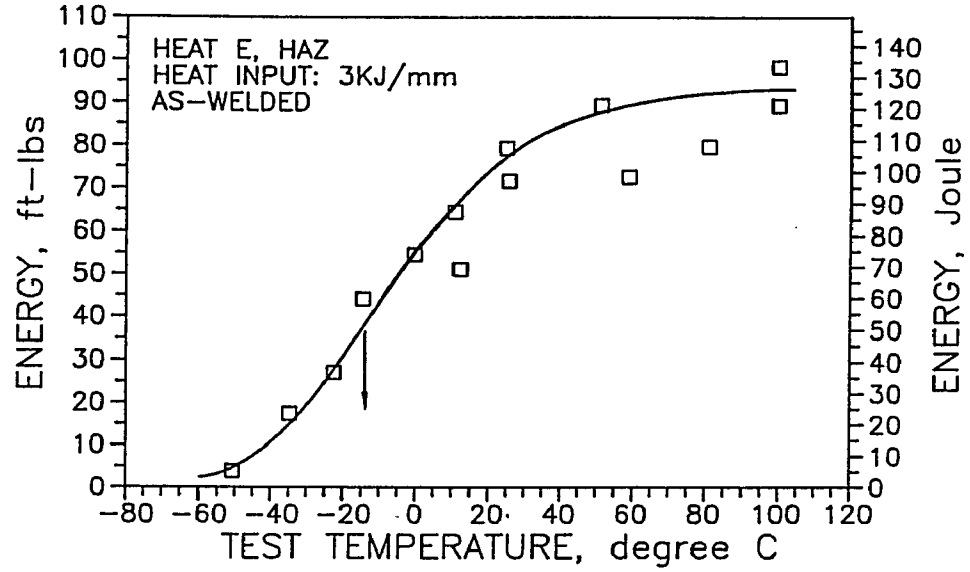

(a)

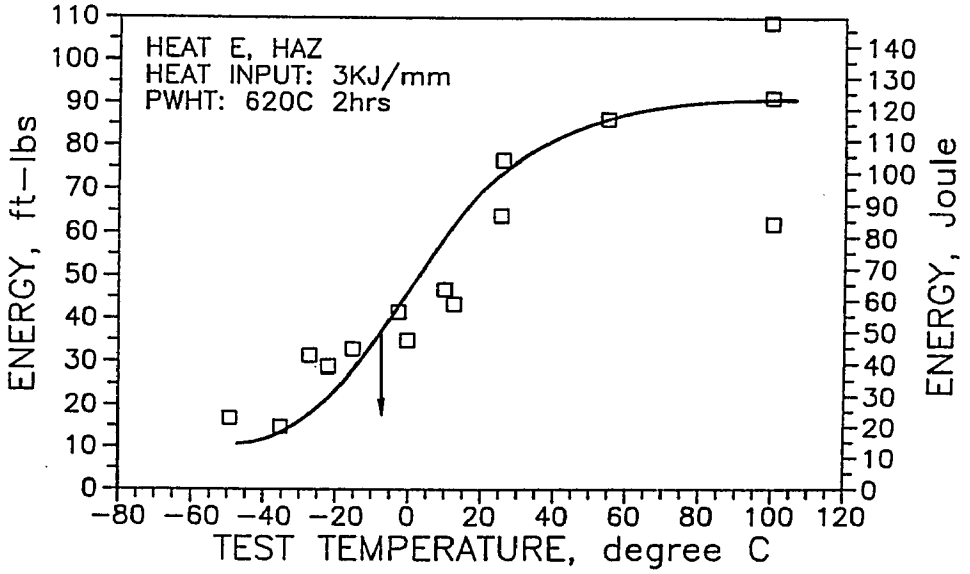

(b)

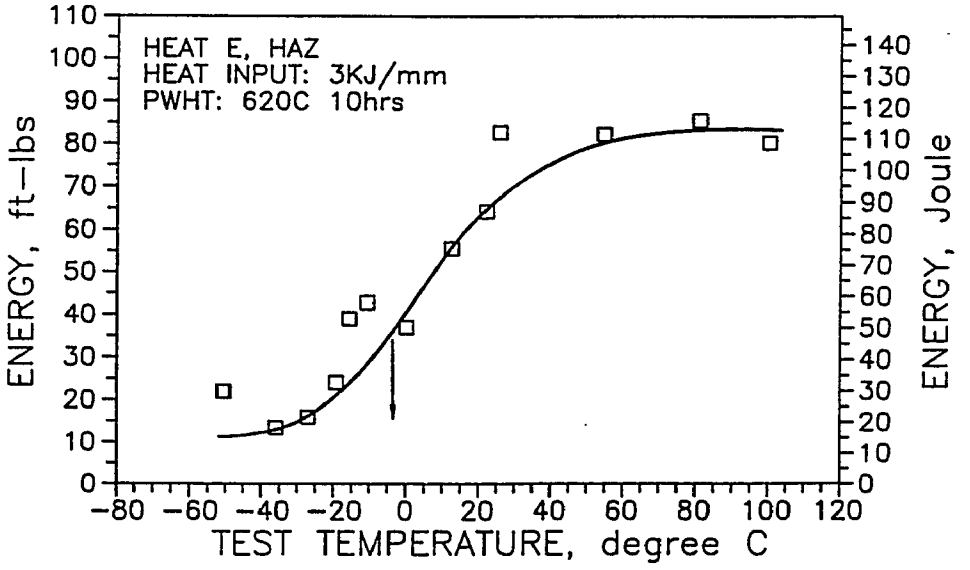

(c)

Figure 4.39 Charpy transition curves of HAZs of heat E, 3KJ/mm. (a) as-welded (b) PWHT 620°C/2hrs. (c) PWHT 620°C/10hrs.

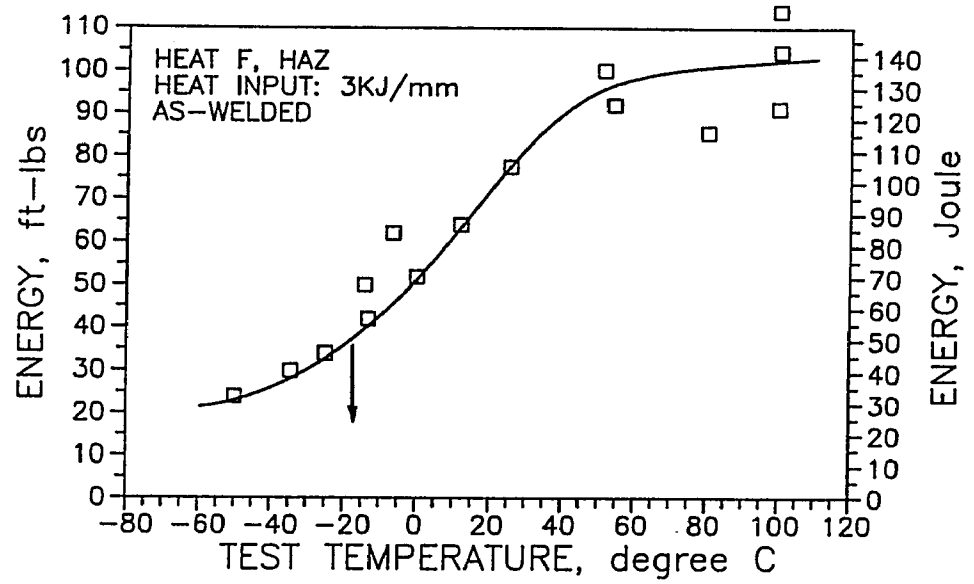

(a)

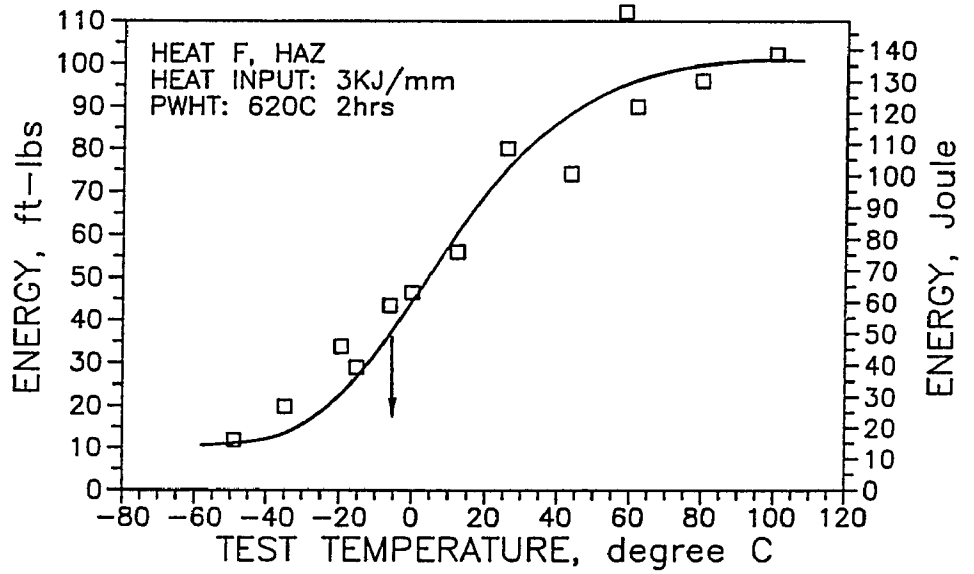

(b)

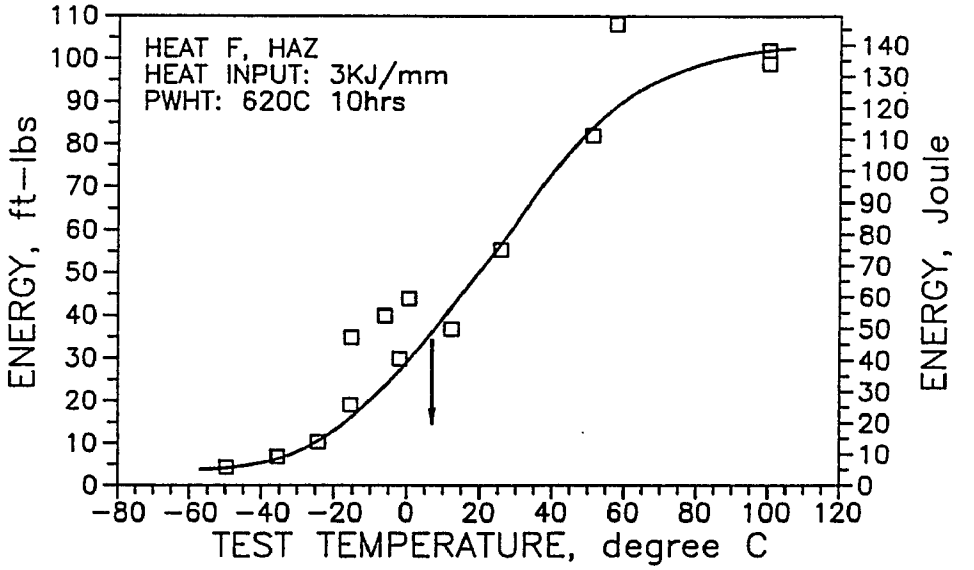

(c)

Figure 4.40 Charpy transition curves of HAZs of heat F, 3KJ/mm. (a) as-welded (b) PWHT 620°C/2hrs. (c) PWHT 620°C/10hrs.

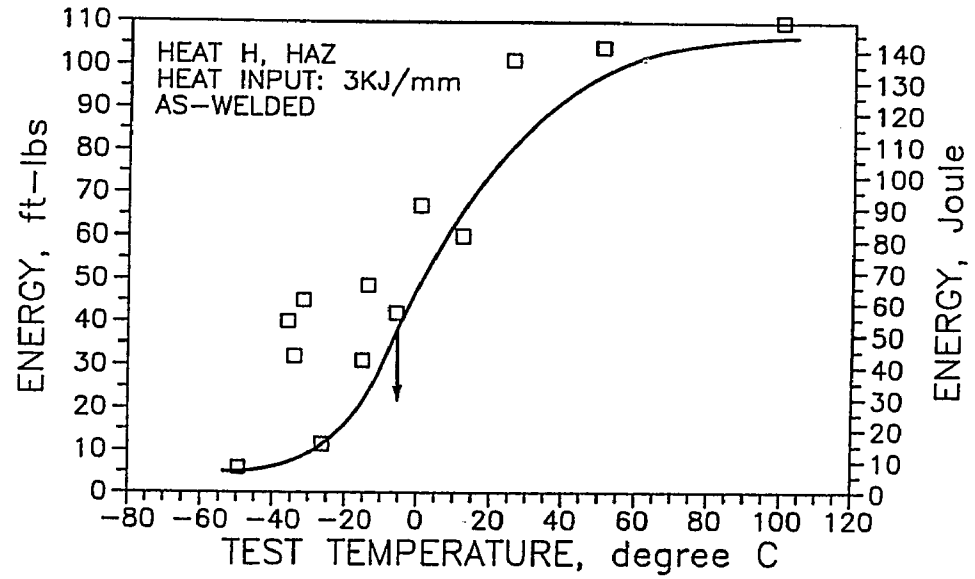

(a)

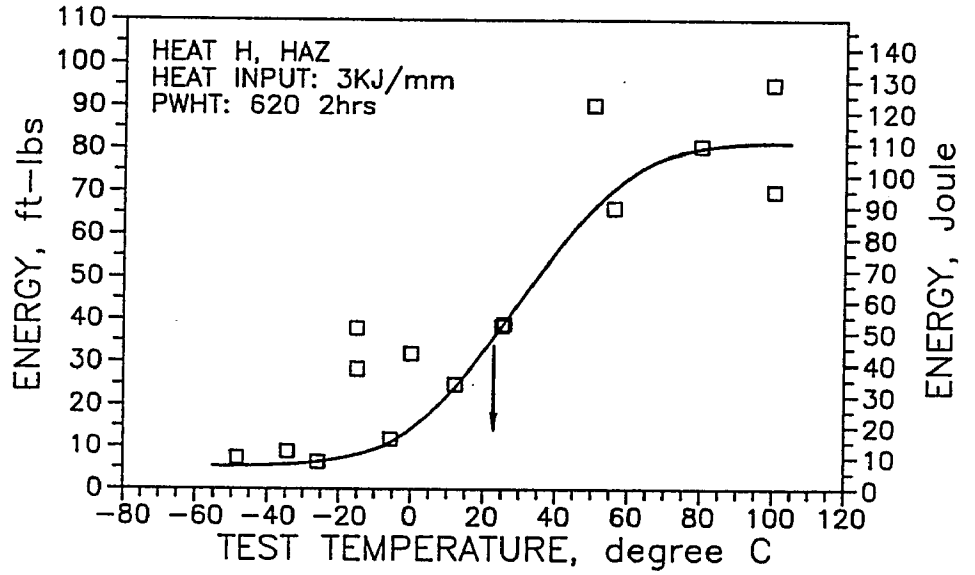

(b)

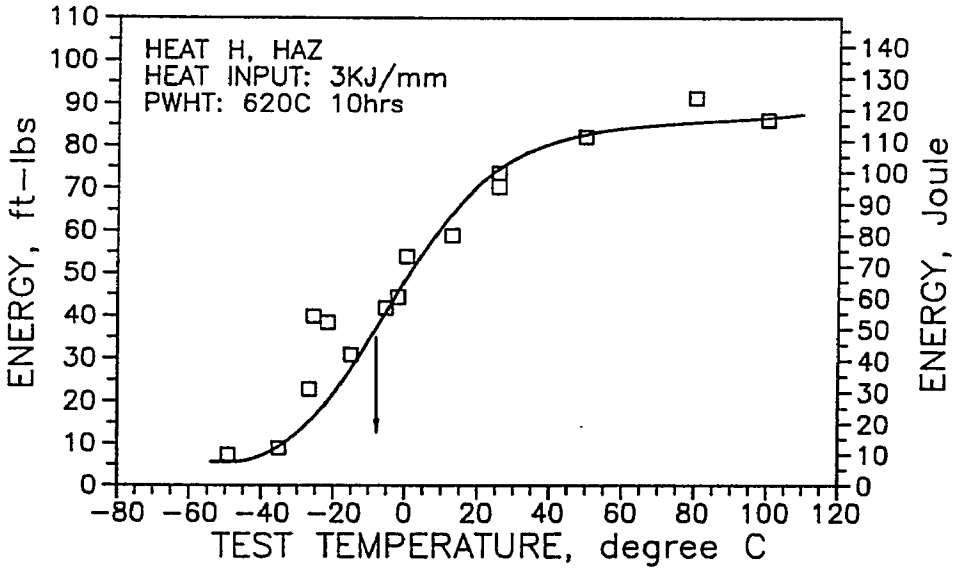

(c)

Figure 4.41 Charpy transition curves of HAZs of heat H, 3KJ/mm. (a) as-welded (b) PWHT 620°C/2hrs. (c) PWHT 620°C/10hrs.

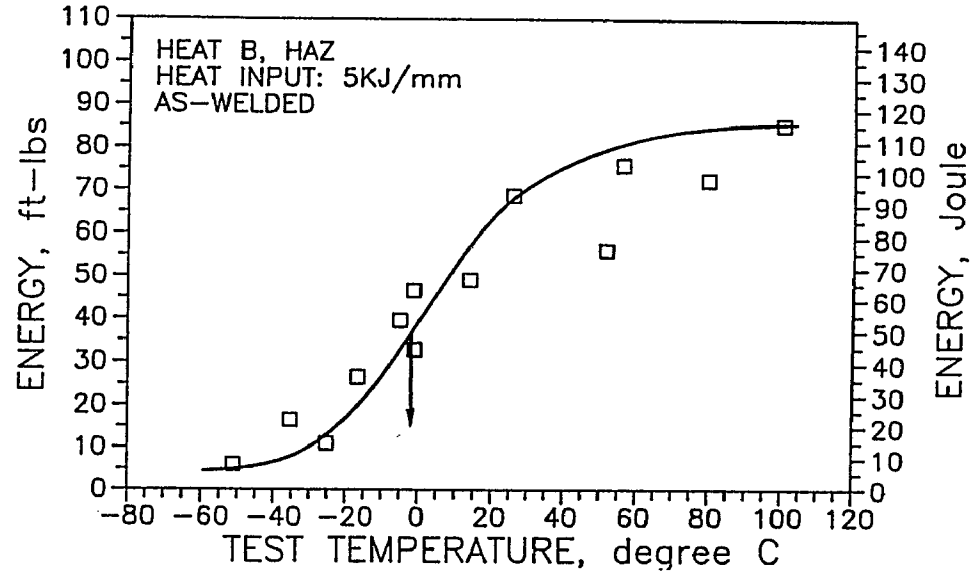

(a)

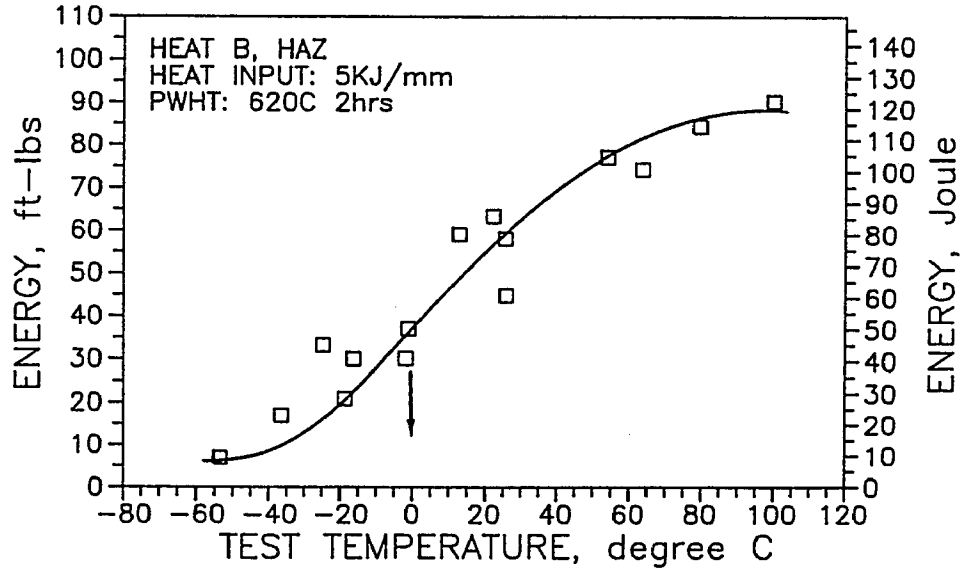

(b)

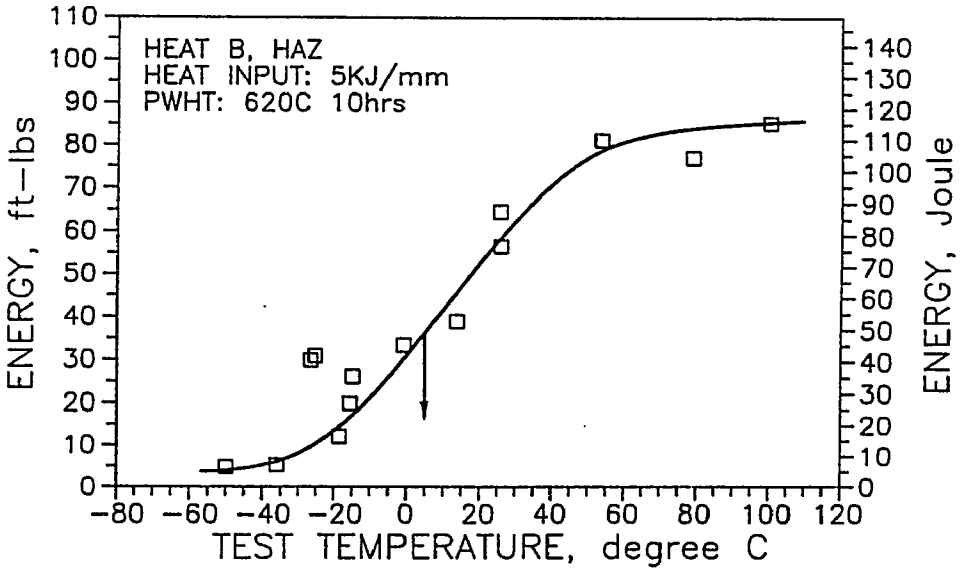

(c)

Figure 4.42 Charpy transition curves of HAZs of heat B, 5KJ/mm. (a) as-welded (b) PWHT 620°C/2hrs. (c) PWHT 620°C/10hrs.

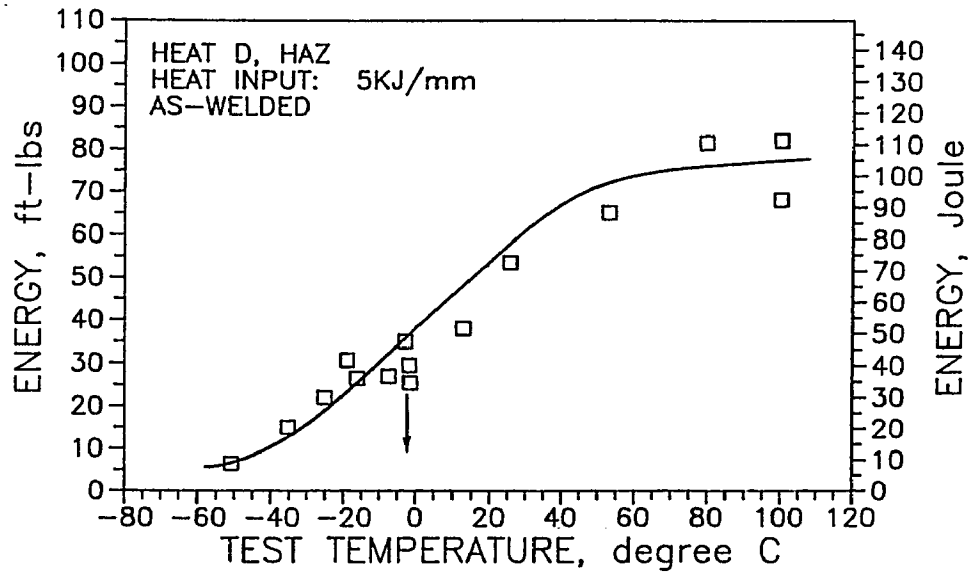

(a)

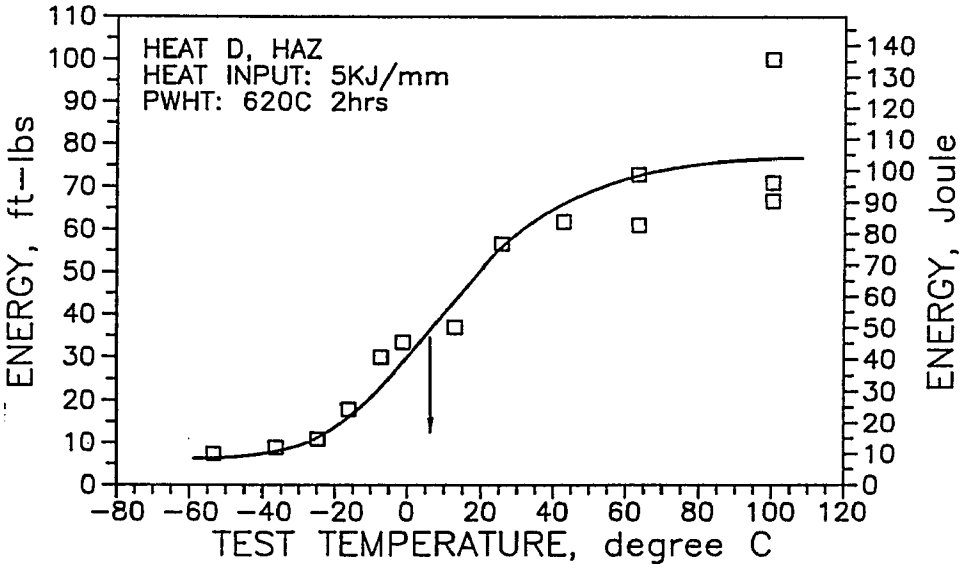

(b)

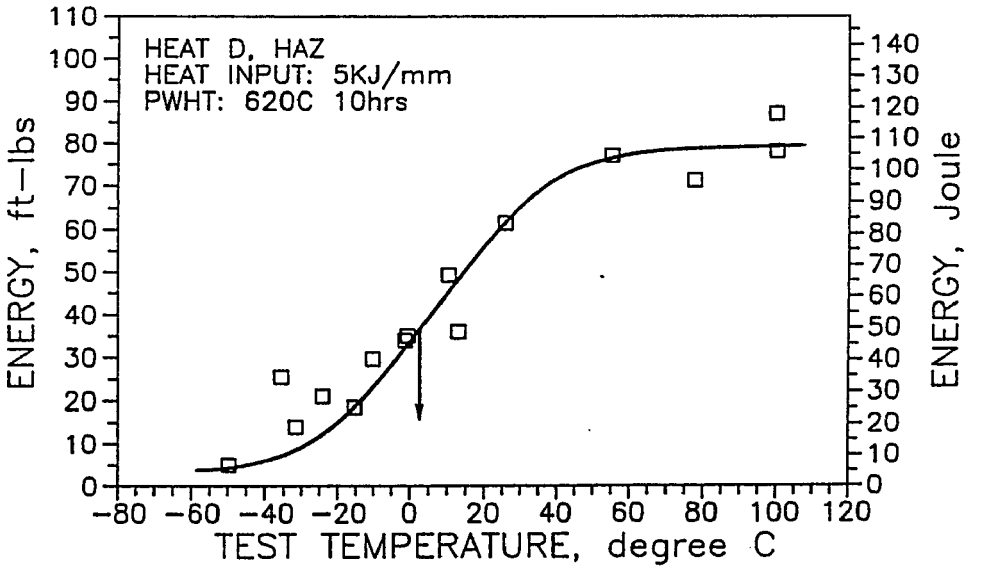

(c)

Figure 4.43 Charpy transition curves of HAZs of heat D, 5KJ/mm. (a) as-welded (b) PWHT 620°C/mm (c) PWHT 620°C/10hrs.

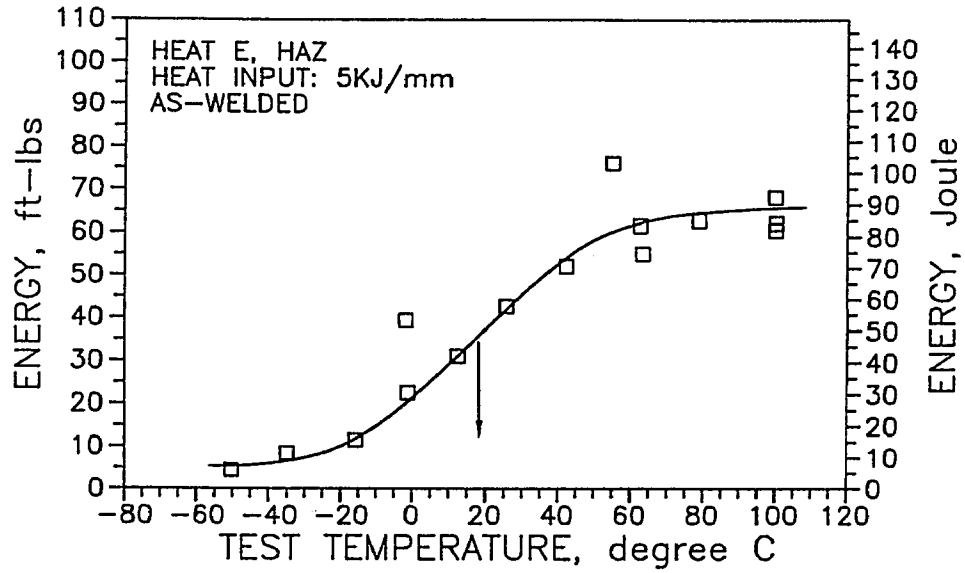

(a)

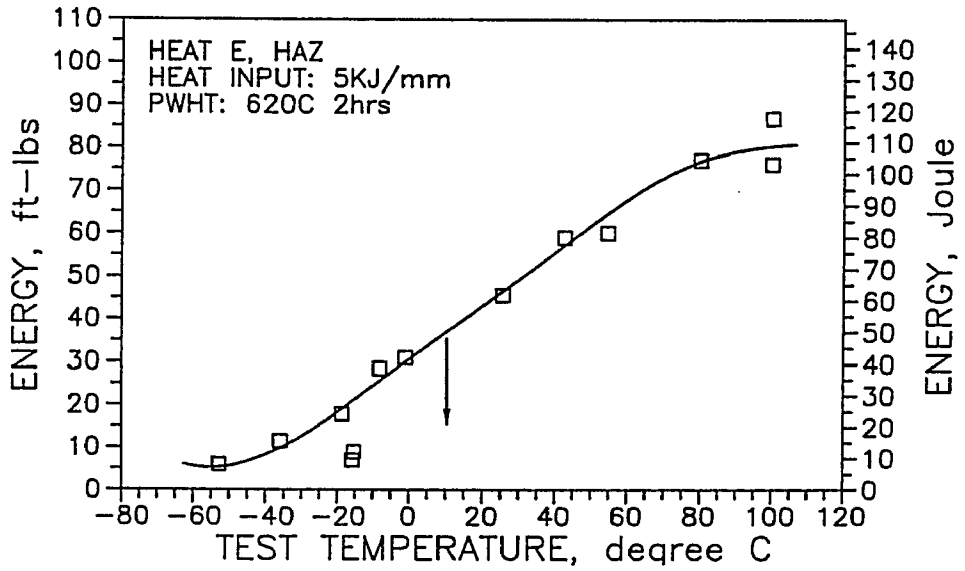

(b)

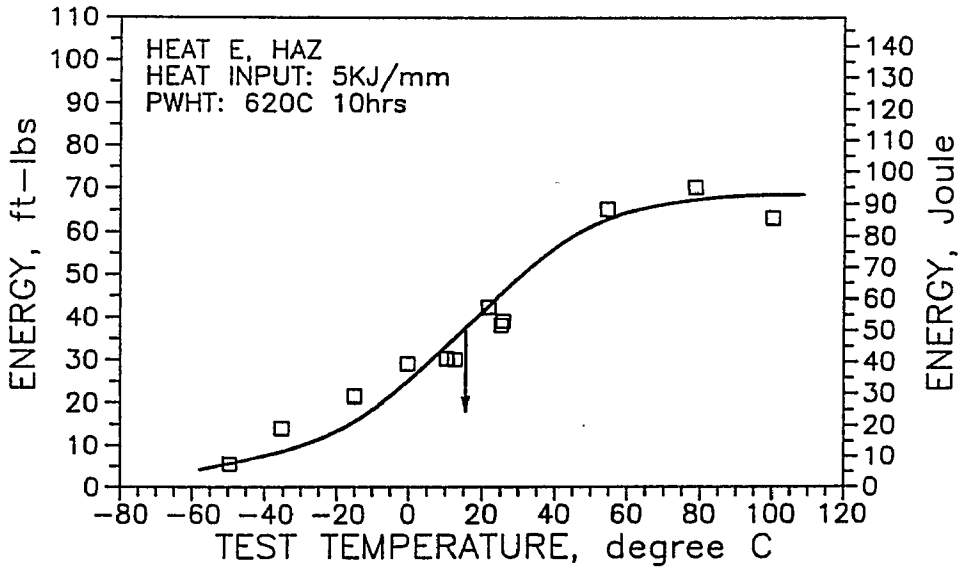

(c)

Figure 4.44 Charpy transition curves of HAZs of heat E, 5KJ/mm. (a) as-welded (b) PWHT 620°C/2hrs. (c) PWHT 620°C/10hrs.

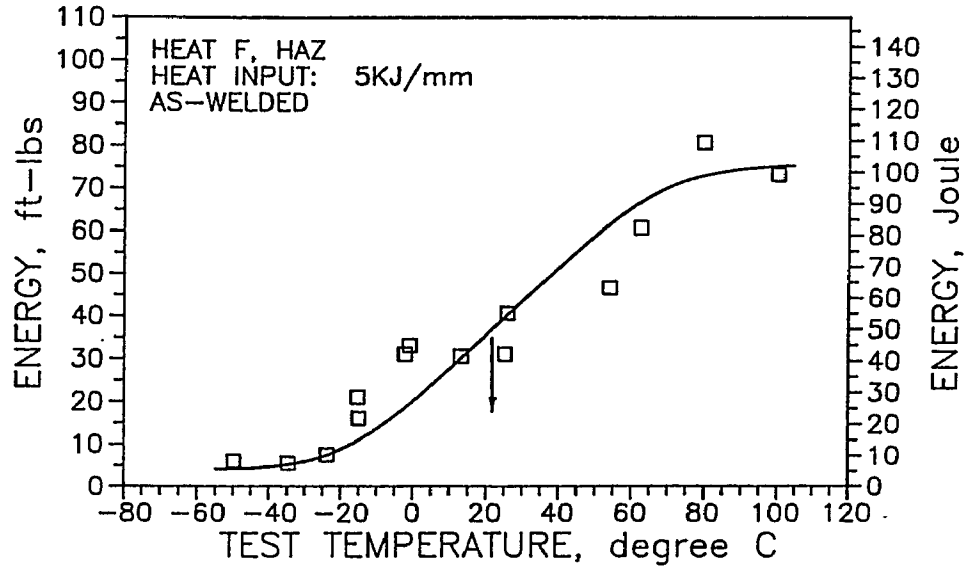

(a)

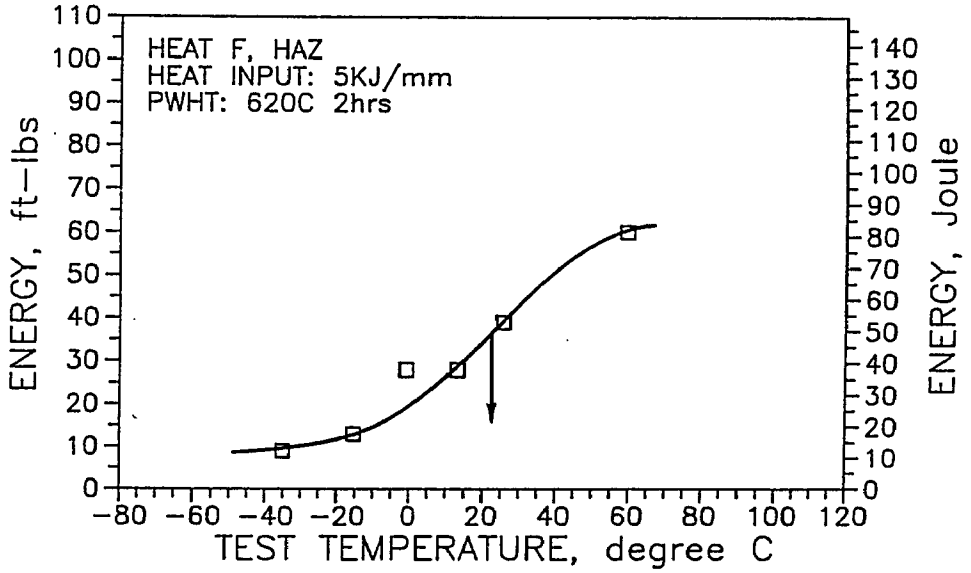

(b)

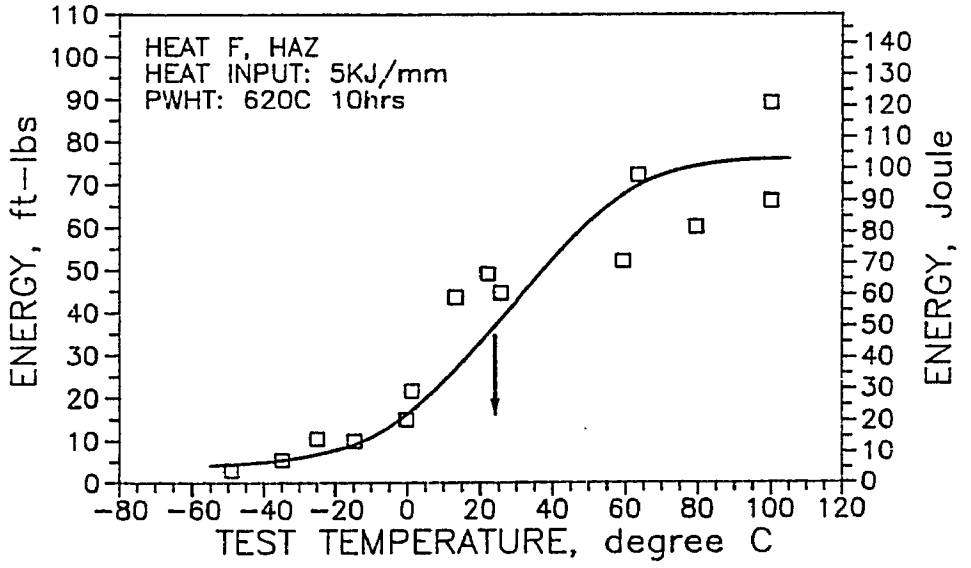

(c)

Figure 4.45 Charpy transition curves of HAZs of heat F, 5KJ/mm. (a) as-welded (b) PWHT 620°C/2hrs. (3) PWHT 620°C/10hrs.

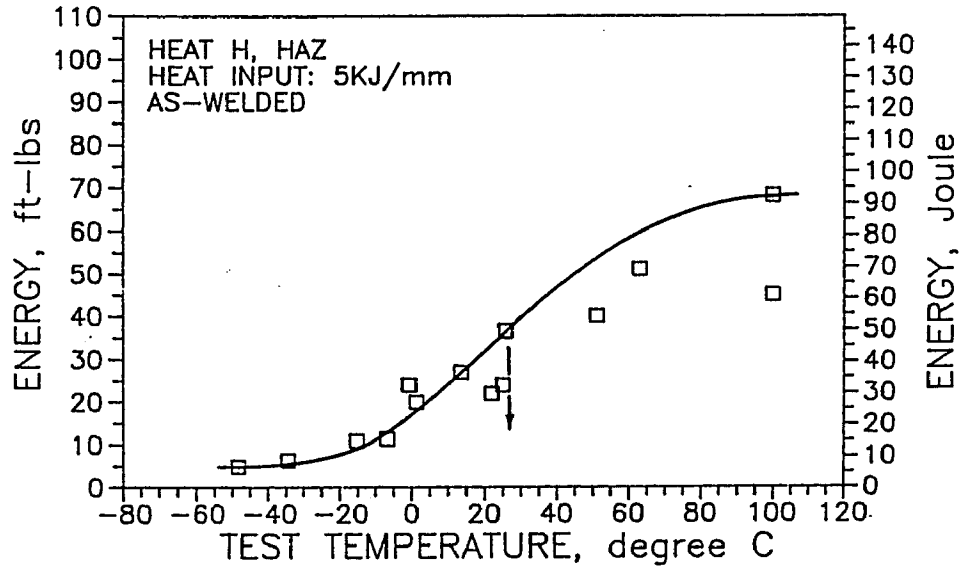

(a)

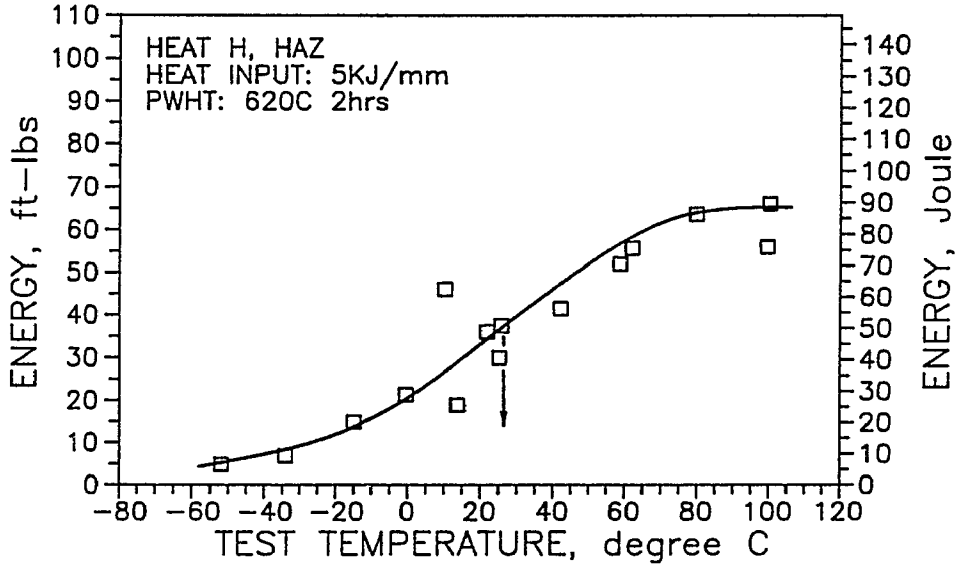

(b)

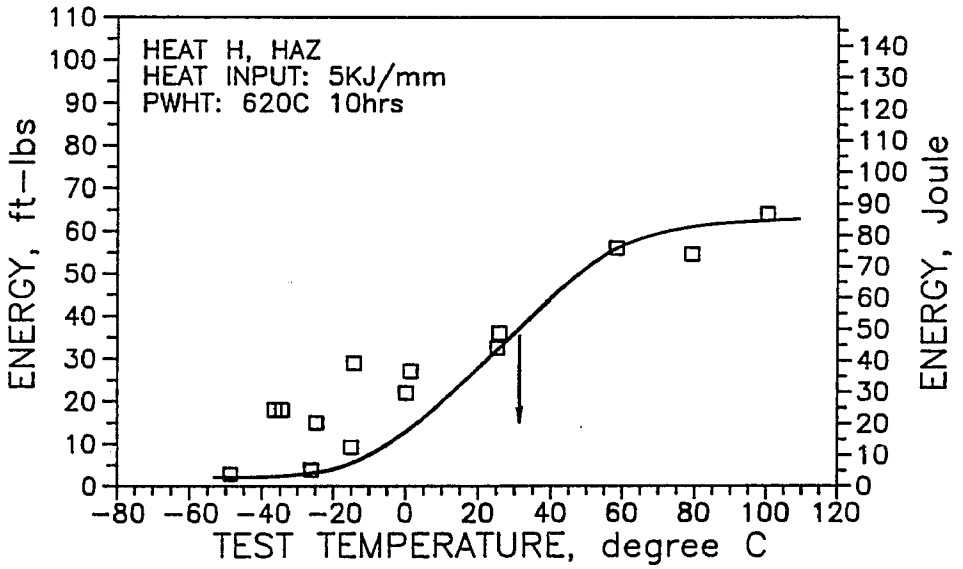

(c)

Figure 4.46 Charpy transition curves of HAZs of heat H, 5KJ/mm. (a) as-welded (b) PWHT 620°C/2hrs. (c) PWHT 620°C/10hrs.

Table 4.5 50 Joule transition temperature of HAZ

Specimens	heat A	heat B	heat C	heat D	heat E	heat F	heat G	heat H	heat I
3KJ/mm as-welded	-9	-18	-20	-17	-14	-17	0	-5	0
3KJ/mm PWHT 620°C/2 hrs	-29	-15	0	-19	-7	-5	-18	22	32
3KJ/mm PWHT 620°C/10 hrs	-19	-12	-4	-12	-3	7	-21	-8	41
5KJ/mm as-welded	-13	-2	-1	-3	18	21	-9	26	10
5KJ/mm PWHT 620°C/2 hrs	-11	0	12	6	19	22	15	27	39
5KJ/mm PWHT 620°C/10 hrs	-13	5	15	2	15	24	6	31	34

1, Unlike the 3-d plots of microhardness, some 3-d plots are rather undulatory, particularly for the plots of as-welded specimens, see Figure 4.47a and Figure 4.48a. This may be imputed to the experimental scatter bands. Tracing back to the curves of CVN impact energy versus test temperature in HAZ specimens, as shown in Figures 4.37 through 4.46, substantial data scatter in some curves can be observed. This reveals the heterogeneous nature in the microstructure of a multipass HAZ. Efforts have been made to gain as flat as possible fusion boundary and to notch the Charpy specimen with the V-notch root in the HAZ adjacent to fusion boundary in order to test the coarse-grained HAZ. However, as pointed out before, the microstructure along the fusion boundary in multipass weld is not constant, and the ligament of a CVN specimen will cover various microstructural constituents which behave differently. The crack frontier will travel across several of these

constituents upon which the overall impact energy depends. Moreover, any slight imperfection in the preparation of the multipass CVN specimen such as a curved fusion boundary or a deviation of the crack plane from the plane parallel to fusion boundary will cause the data variability.

2, Although some data scatter exists, it is clear that the V and/or Nb additions degrade CVN impact toughness in both base plates and HAZs with various conditions.

The detrimental effects of microalloy V and Nb additions on TT50J are particularly visible in post-welded heat treated specimens. The differences in TT50J between heat A which has the lowest microally content and heat I which has the highest microalloy content are summarized in Table 4.6.

Table 4.6 The increase of TT50J from heat A to heat I (°C)

3kJ/mm			5kJ/mm		
As-welded	620°C/2h	620°C/10h	As-welded	620°C/2h	620°C/10h
20	61	60	39	50	51

3kJ/mm specimens with PWHT of 620°C/2hrs of displays the most degradation where the TT50J increases as much as 61°C due to V and Nb additions.

3, Referring to Table 4.5, for each experimental heat, the 50 Joule transition temperature can generally be ranked in the following order: base plate -- as-welded HAZ of 3kJ/mm -- HAZ of 3kJ/mm with PWHT -- as-welded HAZ of 5kJ/mm -- HAZ of

5kJ/mm with PWHT. The base plate has the lowest TT50J while 5kJ/mm with PWHT specimens have the highest TT50J. Three issues are hereby proved: First, CVN impact toughness values of coarse-grained HAZs of both 3kJ/mm and 5kJ/mm are lower than that of base plate. Secondly, in these coarse-grained HAZs, PWHT is detrimental to CVN impact toughness. Thirdly, 5kJ/mm specimens show higher TT50J than 3kJ/mm specimens do; these considerable TT50J shifts are caused by the higher welding heat input.

4, The six 3-d plots of TT50J in the HAZ shown in Figures 4.47 and 4.248 and the corresponding six 3-d plots of maximum HAZ hardness shown in Figures 4.23 and 4.24 can be paired one-to-one. Comparison of these six pairs of TT50J versus maximum HAZ hardness indicates the same trends in the variations of TT50J and maximum HAZ hardness while varying V and/or Nb contents, although there are some nonconformities in as-welded condition. It can be seen that there are direct correlations between the maximum HAZ hardness determined by the local microstructural constituents and the 50 Joule transition temperature for these steels.

4.4.2. THE FRACTURE APPEARANCE EXAMINATION ON CVN SPECIMENS TESTED AT DIFFERENT TEMPERATURES

Fracture surfaces in the broken CVN specimens produced at different test temperatures are commonly characterized by different percentage of crystalline or fibrous fracture.

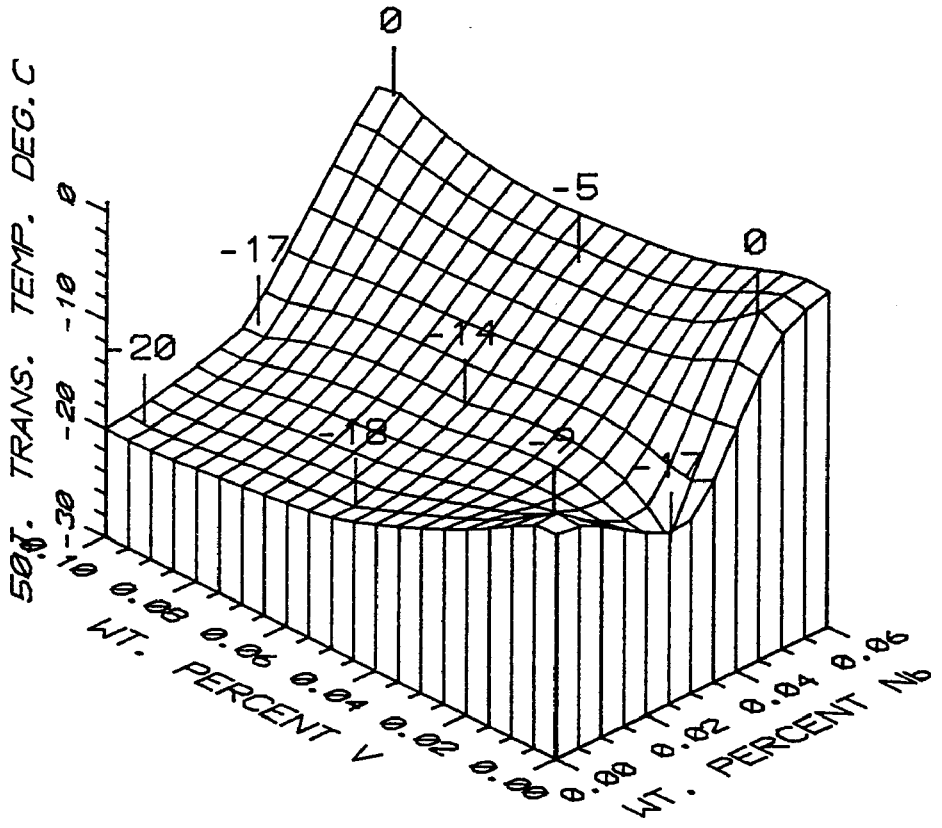

(a) as-welded

Figure 4.47 Three dimensional representation of 50 Joule transition temperature data from HAZ, welded with 3KJ/mm

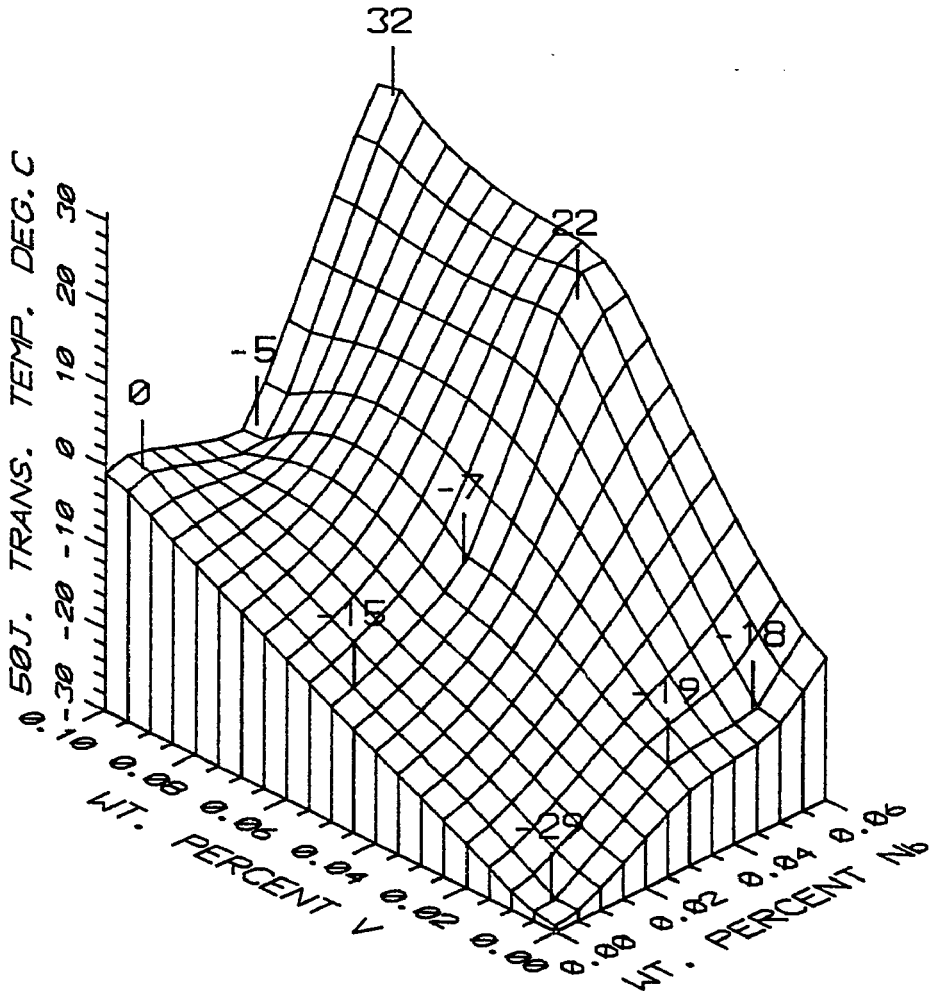

(b) PWHT at 620°C for 2 hours

Figure 4.47 Continued

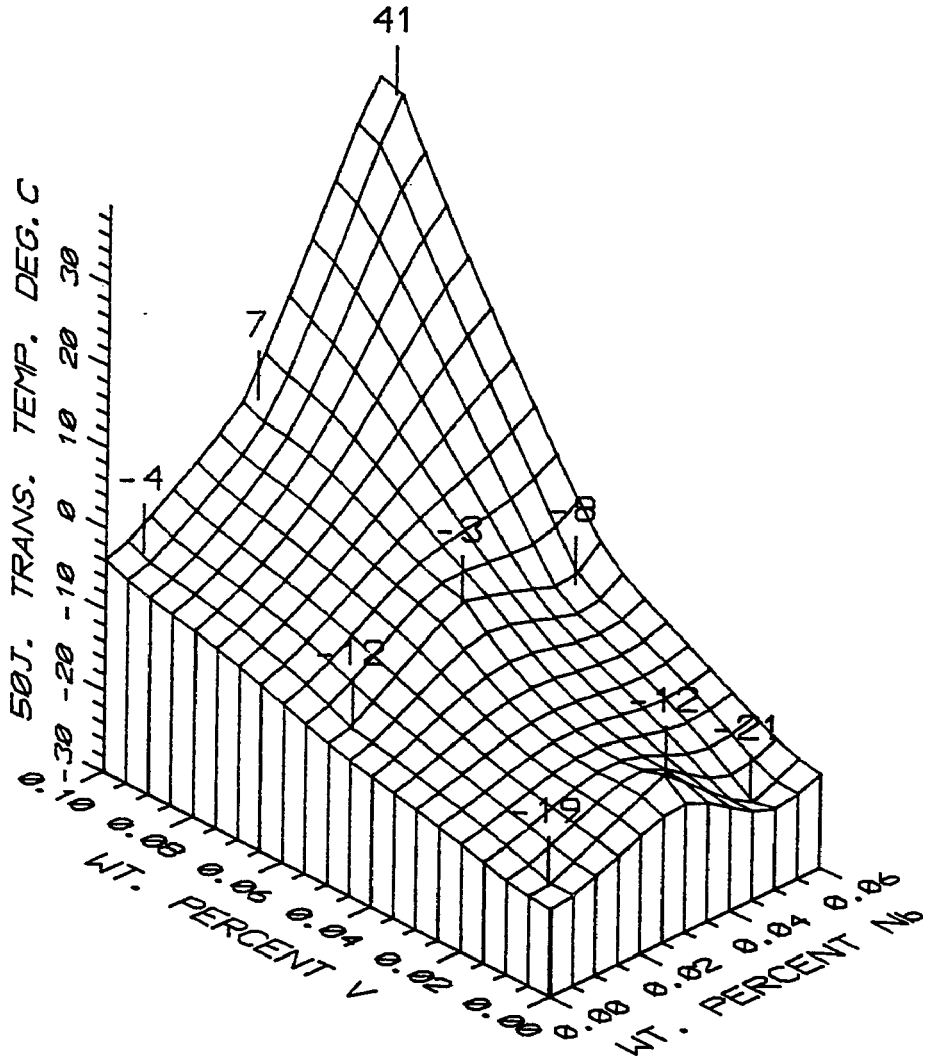

(c) PWHT at 620°C for 10 hours

Figure 4.47 Continued

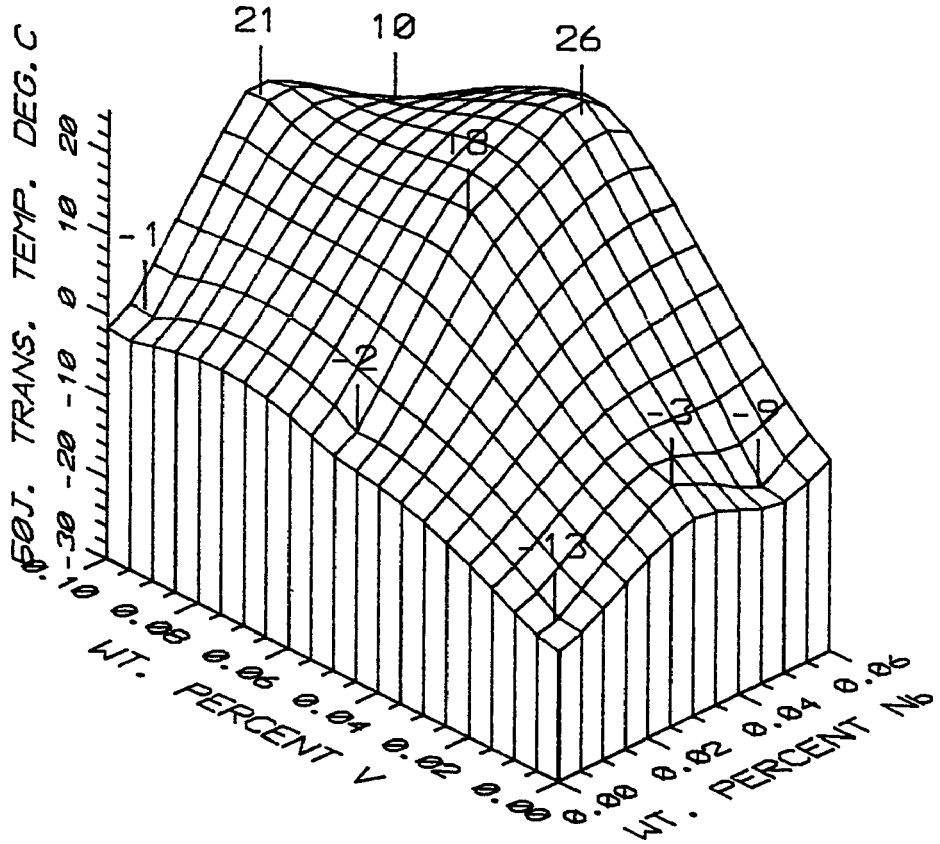

(a) as-welded

Figure 4.48 Three dimensional representation of 50 Joule transition temperature data from HAZ, welded with 5KJ/mm

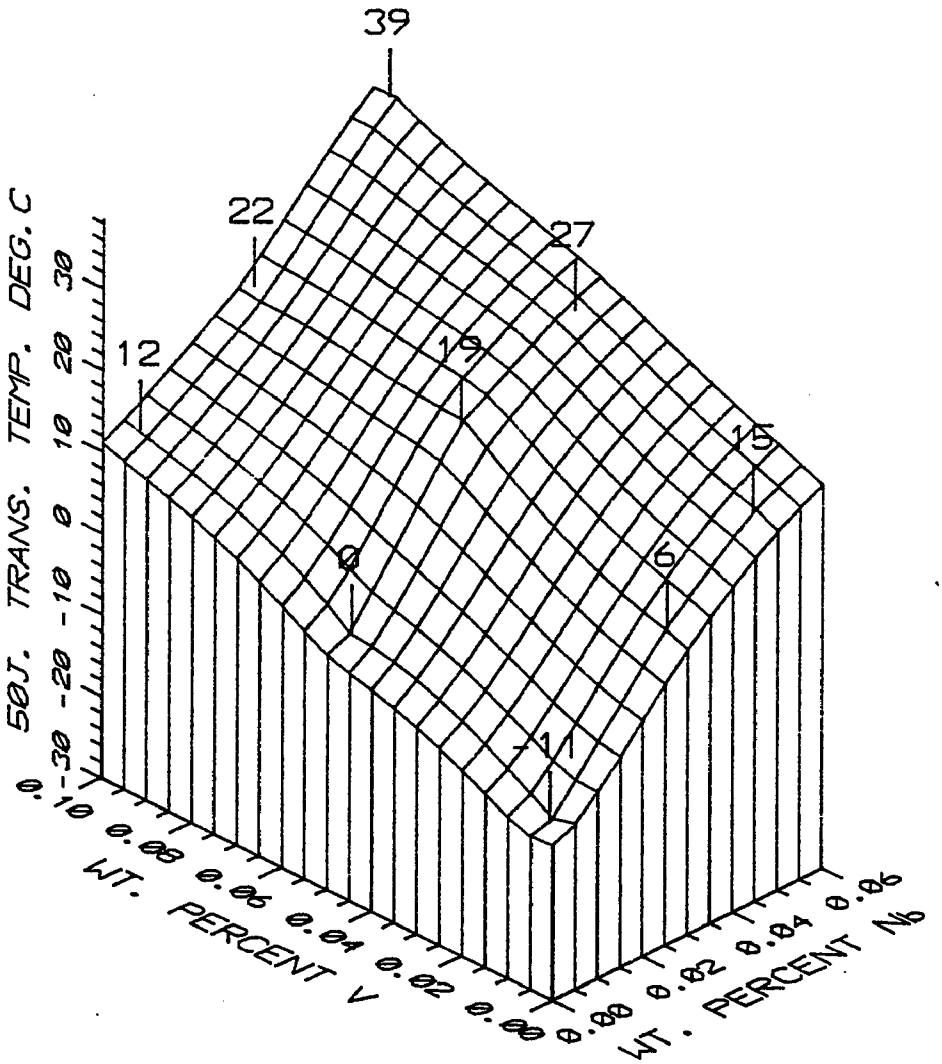

(b) PWHT at 620°C for 2 hours

Figure 4.48 Continued

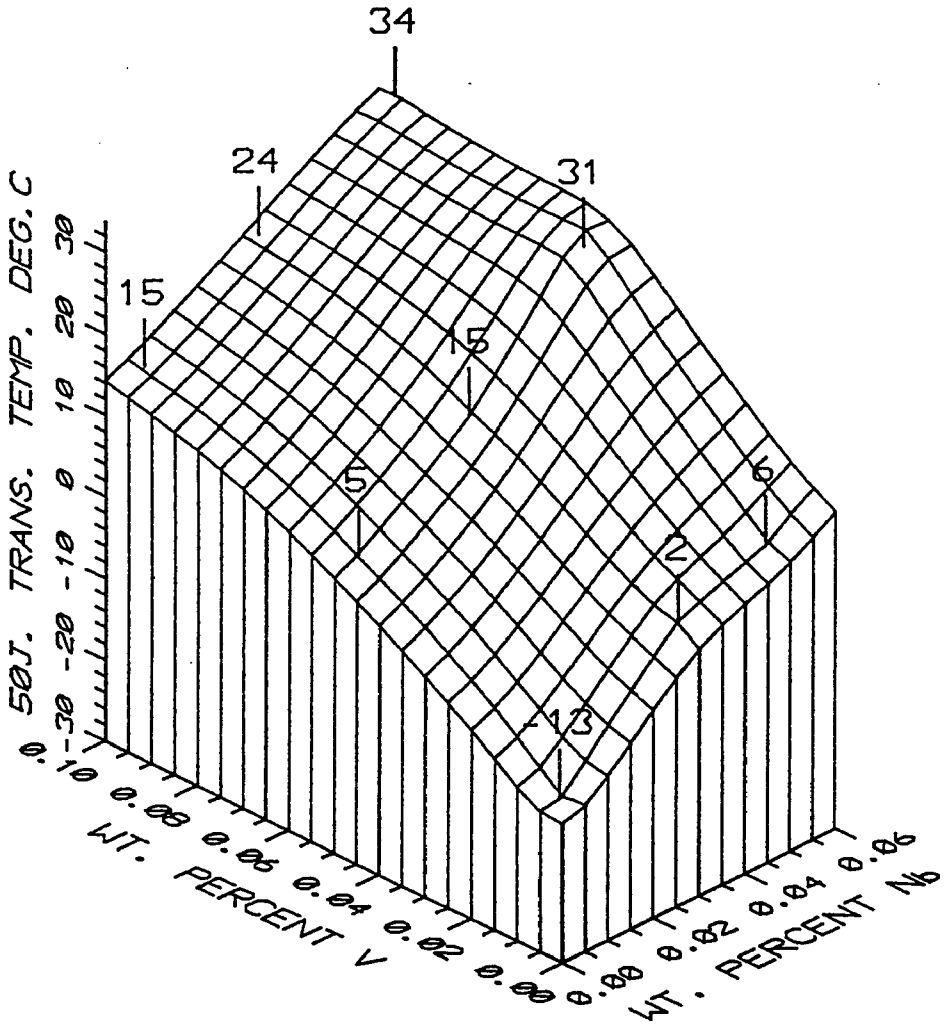

(c) PWHT at 620°C for 10 hours

Figure 4.48 Continued

Different fracture appearances result from different fracture modes. The fracture appearance and its possible change in the transition temperature region are examined here.

A series of HAZ CVN specimens of heat D, welded with 5KJ/mm and PWHT at 620°C for 10 hours prior to testing was selected as a typical example for SEM fracture surface examination. The measured TT50J was 2°C for this series. The surveyed specimens are marked in transition curve with letters A through G, in Figure 4.49. The fractographs of these specimens are to be successively shown below. Brief description for each fractograph is also presented as following.

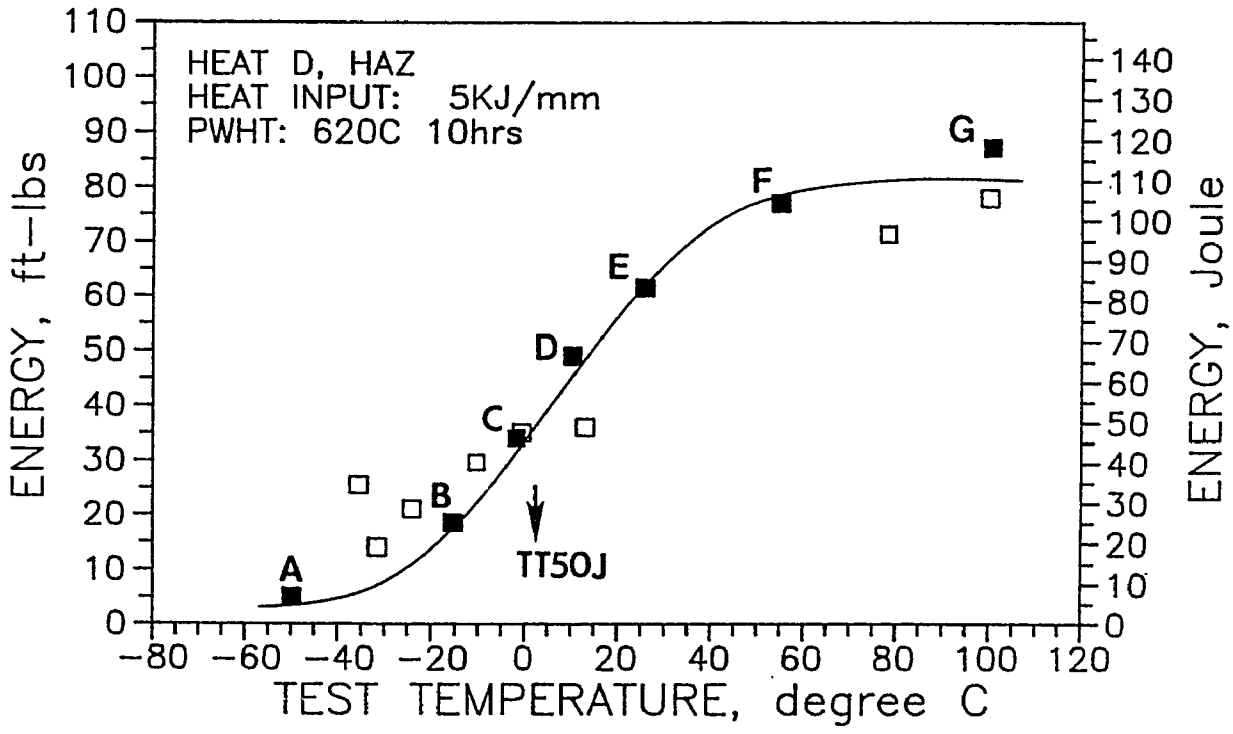

Figure 4.49 Charpy transition curve of HAZ of heat D, showing specimens for fractographic examination

Specimen A - tested at -49.9°C, impact energy 5ft-lbs.

A macroscopic examination on the fracture surface reveals that the vast fracture area is facetted but even at as low as -49.9°C narrow shear lips can still be seen at the fracture edge. The crack initiation site on the fracture surface can be identified by following the chevron markings. The chevron markings are fracture steps which indicate the relative direction of crack motion. Figure 4.50a schematically shows the fracture appearance with chevron markings and Figure 4.50b shows the SEM view of the crack origin in specimen A.

Typical cleavage fracture was observed in the crack origin. The parallel plateau, ledge morphology and river patterns reflect crack propagation along many parallel cleavage planes, which are specific crystallographic planes. The cleavage fracture mode is usually associated with low-energy fracture, e.g., the portion of lower shelf in Charpy transition curve. The high-strain-rate and a high tensile triaxial stress condition beneath the V-notch root also assists the formation of cleavage fracture in CVN testing.

Specimen B - tested at -15.3°C, impact energy 18.5ft-lbs.

Localized plastic deformation can be observed around the notch. Figure 4.51 was taken in the crack initiation site, showing a cleavage facet at the top and the dimple appearance at the bottom. Dimple fracture mode, corresponding to localized plastic deformation in the notch root, takes place prior to the overall fracture. Dimple fracture proceeds by the

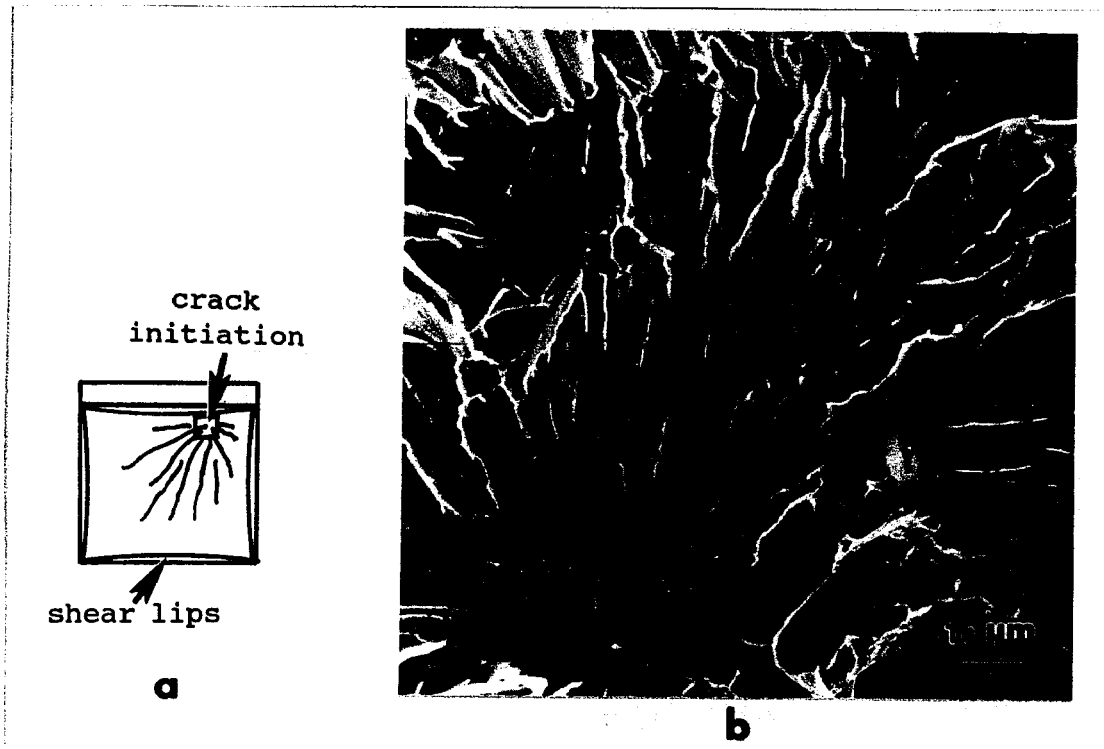

Figure 4.50 (a) Schematic fracture appearance of specimen A, showing crack initiation site and crack propagation direction (b) SEM fractograph of specimen A, tested at -49.9°C

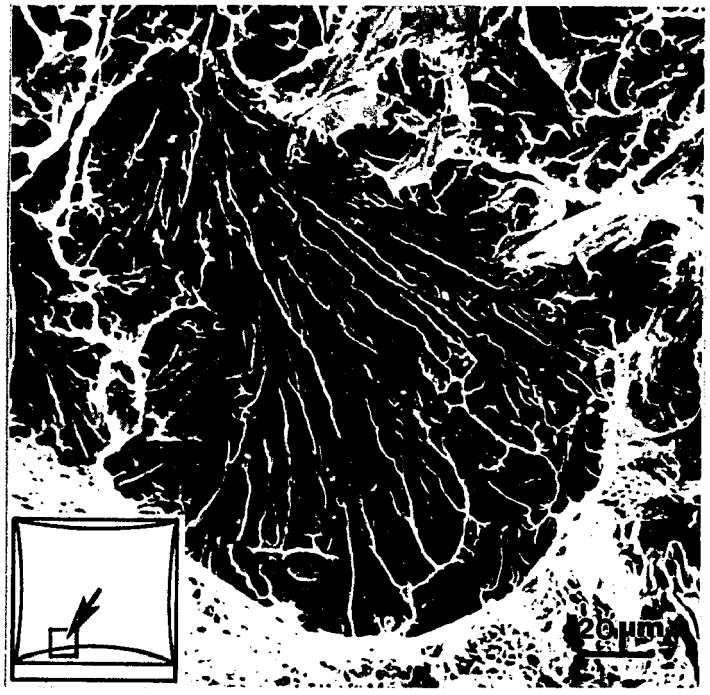

Figure 4.51 SEM fractograph of specimen B, tested at -15.3°C

nucleation of microvoids, and then growth and eventual coalescence. Microvoid coalescence fracture did not develop beyond the initiation site. The overall fracture occurs by cleavage after general yielding due to the attainment of the fracture stress, σ_f, in the ligament. In the cleavage facets shown in Figure 4.51, the "flow" of the "river pattern" is in the direction of microscopic crack propagation.

Specimen C - tested at -1.9°C, impact energy 33.0ft-lbs.

The test temperature of specimen C was just below the transition temperature 2°C. Notch-root deformation and the shear lip in specimen C were more developed than specimen B, but cleavage was still the predominant fracture mode. Figure 4.52 shows the appearance of specimen B, characterized by cleavage facets.

Specimen D - tested at 10.2°C, impact energy 49.0ft-lbs.

This specimen was tested above the transition temperature. Cleavage appearance, along with tear ridges was still observed in the crack initiation site, shown as Figure 4.53. The cleavage "river pattern" marked as "A" on the figure still predominates but is not well developed and the tear-ridge marked as "B" on the figure represents a quasi-cleavage feature.

The examination of specimen C and specimen D reveals that cleavage fracture dominates the crack initiation around the transition temperature.

Specimen E - tested at 25.7°C, impact energy 61.5ft-lbs.

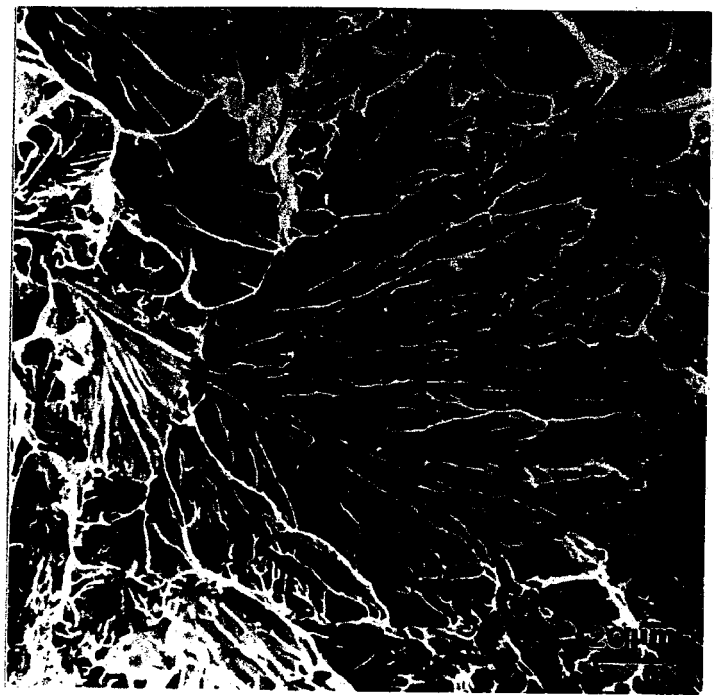

Figure 4.52 SEM fractograph of specimen C, tested at -1.9°C

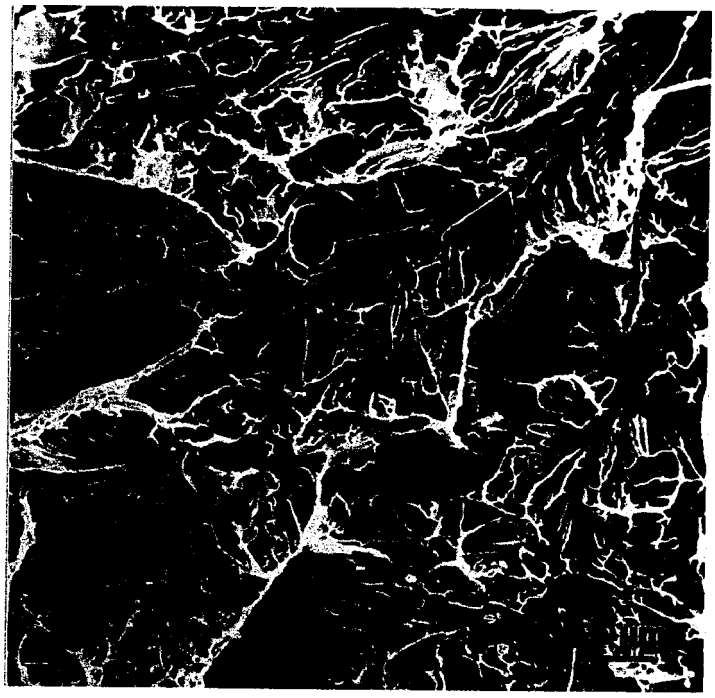

Figure 4.53 SEM fractograph of specimen D, tested at 10.2°C

This specimen was tested at room temperature. The area of notch-root deformation and the shear lip in specimen E were larger than specimen D. The overall fracture surface shows the appearance of a mixture of river patterns, tear ridges and dimples. The crack initiation site shown in Figure 4.54 is characterized by the cleavage river pattern marked as "A", tear ridges marked as "B" and a small amount of dimpled rupture marked as "C". The lateral expansion of specimen was also bigger than those of specimens A, B, C and D. The change in fracture mode was correspondently manifested as the increase in impact energy.

Specimen F - tested at 55°C, impact energy 77ft-lbs.

The microvoid coalesence fracture mode, marked as "A", mixed with quasi-cleavage, marked as "B", was observed in the crack initiation site as shown in Figure 4.55. The crack propagation area was all dimple appearance. This was in accordence with the macroscopic examination of the fracture surface which showed more than 80% of the area was fibrous fracture.

Specimen G - tested at 100°C, impact energy 86.5ft-lbs.

Typical microvoid coalesence fracture mode was clearly identified in both crack initiation and propagation areas. Figure 4.56 shows the dimple appearance around the crack initiation site. Typical fibrous fracture covered 100% of the fracture surface.

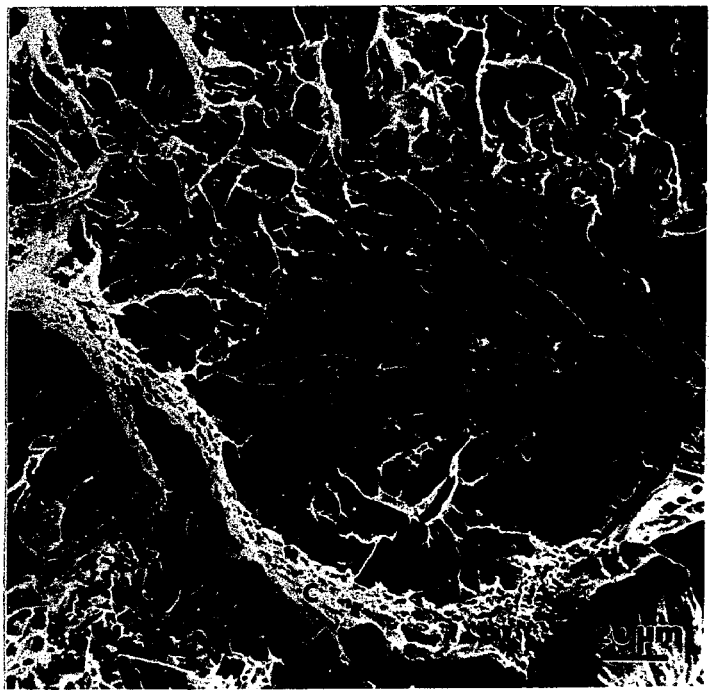

Figure 4.54 SEM fractograph of specimen E, tested at 25.7°C

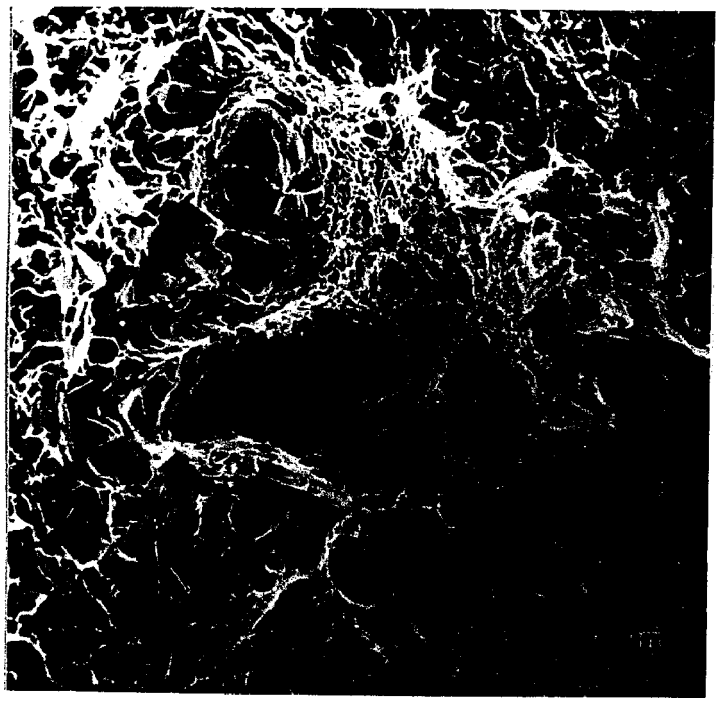

Figure 4.55 SEM fractograph of specimen F, tested at 55°C

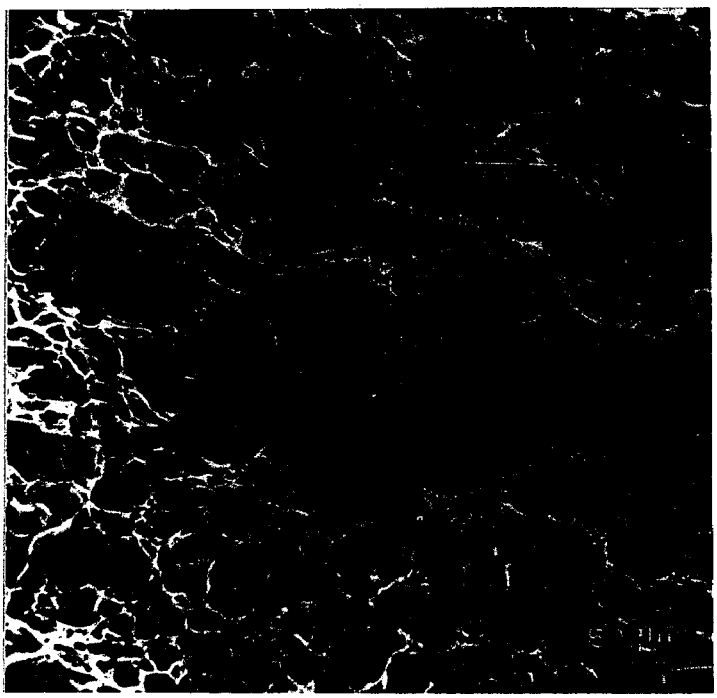

Figure 4.56 SEM fractograph of specimen G, tested at 100°C

4.4.3. DETAILED INVESTIGATION ON CVN SPECIMEN FRACTURE PROCESS

A number of fracture surfaces of CVN specimens which were tested at or close to their transition temperatures were examined. Figure 4.57b gives a typical example. A significant amount of plastic deformation prior to fracture, as evidenced by notch contraction, can be observed. The overall fracture is still 100% facetted. Fracture occurs by cleavage after localized yielding at the notch tip due to the attainment of the critical tensile stress, σ_f, in these specimens. Cleavage can always be observed at the crack initiation site, as described in Section 4.4.2 and shown in Figure 4.57d.

Figure 4.58 schematically shows typical instrumented

Charpy impact testing results for a mild steel [45]. Also recall the schematic load-time curve of the instrumented CVN test shown in Figure 2.15. In region II in Figure 4.58, which corresponds to the transition temperature, 100% cleavage fracture appearance is indicated. The load-time curves of regions I and II indicate that the crack initiation energy is much greater than the crack propagation energy. This suggests that at the transition temperature and below, crack initiation will be the controlling step in the overall fracture process. Since crack initiation is localized in a small region, the microstructure and its mechanical behavior in this region will be significant in determining crack initiation.

Examination of CVN specimen fracture surfaces revealed that the fracture initiation sites in almost all of the examined specimens were not exactly located in the middle of the specimen width. The crack initiation sites were shifted to one side, as typically shown in Figure 4.57a. The maximum degree of stress triaxiality should normally be achieved in the middle of the specimen somewhere beneath the V-notch, and thus the middle should normally be the favored crack initiation site.

To understand this phenomenon, it is appropriate to review the HAZ structure of the multipass weld employed in this study. Figure 4.59 schematically illustrates the sub-zones of the first pass HAZ (Figure 4.59a),indicating how the sub-zones

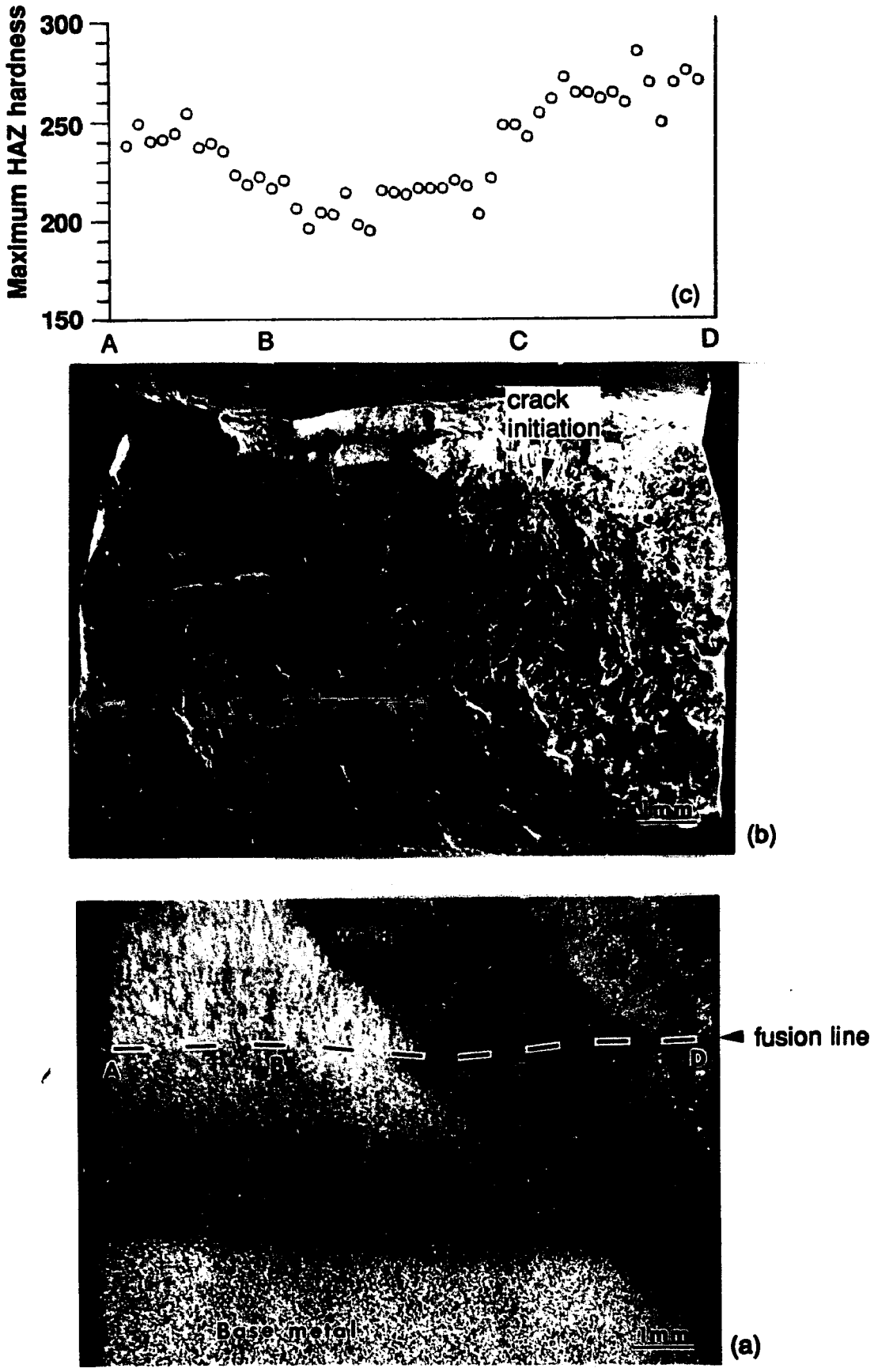

Figure 4.57 A typical demonstration of Charpy specimen of multipass HAZ, heat D, welded with 3KJ/mm and PWHT at 620°C for 10 hours. (a) The appearance of multipass HAZ in a Charpy specimen. (b) The fracture surface of Charpy specimen broken at transition temperature. (c) A microhardness profile in HAZ adjacent to multipass fusion line.

Figure 4.57 (d) Cleavage fracture in crack intiation site

of the first pass are altered by the heat from the second pass (Figure 4.59b) and how Charpy specimens were extracted from this multipass weld (Figure 4.59c). Traveling along the fusion line from the bottom to the top in Figure 4.59c, one first encounters the coarse-grained HAZ of the first pass; then one encounters the region of the coarse-grained HAZ of the first pass affected by the heat of the second pass (which is characterized by refined grains). Finally one encounters the coarse-grained HAZ of the second pass. Referring back to Figure 4.57a, the polished and etched surface of CVN specimen shows the appearance of the multipass HAZ. Microhardness testing was conducted in the HAZ adjacent to the fusion line

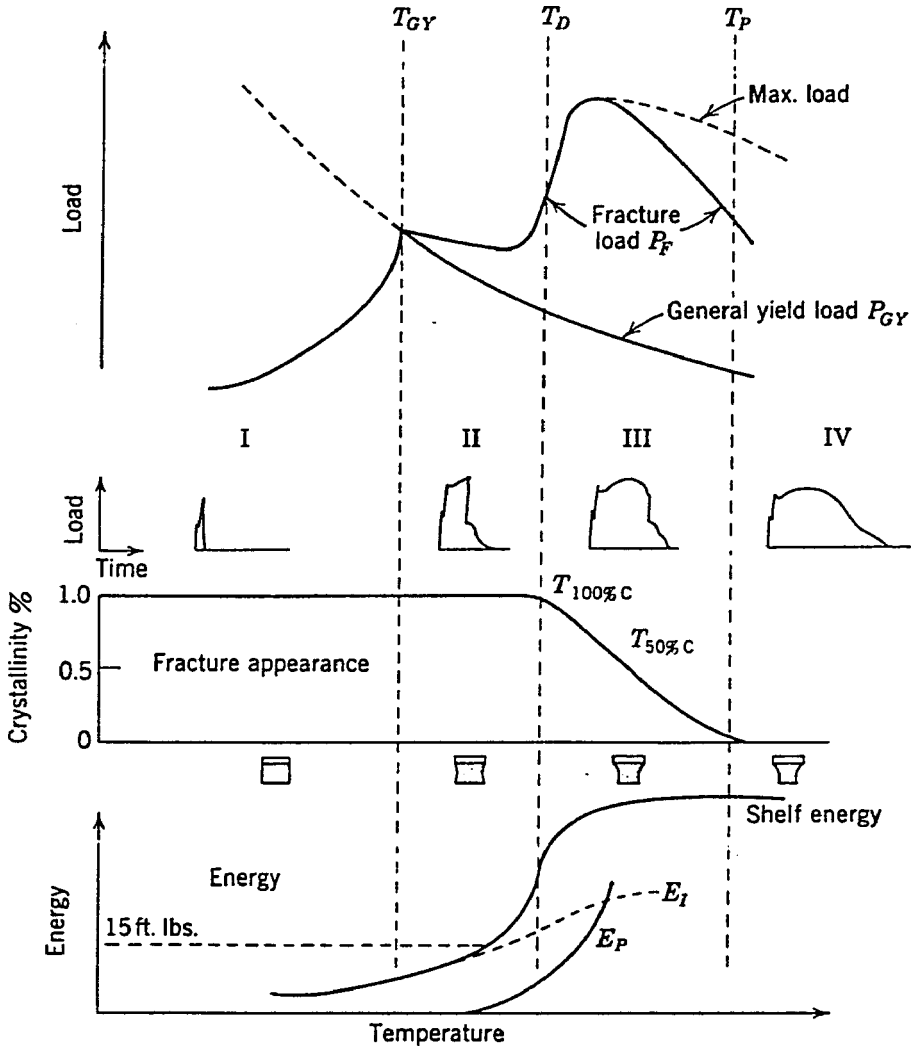

Figure 4.58 Detailed analysis of instrumented Charpy tests, showing the different proportion of energy components at different test temperatures. (E_I-crack initiation energy, E_P-crack propagation energy) [45]

through the width of the CVN specimens. Figure 4.57c shows the microhardness profile.

The portion AB in Figure 4.57a represents the coarse-grained HAZ of the first pass and it is not affected by the

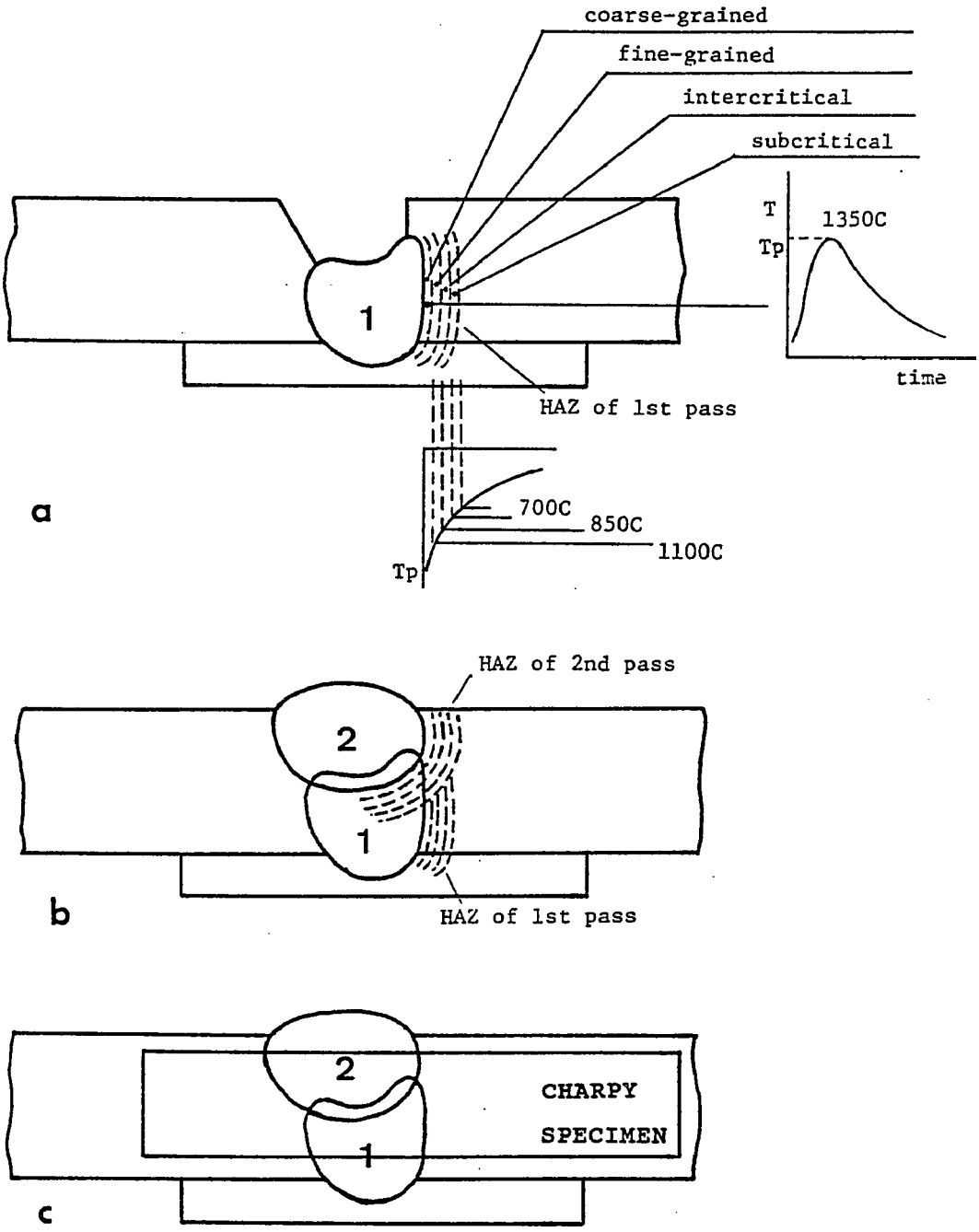

Figure 4.59 The sub-zones of the HAZ of the first pass are altered by the heat from the second pass in a two-pass weldment

heat of the second pass. A higher hardness level, see Figure 4.57c, was observed in this portion. From position B to position C, the coarse-grained HAZ of the first pass was affected by the heat of the second pass, resulting in refined grains and a reduced hardness in this portion. From C to D, hardness gradually increases, reflecting the response as one travels from the overlaping HAZs to the coarse-grained region of the second pass HAZ.

Normally for a homogeneous material, the favorable site of crack initiation should be in the middle of the specimen width, i.e., within the portion BC. Since the material in portion BC had been softened, the crack initiation was therefore shifted to the portion CD which was of higher hardness and lower toughness, but not shifted too far from the center of the specimen width due to the plane stress condition near the specimen side surface. Thus the crack initiation sites in CVN specimens with multipass HAZs are generally observed in higher hardness regions adjacent to the low-to-high hardness transition location. The initiation is normally in the coarse-grained HAZ of either the first pass, unaffected by the heat of the second pass, or in the second pass. This determination is meaningful since the Charpy impact energy, which depends to a great extent on the crack initiation response, and the micro-hardness data which were taken in the coarse-grained HAZ can now be linked through the same microstructural constituents.

On the other hand, the transition temperature which is used as a measure of HAZ toughness depends upon the two temperature-sensitive parameters: the yield strength, σ_{ys}, and the fracture strength, σ_f.

The temperature sensitivity of yield strength is related to the qualitative characteristic of the Peierls-Nabarro stress or, the Peierls stress, σ_p. The value of the Peierls stress depends on the width of the dislocation W, which represents a measure of the distance over which the lattice is distorted because of the presence of a dislocation. It can be expressed in the form [37][46]:

$$\sigma_p \propto G\exp(-2\pi W/b) \qquad (4.6)$$

where $W=a/(1-\nu)$, a is the distance between similar planes; ν is Poisson's ratio and G is shear modulus.

Since the Peierls stress depends on the short range stress field of the dislocation core, it is sensitive to thermal energy in the lattice and, hence, to the test temperature. The thermal enhancement of dislocation motion is limited at low temperature and the Peierls stress is large. In fcc metals that have wide dislocations, the increase in Peierls stress with decreasing temperature is insignificant, since the Peierls stress is negligible to begin with. For bcc metals that have narrow dislocations, however, the Peierls stress rises rapidly with deceasing temperature. The Peierls stress usually represents a large component of the yield strength in the low-temperature regime. The yield-strength temperature

sensitivity is therefore strong for bcc metals.

However, the fracture strength has a different temperature response. By using dislocation models and analysis [37][47], the fracture stress could be given by

$$\sigma_f \approx 4G\gamma_m d^{-1/2}/k_y \qquad (4.7)$$

where σ_f = fracture stress

G = shear modulus

γ_m =plastic work done around a crack as it moves through the crystal

k_y = dislocation locking term from Hall-Petch relation

d = grain size

Tetelman and McEvily indicated that γ_m increases with an increase of unpinned dislocation sources, temperature and decreasing crack velocity [48]. Increasing temperature enhances the number of mobile dislocations, their mobility and speed, and hence increases γ_m and σ_f.

The intersection of the curve of yield strength σ_{ys} versus temperature and the curve of fracture strength σ_f versus temperature herein represents the transition temperature, as schematically illustrated in Figure 4.60.

The three-dimensional diagrams, shown as Figures 4.23 and 4.24, give a clear image of strengthening in HAZs due to the addition of V and Nb, particularly in PWHT conditions. The strengthening mechanisms may include solid solution strengthening, precipitation strengthening and grain boundary strengthening. Since only small amounts of V and Nb were added

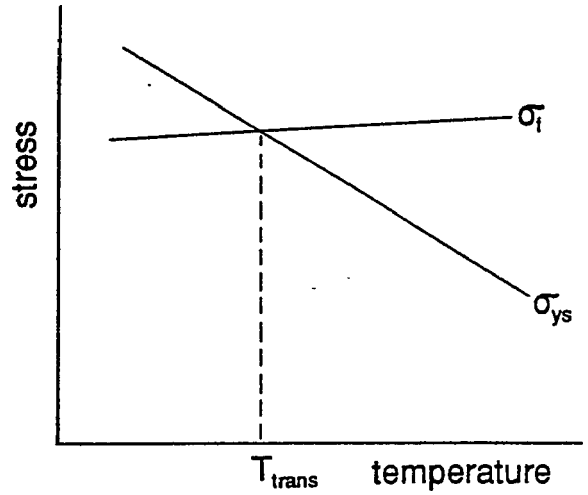

Figure 4.60 Effect of test temperature on yield stress σ_{ys} and fracture stress σ_f. Intersection represents the transition temperature.

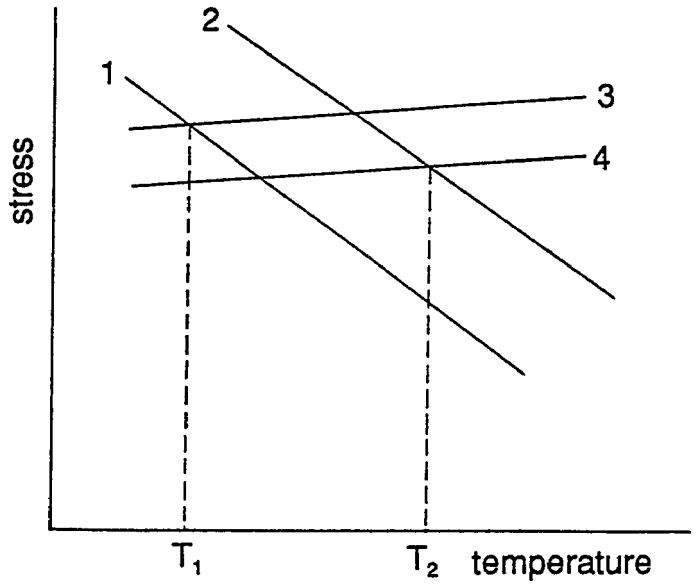

Figure 4.61 Effects of lower and higher microalloy additions on the curves of yield stress σ_{ys} and fracture stress σ_f, indicating the transition temperature shift T_2-T_1

and the solubilities of V and Nb in the steels at room temperature are extremely low, solid solution strengthening can be considered negligible. Grain refinements in the coarse-grained HAZ caused by V and Nb are different, as shown in Figure 4.14 and Figure 4.15, having previously discussed. An increase in Nb content from 0.005% to 0.06% results in an approximately 40% reduction in HAZ grain size, whereas an increase in V content from 0.005% to 0.10% had little effect on grain size, thus it is expected that V and Nb additions will not produce significant grain boundary strengthening in HAZ. The major contribution to strengthening therefore comes from precipitation of VC and NbC particles.

It is commonly accepted that only grain refinement produces simultaneous increase in σ_{ys} and σ_f, and reduction in transition temperature, but the HAZ grain size variations do not exert any beneficial influence on TT50J. In fact, while the grain size decreases from 283μm in 5kJ/mm-HAZ of heat B to 170μm in 5kJ/mm-HAZ of heat H, as shown in Figure 4.14, the 50 Joule transition temperature correspondingly increases from -2°C to 26°C. Obviously the weak effect of grain refinement was concealed.

A comprehensive illustration of the effects of lower and higher microalloy additions on σ_{ys} and σ_f is given in Figure 4.61.

Four stress-vs-temperature curves are drawn in Figure 4.61. Curve 1 represents σ_{ys} of specimens with low V and/or Nb

contents, and curve 2 represents σ_{ys} of specimens with high V and/or Nb contents. No doubt curve 2 occupies a higher position than curve 1 because of relatively stronger precipitation strengthening.

The additions of V and/or Nb strengthen the material through various mechanisms, restricting the number of free dislocations and their mobility, contributing toward increasing σ_{ys}, while at the same time reducing the magnitude of γ_m (ref. Equation 4.7). Likewise, k_y can be adjusted to improve either σ_f or σ_{ys} but only at the expense of the other (compare the Hall-Petch relation $\sigma_{ys}= \sigma_i+ k_y d^{-1/2}$ with Eq. 4.7). Enhanced dislocations locking will increase σ_{ys} but will decrease σ_f directly according to Equation 4.7 and indirectly due to a decrease in the number of mobile dislocations and γ_m. Another term in Equation 4.7 is grain size d. As we just discussed, HAZ grain size decreases from 283μm for heat B to 170μm for heat H, representing the effect of Nb additions. The lower-shelf energies in 5kJ/mm-HAZ CVN transition curves of heat B are 6J, 7J and 5J for as-welded, PWHT 620°C/2hrs and 620°C/10hrs, respectively, and 5J, 5J and 3J, respectively in heat H under the same conditions. This reveals that the reduction in grain size does not win the competition for increasing σ_f, whereas the terms γ_m and k_y are considerably affected by microalloy strengthening, resulting in decrease in σ_f. Recall also that vanadium additions have little effect on HAZ grain size.

Returning now to a consideration of Figure 4.61, curve 3 represents the fracture strength σ_f of specimens with low V and/or Nb contents, while curve 4 represents σ_f of specimens with high V and/or Nb contents. The transition temperature is now increased from T_1 which corresponds to the intersection of σ_{ys} and σ_f for low V and/or Nb heats to T_2 which corresponds to the intersection of σ_{ys} and σ_f for high V and/or Nb heats. A transition temperature shift (T_2-T_1) is hereby produced due to increased additions of microalloy elements V and Nb.

4.5. INVESTIGATION ON PRECIPITATES

4.5.1. IDENTIFICATION OF PRECIPITATES

3mm-diameter-disk thin foil specimens which were extracted from the HAZs of bead-on-plate weldments and twin-jet-polished were examined either in a Philips EM300 operating at 100kV or a Philips EM400 operating at 120kV.

Complex diffraction patterns were always observed in all specimens, including all test heats, welding heat inputs and PWHT conditions.

Prior to an investigation on the precipitation behavior of V/Nb carbides, efforts were made to insure correct indexing of the observed and recorded selected area diffraction patterns (SADP). It is clear that the complex pattern is a superposition of four individual SADPs. They are

(1) matrix α-Fe spots which are usually the strongest spots in the complex SADP,

(2) cementite spots which exist only if there are cementite particles in the selected area,

(3) vanadium/niobium carbide spots, the principal constituents of interest, and

(4) Fe_3O_4 spots which arise from the surface oxidation.

In addition, the multiple diffraction patterns may be produced by two or more orientations of these diffracting substances. The multiple diffraction is also superimposed onto the observed complex SADP.

4.5.1.1. MATRIX α-Fe SPOTS

The SADP of matrix α-Fe is easily identified and indexed because it is strong and well characterized. The identification and indexing of SADP of α-Fe are usually performed and utilized for two applications in this study.

First, the indexing of SADP of α-Fe spots may assist the indexing and identification of other SADPs by means of known orientation relationships, such as the orientation relationship between α-Fe and vanadium or niobium carbide, the orientation relationship between α-Fe and cementite, the relationship between fcc and bcc materials, etc.

Secondly, the indexing of α-Fe spots may be used for calibration of the camera constant. Figures 4.62a and 4.62b show the indexing of two α-Fe patterns with [011] and [012] zones, respectively. The operating accelerate voltage was 120kV and camera length L was 575mm in the EM400 machine, the wave length λ was 0.03345Å and thus the expected camera constant is λL=19.234mmÅ.

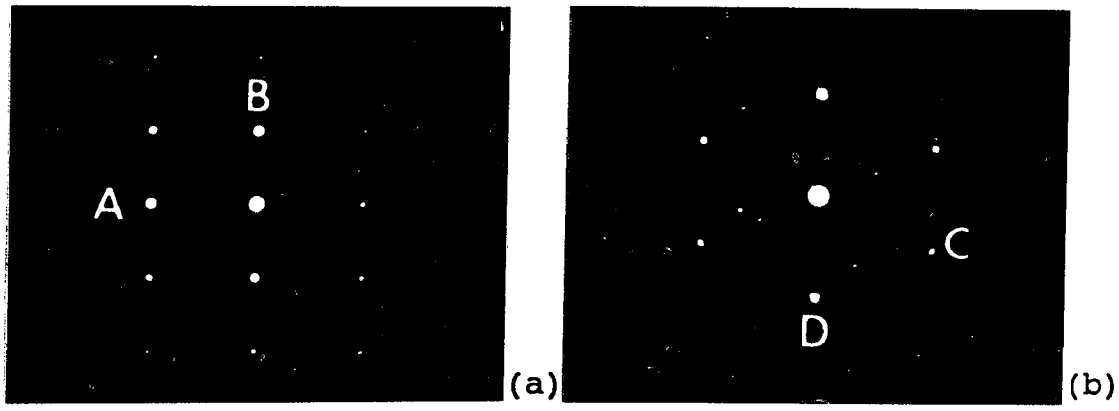

Figure 4.62 SADPs of matrix α-Fe
(a) [011] zone (b) [012] zone

The distance, R, from the spots noted to the center spot in Figures 4.62a and 4.62b were measured, as shown in Table 4.6. By using the lattice parameter of α-Fe 2.866Å and the calculated interplanar spacing d_{hkl} for plane hkl, and by using Rd=λL, the camera constant was measured as average 19.22mmÅ. Compare with λL=19.234mmÅ given by the EM400 setting, good agreement can herein be acknowledged.

4.5.1.2. CEMENTITE SPOTS

As discussed in Section 4.2, the final HAZ microstructural constituents for both 3kJ/mm and 5kJ/mm heat inputs would include ferrite-carbide aggregates and M-A-C, where

Table 4.7 Measured camera constant from α-Fe spots

Spot destination	hkl	d_{hkl} (Å)	measured R (mm)	λL=Rd (mmÅ)
A (Fig.4.62a)	200	1.433	13.5	19.34
B (Fig.4.62a)	011	2.027	9.5	19.26
C (Fig.4.62b)	200	1.433	13.4	19.20
D (Fig.4.62b)	121	1.170	16.3	19.07

Measured Average λL=19.22mmÅ, EM400 setting λL=19.234mmÅ

interlath and intralath cementite exist. Figure 4.18a shows the interlath and intralath cementites in tempered martensite and Figure 4.19 shows the interlath cementite in bainite. In these cases the cementite spots are the basic group in an HAZ SADP.

Two M_3C-type carbides, Fe_3C and Mn_3C, should be taken into

account in the Mn-bearing experimental heats in this study, both have an orthorhombic lattice with 12 metallic atoms and 4 carbon atoms in one cell. Due to the similarity of iron and manganese, Fe_3C and Mn_3C can completely dissolve to each other, forming $(Fe,Mn)_3C$ in steel. The iron atoms in Fe_3C can be substituted by manganese atoms in any ratio. For pure Fe_3C, the lattice parameters are a=4.5235Å, b=5.0888Å and c=6.7431Å. The lattice parameters will slightly change as Mn_3C is dissolved into Fe_3C. The magnitude of this lattice parameter change depends on the percent of Mn in the steel, and no data on this relationship are available. This uncertainty in lattice parameters somewhat complicates the SADP's indexing.

Figure 4.63 shows a bright field (BF) image, a centered dark field (CDF) image and the corresponding SADP for the HAZ of heat A, welded with 5kJ/mm and PWHT at 620°C for 10 hours. The dark field image was imaged from the arrowed spot in SADP, shown in Figure 4.63c, which was indexed as a $(Fe,Mn)_3C$ diffraction spot. The principal feature shown in these BF (Figure 4.63a) and CDF (Figure 4.63b) images is cementite, although some fine particles are noted in the BF image. The fine particles have been identified as surface iron oxide Fe_3O_4, which will be detailed in Section 4.5.1.4.

The indexing of a typical SADP is illustrated in Figure 4.64. In this pattern, three groups of spots were identified: α-Fe, $(Fe,Mn)_3C$ and Fe_3O_4. The recorded SADP was enlarged by 1.932 times for indexing. The interplanar spacing for

$(Fe,Mn)_3C$ was calculated by using

$$1/d_{hkl} = (h/a)^2 + (k/b)^2 + (l/c)^2 \qquad (4.8)$$

and good agreement between the calculated spacing from Equation 4.8 and converted spacing from R in the diffraction pattern was obtained. The orientation relationship $(001)_{cementite} \| (211)_{\alpha\text{-}Fe}$ known as the Bagaryatskii Orientation Relationship between cementite and α-Fe was observed. The Fe_3O_4 spots indexed in Figure 4.64e will be further discussed in Section 4.5.1.4.

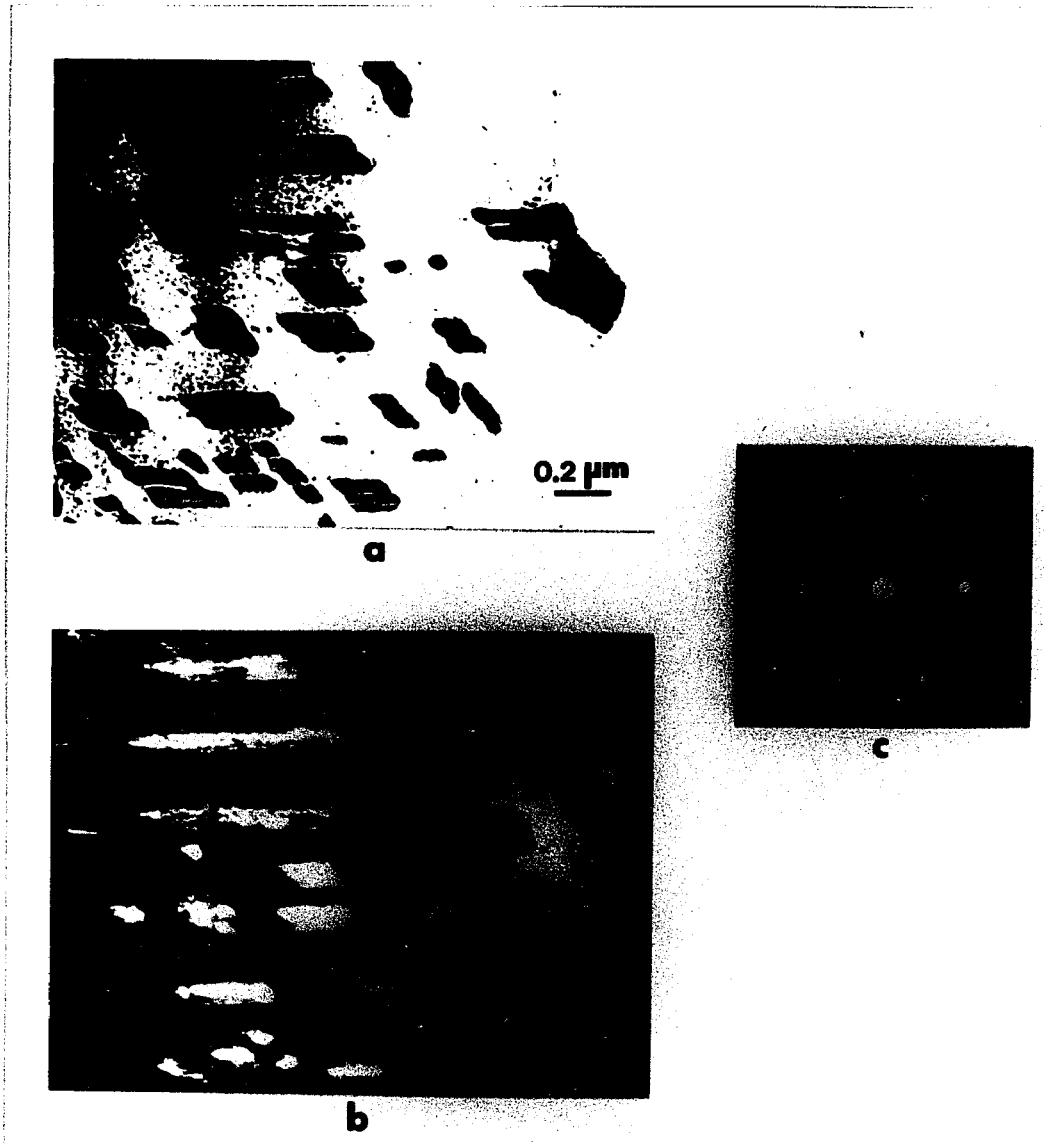

Figure 4.63 Cementite in HAZ of heat A, welded with 5kJ/mm and PWHT at 620°C for 10 hours. (a) BF image (b) CDF image (c) SADP

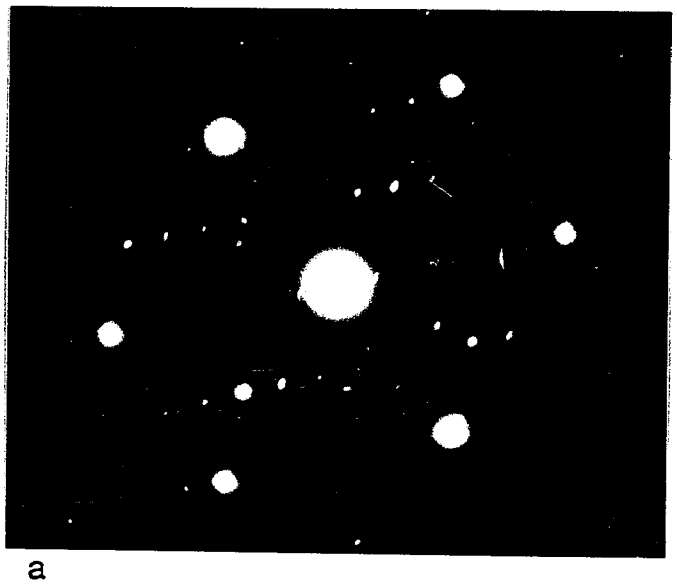

a

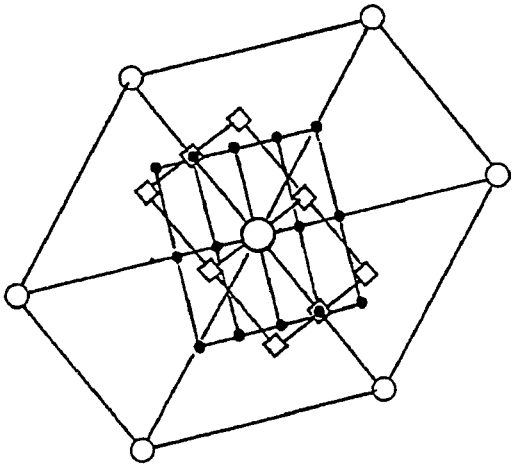

b

○ α-Fe

• $(FeMn)_3C$

▫ Fe_3O_4

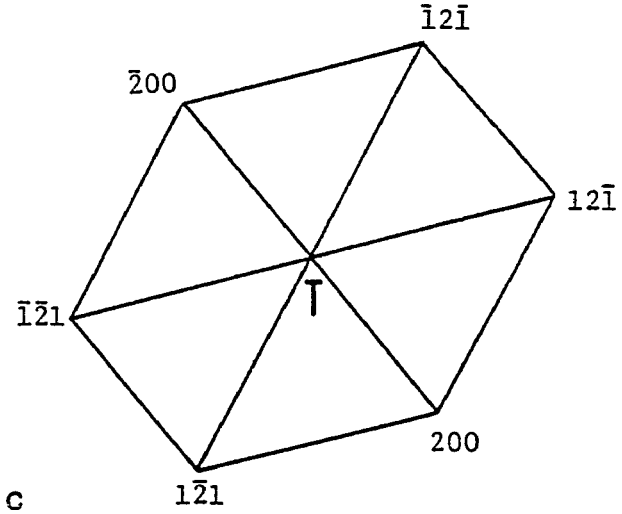

c

[012] α-Fe

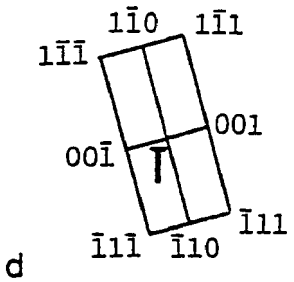

d

$(FeMn)_3C$

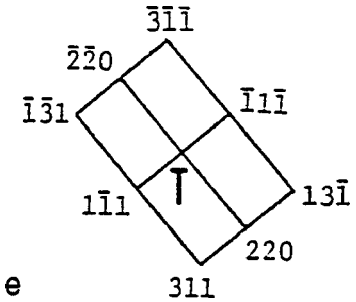

e

$[\bar{1}12]$ Fe_3O_4

Figure 4.64 A complex SADP with cementite spots and its indexing

4.5.1.3. VC/NbC SPOTS

As described in Section 2.1.2, the carbides of V and Nb will be present in the form of VC and NbC when carbon content prevails over the V and Nb contents, as in the case of test heats of this study. VC and NbC, each of which possesses the NaCl crystalline structure, can form a continuous solid solution. The vanadium atoms in VC can be substituted by niobium atoms and vice versa. The lattice parameter of this (V,Nb)C may change with variation of relative concentration of V or Nb in the VC-NbC solution. Stoichiometric VC has a lattice parameter of 4.175Å and stoichiometric NbC has a lattice parameter of 4.460Å. Thus the lattice parameter of (V,Nb)C is expected to be within the range 4.175-4.460Å. Moreover, either VC or NbC could be hypostoichiometric, resulting in a slight reduction of the lattice parameter [12][13]. Hence (V,Nb)C could be so, too. This uncertainty in lattice parameter makes SADP indexing and identification difficult.

Nitrides of V and Nb were not taken into account in this research work because the nitrogen concentration was only 0.006-0.008 wt.%, which is two orders of magnitude lower than carbon concentration in all heats. The nitrides of V and Nb, if any, are isomorphous with the carbides of V and Nb; the nitrogen and carbon atoms can substitute for each other.

The oxide surface layer which often forms on thin foil specimens can be a serious problem. This oxide, identified as

Fe_3O_4, has the fcc spinel structure with a lattice parameter approximately two times that of the (V,Nb)C. Moreover, the morphology of the oxide is small discrete particles with sizes similar to (V,Nb)C precipitates. These oxide particles confuse the identification of (V,Nb)C precipitates.

4.5.1.4. OXIDE SPOTS

It is a common problem in iron alloys that thin foil specimens are slightly oxidized.

Chen and Morris [49] examined the thin oxide film formed on a bcc Fe-Ni alloy surface using high resolution microscopy. They concluded that oxide layer (principally Fe_3O_4) forms spontaneously on bcc Fe-Ni alloy surfaces on exposure to air at room temperature. The oxide layer forms spontaneously on the thin foil specimen as soon as it is polished. This oxide layer consists of dispersed, tiny (~20Å) orientated particles rather than a continuous thin film.

Further work on an fcc Fe-Ni alloy by Reuter et al. [50] indicated that the oxide reflections were observed in SADPs from all TEM thin foil specimens whether they were prepared with a twin-jet electropolisher, ion-beam thinning or jet-polishing followed by ion cleaning. Among these three techniques, however, jet-polishing was reported to minimize the oxidation problem. Reuter et al. also indicated that the oxide forms as small (<30nm) discrete, orientated particles on fcc Fe-Ni specimens, similar to the morphology in bcc Fe-Ni

specimens reported by Chen and Morris.

The Fe_3O_4 has a face-centered cubic spinel structure with a lattice parameter of 8.3963Å [49][50], which is, as stated above, almost exactly two times the lattice parameter of (V,Nb)C. Both phases also have the fcc structure, which makes the distinction of carbide and oxide extremely difficult. The hkl spots of the carbide almost coincide with the 2h2k2l spots of the oxide in most orientations such as [011] α-Fe. Figure 4.65 shows a typical example in this TEM study. The SADP shown in Figure 4.65a was taken with the crystal orientation close to [110] α-Fe zone. The indexed α-Fe pattern is illustrated in Figure 4.65c. Two oxide zones, [111] Fe_3O_4 zone and [211] Fe_3O_4 zone, are presented together and indexed as Figure 4.65d and 4.65e, respectively. The two Fe_3O_4 zones were considered to have arisen from the oxide on the top and bottom surfaces of the thin foil specimen.

Comparing the [110] α-Fe zone and [111] Fe_3O_4 zone, we have

$(0\bar{1}1)$ Fe_3O_4 ∥ (001) α-Fe

$(\bar{1}11)$ Fe_3O_4 ∥ $(\bar{1}10)$ α-Fe

(110) Fe_3O_4 23 degree to $(\bar{1}1\bar{2})$ α-Fe

$(1\bar{3}1)$ Fe_3O_4 4 degree to $(1\bar{1}2)$ α-Fe

All of these are consistent with the Nishiyama-Wassermann orientation relationship between fcc and bcc materials [51].

As previously mentioned, there are some possibilities where (V,Nb)C and Fe_3O_4 may take up specific variants of their

a

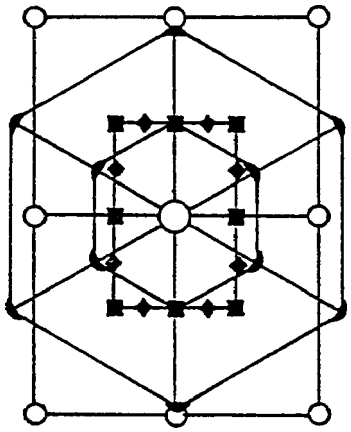

○ [110] α-Fe

◠ [111] Fe_3O_4

■ [2$\bar{1}$1] Fe_3O_4

◆ Double diffraction sports

b

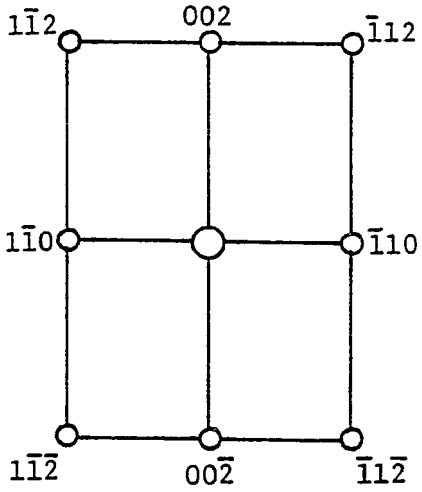

[110] α-Fe

c

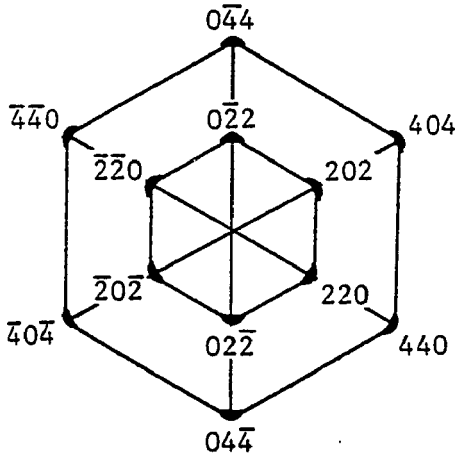

[111] Fe_3O_4

d

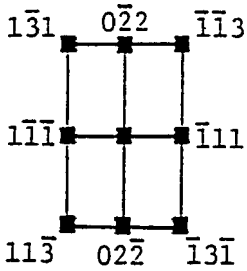

[211] Fe_3O_4

e

Figure 4.65 A complex SADP, showing Fe_3O_4 spots of two variants

respective orientation relationships such that their diffraction spots superimpose or are reinforced by double diffraction from (V,Nb)C to Fe_3O_4 reflections and vice versa. The 440 spots of Fe_3O_4 here could be confused with 220 spots of (V,Nb)C. It is of assistance in distinguishing Fe_3O_4 spots from (V,Nb)C spots that the Fe_3O_4 diffraction spots are characterized by the elongated shape and perpendicular to the radial direction, and that the higher the index the longer is the elongation. This feature can be seen in Figure 4.65a.

Figure 4.66 is an example of a CDF image of Fe_3O_4. The precipitate-like morphology is observed, which is very similar to what reported by Chen and Morris in bcc Fe-Ni alloys [49]. Besides the irregular-shaped particles, Fe_3O_4 can be in the form of tiny oxide islands with size <50nm, as arrowed in Figure 4.66.

Again, Reuter et al. indicated that the oxide layer of Fe_3O_4 is independent of the specimen preparation technique. This oxide can be minimized only by using the jet-polishing technique followed by immediate examination of the foil [50]. This advice has been taken in this TEM study to minimize the oxide confusion.

4.5.1.5. DETECTION OF (V,Nb)C IN HAZ WHEN Fe_3O_4 IS PRESENT

Although the surface oxide problem arises, the carbide (V,Nb)C still can be distinguishable in some orientations where the separation of carbide from oxide patterns may be

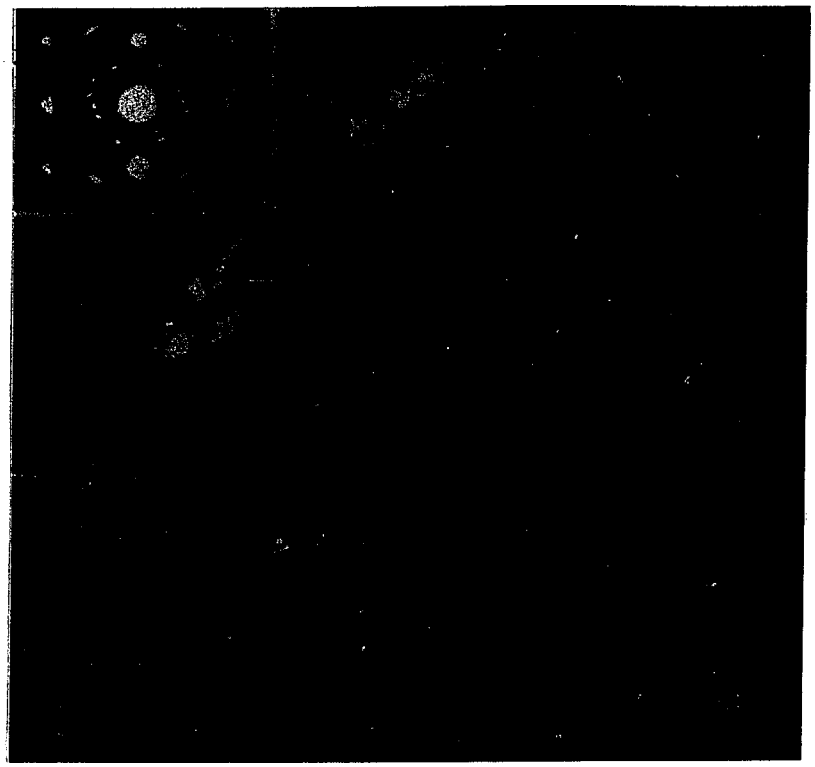

Figure 4.66 Surface oxide Fe_3O_4 morphology, arrows show oxide islands.

easier. Figure 4.67 presents a typical example which was often utilized for CDF imaging in this study. In this complex SADP, the [110] zone and the $[1\bar{1}0]$ zone of (V,Nb)C, and the $[\bar{4}11]$ zone and the $[\bar{4}\bar{1}1]$ zone of Fe_3O_4 are superimposed on the [100] zone of matrix α-Fe. The patterns are individually indexed as Figures 4.67c,d,e,f,g. Four (V,Nb)C spots, the (002) and $(00\bar{2})$ in the [110] (V,Nb)C zone, and the (002) and $(00\bar{2})$ in the $[1\bar{1}0]$ (V,Nb)C zone are separated from the oxide and the α-Fe spots, as arrowed in Figure 4.67b. With these four spots, the CDF imaging can be performed. The diffraction condition shown in Figure 4.67a and the (002) carbide spots

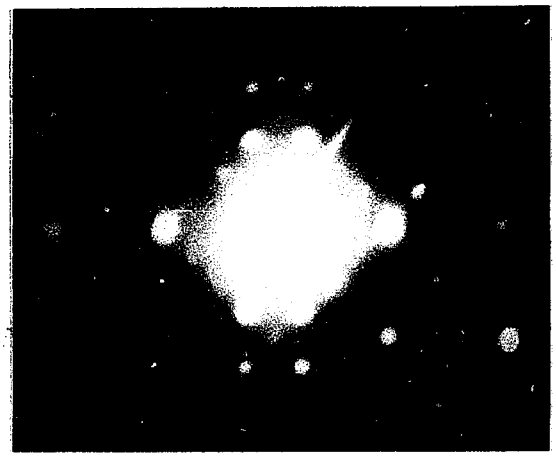

a

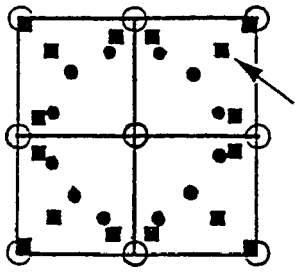

b

○ α-Fe

■ (V,Nb)C

● Fe_3O_4

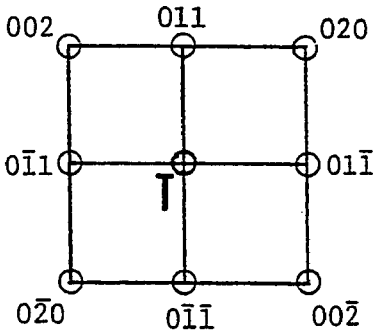

c

[100] α-Fe

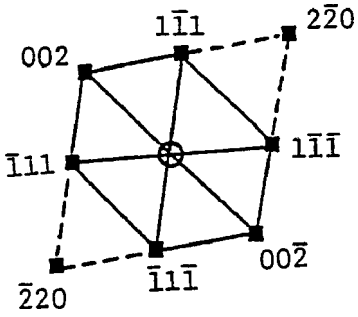

d

[110] (V,Nb)C

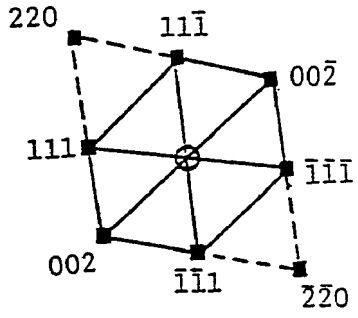

e

[1$\bar{1}$0] (V,Nb)C

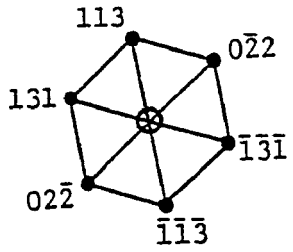

f

[$\bar{4}$11] Fe_3O_4

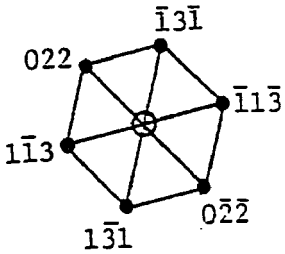

g

[$\bar{4}\bar{1}$1] Fe_3O_4

Figure 4.67 A complex SADP, showing two variants of (V,Nb)C and two variants of Fe_3O_4

were also utilized for CDF imaging to show the NbC precipitates by J.Bosansky et al [52].

4.5.2. MORPHOLOGIES OF (V,Nb)C PRECIPITATES

As discussed in Section 2.1.3, four morphologies of (V,Nb)C precipitates have been identified. They are planar interphase precipitation, non-planar interphase precipitation (curved, irregular bands), random precipitation and fine carbide fibers. The planar and non-planar interphase precipitates are also defined as row-type or fine banded precipitates in the literature.

In this study, the planar and random (V,Nb)C precipitates were observed in the HAZ. The random distribution was the predominant morphology of the precipitate whereas the planar was rarely observed. Z.Yan et al.[53] also concluded that in a vanadium and titanium microalloyed low-carbon steel, both interphase precipitates and matrix precipitates were observed in ferrite grains. The latter is predominant and the former is rarely observed. This is consistent with the results of the examination of precipitate morphology in this study.

4.5.2.1. PLANAR INTERPHASE PRECIPITATION

Figure 4.68 shows an example of planar interphase precipitation. The micrograph was taken from the HAZ of heat I, the heat with the most V and Nb, welded with 5kJ/mm and PWHT at 620°C for 50 hours. It is clear that these

precipitates show a row-type or banded distribution.

A series of papers has been presented for interpreting the formation of the banded morphology of VC or NbC precipitates [15][21][22][54][55][56]. In plain carbon steel, the $\gamma \rightarrow \alpha$ transformation leads to a range of morphologies including polyhedral ferrite and massive cementite, pearlite and several forms of bainite. However, in V/Nb microalloyed steels, the partial or complete replacement of cementite by alloy carbides of VC and/or NbC takes place. Alloy carbides precipitate from supersaturated austenite before the $\gamma \rightarrow \alpha$ transformation or from supersaturated ferrite after the $\gamma \rightarrow \alpha$ transformation. Alternatively, they can form simultaneously with ferrite during the $\gamma \rightarrow \alpha$ transformation in the form of a very fine dispersion apparently in regular rows. These rows are actually sheets of carbide nucleated at the γ/α boundaries during transformation and are therefore called interphase precipitates.

In a $\gamma \rightarrow \alpha$ transformation, the speed of the movement of the γ/α interface is controlled by the diffusion rate of carbon at the austenite frontier. As the α phase grows, the carbon content at the austenite front gradually increases. The alloy carbides nucleate and grow at the γ/α interface when the increasing carbon content reaches a certain value. While the carbides nucleate and grow, the γ/α interface becomes stationary and carbon concentration drops. As the carbon concentration lowers, the alloy carbides stop growing. The α

phase again begins to grow and the γ/α interface moves forward, leaving a planar sheet of carbide behind. This process is repeated again and again, resulting in the formation of a parallel banded morphology of precipitation. This morphology is particularly found in vanadium-containing steels where the higher solubility of VC allows a larger volume fraction of precipitates in both austenite and ferrite.

A more detailed explanation of the planar interphase precipitation in V and Nb microalloy steels has been presented by Campbell and Honeycombe [15][57]. In the $\gamma \rightarrow \alpha$ transformation, the orientation relationship most commonly found to develop between fcc and bcc phases is either the Kurdjumov-Sachs or the Nishiyama-Wassermann relationship. For the low energy interfaces which are commonly $(111)_{austenite} \parallel (110)_{ferrite}$, the growth of ferrite can only be accomplished by a ledge mechanism as schematically shown in Figure 4.69. The planar α/γ boundaries are relatively low energy interfaces and thus posses intrinsically low mobility. Steps involving higher energy interfaces can move much more rapidly and so accommodate the transformation. However the nucleation of carbide particles does not normally occur on migrating steps, otherwise the transformation would cease. Instead, the nucleation occurs on the newly created planar interface behind the steps, resulting in a banded dispersion where the band spacing is the same as the step height. The step height is largest at the highest transformation temperature and

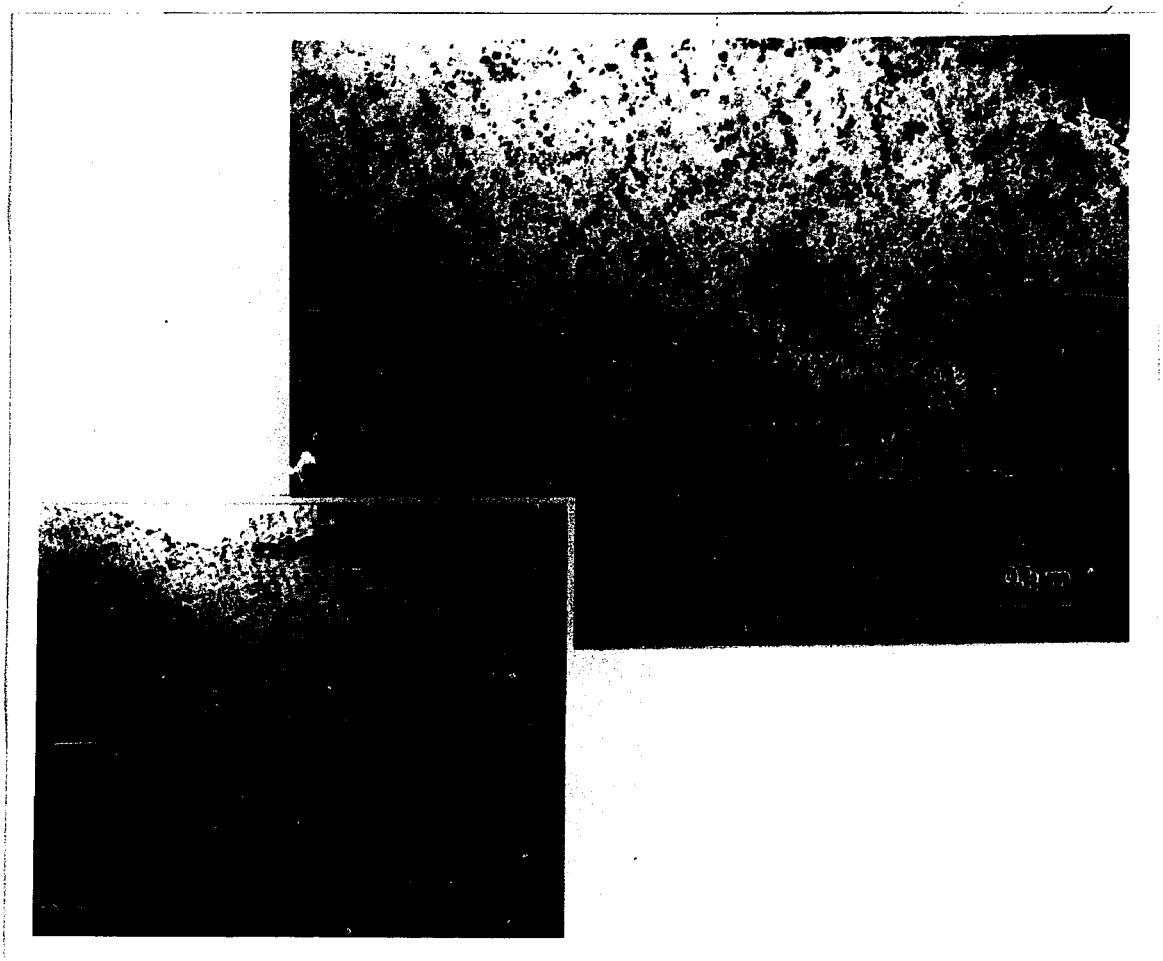

Figure 4.68 (V,Nb)C precipitates with banded morphology, observed in the HAZ of heat I, welded with 5kJ/mm and PWHT at 620°C for 50 hours

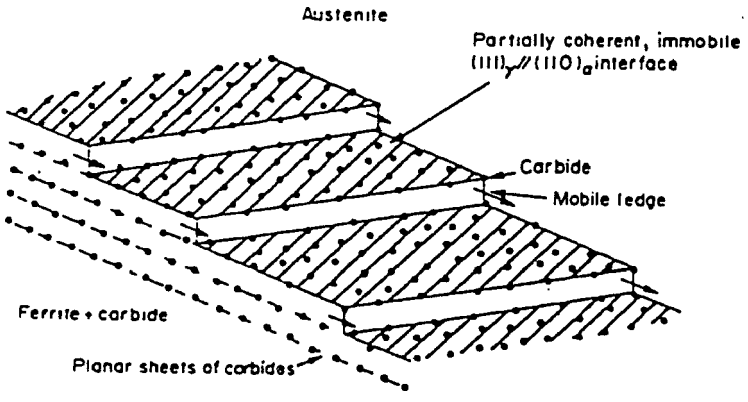

Figure 4.69 Planar interphase precipitation (schematic)

decreases as the temperature is lowered. It is obvious that the banded morphology and the relevant mechanism apply only during the $\gamma \rightarrow \alpha$ transformation (not before or after) and that the cooling rate must be slow enough so that the diffusion of microalloy atoms can take place.

In this study, the banded morphology of precipitates was only observed in very few areas in the HAZ of heat I welded with 5kJ/mm, which represents the most microalloy addition and lower cooling rate. This indicates that in the HAZ the special requirements for interphase precipitation can rarely be met.

4.5.2.2. RANDOM PRECIPITATION

Random distribution of precipitates is the predominant morphology observed during the HAZ electron microscopic examination. To produce these random precipitates, three precipitation sequences are possible:

1, Precipitation before the $\gamma \rightarrow \alpha$ transformation.

2, Precipitation after the $\gamma \rightarrow \alpha$ transformation, including during cooling and subsequent post-weld heat treatment.

3, Precipitation during the $\gamma \rightarrow \alpha$ transformation, nucleating on higher energy γ/α interfaces which do not require step propagation in order to migrate, and hence no banded morphology will be produced.

Figure 4.70 shows a common example of precipitates randomly distributed in ferrite. It is difficult to distinguish the particles which are precipitated before,

during or after the $\gamma \rightarrow \alpha$ transformation. Detailed examination shows that the random precipitates are distributed on dislocations and in the matrix of ferrite. The matrix precipitation is related to homogeneous nucleation which needs higher driving force; hence a higher supersaturation is required. Whereas in the case of heterogeneous dislocation precipitation, particle nucleation at much lower supersaturation can be observed. The dislocation precipitation of (V,Nb)C will be discussed in the next section.

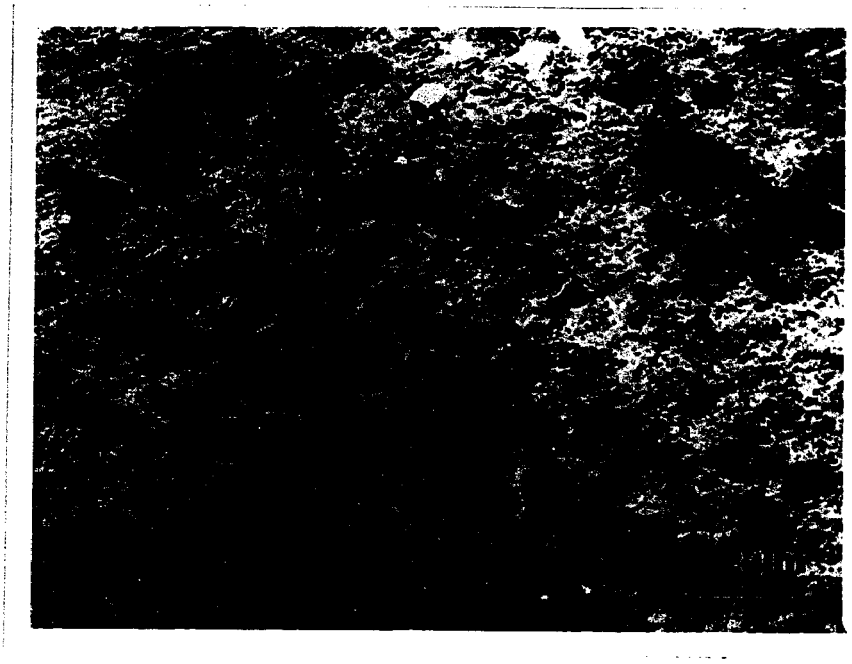

Figure 4.70 Random precipitation of (V,Nb)C in the HAZ of heat I, welded with 3KJ/mm and PWHT at 620°C for 10 hours.

4.5.3. DISLOCATION PRECIPITATION OF (V,Nb)C

Particles preferentialy precipitate on crystalline defects such as dislocations, grain boundaries and sub-boundaries. Figures 4.71a and 4.71b show the (V,Nb)C particles precipitated in dislocations. Figure 4.71a is a micrograph taken from the HAZ of heat I welded with 3kJ/mm and PWHT at 620°C for 10hours, showing ferrite laths with interlath cementite and intralath (V,Nb)C carbide particles. Arrows indicate the particles precipitated on dislocations. The low angle boundary marked as A-A in Figure 4.71a is characterized by fringe contrast (due to a network of parallel dislocations) and large cementite particles. Here, by using the dislocation model for tilt grain boundaryies [58], the relationship between the dislocation spacing, D, in the array, the Burgers vector, b, and the tilt angle, θ, has been established as $D \approx b/\theta$. For a rough estimation, D is measured from Figure 4.71a as 8nm (80Å) and taking b=a=2.866Å for α-Fe, the tilt boundary model, $\theta \approx 2°$ (0.035rad), is satisfied.

The (V,Nb)C particles precipitated in the dislocation array are visible, as arrowed and marked with "P" in Figure 4.71a.

Figure 4.71b, also showing dislocation precipitation in ferrite, is taken in the HAZ of the same heat I after PWHT but welded with 5kJ/mm.

Beside dislocation precipitation, matrix precipitation is also observed in Figures 4.71a and 4.71b. For either

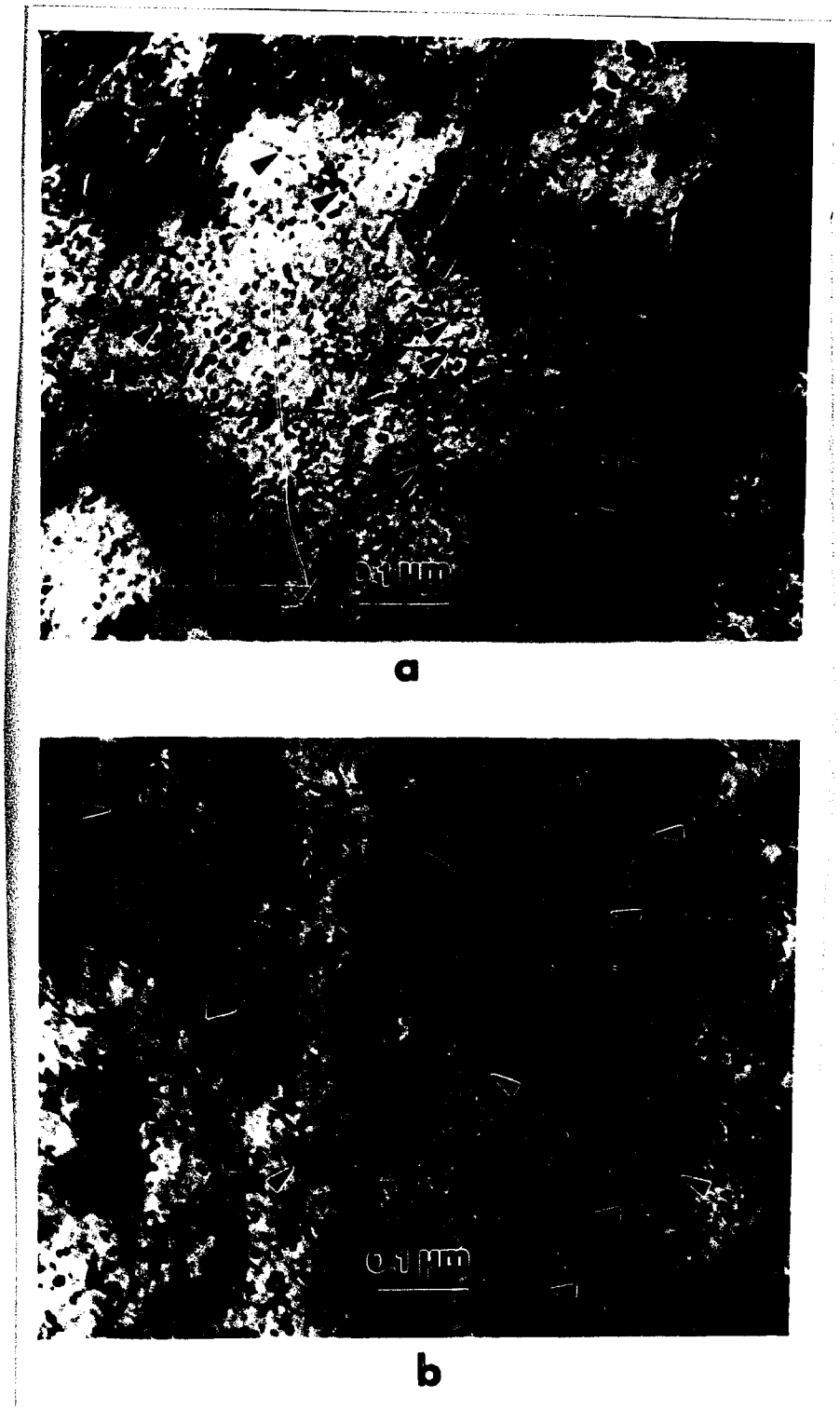

Figure 4.71 Dislocation precipitation of (V,Nb)C in the HAZ of heat I, (a) 3kJ/mm and PWHT 620°C/10hrs. (b) 5kJ/mm and PWHT 620°C/10hrs.

dislocation precipitation and matrix precipitation, the (V,Nb)C particle sizes of 5nm-15nm can be estimated.

The (V,Nb)C particles precipitated on dislocations and in the matrix serve as obstacles to the movement of dislocations. The extremely high hardness of V and Nb carbides, HV2094 for VC and HV2400 for NbC, and some expected similar high number for (V,Nb)C, indicates that the particles are sufficiently strong to force the dislocations to bow between them as shown in Figure 2.14. The Orowan mechanism, or looping mechanism, applies in this situation and the mechanism has been described in Section 2.3.3. In terms of Equations 2.8. and 2.9, the increment in flow stress due to particle resistance will be dependant on the volume fraction of the precipitates. The amount of microalloy additions, the weld heat input and PWHT will considerably affect the volume fraction of precipitates in the HAZ. However, the quantification of the volume fraction of precipitates in the HAZ is difficult, as explained below.

4.5.4. QUALITATIVE OBSERVATION ON PRECIPITATION

Three problems arise in quantification of the volume fraction of (V,Nb)C particles in the HAZ. First, the HAZ is a narrow region characterized by inhomogeneity in the microstructure, including the distribution of precipitates. It is difficult to choose the examination areas in the thin foil to be exactly representative of the distribution of the particles. Secondly, the (V,Nb)C particles observed in a TEM

bright field image could frequently be confused by the surface oxide particles as discussed before. Thirdly, using a centered dark field image may alleviate the oxide confusion, but (V,Nb)C usually precipitates with several variants, as shown in Figure 4.67. A CDF image from one (V,Nb)C reflection can not include the (V,Nb)C particles of other variants. Hence, particles counted in the CDF image may be far fewer than the overall number of the (V,Nb)C precipitates.

Nevertheless, some qualitative comparisons in precipitation behavior have been made, and are presented here:

(1) The content of vanadium and/or niobium in experimental heats is the principal variable that affects the volume fraction of precipitates in the HAZ.

Four representative heats, A,C,G and I, the four corners in the composition matrix, have been examined. The results of TEM examination on the HAZ are discussed as follows:

Heat A, welded with 3kJ/mm, PWHT at 620°C for 10hours.

Heat A has the least V and Nb contents (0.005%V and 0.004%Nb). Due to the lack of strong carbide-forming elements, V and Nb, the iron and manganese carbide, cementite $(Fe,Mn)_3C$ developed in the HAZ, as shown in Figure 4.63. No alloy carbide (V,Nb)C reflection was detected in the TEM SADP and the precipitate-like particles observed in the BF image were identified as Fe_3O_4.

Heat C, welded with 3kJ/mm, PWHT at 620°C for 10hours.

Heat C contains the most V (0.097%) and the least Nb (0.005%). Figures 4.72a,b,c, show the BF image, CDF image and SADP in the HAZ of heat C, respectively. The randomly distributed precipitates were examined. The CDF image was imaged from the (002) spot of (V,Nb)C.

Heat G, welded with 3kJ/mm, PWHT at 620°C for 10hours.

Heat G contains the most Nb (0.049%) and the least V (0.005%). Figure 4.73a,b,c shows the BF image, CDF image and SADP in the HAZ of heat G, respectively. The randomly distributed precipitates with similar particle size and distribution density to those of heat C (Figure 4.72) were observed.

Heat I, welded with 3kJ/mm, PWHT at 620°C for 10hours.

Heat I, with the most V (0.097%) and Nb (0.06%) contents, shows the largest volume fraction of (V,Nb)C particles, as shown in Figures 4.71a and 4.71b.

(2) The welding heat input somewhat affects the precipitation process.

Both Figure 4.71a and Figure 4.71b are taken from the HAZ of heat I at the same magnification. Figure 4.71a is of 3kJ/mm heat input whilst Figure 4.71b is of 5kJ/mm. Particles precipitated in the matrix in Figure 4.71b, the 5kJ/mm specimen, are somewhat coarser, compared with those in Figure 4.71a, the 3kJ/mm specimen. The former were precipitated during cooling and coarsening arose from the slower cooling rate and longer duration at higher temperatures due to the

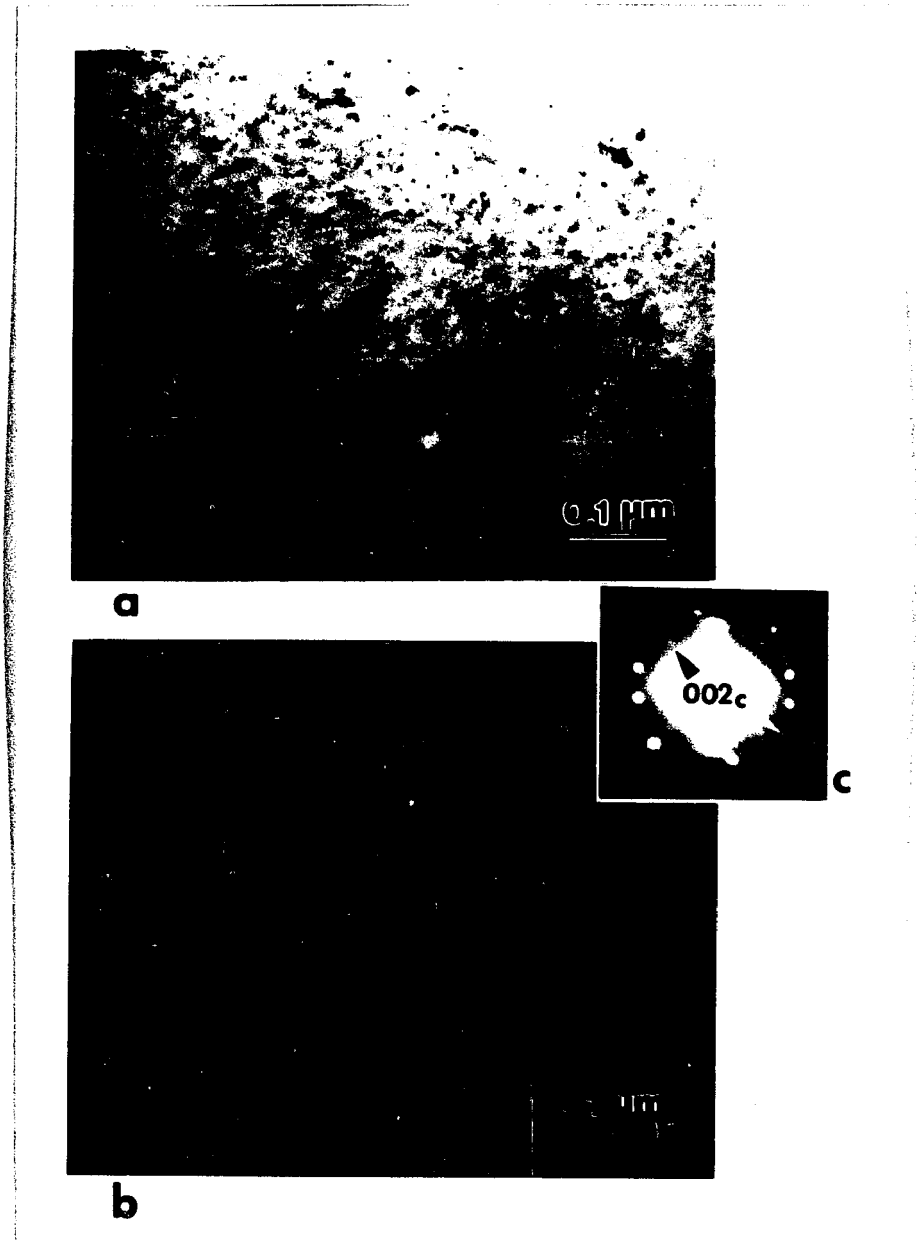

Figure 4.72 (V,Nb)C precipitates in HAZ of heat C, welded with 3KJ/mm and PWHT at 620°C for 10 hours. (a) BF image (b) CDF image (c) SADP

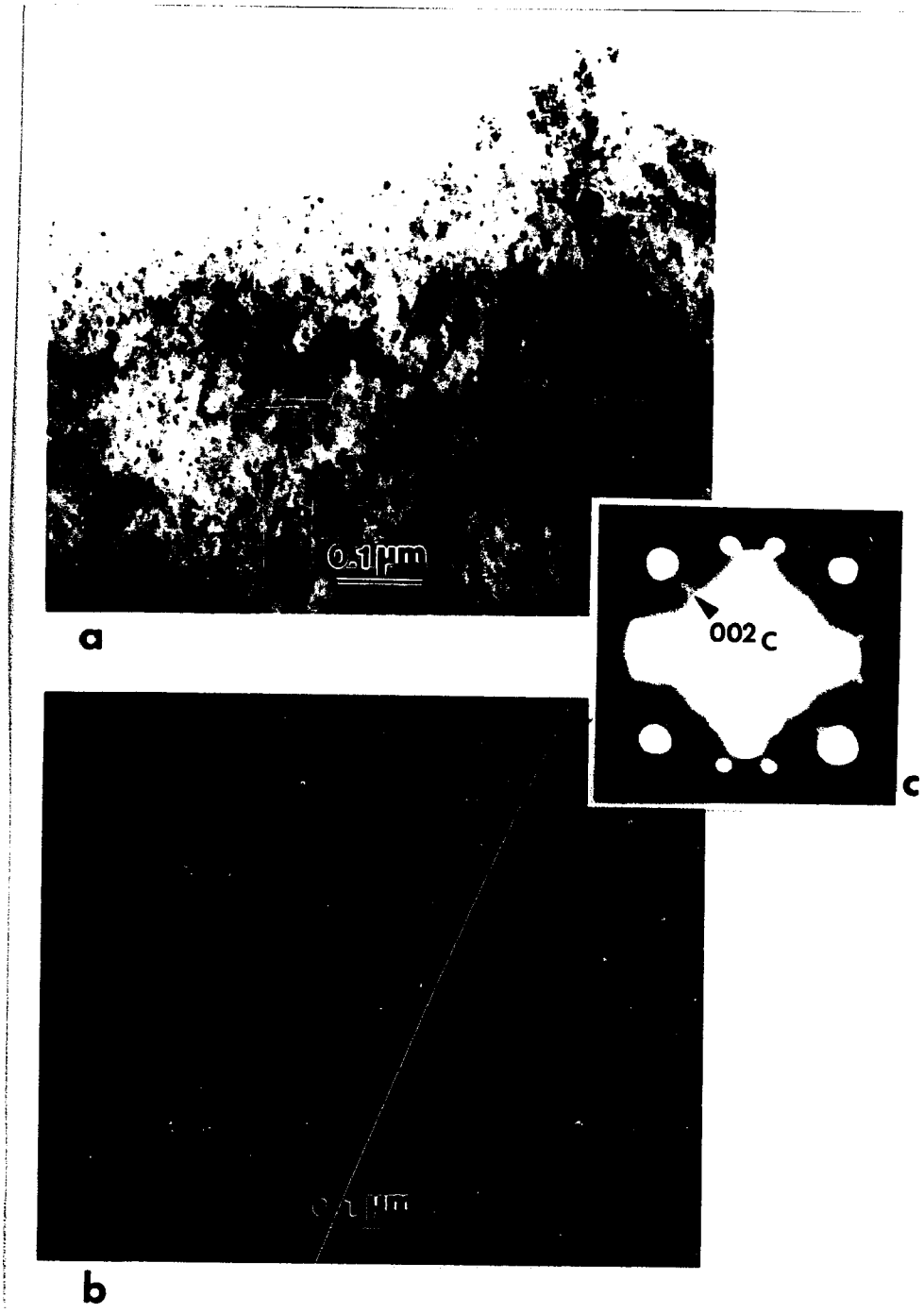

Figure 4.73 (V,Nb)C precipitates in HAZ of heat G, welded with 3KJ/mm and PWHT at 620°C for 10 hours. (a) BF image (b) CDF image (c) SADP

higher welding heat input. The dislocation precipitates, however, show similar particle size in both 3kJ/mm and 5kJ/mm specimens, suggesting that the dislocation precipitation occurs at relatively lower temperatures on cooling and during PWHT. These results agree with the results of Balliger and Honeycombe [54].

(3) The volume fraction of precipitates, as expected, increases with increasing PWHT time.

Figures 4.74a and 4.74b are the electron micrographs taken from the HAZ of heat C welded with 3kJ/mm and in the as-welded condition. Figures 4.73a and 4.73b are the same heat but post-weld heat treated at 620°C for 10hours. It is noticeable that the (V,Nb)C particle density increased as the PWHT was performed.

It can be summarized that the volume fraction of (V,Nb)C precipitates increases with increasing V and/or Nb contents, and with PWHT time. This is consistent with the variation in mechanical behavior described in previous sections, revealing the predominant contribution of (V,Nb)C precipitation. The slight coarsening of (V,Nb)C particles in the 5kJ/mm HAZ can be partially account for the lower hardness in the 5kJ/mm HAZ than in the 3kJ/mm HAZ.

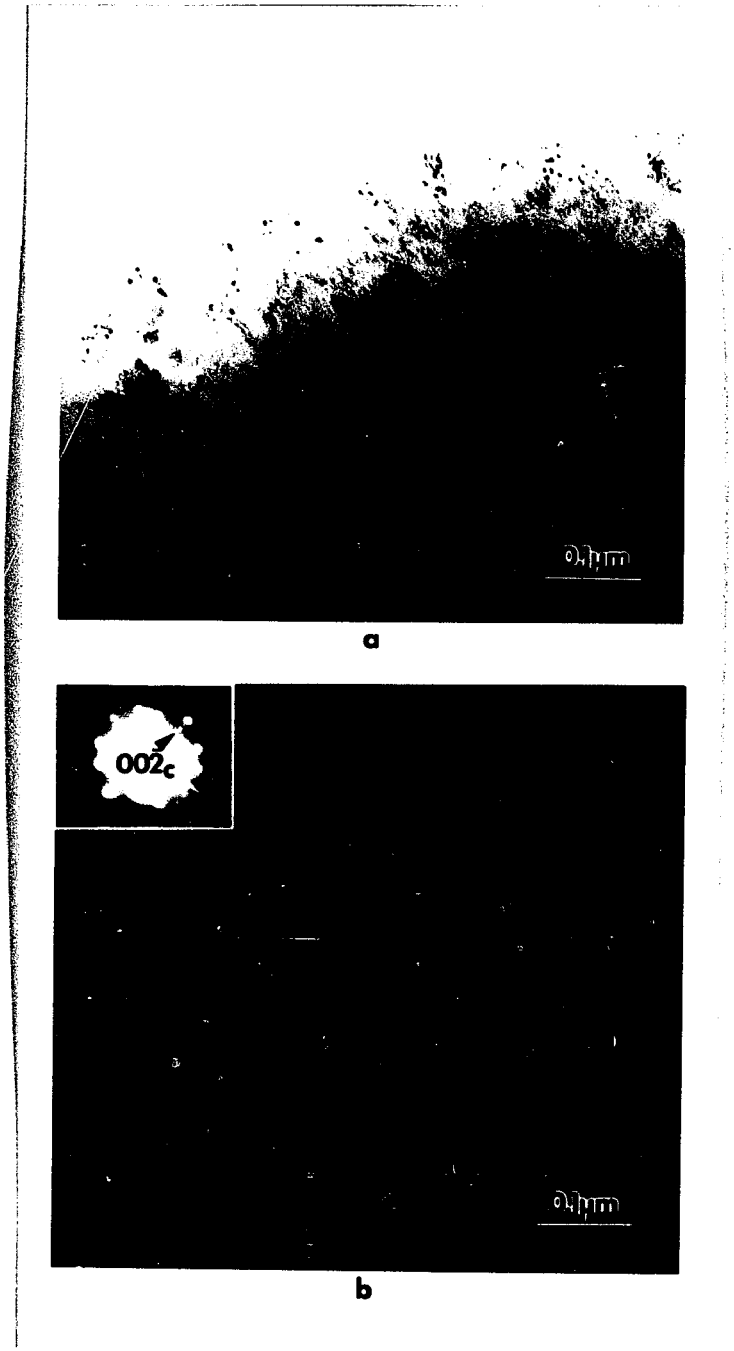

Figure 4.74 (V,Nb)C precipitates in the HAZ of heat C, welded with 3kJ/mm, as-welded condition

5. CONCLUSIONS

As a result of this investigation, a better understanding of the detrimental effect of the additions of microalloy V and Nb on impact toughness of the multipass heat affected zone (HAZ) of C-Mn steels was achieved. The following conclusions may be drawn from the research:

1, The average maximum microhardness in the coarse-grained HAZ increases with increasing additions of the microalloy elements V and Nb in all six experimental conditions (3kJ/mm and 5kJ/mm welding heat inputs, as-welded and PWHT at 620°C for 2 hours and 10 hours). The increase in HAZ hardness is caused by the precipitation of V and Nb carbides (V,Nb)C. Niobium is found to be a stronger precipitation hardening element than vanadium in the HAZ. Among the as-welded, PWHT 620°C/2hrs and PWHT 620°C/10hrs conditions, the greatest precipitation hardening is observed in the PWHT 620°C/2hrs condition in both 3kJ/mm and 5kJ/mm specimens.

2. The Nb addition effectively reduces the grain size in the coarse-grained HAZ whilst the V addition has little effect. Both Nb and V additions suppress development of grain boundary ferrite. Nb is more effective than V in suppressing grain boundary ferrite.

3. It is clear that the V and Nb additions degrade Charpy impact toughness of both normalized base plates and

HAZs in various conditions. The most significant detrimental effects of V and/or Nb additions on 50 Joule transition temperature (TT50J) are found in post-weld heat treated specimens. The worst case observed was the HAZ of Heat I, containing 0.097%V and 0.06%Nb (the highest microalloy addition), welded with 3kJ/mm and PWHT 620°C/2hrs, where the shift in TT50J is as much as 61°C due to V and Nb additions.

The same trends are observed in variations of HAZ TT50J toughness and the maximum HAZ hardness with varying V and Nb contents.

Post-weld heat treatment must be used with caution in HSLA steels microalloyed with V and/or Nb because it enhances the HAZ hardness but causes detrimental effects to HAZ toughness.

4, In multipass HAZ Charpy specimens tested at approximate transition temperatures, crack initiation sites are somewhat shifted from regions of maximum stress triaxiality to lower stress but higher hardness locations and show a cleavage appearance. In this case, the increase in transition temperature is attributed to the influences of V and Nb additions on the yield stress, σ_{ys}, and fracture stress, σ_f.

5, In the untempered HAZ region , during specimen preperation for electron microscope examination, iron oxide, Fe_3O_4, forms spontaneously on thin foil specimens as small, discrete and orientated particles. Both oxide and V/Nb carbide

(V,Nb)C have fcc structures and the former has a lattice parameter twice the latter. This makes study of (V,Nb)C precipitation difficult. The confusion of (V,Nb)C with oxide can be minimized by using jet-polishing followed by immediate examination of the foil. The V/Nb carbide can be distinguished from the oxide under some specific orientations.

6, Random distribution of precipitates of (V,Nb)C is the predominant morphology in HAZs, including matrix precipitation and dislocation precipitation, with particle sizes of 5-15nm. Banded morphology of (V,Nb)C precipitates is rarely observed in the HAZ.

7, The volume fraction of (V,Nb)C precipitates increases as increasing V and/or Nb contents in experimental heats. The volume fraction of (V,Nb)C precipitates also increases as PWHT is used.

6. SUGGESTIONS FOR FUTURE RESEARCH WORK

It has been noted that there are difficulties in preparing the HAZ Charpy specimens with a perfectly straight fusion line. Since the coarse-grained HAZ is so narrow it is difficult to test. Any slight imperfection in specimen preparation, such as a not flat fusion boundary or inaccurately placed notch, may cause data scatter. Weld simulation was at first considered in place of actual welding, however, the microstructural complexity of the multipass HAZ makes the simulation difficult. The ligament in a Charpy specimen with a multipass HAZ through which the crack frontier travels across includes various microstructural constituents resulting from more than one thermal cycle. A desirable alternative is a Gleeble simulation of a multipass weld which could duplicate the microstructural features presented in the ligament. A proper simulation design needs to be determined. This would have the advantage of thermal process control and thermal process repeatability. Using weld simulation of a multipass weld is therefore attractive and is suggested for future research work in this area.

REFERENCES

[1] L.Mayer Effect and Present Application of the Microalloying Elements Nb, V, Ti, Zr and B in HSLA Steel, HSLA Steels: Metallurgy and Applications, Proceedings of an International Conference on HSLA Steels '85, Beijing, China. Published by ASM, pp.29-44

[2] N.E.Hannerz Weld Metal and HAZ Toughness and Hydrogen Cracking Susceptibility of HSLA Steels as Influenced by Nb, Al, V, Ti and N, Proceedings of International Conference, November 1976, Rome, Italy, Published by ASM, pp.365-401

[3] N.E.Hannerz and M.M.Jonsson-Holmquist Influence of Vanadium on the Heat-Affected zone properties of mild steel, Metal Science, Vol.8, 1974, p.228

[4] G.R.Wang, T.H.North and K.G.Lewis Microalloying Additions and HAZ Fracture Toughness in HSLA Steels, Welding Journal, Vol.69, January 1990, p.14s

[5] R.E.Dolby The Effect of Niobium on the HAZ Toughness of High Input Welds in C-Mn Steels, Welding of HSLA Structural Steels, Proceedings of an International Conference, November 1976, Rome, Italy, published by ASM, pp.212-234

[6] E.G.Signs and J.C.Baker Effect of Columbium and Vanadium on the Weldability of HSLA Steels, Welding Journal, Vol.58, June 1979, p.179s

[7] M.Sato and M.Sakakibara A Study of Notch Toughness and Weld Softening in Submerged Arc Weld Heat Affected Zone for Q and T High Tensile Steels, Journal of Japanese Welding Society, Vol.40, 1971, p.649

[8] I.Kozasu Recent Development of Microalloyed Steel Plate (Metallurgical Design of 500 MPa Arctic Grade Plate), HSLA Steels: Technology and Applications, Conference Proceedings, 1983, Philadelphia, published by ASM, pp.593-607

[9] M.Okumura, N.Yurioka, T.Kasuya and H.J.Cotton Precipitation of HAZ Hardness After PWHT Stress Relieving Heat Treatments of Welded Steel Constructions, Proceedings of International Conference held in Sofia, Bulgaria, July 1987, published by PER-GAMON PRESS, p.61

[10] W.Bolliger, R.Varughese, E.Kaufmann, W.F.Qing, A.W.Pense and R.D.Stout The Effect of Welding and Fabrication Operations on the Toughness of A710 Steel, Proceedings of Microalloying '88, held in conjunction with the 1988 World Materials Congress, Chicago, Illinois, September 1988, Published by ASM, pp.277-290

[11] S.H.Zhang, Alloy Steel, Metallurgical Press, Beijing, China, 1980

[12] T.B.Massalski et al Binary Alloy Phase Diagrams
2nd Edition, August 1987, published by ASM

[13] J.F.Smith Phase Diagrams of Binary Vanadium Alloy, ASM International, July 1989, p.36

[14] X-Ray Powder Data File, Joint Committee on Chemical Analysis by Powder Diffraction Methods, published by ASTM

[15] R.W.K.Honeycombe Fundamental Aspects of Prediction in Microalloyed Steels, HSLA Steels: Metallurgy and Applications, Proceedings of an International Conference on HSLA Steels '85, November 1985, Beijing, China, published by ASM, pp.243-250

[16] P.H.Wright Microalloyed Forging Steels: a New Generation, Advanced Materials and Processes, Vol.137, December 1988, p.22

[17] K.J.Irvine Strong Structural Steels, Symposium Low Alloy High Strength Steels, Nuremberg, BRD, May 1970, p.p.1-7

[18] F.B.Pickering The Spectrum of Microalloyed High Strength Low Alloy Steels, Proceedings of International Conference on Technology and Applications of HSLA Steels, October 1983, Philadelphia, published by ASM

[19] T.N.Baker Twins in Iron Alloys Containing Vanadium, Acta Metallurgica, Vol.21, 1973, pp.261-266
Acta Met. 21,271,1972

[20] G.M.Smith and R.W.K.Honeycombe
Proceedings of 6th International Conference on Strength of Metals and Alloys, Melbourne, 1982, p.407

[21] T.Sakuma and R.W.K.Honeycombe Microstructures of Isothermally Transformed Fe-Nb-C Alloys, Metal Science, Vol.18, Sept. 1984, p.449

[22] T.Sakuma and R.W.K.Honeycombe Effect of Manganese on Microstructure of an Isothermally Transformed Fe-Nb-C Alloy, Materials Science and Technology, Vol.1, May 1985, p.351

[23] K.Easterling Introduction to the Physical Metallurgy of Welding, Butterworths Monographs in Materials, 1983, p.104

[24] R.M.Denys Wide-Plate Testing of Weldments: Part III - Heat-Affected Zone Wide-Plate studies, Fatigue and Fracture Testing of Weldments, ASTM STP 1058, p.204

[25] J.H.Devletion and W.E.Wood Principles of Joining Metallurgy, Metals Handbook, Vol. Vol.6, 9th Ed.1983, ASM, p.21

[26] R.W.K.Honeycombe The Plastic Deformation of Metals, London, 1984, p.181

[27] A.Kelly and R.B.Nicholson Precipitation Hardening, Progress in Materials Science, Vol.10, 1963, p.151

[28] H.Gleiter and E.Hornbogen Precipitation Hardening by Coherent Particles, Materials Science and Engineering, Vol.2, 1967/1968, pp.285-302

[29] L.M.Brown and R.K.Ham Strengthening Methods In Crystals, A.Kelly and R.B.Nicholson Eds., Applied Science, London, 1971, p.9

[30] V.Gerold and H.Haberkorn On the Critical Resolved Shear Stress of Solid Solutions Containing Coherent Precipitates, Physica Status Solidi, Vol.16, 1966, pp.675-683

[31] E.Nembach and E.Neite Precipitation Hardness of Superalloys by Ordered γ'-Particles, Progress in Materials Science, Vol.29, 1985, p.777

[32] H.Gleiter and E.Hornbogen Theorie der Wechselwirkung von Versetzungen mit kohärenten geordneten Zonen (I), Phys. Status Solidi. Vol.12, 1965, pp.235-250

[33] R.K.Ham, Trans. Japan Inst. Met. Vol.9 (supplement), 1968, p.52

[34] E.Orowan, Proceedings of the International Conference on Stress in Metals and Alloys,Institute of Metals, London, 1984, p.451

[35] J.C.Fisher, E.W.Hart and R.R.Pry The hardening of Metal Crystals by Precipitate 2 Particles, Acta Metallurgica, Vol.1, 1953. pp.336-339

[36] G.S.Ansell and F.V.Lenel Criteria for Yielding of Dispersion-Strengthened Alloys, Acta Metallurgica, Vol.8, 1960. pp.612-616

[37] R.W.Hertzberg Deformation and Fracture Mechanics of Engineering Materials, 3rd Ed., 1989, pp.54-56

[38] J.N.Cordea Effect of Composition and Processing on Strength and Toughness of Nb and V Treated Low Alloy High Strength Plate, Symposium Low Alloy High Strength Steels, May 1970, Nuremburg, BRD, pp.61-80

[39] L.Meyer, C.Straβburger and C.Schneider Effect and Present Application of the Microalloying Elements Nb, V, Ti, Zr and B in HSLA Steels, HSLA Steels: Metallurgy and Applications, Proceedings of an International Conference on HSLA Steels, November 1985, Beijing, China, published by ASM, p.33

[40] D.J.Abson, R.E.Dolby and P.H.M.Hart Trend in Steel and Consumables for Welding, Proceedings of Conference, The Welding Institute, London, Nov.1978, pp.75-101

[41] D.L.Albright, S.Bechet and K.Röhrig Principles, Properties and Applications of Tough High Strength Steel Castings, HSLA Steels: Technology and Applications, Proceedings of International Conference on Technology and Applications of HSLA Steels, October 1983, Philadelphia, published by ASM. pp.1137-1154

[42] R.E.Dolby HAZ Toughness of Structural and Pressure Vessel Steels - Improvement and Prediction, Welding Journal, August 1979, pp.225s-238s

[43] Same as [22], p.215

[44] Same as [22], p.371

[45] T.R.Wilshaw and A.S.Tetelman Fracture Testing at Low Strength Materials, Measurement of Mechanical Properties, Editor R.F.Bunshah, 1971, pp.103-121

[46] J.Weertman and J.R.Weerman Elementary Dislocation Theory, 1964, London, p.159

[47] N.J.Petch The Ductile-Brittle Transition in Fracture of α-Iron: I, Philosophical Magazine, Vol.3, 1958, pp.1089-1099

[48] A.S.Tetelman and A.J.McEvily,Jr. Fracture of Structural Materials, Wiley Press, New York, 1967

[49] S.H.Chen and J.W.Morris,Jr. Electron Microscopy Study of the Passivating Layer on Iron-Nickel Martensite, Met. Trans., Vol.8A, January 1977, pp.19-26

[50] K.B.Reuter, D.B.Williams, J.I.Goldstein and E.P.Butler Surface Oxide on fcc Iron-Nickel Alloys, Met. Trans., Vol.17A, Jan., 1986. pp.163-167

[51] J.W.Edington Practical Electron Microscopy in Materials Science, Macmillan Press, London, 1976, p.324

[52] J.Bosansky, D.A.Poter, H.Astrom and K.E.Easterling The Effect of Stress Annealing Treatments on the Structure of High Heat-Input Welds Containing Nb and Mo, Scandinavian Journal of Metals, Vol.6, 1977. p.125

[53] Z.Yan, W.Zhang and Y.Zhang Investigation of Carbonitride Precipitation and Strengthening Effect in As-rolled Low Carbon Steels Microallyed with Vanadium and Titanium, HSLA Steels: Metallurgy and Applications, Proceedings of an International Conference, November 1985, Beijing, China, pp.299-304

[54] N.K.Balliger and R.W.K.Honeycombe The Effect of Nitrogen on Precipitation and Transformation Kinetics in Vanadium Steels, Met. Trans., Vol 11A, March 1980, pp.421-429

[55] R.A.Ricks and P.R.Howell Rowing Mechanism for Interphase Boundary Migration in Alloy Steels, Metal Science, Vol.16, June 1982, pp.317-321

[56] R.A.Ricks and P.R.Howell The Formation of Discrete Precipitate Dispersions on Mobil Interphase Boundaries in Iron-Base Alloys, Acta Metallurgica, Vol.31, No.66, 1983, pp.853-861

[57] K.Campbell and R.W.K.Honeycombe The Isothermal Decomposition of Austenite in Simple Chromium Steels, Metal Science, Vol.8, 1974, pp.197-203

[58] A.G.Guy and J.J.Hren Elements of Physical Metallurgy, 3rd Ed., 1974

VITA

Mr. Peiyuan Xu was born on January 3, 1944 to Mr. Zhengnan Xu and Mrs. Debao Lu in Shanghai, China. He received his B.S. degree in Metallurgy in August of 1965 from Shanghai Jiao Tong University, Shanghai, China.

In September of 1965, Mr. Xu joined the Ship Material Research Institute, located in Dairen, China. As a metallurgical engineer, he was responsible for research and development of new ship steels and welding materials, as well as the applications of fracture mechanics to welded ship structure.

In October of 1978, Mr. Xu returned to Shanghai Jiao Tong University to obtain his M.S. degree in Materials Science and Engineering. Upon completion of his M.S. degree in January of 1981, he became a faculty member in the Department of Materials Science and Engineering, Shanghai Jiao Tong University. He offered the undergraduate courses of "Mechanical Properties of Metals" and " Strength and Fracture of Metals". He was awarded the "Outstanding Teaching, First Prize" award by the University in 1985 for his achievements in teaching. His research work in Shanghai Jiao Tong University was also in the area of Mechanical Behavior of Metals. with the emphasis on the Stress Corrosion and Corrosion Fatigue of High Strength Steels.

In September of 1987, Mr. Xu came to Lehigh University as a visiting scholar. At first he worked with Professor Robert P. Wei in the area of Electrochemical Mechanism(s) on Environment-Assisted Cracking. One year later, Mr. Xu was enrolled in a Ph.D. program. He entered the ATLSS Center in January of 1990 to continue his work on Ph.D. His advisor was Professor Alan W. Pense and his dissertation is entitled "Vanadium and Niobium Additions in Pressure Vessel Steels".

Mr. Xu is a member of over six professional societies, including ASM International, TMS, American Welding Society, Chinese Society for Metals, Chinese Society of Naval Architecture and Marine Engineering, Chinese Society for Corrosion and Protection.

In 1971 Mr. Xu was married to Fengmei Xu in Shanghai. Their son, Dingying was born in 1972.